A Role for Tunneling Nanotubes in Autophagy

Dissertation

der Mathematisch-Naturwissenschaftlichen Fakultät der

Eberhard Karls Universität Tübingen

zur Erlangung des Grades eines

Doktors der Naturwissenschaften

(Dr. rer. nat.)

vorgelegt von

Ana Luíza Diogo de Oliveira

aus Fortaleza, Brasilien

Tübingen

2023

Gedruckt mit Genehmigung der Mathematisch-Naturwissenschaftlichen Fakultät der Eberhard Karls Universität Tübingen.

Tag der mündlichen Qualifikation:	28.06.2024
Dekan:	Prof. Dr. Thilo Stehle
1. Berichterstatter:	Prof. Dr. Tassula Proikas-Cezanne
2. Berichterstatter:	Prof. Dr. Birgit Schittek

This doctoral thesis was supervised by Prof. Dr. Tassula Proikas-Cezanne and carried out between 1st August 2020 and 31st July 2023 at the Interfaculty Institute for Cell Biology at the Eberhard Karls University of Tübingen.

Erklärung

Hiermit erkläre ich,

- dass ich diese Arbeit selbst verfasst und keine anderen als die angegebenen Quellen und Hilfsmittel benutzt habe,

- dass ich die Richtlinien zur Sicherung guter wissenschaftlicher Praxis und zum Umgang mit wissenschaftlichen Fehlverhalten an der Eberhard Karls Universität Tübingen beachtet habe,

- dass die eingereichte Arbeit weder vollständig noch in wesentlichen Teilen Gegenstand eines anderen Prüfungsverfahrens gewesen ist.

Tübingen, den

Ana Luíza Diogo de Oliveira.

Explanation concerning manuscript

Part of the data produced by myself included in this thesis was published on the manuscript “The ABL-MYC axis controls WIPI1-enhanced autophagy in lifespan extension” (Sporbeck et al., 2023). Below, the detailed list of the data included in this thesis which has been published in the above-mentioned manuscript.

Data in this thesis	**Corresponding data in the manuscript**
Figure 9a (top row)	Figure 6b
Figure 9b, 9c and 9d	Figure 6d
Figure 10-8	Figure 6b (left)
Figure 11 (time lapse)	Figure 6g
Figure 21-8	Figure 6b (right)
Figure 34a	Suppl. Figure S8c
Figure 34b	Figure 6e
Figure 35a	Suppl. Figure S8d
Figure 35b	Figure 6f

Acknowledgments

First, I would like to thank Prof. Dr. Tassula Proikas-Cezanne once again for welcoming me in her laboratory and giving me the opportunity to pursue my life-long dream of doing a PhD. The past 3 years have been of so much learning for me, and for that I am immensely grateful. Thank you for all the time, patience, support, encouragement, and guidance.

In addition, I would like to thank Prof. Dr. Birgit Schittek for being my second supervisor, as well as for her time and attention.

Of course, all those lab days would not have been the same without the company and support of such amazing lab members: Katharina Sporbeck, Catherine Hunter, David Sebastian Schüssele, Patricia Katharina Haller, Carmen Julia Pastor Maldonado, and Maximilian Lucas Haas. For the constant lab support I also thank Heidemarie Riehle, Elena Kullmann and Anke Biedermann. Each of them has left a mark in me, and I am thankful for that. Thank you for all the time we got to spend together, the companionship, advices, technical tips in the lab, and most specially for the lunch breaks and all the chats about not-lab-related topics. My special thanks go to Patricia, Carmen and Catherine, for the friendship, support and cheering beyond the workspace.

For the financial support throughout my PhD studies, I would like to thank the Image-guided and Functionally Instructed Tumor Therapies (iFIT) Cluster of Excellence.

I would also like to thank Chara Charsou and Prof. Dr. Anne Simonsen for providing cells which facilitated my TNT investigation.

Many thanks to Nicole Fedrizzi, Nisha Prakash and Melek Özbek, for the friendship and companionship. I am also very grateful to Thalita Maranhão, for helping me stay sane with her attentive listening and always kind words. To Dr. Stefan Lutz, thank you for listening, understanding, and giving me time when I most needed it.

Additionally, I am so very grateful to my parents Verônica Diogo and Delmy Oliveira, and to my siblings Delmy Diogo and Beatriz Diogo Klein, for always believing in me, and for the constant support and cheering. Finally, I would like to thank my life partner Viktor Heidelbach, for the immense support, encouragement, care, love, and companionship. I do not see how this would have been possible without him by my side, so this is also his achievement.

Table of Contents

List of Figures

List of Tables

List of Abbreviations

2D	Two-dimensional
3D	Three-dimensional
ADP	Adenosine diphosphate
AIM	ATG8-interaction motif
AMP	Adenosine monophosphate
AMPK	Adenosine monophosphate-activated protein kinase
APS	Ammonium peroxydisulfate
APG	Autophagy related genes
ATG	Autophagy related gene
ATP	Adenosine triphosphate
AUTs	Autophagy genes
AVI	Audio video interleave
BPAN	Beta-propeller protein-associated neurodegeneration
BSA	Bovine serum albumin
CaMK	Calmodulin-dependent protein kinase
CaMKK	Calmodulin-dependent protein kinase kinase
Cas9	CRISPR-associated protein 9
cDNA	Complementary DNA
CMA	Chaperone-mediated autophagy
CRISPR	Clustered regularly interspaced short palindromic repeats
CVTs	Cytoplasm to vacuole targeting genes
DAPI	4’,6-Diamidino-2-phenylindole
DFX	Deferasirox
DIC	Differential interference contrast microscopy
DMEM	Dulbecco’s modified eagle’s medium
DMSO	Dimethyl sulfoxide
DNA	Deoxyribonucleic acid
DPBS	Dulbecco’s phosphate-buffered saline
DTT	Dithiothreitol
EBSS	Earle’s balanced salt solution
ECL	Enhanced chemiluminescence
EDTA	Ethylenediaminetetraacetic acid
EGFP	Enhanced green fluorescent protein
ER	Endoplasmic reticulum
ERK	Extracellular signal-regulated kinase
ESID	Electronically switchable illumination and detection
esiRNA	Endoribonuclease-prepared siRNA
FAC	Ammonium ferric citrate
FBS	Fetal bovine serum
FCS	Fetal calf serum
FM	Fluorescence microscopy

FTH	Ferritin heavy chain
FTL	Ferritin light chain
GABARAP	γ-aminobutyric acid receptor-associated protein
GFP	Green fluorescent protein
GIM	GABARAP-interacting motif
GSAs	Glucose-induced selective autophagy genes
GSK3	Glycogen synthase kinase 3
HCC	Hepatocellular carcinoma
HSC	Hepatic stellate cell
HSC70	Heat shock-cognate protein of 70kDa
HTT	Huntingtin
IGFs	Insulin-like growth factors
IM	Inverted microscope
IRS	Insulin receptor substrate
kDa	Kilodalton
KO	Knockout
LAMP-2A	Lysosome-associated membrane protein type 2A
LC3	Microtubule-associated protein 1A/1B light chain 3
LIR	LC3-interacting region
LRRK2	Leucine rich repeat kinase 2
LSM	Laser scanning microscope
MCR	Mitochondrial cargo receptor
MEK	Mitogen-activated protein kinase kinase
mRFP	Monomeric red fluorescent protein
mTOR	Mammalian target of rapamycin
mTORC	Mammalian target of rapamycin complex
NBIA	Neurodegeneration with brain iron accumulation
NudC	Nuclear distribution C
OMM	Outer mitochondrial membrane
ULK1	Unc-51-like kinase complex 1
p62/SQSTM1	Ubiquitin-binding protein p62/Sequestosome 1
PAGs	Peroxisome degradation by autophagy genes
PAZs	Peroxiphagy zeocin-resistant genes
PBS	Phosphate-buffered saline
PDDs	Peroxisome degradation-deficient genes
PDGFR	Platelet-derived growth factor
PFA	Paraformaldehyde
PHB-2	Prohibitin-2
PI3K	Phosphatidylinositol 3-kinase
PI3KC3	Phosphatidylinositol 3-kinase class III
PI3P	Phosphatidylinositol 3-phosphate
PI(3,5)P_2	Phosphatidylinositol 3,5-bisphosphate
PROPPIN	β-propellers which bind to phosphoinositides
PVDF	Polyvinylidene fluoride

Raf	Rapidly accelerated fibrosarcoma
Ras	Rat sarcoma virus
RFP	Red fluorescent protein
RNA	Ribonucleic acid
ROS	Reactive oxygen species
RPM	Rotations per minute
siRNA	Small interferent ribonucleic acid
SD	Standard deviation
SDS	Sodium dodecyl sulfate
siRNA	Small interfering RNA
STX17	Syntaxin 17
TBS	Tris-buffered saline
TEMED	N,N,N',N'-Tetramethyl ethylenediamine
TECPR1	Tectonin domain-containing protein
TNT	Tunneling Nanotube
TRIS	Tris (hydroxymethyl) aminomethane
TSC	Tuberous sclerosis complex
ULK1	Unc-51 like activating kinase 1
VEGF	Vascular endothelial growth vector
WB	Western blot
WGA	Wheat germ agglutinin
WIPI	WD-repeat protein interacting with phosphoinositides
WIR	WIPI interacting region

Abstract

Autophagy is a mechanism of clearance, through which cytoplasmic material is stochastically engulfed in a double membrane vesicle, named autophagosome, and degraded upon fusion with lysosomes. Four crucial players in autophagosome formation are the WIPI proteins, from WIPI1 to WIPI4, which participate in phagophore initiation, elongation, and closure. Interestingly, lysosomes and double membrane vesicles have been observed to travel intercellularly via Tunneling Nanotubes (TNTs), structures capable of mediating long-distance cytoplasmic exchange between cells. Both autophagy and TNTs have been linked to human health conditions such as cancer and neurodegeneration. This study aimed to investigate on the intersection between autophagy and TNTs, which so far remained to be unraveled.

Here, the traffic of autophagic membranes, decorated with WIPI proteins, via TNTs was observed. Moreover, this study revealed that modulation of autophagy levels also modulates the formation of TNTs, as well as the transfer of autophagic membranes from one cell to the other through TNTs.

Following the concepts of TNT intercellular communication, the present study also demonstrated TNT-mediated transfer of mitochondria in vitro, as well as mitochondria in association with the autophagy marker LC3.

Furthermore, the transfer of ferritin and its autophagic cargo receptor, NCOA4, via TNTs was visualized, and quantitative assessments revealed that iron overload can enhance TNT-mediated intercellular traffic of ferritin.

Finally, the presence of TNTs in liver cancer cell lines was observed, and in this context, it was found that the interaction partner of WIPI proteins, NUDC, is important for TNT formation. Surprisingly, WIPI1 itself was uncovered as a novel player in TNT biogenesis.

In summary, imaging and image processing techniques were employed to dynamically visualize TNT structures, and to identify the traffic of autophagic membranes, mitochondria, and ferritin between different types of cells in vitro. A role for TNT-mediated intercellular communication as a compensatory mechanism is discussed.

Zusammenfassung

Autophagie ist ein Clearance-Mechanismus, durch den zytoplasmisches Material stochastisch in einem Doppelmembranvesikel, dem sogenannten Autophagosom, eingeschlossen und bei der Fusion mit Lysosomen abgebaut wird. Vier entscheidende Akteure bei der Bildung von Autophagosomen sind die WIPI-Proteine, von WIPI1 bis WIPI4, die an der Initiierung, Verlängerung und Schließung von Phagophoren beteiligt sind. Interessanterweise wurde beobachtet, dass sich Lysosomen und Doppelmembranvesikel interzellulär über Tunnelnanoröhren (TNTs) bewegen, Strukturen, die den zytoplasmatischen Austausch über große Entfernungen zwischen Zellen vermitteln können. Sowohl Autophagie als auch TNTs wurden mit menschlichen Gesundheitszuständen wie Krebs und Neurodegeneration in Verbindung gebracht. Ziel dieser Studie war es, die Schnittstelle zwischen Autophagie und TNTs zu untersuchen, die bisher noch ungeklärt ist.

Dabei wurde der Transport von mit WIPI-Proteinen dekorierten autophagischen Membranen über TNTs beobachtet. Darüber hinaus ergab diese Studie, dass die Modulation des Autophagieniveaus auch die Bildung von TNTs sowie die Übertragung autophagischer Membranen von einer Zelle zur anderen durch TNTs moduliert.

Den Konzepten der interzellulären TNT-Kommunikation folgend, zeigte die vorliegende Studie auch den TNT-Transfer von Mitochondrien in vitro sowie von Mitochondrien in Verbindung mit dem Autophagie-Marker LC3.

Darüber hinaus wurde die Übertragung von Ferritin und seinem autophagischen Frachtrezeptor NCOA4 über TNTs visualisiert, und quantitative Bewertungen ergaben, dass eine Eisenüberladung den TNT-vermittelten interzellulären Verkehr von Ferritin verstärken kann.

Schließlich wurde das Vorhandensein von TNTs in Leberkrebszelllinien beobachtet und in diesem Zusammenhang festgestellt, dass der Interaktionspartner der WIPI-Proteine, NUDC, für die TNT-Bildung wichtig ist. Überraschenderweise wurde WIPI1 selbst als neuartiger Akteur in der TNT-Biogenese entdeckt.

Zusammenfassend wurden Bildgebungs- und Bildverarbeitungstechniken eingesetzt, um TNT-Strukturen dynamisch zu visualisieren und den Verkehr von autophagischen Membranen, Mitochondrien und Ferritin zwischen verschiedenen Zelltypen in vitro zu identifizieren. Eine Rolle der TNT-vermittelten interzellulären Kommunikation als Kompensationsmechanismus wird diskutiert.

CHAPTER 1 Introduction

1.1 Historical introduction into autophagy

The term autophagy originates from the Greek language and translates to "self-eating". It was brought into to the scientific community in 1860, when M. Auselmier stated in *Progress of Medical Science* that "Experimental researches made on animals subjected to a more or less absolute privation of food have shown that life may be maintained for a certain period at the expense of the substance of the organs, as is proved by the progressive diminution of the weight of the animal suffering from inanition. This mode of nutrition has long been termed autophagy…" (Karanasios & Ktistakis, 2016).

However, the term was only first coined to the cellular mechanism in 1963, by de Duve, after several important findings following the discovery of the lysosome. Most importantly, de Duve made sure to emphasize that autophagy might be not only a defense mechanism against stress, but actually a normal process which takes place in healthy cells, functioning in correlation with metabolic fluctuations (De Duve, 1963; de Duve, 1969).

Until the 1990's, thorough investigation was done on the regulation of autophagy through growth factor and amino acid depletion, and in 1993 the breakthrough discovery of the first autophagy related genes in yeast, termed APGs, brought the field one step further (Tsukada & Ohsumi, 1993). Several independent groups uncovered other autophagy genes in the following years: AUTs (autophagy) (Thumm et al., 1994), CVTs (cytoplasm to vacuole targeting) (Harding et al., 1995), PDDs (peroxisome degradation-deficient) (Titorenko et al., 1995), GSAs (glucose-induced selective autophagy) (Yuan et al., 1997), PAGs (peroxisome degradation by autophagy) (Sakai et al., 1998) and PAZs (peroxiphagy zeocin-resistant) (Mukaiyama et al., 2002). In 2003, a gene nomenclature was unified for these genes, namely "autophagy-related (ATG) genes" (Klionsky et al., 2003).

1.2 Autophagy

Autophagy is a highly evolutionarily conserved and essential mechanism for the maintenance of homeostasis, which mediates the degradation of cytoplasmic content (Mizushima et al., 2008). It acts as an important cytoprotective mechanism, promoting the clearance of unwanted material, such as damaged proteins and protein aggregates, old DNA molecules, defective organelles and even pathogens. Autophagy also contributes to the recycling of cellular resources, thereby providing nutrient and maintaining a constant cellular renewal. Therefore,

it plays a crucial role in cell development, growth, survival, immunity, and life span (Dikic & Elazar, 2018; Mizushima et al., 2008).

Briefly, autophagy involves the engulfment of intracellular cargo by a double-membrane vesicle, which is digested by acidic hydrolases obtained from lysosomal vesicles. It takes place even in basal levels but can also be induced as a response to cellular stresses, such as starvation and oxidative stress. Such process is strictly regulated, as it must be modulated upon necessity, but otherwise kept at low basal levels (Dikic & Elazar, 2018; Mizushima et al., 2008).

1.2.1 Types of autophagy

Autophagy may be divided in three main categories: macroautophagy, microautophagy and chaperone-mediated autophagy (CMA), which are all necessary for cellular homeostasis (Figure 1). Through macro- and microautophagy, large vesicles and organelles can be degraded, with macroautophagy comprising the engulfment of cargo by autophagosomes which only then fuse with lysosomes for digestion. Microautophagy involves the direct breakdown of cargo sequestered by endosomal vesicles or lysosomes (Klionsky, 2005; Mizushima & Komatsu, 2011; Mizushima et al., 2008). CMA, in its turn, involves the interaction of a constitutive chaperone, known as heat shock-cognate protein of 70kDa (HSC70), with the receptor lysosome-associated membrane protein type 2A (LAMP-2A) and promotes the selective degradation of soluble proteins (Massey et al., 2006).

Macroautophagy is composed of a few distinct and well characterized steps. Upon stimulation of autophagy, the first step is initiation, when an isolation membrane begins to form. Several proteins are recruited to participate in the process and contribute to the next step, namely elongation of the isolation membrane. Elongation is followed by the step of closure, where the isolation membrane becomes an autophagosome. The final step is recycling, where the autophagosome fuses with a lysosome, acquiring acidic hydrolases which promote digestion of the cytoplasmic cargo previously enclosed (Codogno et al., 2012). The detailed process of macroautophagy will be introduced further in this thesis. Here, the term “autophagy” is used to refer to macroautophagy.

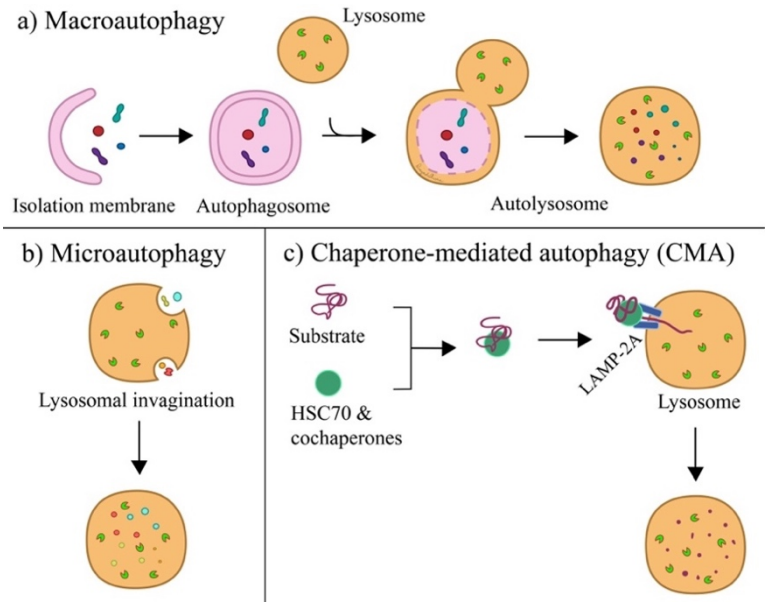

Figure 1. Autophagy may be divided into three main categories. a) Macroautophagy consists in the formation of an autophagosome in distinct steps. The first step is initiation, in which an isolation membrane starts to form. In elongation, the isolation membrane is extended until closure. Recycling takes place once the autophagosome fuses with a lysosome, forming an autolysosome and resulting in the degradation of cytosolic cargo. **b)** Microautophagy does not require the formation of autophagosomes and can directly degrade cargo by lysosomal invaginations. **c)** CMA comprises the specific degradation of a substrate, mediated by the direct delivery of cargo to lysosomes through the interaction of chaperone HSC70 and LAMP-2A. Figure prepared according to (Mizushima & Komatsu, 2011).

Autophagy takes place stochastically or selectively, where specific cellular components are targeted for degradation under diverse circumstances. Mostly, the process of selective autophagy relies on a certain cargo being targeted by receptor proteins, which mediate cargo's delivery to the autophagic machinery. There are several types of specific autophagy, among which are mitophagy and ferritinophagy (Gatica et al., 2018; Klionsky Abdel-Aziz, et al., 2021).

Mitophagy involves the specific degradation of mitochondria via autophagy (Lemasters, 2005). Mitochondria are of great importance for the maintenance of metabolic homeostasis. Processes such as fusion and fission must work in close association with mitophagy in order to keep a balanced mitochondrial turnover. However, when these processes do not function properly, damaged mitochondria can easily become a burden due to high production of ROS (reactive oxygen species), potentially resulting in apoptosis (Stotland & Gottlieb, 2015).

The specific degradation of mitochondria through autophagy is promoted by numerous cargo receptors. Mitochondrial cargo receptors (MCRs) localize to mitochondria and possess a LIR (LC3-interacting region) domain, which allows mitochondrial delivery by directly associating with members of the ATG8/LC3 family, important players found on the autophagic double membrane vesicle which will be later introduced. The list of known MCRs is long and continues to grow, including proteins as BNIP3, BNIP3L (NIX), BCL2L13, Cardiolipin, FUNDC1, FKBP8 and Prohibitin-2 (PHB-2). Proteins such as PINK and Parkin may additionally promote mitophagy by mediating ubiquitination and phosphorylation of proteins on the outer mitochondrial membrane (OMM). This results in their interaction with cargo receptors such as Optineurin and p62/SQSTM1, which also contain a LIR domain and can promote cargo delivery for autophagic digestion (Palikaras et al., 2018; Poole & Macleod, 2021).

Another type of selective autophagy is ferritinophagy, the specific degradation of ferritin, a protein responsible for cellular iron storage (Mancias et al., 2014). Iron is an essential metal for numerous cellular processes, among which are mitochondrial activity, oxygen transport and DNA metabolism (Zhang, 2014). The concentration of cytoplasmic free iron must be tightly regulated, as it may be cytotoxic and result in cell death. Within cells, iron is stored by a protein complex named ferritin, which is highly conserved throughout from bacteria to animals. The complex is composed of 24 subunits of two types, ferritin heavy chain (FTH) and ferritin light chain (FTL), which self-assemble in a nanocage: a hollow spherical structure capable of sequestering iron ions. Upon necessity, free iron can be released by the degradation of ferritin (De Domenico et al., 2006; Lee et al., 2022; Pantopoulos et al., 2012).

To date, the cargo receptor identified to be involved in the delivery of ferritin for autophagic degradation is the nuclear receptor coactivator-4 (NCOA4). NCOA4 directly associates with FTH1 and co-localizes with autophagy markers, such as LC3 and GABARAP, indicating its localization to autophagosomes. Although no LIR domain has been found in NCOA4, in contrast to other autophagic cargo receptors, its absence was observed to significantly impair ferritinophagy, indicating it as a genuine cargo receptor for ferritin (Dowdle et al., 2014; Mancias et al., 2015; Mancias et al., 2014).

1.2.2 The regulation of autophagy

Autophagy is modulated in response to nutrient availability through two major pathways: the mammalian target of ramapycin (mTOR) and the adenosine monophosphate (AMP)-activated

protein kinase (AMPK). The mTOR pathway is an important regulator of cell growth and is triggered by the presence of amino acids. AMPK, on its turn, senses low energy in the cell caused by declining levels of glucose. Together, mTOR and AMPK modulate the balance between catabolism and anabolism through the regulation of autophagy in a complex sequence of events (Dikic & Elazar, 2018).

Traditionally, several ATG and non-ATG proteins function in a hierarchical cascade of events to build autophagosomes in response to signals from AMPK or mTOR, a mechanism known as canonical autophagy. In canonical autophagy, autophagosomes are formed following the steps of initiation, nucleation, elongation, closure, and recycling. However, these steps may be bypassed, characterizing what is known as non-canonical autophagy. Through non-canonical autophagy, a cytoplasmic cargo can be degraded independent of AMPK or mTOR modulation and without the participation of proteins typically involved in canonical autophagy (Codogno et al., 2012; Reid et al., 2022).

1.2.2.1 Regulation of mTORC1

mTOR is a serine/threonine kinase that belongs to the phosphoinositide 3-kinase (PI3K)-related kinase family, which may be found in two different complexes, mTOR Complex 1 (mTORC1) and mTOR Complex 2 (mTORC2) (Dikic & Elazar, 2018; Wullschleger et al., 2006). Only mTORC1 can directly modulate autophagy (Dikic & Elazar, 2018; González & Hall, 2017; Wullschleger et al., 2006).

mTORC1 signaling plays an important role in protein, lipid and nucleotide synthesis, as well as in cell growth and autophagy, therefore acting on metabolic related conditions and cancer progression. Regulation of the TOR signaling pathway is modulated by numerous upstream players in an intricate system in response to growth factors, nutrient availability, energy levels and stress. Upon feeding, mTORC1 is active and the cellular metabolism shifts in the direction of anabolic processes, leading the cell towards energy storage and cell growth. mTORC1 is deactivated under nutrient deprivation, which directs cells towards catabolism (Dikic & Elazar, 2018; González & Hall, 2017; Wullschleger et al., 2006).

Hormones or growth factors which regulate the human metabolism, for instance insulin/the insulin-like growth factors (IGFs), play a fundamental role in the modulation of autophagy through the control of mTORC1. Phosphorylation of the insulin receptor substrate (IRS) results in the recruitment of phosphatidylinositol-3-kinase (PI3K), leading to the recruitment of pyruvate dehydrogenase kinase 1 (PDK1), which activates the protein kinase B

(AKT) by phosphorylation (Manning, 2004; Wullschleger et al., 2006). The AKT pathway is able to stimulate mTORC1 not only through the direct phosphorylation and inhibition of the tuberous sclerosis complex 2 (TSC2), which on its turn inhibits mTORC1 function, but also by altering the cellular AMP/ATP ratio, therefore inhibiting the activation of AMPK and its consequent stimulation of TSC2 (Hahn-Windgassen et al., 2005). In addition, AMPK can inhibit mTORC1 via direct phosphorylation of the complex (Gwinn et al., 2008). Another major pathway involved in the modulation of mTORC1 activity is MAPK/ERK. This pathway can also be activated by insulin signaling, initially leading to the activation of the Rat sarcoma virus, Ras. This results in the sequential activation of the proto-oncogene c-Raf, the mitogen-activated protein kinase kinase MEK1/2, and finally the mitogen-activated protein kinase ERK1/2, which inhibits TSC2 by phosphorylation (Ma et al., 2005; Wullschleger et al., 2006). Additionally, the Wnt pathway can also induce mTORC1 by inhibiting the glycogen synthase kinase 3β (GSK3-β)-mediated activation of TSC2 (Inoki et al., 2006). Finally, the TSC complex inhibits the small GTPase Rheb, which on its turn directly binds to and can activate mTOR through a GTP-dependent mechanism (Wullschleger et al., 2006). Figure 2 illustrates part of the regulation of mTORC1, as described above.

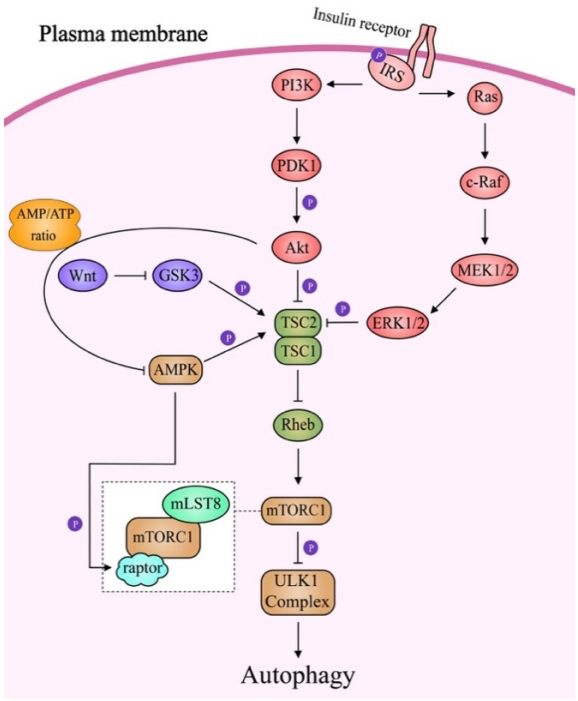

Figure 2. The regulation of mTORC1. mTORC1 responds to hormones and growth factors and can be modulated by several upstream players. Some of the main signaling pathways involved in mTORC1 modulation are the PI3K/Akt and the MAPK/ERK pathways. In addition, the Wnt pathway is also involved in mTORC1

regulation, through GSK3. Along with AMPK, these factors determine whether mTORC1 is activated or inactivated through the phosphorylation of the TSC complex. When active, mTORC1 inhibits the ULK1 complex, thereby hampering autophagy.

1.2.2.2 Regulation of AMPK

AMPK is a highly conserved and ubiquitously expressed energy sensor in eukaryotic cells. It is a serine/threonine-specific protein kinase found as heterotrimers, with one catalytic subunit α and two regulatory subunits β and γ.

AMPK modulates cellular metabolism, growth, and differentiation by sensing intracellular levels of ADP, AMP, and ATP. It is, therefore, a crucial player in the regulation of autophagy, positively modulating it in the direction of catabolism when activated (Hardie, 2007; Mihaylova & Shaw, 2011).

Upon low levels of ATP or elevated levels of Ca^{2+}, AMPK is activated by phosphorylation in its catalytic α subunit, promoted respectively by the serine-threonine kinase LKB1 or the calmodulin-dependent protein kinase kinase (CaMKKs) (Hawley et al., 2005; Oakhill et al., 2011; Stein et al., 2000; Woods et al., 2003). Simultaneously, both ADP and AMP can bind to the regulatory subunit γ, resulting in an allosteric effect that favours its phosphorylation by LKB1 or CaMKKβ, preventing dephosphorylation to ensure that AMPK remains active (Davies et al., 1995; Suter et al., 2006; Xiao et al., 2011). Furthermore, ATP competes with ADP and AMP to interact with the binding pocket in the regulatory subunit, in which case it promotes the dephosphorylation of AMPK (Mihaylova & Shaw, 2011; Suter et al., 2006; Xiao et al., 2011).

The AMPK-related protein kinases NUAK2 and BRSK2, also modulated by LKB1, phosphorylate AMPK, thereby stimulating autophagy in a long and complex cascade of events. In this context, the most important pathway regulated by AMPK is the mTORC1 pathway. In connection with the Wnt pathway, AMPK and GSK3 work together to sequentially phosphorylate TSC2 and inhibit mTOR signalling (Inoki et al., 2006). The regulation of AMPK, as just described, is illustrated in Figure 3.

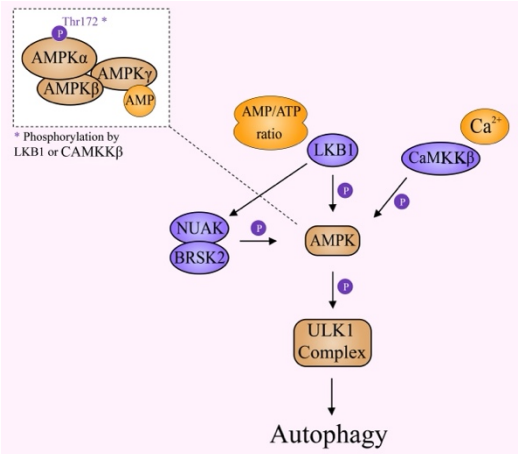

Figure 3. The regulation of AMPK. AMPK modulation responds to elevated levels of ATP and Ca^{2+}, which can stimulate the kinases LKB1, CaMKKβ, NUAK and BRSK2, the latter two also modulated by LKB1. These kinases induce AMPK, which on its turn activates the ULK1 complex, consequently leading to autophagy.

1.2.3 The formation of the autophagosome

Upon induction of autophagy, several ATG and non-ATG proteins are recruited to a particular region on the rough endoplasmic reticulum (RER) known as the phagophore assembly site (PAS). At the PAS, an omega-like shape structure known as the omegasome is formed (Walker et al., 2008). In this process, ATG proteins act hierarchically, participating in complexes or groups such as the ULK1 complex, the PI3KC3 complex I and the WIPI family of proteins, as well as the ATG12-5-16L1 and the ATG8/LC3 conjugation systems, all of which will be thereafter introduced. Recruitment of these proteins to the omegasome results in the de novo formation of a cup-shaped isolation membrane known as the phagophore (Dikic & Elazar, 2018). As the isolation membrane is gradually elongated, cytoplasmic cargo is progressively engulfed by it. Ultimately, the structure is sealed into a double-membrane vesicle known as the autophagosome. At this point, the autophagosome must be delivered to lysosomes for degradation of its cargo. This task is performed by cytoskeleton and motor adaptor proteins, which associate with autophagosomes and lysosomes to promote their movement towards each other along microtubules (Lorincz & Juhasz, 2020). Autophagosome fusion with lysosomes forms autolysosomes, in which a single membrane autophagic body is released into the lysosomal acidic environment. This results in the digestion of the autophagic body all together (Dikic & Elazar, 2018). Finally, membrane components can be retrieved, and nutrients are released into the cytoplasm, available for reuse by the cell (Zhou et al., 2022).

As above described, autophagy is modulated by mTORC1 and AMPK. In detail, initiation of autophagy takes place once the ULK1 complex, composed of ULK1, ATG13, FIP2000 and ATG101, is phosphorylated by AMPK (Kim et al., 2011) or dissociates from mTORC1 (Hosokawa et al., 2009). The active ULK1 complex phosphorylates elements of the phosphoinositide 3-kinase class III (PI3KC3) formed by VPS34, Beclin 1, ATG14, AMBRA1 and p115, giving start to phagophore formation (Karanasios et al., 2013).

Once active, the PI3KC3 complex mediates the localized production of phosphatidylinositol 3-phosphate (PI3P) at the omegasome, an important signaling mechanism for the recruitment of PI3P-effectors, for instance members of the WIPI (WD-repeat protein interacting with phosphoinositides) family of proteins (Itakura & Mizushima, 2010). The first WIPI proteins to arrive at the isolation membrane upon PI3P accumulation are WIPI1 and WIPI2, which heterodimerize and recruit ATG proteins involved in membrane elongation, such as the ATG12-5-16L1 conjugation system (Dooley et al., 2014; Polson et al., 2010).

In the ATG12-5-16L conjugation system, ATG12 and ATG5 are irreversibly bounded by the activities of ATG7, an E1-like ubiquitin-activating enzyme, and ATG10, an E2-like ubiquitin-conjugating enzyme (Mizushima et al., 1998). Then, the ATG12-5 complex associates with ATG16, resulting in the ATG12-5-16 complex. ATG16 is not necessary for the establishment of the ATG12-5 complex but is required for the formation of ATG12-5-16 oligomers, a feature functionally essential for autophagy (Kuma et al., 2002; Mizushima et al., 1999).

The ATG8/LC3 conjugation system depends on the action of the ATG12-5-16L1 complex. Initially, Pro-LC3 is cleaved by ATG4 proteases, producing its mature cytosolic form, namely LC3-I. Next, ATG7 and ATG3, respectively acting as E1 and E2-like ubiquitin enzymes, process LC3-I and deliver it to the ATG12-5-16L1 complex (Geng & Klionsky, 2008). Finally, the ATG12-5-16L1 complex mediates localized LC3-I lipidation, a process through which LC3-I is conjugated to phosphatidylethanolamine (PE) on the membrane of the nascent phagophore, therefore becoming membrane bound as LC3-II (Dooley et al., 2014; Kabeya et al., 2000; Kabeya et al., 2004). Furthermore, members of the ATG8/LC3 family continue recruiting elements of the autophagic machinery which contain a LIR domain, such as cargo receptors involved in specific autophagy (Dikic & Elazar, 2018; Johansen & Lamark, 2020). Finally, LC3-II found on the external autophagosomal membrane can be retrieved by ATG4, whereas LC3-II on the internal membrane is degraded along with the cargo (Kirisako et al., 2000).

Other contributors to membrane elongation are mitochondria, the Golgi complex, recycling endosomes and the plasma membrane, which provide membrane matter via ATG9-containing vesicles (Karanasios et al., 2013).

The remaining WIPI proteins, WIPI3 and WIPI4, are also directly connected with autophagosome formation. Whereas WIPI3 has been observed to localize to nascent phagophores and the lysosomal compartment upon starvation, interacting with FIP200 and the lysosomal marker LAMP2 (Bakula et al., 2017), WIPI4 directly interacts with ATG2, a lipid transfer protein. Together in a complex, WIPI4 and ATG2 function not only on membrane elongation, but also on the control of phagophore size (Bakula et al., 2017; Osawa et al., 2019). Additionally, recent research has demonstrated that WIPI3 also possesses an interacting region for ATG2, thereby contributing to membrane elongation of the nascent phagophore (Strong et al., 2021). Figure 4 depicts the autophagic machinery during autophagosome formation.

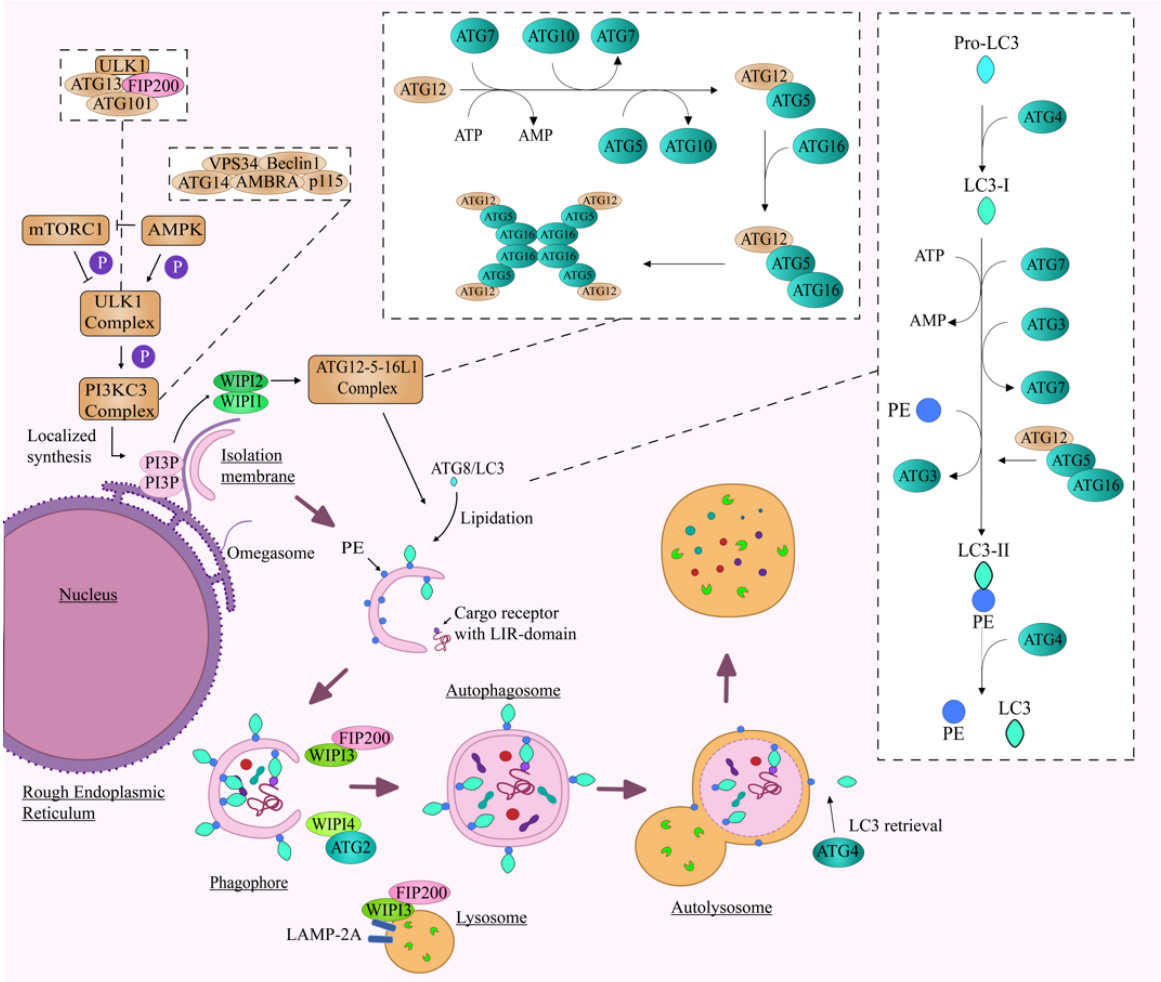

Figure 4. Autophagosome formation and the autophagic machinery. Autophagy is initiated by the modulation of ULK1, which is influenced by mTORC1 and AMPK. ULK1 activates the PI3KC3 complex, giving start to the

localized production of PI3P on the RER, where an isolation membrane starts to form. This structure, also known as phagophore, elongates with the support of several ATG proteins, among which are the WIPI family, the ATG12-5-16L1 complex and the ATG8-LC3 family. Eventually, the double membrane containing cytoplasmic cargo is sealed, becoming an autophagosome. Upon fusion with lysosomes, the autophagosome becomes an autolysosome which can successfully digest the engulfed cargo.

1.2.4 WIPI proteins

The β-propellers which bind to phosphoinositides (PROPPIN) protein family are a highly evolutionarily conserved group of proteins which are essential in the formation of autophagosomes (Proikas-Cezanne et al., 2015). The first human PROPPIN member to be identified was WIPI1, during a liver cDNA library screening in the fission yeast *Schizosaccharomyces pombe* in search of novel inhibitory factors of p53. Analysis of the human genome database allowed identification of other WIPI homologs and some of their corresponding splice variants, among these WIPI2, WIPI3 and WIPI4 (Proikas-Cezanne et al., 2004; Waddell et al., 2001). WIPI proteins are divided into two paralogous groups, one comprising WIPI1 and WIPI2, while the other group is formed by WIPI3 and WIPI4 (Proikas-Cezanne et al., 2004). All four WIPI homologs fold into an open "Velcro" seven-bladed β-propeller, with the most conserved blades, 5 and 6, acting as PI3P- or PI(3,5)P2-binding sites. On the other side of the β-propeller, blades 1 to 3 provide a site for numerous protein-protein interactions, functioning as a binding site for regulatory proteins (Figure 5) (Baskaran et al., 2012; Krick et al., 2012; Proikas-Cezanne et al., 2004).

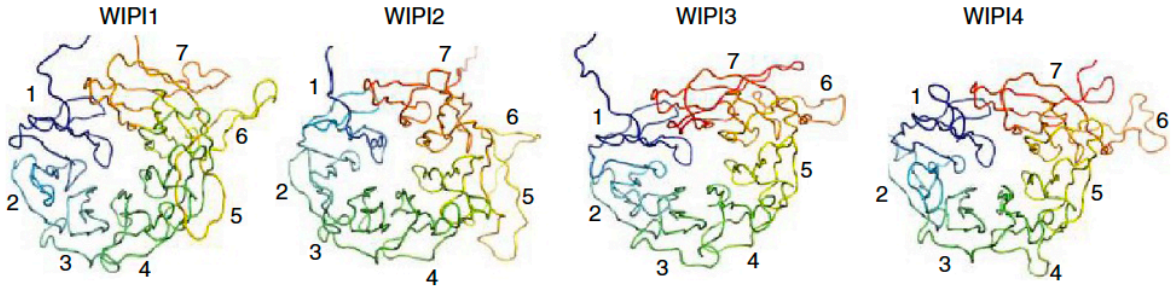

Figure 5. WIPI proteins fold into an open "Velcro" seven-bladed β-propeller. WIPI1-4 family members represented as revealed with structural homology modelling, with blades 1 to 7 depicted in different colors. Figure from (Bakula et al., 2017).

Proteomics analysis in the investigation of WIPI proteins has shown that WIPI1, WIPI2 and WIPI4 members interact with each other, and all four WIPI members display essential networks of complex protein interactions in the task of autophagosome formation (Figure 6). In the same study, NUDC, which will be thereafter introduced, was discovered as a new interaction partner of WIPI1, WIPI2 and WIPI4 (Bakula et al., 2017).

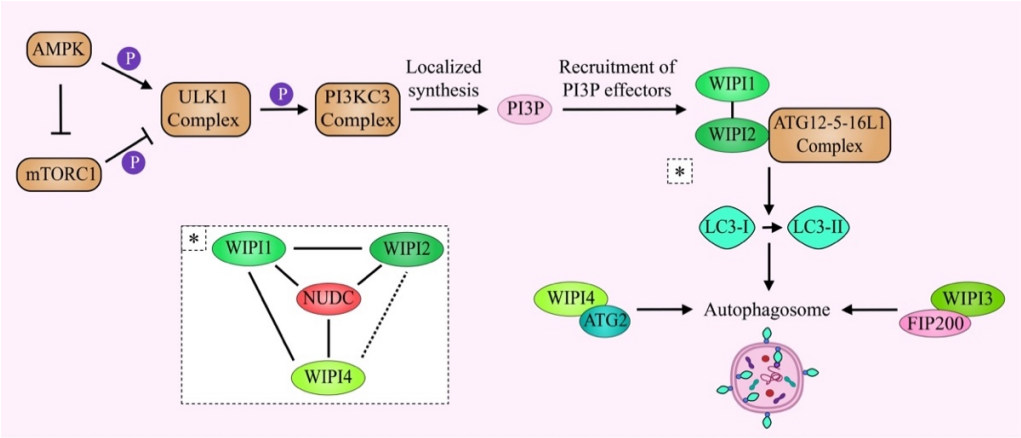

Figure 6. Schematic of WIPI proteins in the initiation of autophagy and autophagosome formation. Activated AMPK initiates autophagy by activating ULK1 complex, resulting in the localized production of PI3P. PI3P accumulation recruits WIPI1 and WIPI2, the latter directly interacting with Atg16L complex and mediating LC3 lipidation. AMPK activation releases WIPI4-ATG2A, which re-localizes to the growing phagophore, interacting with WIPI1. Meanwhile, the TSC complex inhibits mTORC1 while in association with WIPI3-FIP200. WIPI3-FIP200 also re-localize to the forming autophagosome and together with WIPI4-ATG2A, control phagophore elongation. In addition, WIPI1, WIPI2 and WIPI4 interact with NUDC. Protein interaction between WIPI2 and WIPI4 represented with dotted line to indicate low peptide count, according to LC-MS/MS analysis (Bakula et al., 2017).

1.2.4.1 WIPI1

WIPI1 was not only the first human PROPPIN to be identified, but also the first WIPI demonstrated to play a role in autophagy. Amino acid deprivation assays demonstrated how WIPI1 accumulated at vesicular structures in the shape of puncta, and that such process could be inhibited with Wortmannin, a PI3K inhibitor (Proikas-Cezanne et al., 2004). Furthermore, it was reported that WIPI1 partially co-localized with the autophagosomal marker LC3 (Kabeya et al., 2000), which also happened upon induction of autophagy through amino acid starvation (Proikas-Cezanne et al., 2004). The assessment of mammalian autophagy based on the observation and quantification of WIPI1 puncta was first published in 2007, as a novel tool for the further investigation of such crucial cellular mechanism (Proikas-Cezanne et al., 2007).

Induction of autophagy mediated by starvation or drug treatment promotes a substantial relocalization of WIPI1 to phagophores where LC3, ATG12 and ATG16L are present (Itakura & Mizushima, 2010; Vergne et al., 2009). Nevertheless, it is WIPI1's PI3P effector activity which is essential for its proper localization to autophagosomal membranes once the inhibition of PI3P production or downregulation of PI3KC3 successfully impair it (Itakura & Mizushima, 2010; Proikas-Cezanne et al., 2004). In line with this, WIPI1 mutants which are not able to bind PI3P do not colocalize to phagophores (Gaugel et al., 2012; Proikas-Cezanne et al., 2007). In addition, the correct localization of WIPI1 seems to be supported by WIPI2, the two forming a heterodimer, allowing for WIPI1's indirect interaction with the ATG12-5-16L1 complex (Bakula et al., 2017; Strong et al., 2021). Furthermore, the motion of WIPI1 to autophagosomes was shown to be facilitated by labile microtubules, on which WIPI1 moves bidirectionally (Geeraert et al., 2010).

WIPI1 decorates not only the outside of autophagosomal membranes, but also the inside of it, as seen in freeze-fracture immune-electron microscopy (Proikas-Cezanne & Robenek, 2011). This property of WIPI1 is exactly the basis for the monitoring of autophagy based on puncta assessment with fluorescence microscopy (Proikas-Cezanne et al., 2007).

Modulation of WIPI1 mostly follows the canonical route, through the inhibition of mTORC1, which results in the activation of ULK1 and PI3KC3 (Codogno et al., 2012). Most recently published, the expression of WIPI1 can also be modulated by the ABL/MYC axis, in which the tyrosine-protein kinase ABL induces ERK. This results in the activation of the transcription factor MYC/MAX, which supresses WIPI1 expression (Sporbeck et al., 2023). Although elevated cytoplasmic levels of Ca^{2+} can initiate canonical autophagy through CaMKK-mediated phosphorylation of AMPK (Hawley et al., 2005; Hoyer-Hansen et al., 2007), WIPI1 localization to nascent phagophores can also be directed non-canonically by increased levels of Ca^{2+} alone, independently of AMPK (Grotemeier et al., 2010; Pfisterer et al., 2011).

While increased levels of WIPI1 expression have been linked to extended lifespan (Xiao et al., 2018), abnormal levels of WIPI1 have been observed in several types of human cancer (Proikas-Cezanne et al., 2015). Additionally, WIPI1 has been reported as a prospective biomarker of acute myocardial infarction, facilitating early diagnostic (Liu et al., 2021). Moreover, mutations in WIPI1 have been associated with cases of anencephaly (Wang et al., 2019).

1.2.4.2 WIPI2

WIPI2 has several known splice variants, however only WIPI2B and WIPI2D accumulate in the shape of punctate structures on the nascent phagophore upon induction of autophagy (Mauthe et al., 2011). Initially, WIPI2 seems to act in a similar way as WIPI1. It is also downstream of ULK1, likewise acting as a PI3P effector which localizes to phagophores once autophagy is initiated, both on the inside and outside of autophagosomal membranes (Polson et al., 2010; Proikas-Cezanne & Robenek, 2011). On the nascent phagophore, WIPI2 co-localizes and interacts with WIPI1, where they heterodimerize. WIPI2 specifically uses a site between its blades 2 and 3 for binding ATG16L1's WIPI2 interacting region (W2IR) for recruitment of the ATG12-ATG5-ATG16L1 complex, thereby promoting local lipidation of LC3 (Bakula et al., 2017; Dooley et al., 2014; Polson et al., 2010; Strong et al., 2021). Assisted by WIPI1, WIPI2 is essential for LC3 conjugation (Dooley et al., 2014; Polson et al., 2010), as its downregulation resulted in the accumulation of omegasome structures which did not contain LC3, indicating that membrane elongation and phagophore assembly could not take place (Polson et al., 2010).

In addition to its function in canonical autophagy, WIPI2 also participates in xenophagy for clearance of the bacterial pathogen *Shigella*. The cargo receptor Tectonin domain-containing protein (TECPR1) was identified co-localizing with ATG5 and directly interacting with WIPI2 at phagophores containing *Shigella*, mediating its specific targeting for digestion by selective autophagy (Ogawa et al., 2011). Another example of WIPI2 in xenophagy is during *Salmonella* infection. Targeted by p62, *Salmonella*-containing vacuoles are engulfed by phagophores, where WIPI2 promotes LC3 lipidation through the recruitment of the ATG12-5-16L1 complex (Dooley et al., 2014). Finally, WIPI2 may also be modulated in a non-canonical fashion independent of mTORC1 by the leucine rich repeat kinase 2 (LRRK2), a protein which plays a significant role in Parkinson's disease (Manzoni et al., 2013).

Abnormal expression of the WIPI2 gene has been associated with various types of cancer (Proikas-Cezanne et al., 2015). Moreover, WIPI2 is deeply connected to neuronal autophagy and neurodegeneration, which will be elaborated upon in a subsequent section of this study.

1.2.4.3 WIPI3

WIPI3 also binds PI3P and PI(3,5)P2, and is able to localize to nascent phagophores, co-localizing with autophagy markers such as ATG12, LC3 and p62. Although WIPI3 puncta are

smaller and simpler than the ones formed by WIPI1 and WIPI2, a significant increase in the number of puncta positive cells was observed upon starvation and lysosomal inhibition, while inhibition of PI3K resulted in less puncta. WIPI3 has been shown to act further down the cascade in the control of phagophore size during biogenesis, as its downregulation resulted in the accumulation of elongated double-membrane structures. Under the same circumstances, accumulation of WIPI2 punctate structures, in fluorescence microscopy, and conjugated LC3, in western blotting analysis, were also observed, confirming a block in autophagosome biogenesis downstream of WIPI2 (Bakula et al., 2017).

Interestingly, WIPI3 seems to function not only controlling phagophore expansion and closure, but also upstream of WIPI1 and WIPI2. WIPI3 also localizes to the lysosomal compartment, where it interacts directly with FIP200 and the TSC complex through AMPK-phosphorylated TSC2, thereby playing a crucial role in the modulation of mTORC1. Once mTORC1 is active and localizes to lysosomal membranes, WIPI3 is no longer observed there. Starvation also leads to the re-localization of WIPI3 to nascent autophagosomes, where it is seen to co-localize with FIP200 and other WIPI proteins (Bakula et al., 2017).

Recently, WIPI3 has been observed interacting with ATG2's WIR-motif, an association which takes place between blades 1 and 3 (Ren et al., 2020; Zheng et al., 2017), similar to WIPI2's binding to ATG16L1 and WIPI4's binding to ATG2 itself (Strong et al., 2021). However, the WIPI3-ATG2 interaction seems to be weaker than the one between WIPI4-ATG2 (Ren et al., 2020).

As for other WIPIs, abnormal expression of WDR45B, the gene coding for WIPI3, in the cancer field has been linked to numerous types of human tumors (Proikas-Cezanne et al., 2015). Additionally, WIPI3 plays a crucial role in neuronal autophagy (Ji et al., 2021), and has been associated with neurodevelopmental disorders (Almannai et al., 2022; Najmabadi et al., 2011; Suleiman et al., 2018). This topic will be further explored in an upcoming section of this thesis.

1.2.4.4 WIPI4

WIPI4 is also a PI3P effector, and like WIPI3, forms small puncta while discreetly localizing to the membranes of nascent autophagosomes upon nutrient deprivation. Downregulation of WIPI4 similarly results in a blockage of autophagosome formation, with the accumulation of open double-membrane structures at omegasomes, as well as the accumulation of WIPI2 puncta and higher LC3-II/LC3-I ratio (Bakula et al., 2017).

Downstream of WIPI1 and WIPI2, WIPI4 acts in complex with ATG2, controlling phagophore elongation (Bakula et al., 2017; Ren et al., 2020). The specific and strong binding between WIPI4 and ATG2 takes place exactly in blade 1, closely related to WIPI3's site for ATG2 binding (Bakula et al., 2017; Ren et al., 2020; Zheng et al., 2017). ATG2 is involved in lipid metabolism and is responsible for mediating direct lipid transfer to the elongating phagophore membrane (Osawa et al., 2019; Valverde et al., 2019). The correct localization of ATG2 to omegasomes seems to be dependent on PI3P (Pfisterer et al., 2014).

Interestingly, WIPI4-ATG2 has also been reported to play a critical role upstream of WIPI1 and WIPI2, whereby it forms a complex with AMPK and ULK1 under basal conditions. Once AMPK is activated and autophagy initiation takes place, WIPI4-ATG2 dissociates from it, migrating to nascent phagophores to control its maturation and elongation (Bakula et al., 2017). In contrast with previous data, where WIPI1 and WIPI2 did not respond to glucose deprivation (McAlpine et al., 2013), Bakula et al., reported enhanced localization of WIPI4 to phagophores upon glucose starvation, confirming the direct link between AMPK-ULK regulation and WIPI4 activity (Bakula et al., 2017).

Mutations in the WDR45 gene, which codes for WIPI4, have been reported in several human tumor types (Proikas-Cezanne et al., 2015). In addition, although ubiquitously expressed in all tissues, WIPI4 is a pivotal player in brain development (Noda et al., 2021). Accordingly, mutations in WDR45 have been consistently linked to neurodegeneration. More in-depth coverage on WIPI4 and neurodegenerative conditions will be provided in a later section of this introduction.

1.2.5 NUDC

Recent proteomics analysis uncovered NUDC, the nuclear distribution C, as a novel interaction partner of WIPI1, WIPI2 and WIPI4, a discovery later confirmed with co-immunoprecipitation (Bakula et al., 2017).

NUDC was first identified in fungi as a modulator of nuclear movement (Osmani et al., 1990). Nowadays, it is known that NUDC regulates actin dynamics (Zhang et al., 2016) and dynein-promoted actions (Aumais et al., 2001), such as nuclear transport, neuronal vesicle transport, lysosome or endosomal transport, as well as phagosome movement (Riera & Lazo, 2009). Most importantly, NUDC plays a role in mitosis and cytokinesis, and research has shown that its loss affects the stabilization of the microtubule/dynein/dynactin complex,

leading to cytokinesis failure and resulting in bi- or multinucleated cells with enlarged nuclei (Aumais et al., 2003; Zhou et al., 2003).

In cancer, members of the NUDC family have been linked to invasion, proliferation, and metastasis (Han et al., 2018; Suzuki et al., 2007). More specifically, in the context of liver cancer, NUDC has been pointed out by the Human Protein Atlas as an unfavorable prognostic marker, with poor survival rates when highly expressed (Ponten et al., 2008).

1.3 Image-based autophagy assessments

One straightforward and convenient method for investigating on autophagy is the assessment of puncta through fluorescence microscopy. As above introduced, upon induction of autophagy several ATG and non-ATG proteins, for instance members of the WIPI family or LC3, localize to the forming phagophore to assist autophagosome formation. Based on this principal, fluorescently labelled autophagy markers may be employed to allow visualization and quantification of the abundance of autophagosomes in cells (Figure 7). These are observed as punctate structures, also known as puncta. The application of cell lines stably expressing fluorescently tagged WIPIs or LC3 constitutes a robust tool for the investigation of autophagy (Klionsky Abdel-Aziz, et al., 2021; Thost et al., 2015). Alternatively, cells may also be transiently transfected or immunostained (Klionsky Abdel-Aziz, et al., 2021; Schussele et al., 2022).

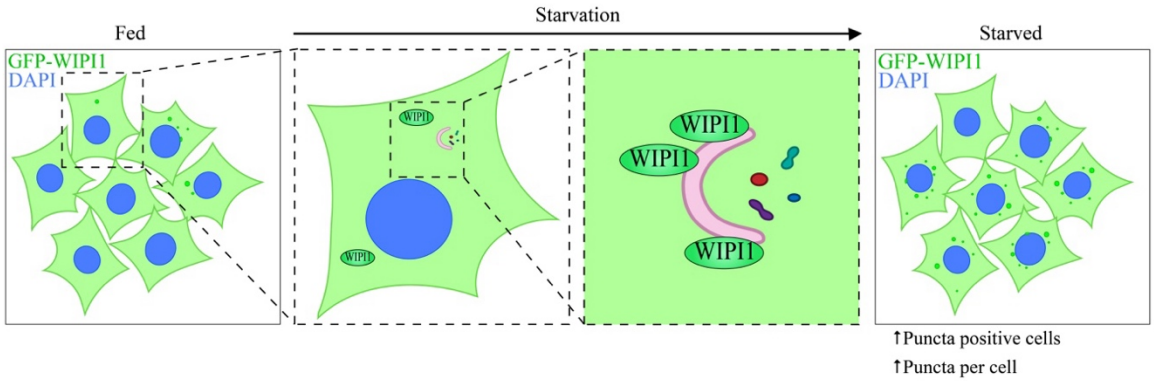

Figure 7. Monitoring autophagy based on the assessment of puncta. Upon starvation and consequent initiation of autophagy, WIPI1 protein localizes to nascent phagophore membranes and forms punctate structures. Autophagy may therefore be assessed via the quantification of puncta-positive cells or puncta per cell. Figure prepared according to (Thost et al., 2015).

Quantifying fluorescent WIPI, as well as LC3, puncta through fluorescence microscopy may be achieved in different manners. For WIPIs, one can quantify the number of puncta positive cells over the total amount of cells, or the abundance of puncta per cell. If investigating on LC3, the quantification of puncta per cell is more appropriate. At present, automated quantification offers powerful and efficient analysis of large sample sizes, although automation is not always an option. In these cases, one may rely on manual quantification as a steady method, although labor intensive (Klionsky Abdel-Aziz, et al., 2021; Schussele et al., 2022; Thost et al., 2015).

Furthermore, the application of tandem fluorescence constructs, such as RFP-GFP, to tag autophagy proteins provides information regarding autophagic flux. After closure, autophagosomes must be fused with lysosomes to mediate cargo digestion. However, in an acidic environment, GFP is quenched due to its sensitivity to acidic conditions. The result is a red only signal instead of red and green, thereby allowing differentiation between autophagosomes and autolysosomes (Klionsky Abdel-Aziz, et al., 2021).

1.4 Autophagy in health and disease

Autophagy's impact extends from the cellular to the physiological level. Physiologically, autophagy plays a role in aging and lifespan, as well as in several health conditions, such as cancer, neurodegeneration, metabolic syndromes, infection and immunity, heart and liver diseases, among others (Dikic & Elazar, 2018; Klionsky, Petroni, et al., 2021; Mizushima et al., 2008).

In cancer, autophagy acts as a double-edge sword depending on the disease stage. Before the onset of cancer, autophagy can be cytoprotective, with its deficiency increasing the risk of disease (Klionsky, Petroni, et al., 2021; Liang et al., 1999). On the other hand, once tumorigenesis has established itself, autophagy can contribute to treatment resistance in the tumor microenvironment, resulting in disease progression (Apel et al., 2008; Klionsky, Petroni, et al., 2021; Liu et al., 2011). However, mechanistic details concerning autophagy's role in the development of drug resistance remain to be elucidated. The aberrant expression of human WIPI genes has been associated to numerous types of tumors, and autophagy seems to contribute to tumor occurrence and therapy resistance (Proikas-Cezanne et al., 2015; Proikas-Cezanne et al., 2004). Furthermore, there is evidence that mitochondria plays a key role in chemoresistance (Pasquier et al., 2013; Pinto et al., 2021), where the modulation of mitophagy has been proposed as a crucial factor (Sun et al., 2023).

The main feature of many neurodegenerative diseases consists in the neuronal accumulation of mis- or unfolded protein aggregates, which ultimately results in cell death. A deficiency in autophagy may as well result in the accumulation of such aggregates once the mechanism for cellular clearance does not function effectively (Karsli-Uzunbas et al., 2014; Komatsu et al., 2006). Besides the accumulation of protein aggregates, loss of mitochondrial homeostasis and the buildup of dysfunctional mitochondria resulting in elevated cellular levels of ROS have also been indicated as causative of neurodegeneration (Fivenson et al., 2017; Pickrell et al., 2015). Indeed, several proteins which have been linked to the development of neurodegenerative conditions play a role in either autophagic or lysosomal degradation - such as WIPI proteins (Gan-Or et al., 2015; Jackson et al., 2017).

Proteins belonging to the WIPI family have been associated with neuronal developmental issues and neurodegeneration as well. Missense mutations in the WIPI1 gene have been reported as causative of anencephaly, due to its potential role in neuronal tube formation during embryonic development (Wang et al., 2019). In WIPI2, missense mutations have been identified in patients with neurological conditions characterized by microcephaly, global developmental delay, and skeletal abnormalities (Jelani et al., 2019; Maroofian et al., 2021). Furthermore, research has recently linked age-related decline of neuronal autophagy to a decay in the phosphorylation of WIPI2, a process which could potentially lead to neurodegeneration (Stavoe et al., 2019). WIPI3 seems to also play an essential role in neuronal autophagy (Ji et al., 2021), with its absence resulting in impaired memory and learning, as well as motor deficiency in mice (Ji et al., 2020). In line with this, a neurodevelopmental disorder characterized by global developmental delay, microcephaly, cerebral atrophy, spastic quadriplegia, and refractory epilepsy was identified in patients possessing mutations in the WDR45B gene. The condition has been documented in various clinical reports and is now identified as El-Hattab-Alkuraya syndrome (Almannai et al., 2022; Najmabadi et al., 2011; Suleiman et al., 2018). Lastly, concerning WIPI4 proteins, *de novo* variants of the WDR45 gene have been pointed as causative of a condition characterized by neurodegeneration with brain iron accumulation (NBIA), in which patients suffer from psychomotor and cognitive developmental delay, as well as early onset parkinsonism and dementia (Haack et al., 2012; Saitsu et al., 2013). The condition is currently known as Beta-Propeller Protein-Associated Neurodegeneration (BPAN) (Hayflick et al., 2013). Furthermore, mutations in WDR45 have been associated to other neurodegenerative diseases besides BPAN, among which are Rett-like syndrome and West syndrome (Cong et al., 2021).

1.5 Intercellular communication and Tunneling Nanotubes

Tunneling nanotubes (TNTs) are cellular structures which allow for cytoplasmic continuity and intercellular communication with the transfer of distinct cargoes, such as calcium, nucleic acids, proteins, mitochondria, lysosomes, vesicles, and pathogens (Dupont et al., 2018; Zurzolo, 2021). TNTs were first reported in 2004 by Rustom et al. (Rustom et al., 2004), after being observed in cell culture of rat PC12 cells. These cell-to-cell connections have already been reported not only in numerous mammalian cell lines but also in several bacterial species, fungi, a parasite, and even plants, indicating it is an evolutionarily conserved mechanism (Dettmann et al., 2014; Dubey & Ben-Yehuda, 2011; Pande et al., 2015; Rupp et al., 2011; Stonebloom et al., 2012).

Previously, the structures were described to have a diameter of 50 to 200 nm and average length of numerous cell diameters (Rustom et al., 2004). Nowadays it is known their diameter can range from 20 to 700 nm, with a length between 10 to hundreds of microns (Zurzolo, 2021). Currently, the main criteria to define a certain cellular structure as a TNT in mammalian cell culture are: 1. it contains F-actin; 2. it binds at least two cells mediating membrane continuity between them; and 3. it does not touch the substrate (Rustom et al., 2004; Zurzolo, 2021). The main features of TNTs are summarized in Figure 6.

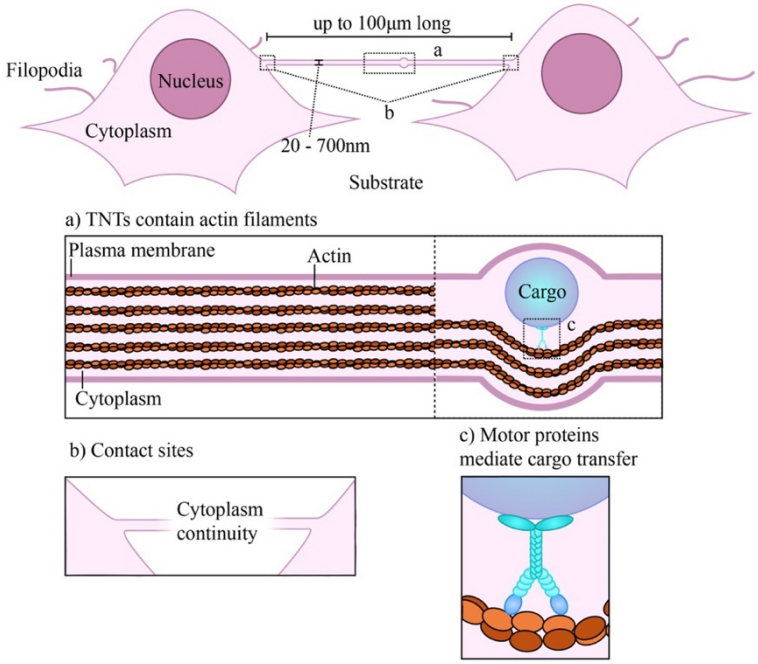

Figure 8. Attributes of Tunneling Nanotubes. TNTs are cellular structures which range between 20-700nm thick and may be up to 100 µm long, connecting at least two cells and hovering above the substrate; **a)** TNTs

contain actin filaments; **b)** Open-ended TNTs allow for cytoplasm continuity; **c)** TNTs mediate the intercellular transfer of cargo via motor proteins on actin filaments. Figure prepared according to (Cordero Cervantes & Zurzolo, 2021).

1.5.1 Formation of Tunneling Nanotubes

TNTs are mostly formed in response to stress, inflammation, and diseases, occurring in much lower abundance in healthy adult tissues, except for immune cells (Zurzolo, 2021). Currently, there are two proposed mechanisms of TNT biogenesis: actin-driven protrusions or cell dislodgment (Abounit & Zurzolo, 2012; Ljubojevic et al., 2021), which can both result in open- or close-ended TNTs (Dupont et al., 2018). Different cell lines behave differently in this matter, and there might be distinct types of TNTs even within the same cell line (Rustom, 2016; Zurzolo, 2021). Furthermore, it is speculated that the type of cargo is intrinsically related to the mechanism of TNT formation, therefore determining the type of TNT to be formed (Zurzolo, 2021).

What seems to be a decisive factor in the formation of TNTs so far is the polymerization of actin, as the use of inhibitors of actin polymerization hinders TNT biogenesis (Rustom et al., 2004). Accordingly, numerous proteins involved in cytoskeleton remodeling have been shown to play a role in TNT formation, although there are still no known TNT-exclusive molecular markers. For instance, M-Sec, regulated by the p53 pathway, has been early pointed out as a promotor of TNTs through its interaction with the exocyst complex and Ra1 in macrophages (Hase et al., 2009; Wang et al., 2011). Also in macrophages, Cdc42 and Rac1, a Rac GTPase, are necessary for TNT protrusions, whereas their inhibition in fact increases the number of TNTs in neuronal cells (Delage et al., 2016; Hanna et al., 2017). In addition, it has been suggested that Cdc42 might play a role in the stabilization and elongation of TNTs, once they are already formed (Hase et al., 2009). Eps8, a protein involved in actin regulation which directly interacts with Cdc42, has also been reported to increase TNT formation (Delage et al., 2016; Kretschmer et al., 2019). Downstream of Cdc42, Myo10 is another positive effector in TNT formation and consequent vesicle transfer (Gousset et al., 2013). Furthermore, inhibition of Arp2/3 in macrophages and pancreatic cancer cells led to a decrease in TNTs, while increasing it in neuronal cells (Hanna et al., 2017; Sartori-Rupp et al., 2019). Moreover, the Wnt/Ca2+ pathway has also been proposed as crucial in the modulation of TNTs in primary neuron cells, as its activation promotes TNT biogenesis (Vargas et al., 2019).

1.5.2 Investigating on Tunneling Nanotubes

To date, there is still no consensus regarding a unified nomenclature of TNTs, which complicates the investigation of TNTs. So far, TNTs have been referred to as tunneling nanotubes, tumor microtubes, membrane nanotubes, cytonemes, and others. Among the technical difficulties are the absence of an exclusive marker of TNT structures. Furthermore, TNTs are sensitive to mechanical stress, chemical fixation, trypsinization, as well as to long exposure to light, as the resultant vibrations can lead to its rupture. They are also dependent on cell density and type of cell culture (2D or 3D). Notwithstanding, TNTs are quite dynamic structures which can last from a few seconds to several hours. In addition, the elevated variability in the content, length and thickness of TNTs contribute to making their investigation a truly challenging task (Zurzolo 2021, Dubois et al., 2020).

When designing experiments, a few steps in sample processing may be decisive in the successful study of TNTs. In the case of *in vitro* cell culture, it already begins with the choice of culture surface (glas versus plastic). Next, there is cell density, which should allow just enough space for the formation of such cellular connections. Following trypsinization, the cells should be given enough time for membrane recovery, as it also influences TNT formation. Fixation should be performed as gently as possible, once chemical toxicity is another factor capable of disturbing TNTs (Dubois et al., 2020).

For TNT visualization and analysis, brightfield, fluorescence, and live time-lapse microscopy are broadly applied imaging methods. In fluorescence microscopy, fluorescent labelling of F-actin, plasma membrane or tubulin are commonly applied in the identification of TNTs. It should be kept in mind that the three criteria for identification of TNTs must be met. Therefore, acquiring Z-stacks when imaging with a confocal microscope becomes necessary to confirm that the structures do not touch the substrate. One advantage of Z-stacks is the possibility of 3D reconstruction for an even better representation of TNTs. However, due to their high morphological heterogeneity, automatic imaging and analysis are not always suitable methods (Dubois et al., 2020).

Live time-lapse imaging allows a more dynamic visualization, with the possibility to easily distinguish donor- from acceptor-cell. Nevertheless, one should be mindful regarding imaging settings when associating this method with fluorescence microscopy, as extended imaging would be necessary, increasing exposure, bleaching and TNT disturbance (Dubois et al., 2020).

1.5.3 Tunneling Nanotubes in human diseases and their clinical relevance

Tunneling nanotubes have been pointed out as potential key players in several aspects of human health. Research shows that several viruses and bacteria are capable of using TNTs as a mechanism of immune evasion and spreading, travelling through or even surfing on top of them (Caldas et al., 2020; Ganti et al., 2021; Jahnke et al., 2022; Onfelt et al., 2006; Panasiuk et al., 2018; Pepe et al., 2022; Sowinski et al., 2008).

Intercellular communications are a determinant factor in the maintenance of tissue homeostasis, and it becomes even more complex in the cancer field. Research shows that cell-to-cell communication between cancer and surrounding non-cancer cells in the tumor microenvironment contributes to disease progression once the exchange of oncogenic genetic material may increase invasion and proliferation. In addition, TNTs might promote angiogenesis by forming bridges between pericytes-pericytes and pericytes-endothelial cells (Errede et al., 2018). Furthermore, TNTs allow the sharing of mitochondria and other organelles and vesicles, which are thought to facilitate survival of tumor cells, consequently leading to the development of drug resistance (Roehlecke & Schmidt, 2020). TNTs have already been reported in numerous types of cancer cells in vitro, such as prostate cancer, breast cancer, ovarian cancer, laryngeal carcinoma, among others (Antanaviciute et al., 2014; Kretschmer et al., 2019; Pasquier et al., 2013; Saha et al., 2022). In 2012, Lou et al., provided the first evidence of TNTs in vivo, with 3D reconstructed sections of surgically obtained samples of human lung adenocarcinoma tumor and human mesothelioma, and in 2015 Osswald et al., reported the formation of "ultra-long cellular protrusions" in gliomas growing in mouse brain, which were monitored with a multiphoton laser-scanning microscope (Lou et al., 2012; Osswald et al., 2015).

In the context of neurodegeneration, TNTs play a dual role. On one side, TNTs have been seen to facilitate the propagation of protein aggregates such as tau, α-synuclein and HTT, in Alzheimer's, Parkinson's and Huntingtin's diseases, respectively. On the other side, TNTs can function as a rescue mechanism in which unhealthy cells receive functional mitochondria and other beneficial cellular content to handle the stress of accumulating protein aggregates (Chastagner et al., 2020; Costanzo et al., 2013; Dilsizoglu Senol et al., 2021; Victoria & Zurzolo, 2017). As α-synuclein protein aggregates resulted in enhanced intracellular ROS levels, which is detrimental to mitochondria, damaged mitochondria are also seen in motion from unhealthy to healthy cells, indicating a bidirectional transfer of mitochondria also takes place upon necessity (Scheiblich et al., 2021).

1.6 Aims

Double membrane vesicles, lysosomes and numerous other organelles have been observed within TNTs. While taking this into consideration, the aims of this study were:

1. To investigate whether autophagic membranes could be trafficked via TNTs as well, therefore questioning the potential of TNTs as a probable cellular rescue mechanism. For this, the presence of WIPI1, WIPI2B, WIPI4 and LC3 in such cellular structures was to be assessed.
2. To complement the first aim, the second aim of this thesis questioned whether autophagic cargoes can also be intercellularly transferred through TNTs. To assess this aspect of TNT transfer, mitochondria, ferritin and NCOA4 were chosen as targets to represent autophagic cargo.

CHAPTER 2 Materials and methods

2.1 Materials

2.1.1 Devices

Table 1. Listed devices used for all experiments

Device	Product	Manufacturer
Cell imaging system	EVOS FLoid Cell Imaging Station	Invitrogen
Cell culture centrifuge	Megafuge 2.0 R	Heraeus
Cell culture table centrifuge	Pico Centrifuge	Heraeus
Table centrifuge	Pico 21 Centrifuge	Heraeus
Chemiluminescence imaging device	iBright™ CL750 Imaging System	Invitrogen™
Electrophoresis power supply	Powerpac 300	Bio-Rad
Fluorescence microscope (FM)	Axiovert 200M with Axiovision Rel 4.7 software	Carl Zeiss GmbH
FM objective	40x LD-Plan Neofluar oil immersion objective	Carl Zeiss GmbH
Forceps	Nr. 5 Inox, extra-fine, straight	Dumont
Freezer (-20 °C)	-	Liebherr
Freezer (-80 °C)	Forma 8800 Series	Thermo Scientific
Freezing container	Mr. Frosty	Thermo Scientific
Fridge (4 °C)	-	Liebherr
Fume hood	-	Wesemann
Cell culture incubator	BBD 6220 220L	Heraeus
Incubator	Function line BB16	Heraeus
Inverted microscope (IM)	Axiovert 25	Zeiss
IM 10x objective	Achroplan 10x 0.25 Ph1	Zeiss
Laser scanning microscope (LSM)	LSM 800	Zeiss
Fluorescence DIC phase contrast inverted microscope	Axiovert 200M	Zeiss
LSM 40x objective	40x 1.3 Plan-Neofluar oil-immersion objective	Zeiss
LSM 63x objective	63x 1.4 DIC Plan-Apochromat Oil-Immersion Objective	Zeiss
Magnetic stirrer with hot plate	MR 3001 K	Heidolph
Micro scales	BP 2100 S	Sartorius
pH-meter	HI2002 edge	Hanna Instruments
Pipette controller	Pipetboy	Integra Biosciences
Precision scale	M-Pack AX224	Sartorius
Refrigerator incubator shaker	Innova 4230	New Brunswick Scientific
Rocking shaker	3013	GFL
Rotating shaker	3025	GFL
SDS-PAGE electrophoresis system	PROTEAN® II xi Cell	Bio-Rad
Single channel microliter pipette	Transferpette® S 1 µl	Labmate

Single channel microliter pipette	Transferpette® S 20 µl	Labmate
Single channel microliter pipette	Transferpette® S 200 µl	Labmate
Single channel microliter pipette	Transferpette® S 1000 µl	Labmate
Sterile hood	Tecnoflow 3F120-II GS	Integra Biosciences
Sterile hood	Tecnoflow 3F150-II GS	Integra Biosciences
Vacuum pump	MD 4C diaphragm vacuum pump	Vacuubrand
Water bath	-	GFL
Water bath	W22	Medingen
Western blotting transfer system	Trans-Blot Turbo Transfer System	Bio-Rad

2.1.2 Consumables

Table 2. List of consumables used

Product	Manufacturer	Catalog-Number
20 µl pipette tips	Sarstedt	701.116
200 µl pipette tips	Sarstedt	70.760.002
1,000 µl pipette tips	Nerbe plus	07-132-0095
1 ml syringes	Braun	9167006V
23G needle	Braun	4657640
35mm Glass Bottom Dishes No. 1.5	MatTek Corporation	P35G-1.5-14-C-GRID
Aluminium foil	Toppits	01-2455/1
BioLife 100mm Tissue Culture Dish	Thermo Scientific	130182
BioLite 24 well Multidish	Thermo Scientific	930186
BioLite 6 well Multidish	Thermo Scientific	130184
CoverGrip™ Coverslip Sealant	Biotium	23005-1
Cryogenical vial	Corning	431386
Disposable latex gloves	Roth	L949.1
Disposable nitrile gloves	KCL	740
Filter unit with PES membranes 0.2 µm	Thermo Scientific	151-4020
Filter unit 0.45 µm	Roth	P667.1
Glass pipettes 1 ml	Hirschmann	1180133
Glass pipettes 5 ml	Hirschmann	1180154
Glass pipettes 10 ml	Hirschmann	1180160
Glass pipettes 25 ml	Hirschmann	1180170
Immersol 518 F immersion oil	Zeiss	444960-0000-000
Microscopical cover slips	Thermo Scientific	CB00120RA120MNTO
Prolong Antifade Gold	Invitrogen	P36930
PVDF Transfer Membrane, 0.45µm	Thermo Scientific	88518
SafeSeal reaction tube, 0.5 ml	Sarstedt	72704
SafeSeal reaction tube, 1.5 ml	Sarstedt	72706
SafeSeal reaction tube, 2 ml	Sarstedt	72695500
Screw cap tube, 15 ml	Sarstedt	62.554.502
Screw cap tube, 50 ml	Sarstedt	62.547.254
Slides box	Thermo Scientific	12392138
SuperSignal™ West Femto Maximum Sensitivity Substrate	Thermo Fisher	34095

Whatman™ Grade 3MM CHR Cellulose Western Blotting Paper	Whatman/GE Healthcare	3030-917
Whatman™ lenscleaning tissues	Whatman/GE Healthcare	2105-841
Western Blotting Filter Paper, Extra Thick	ThermoFischer	88605

2.1.3 Cell culture

Table 3. List of cell lines used

Cell line	Description
U2OS	Human osteosarcoma cell line, ATCC® HTB-96, USA
U2OS GFP-WIPI1	Human osteosarcoma cell line stably expressing GFP-WIPI1, Proikas-Cezanne (Proikas-Cezanne & Robenek 2011)
U2OS GFP-WIPI2B	Human osteosarcoma cell line stably expressing GFP-WIPI2B, Proikas-Cezanne (Proikas-Cezanne & Robenek 2011)
U2OS mRFP-EGFP-WIPI4	Human osteosarcoma cell line stably expressing mRPF-EGFP-WIPI4, Proikas-Cezanne Laboratory, Thost and Proikas-Cezanne, unpublished
U2OS GFP-LC3	Human osteosarcoma cell line stably expressing GFP-LC3, Proikas-Cezanne Laboratory (Mauthe et al., 2011)
U2OS mRFP-EGFP-LC3	Human osteosarcoma cell line stably expressing mRFP-EGFP-LC3, Proikas-Cezanne Laboratory, Thost and Proikas-Cezanne, unpublished
U2OS NLS-M-Scarlet	Human osteosarcoma cell line stably expressing NLS-M-Scarlet, Simonsen Laboratory, University of Oslo, (Sporbeck et al., 2023)
U2OS ATG16L1 WT MLS-EGFP-mCherry	Human osteosarcoma cell line stably expressing NLS-M-Scarlet, Simonsen Laboratory, University of Oslo, (Lystad et al. 2019)
hTERT-U2OS Cas9	Immortalized human osteosarcoma cell line expressing hTERT, Andrew Holland Laboratory, (Sporbeck et al., 2023)
hTERT-U2OS Cas9 WIPI1 KO	Immortalized human osteosarcoma cell line expressing hTERT lacking WIPI1, Proikas-Cezanne Laboratory, (Sporbeck et al., 2023)
LX-2	Human hepatic stellate cell line, Merck, SCC064
HuH7	Human liver carcinoma cell line, CLS Cell Lines Service GmbH, 300156

Table 4. Listed products used for cell culture

Substance	Manufacturer	Product Number
Blasticidin	Life Technologies	A11139-03
Dulbecco's Modified Eagle Medium (DMEM), high glucose, GlutaMAX™ supplement, pyruvate	Life Technologies	31966
Dulbecco's Modified Eagle Medium:Nutrient Mixture F-12 (DMEM / F-12)	Life Technologies	11320-074
Dulbecco's Phosphate-Buffered Saline (DPBS), no calcium, no magnesium	Life Technologies	REF 14190-094
Earle's Balanced Salt Solution (EBSS), calcium, magnesium, phenol red	Life Technologies	24010-043
Fetal Bovine Serum, qualified	Life Technologies	10270-106
Geneticin G-418 Sulfate	Life Technologies	11811-031
Lipofectamine2000	ThermoFischer Scientific	11668-019
Lipofectamine RNAiMAX	ThermoFischer Scientific	13778-075
Live cell imaging solution	Invitrogen™	A14291DJ

OPTI.MEM	Life Technologies	51985-026
Penicillin-streptomycin (10,000 U/mL)	Life Technologies	15140122
Trypsin-EDTA (0.05%)	Life Technologies	25300054

2.1.4 Cell culture medium

Table 5. List of cell culture medium used in this study

Solution/Buffer	Composition	
DMEM/FCS	- 10% (v/v) FSC - Dulbecco's Modified Eagle Medium GlutaMAX	
DMEM/FCS/PenStrep	- 10% (v/v) FCS - 100U/ml penicillin - 100µg/ml streptomycin - Dulbecco's Modified Eagle Medium GlutaMAX	
DMEM/FCS/PenStrep/G418	- 10% (v/v) FCS - 100U/ml penicillin - 100µg/ml streptomycin - 0.6 mg/ml G418 - Dulbecco's Modified Eagle Medium GlutaMAX	
DMEM/F-12/ FCS/PenStrep/Blasticidin	- 10% (v/v) FCS - 100U/ml penicillin - 100µg/ml streptomycin - 0.01 mg/ml Blasticidin - Dulbecco's Modified Eagle Medium:Nutrient Mixture F-12	
DMEM/FCS/DMSO (Freezing medium)	U2OS and LX-2	- 20% (v/v) FCS - 10% (v/v) DMSO - Dulbecco's Modified Eagle Medium GlutaMAX
	HuH-7	- 20% (v/v) FCS - 5% (v/v) DMSO - Dulbecco's Modified Eagle Medium GlutaMAX
Live cell imaging solution/Glucose	After starvation treatment	- 5mM Glucose - Live cell imaging solution
	After fed treatment	- 20mM Glucose - Live cell imaging solution

2.1.5 Plasmids

Table 6. List of plasmids used

Product	Manufacturer	Product Number
pEGFP-C1	BD Biosciences	6084-1
pEGFP-C1-hWIPI1α	Proikas-Cezanne laboratory (Proikas-Cezanne et al., 2004)	-
Myc-pCMV6	OriGene	PS100001
Myc-NCOA4 Variant 1	Origene	RC226666
Myc-NCOA4 Variant 2	Origene	RC226676
Myc-NCOA4 Variant 4	Origene	RC226707

tGFP-pCMV6	Origene	PS100010
tGFP-FTH1	Origene	RG209845

2.1.6 Small interfering RNAs and endoribonuclease-prepared small interfering RNAs

Table 7. List of siRNAs and esiRNAs used

Product	Manufacturer	Product Number
Trilencer-27 Fluorescent-labeled transfection control siRNA duplex	OriGene	SR30003
NUDC Human siRNA Oligo Duplex	OriGene	SR307310
MISSION® esiRNA targeting FLUC	Sigma-Aldrich	EHUFLUC
MISSION® esiRNA targeting human WDR45	Sigma-Aldrich	EHU023161

2.1.7 Antibodies and dyes

Table 8. List of used antibodies and dyes

Product	Manufacturer	Product Number	Dilution
Antibodies (Primary)			
anti-α-Tubulin	Sigma-Aldrich	T5168	1:50,000 (WB), 1:2000 (IF)
anti-Ferritin	Rockland	200-401-090-0100	1:50 (IF)
anti-NCOA4 (E8H8Z)	Cell Signaling	66849	1:1,000 (WB)
anti-NudC	OriGene	TA340119	1:500 (WB)
anti-TOM20	Santa Cruz	sc-17764	1:50 (IF)
anti-WIPI4	ProteinTech	19194-2-AP	1:500 (WB)
Antibodies (Secondary)			
anti-Mouse IgG, HRP-linked antibody	Cell Signaling	7076	1:10,000
anti-Rabbit IgG, HRP-linked antibody	Cell Signaling	7074	1:10,000
Alexa Fluor 488 goat anti-mouse IgG	Life Technologies	A-11001	1:200
Alexa Fluor 488 goat anti-rabbit IgG	Life Technologies	A-11008	1:200
Alexa Fluor 546 goat anti-mouse IgG	Life Technologies	A-11003	1:200
Alexa Fluor 633 goat anti-mouse IgG	Life Technologies	A-21050	1:200
Alexa Fluor 633 goat anti-rabbit IgG	Life Technologies	A-21070	1:200
Dyes			
4,6-diamidino-2-phenylindole (DAPI)	AppliChem	28718-90-3	1:1,000
Alexa Fluor 546 Phalloidin	Thermo Scientific	A22283	1:1000
Alexa Fluor 647 Phalloidin	Thermo Scientific	A22287	1:400
Vybrant™ Multicolor Cell-Labeling Kit (DiO, DiI, DiD Solutions)	Thermo Scientific	V22889	-
Wheat Germ Agglutinin, Alexa Fluor 488 conjugate	Thermo Scientific	W11261	1:200
Wheat Germ Agglutinin, Alexa Fluor 647 conjugate	Thermo Scientific	W32466	1:200

2.1.8 Chemicals

Table 9. List of chemicals used for all experiments

Product	Manufacturer	Product Number
2-Mercaptoethanol	Sigma	M3148-100ml
6-aminohexanoic acid	AppliChem	A2266,0500
Acrylamide 4K-solution (30 %)	AppliChem	A1672,1000
Albumine (BSA) fraction V (pH 7)	AppliChem	A1391,0500
Ammonium peroxodisulfate (APS)	Merck	1.01201.0100
Bromophenol blue	Bio-Rad	161-0404
Color-coded Prestained Protein Marker, Broad Range 10-250kDa	CellSignaling	74124
Color Protein Standard Broad Range	BioLab	P7712S
Deferasirox (ICL-670)	Selleckchem	S1712
Dimethyl sulfoxide (DMSO) for cell culture	AppliChem	A3672
Dithiothreitol (DTT)	AppliChem	A1101,0025
EDTA disodium salt 2-hydrate	AppliChem	A2937,1000
Ethanol	Honeywell	603-002-00-5
FAC (Ammoniumeisen(III)-citrat)	Merck	F5879
Glycerol 87 %	AppliChem	A23739,1000
Glycine	AppliChem	A1067,1000
Hydrochloric acid	VWR CHEMICALS	UN1789
Isopropanol	Honeywell	34863-2.5L
Methanol	Honeywell	34885-2.5L-M
Milk	AppliChem	A0830,1000
Paraformaldehyde (PFA)	Sigma-Aldrich	441244
PBS Buffer (10x Dulbecco's) - Powder	AppliChem	A0965
SDS ultrapure	AppliChem	A1112,1000
Sodium chloride	Sigma-Aldrich	S-5886
Sorafenib tosylate	Selleckchem	S1040
SuperSignal West Femto Maximum Sensitivity Substrate	Thermo Scientific	34095
TEMED	AppliChem	A1148,0100
Tris(hydroxymethyl)aminomethane (TRIS)	Sigma-Aldrich	252859-500G
Tween20	AppliChem	A4974,0500
β-mercaptoethanol	AppliChem	A1108,0100

2.1.9 Solutions and buffers

Table 10. List of general solutions and buffers prepared for this thesis

Solution/Buffer	Composition and preparation
1M TRIS pH 6.8	Composition: -121.14g/l TRIS - ddH2O Preparation: Thoroughly dissolve, adjust pH to 6.8 and autoclave. Store at room temperature.
1M TRIS pH 7.6	Composition: - 121.14g/l TRIS - ddH2O

	Preparation: Thoroughly dissolve, adjust pH to 7.6 and autoclave. Store at room temperature.
1.5M TRIS pH 8.8	Composition: - 181.71g/l TRIS - ddH2O Preparation: Thoroughly dissolve, adjust pH to 8.8 and autoclave. Store at room temperature.
2x Laemmli buffer	Composition: - 25 % (v/v) Glycerol - 4% SDS - 100 mM Tris, pH 6.8 - 5% (v/v) β-mercaptoethanol - 2.5 mM EDTA, pH 6.8 - 100 mM DTT - 0.05% (w/v) Bromophenol blue - ddH2O Preparation: In a fume hood, mix all components carefully, and adjust the final volume with ddH2O. Finally, aliquot and store at -20ºC.
3.7% (w/v) PFA	Composition: - 37g/l Paraformaldehyde - PBS Preparation: In a fume hood, carefully weigh PFA and add it to PBS. Thoroughly dissolve while heating in water bath at 72ºC, occasionally mixing. Adjust pH to 7.2 – 7.6 and filter sterilize (0.45µm). Aliquot and store at -20ºC.
10% (w/v) APS	Composition: - 100g/l APS - ddH2O Preparation: Thoroughly dissolve and tore at -20ºC.
10% (w/v) BSA	Composition: - 100g/l Albumin BSA - ddH2O Preparation: Thoroughly dissolve with mild heating. Filter sterilize (0.2µm) and store at 4ºC.
10% (v/v) Tween20	Composition: - 100ml/l Tween20 - ddH2O Preparation: Dilute Tween20 in ddH2O in water bath set to 55ºC. Prepare already in aliquots and store at 4ºC.
20% (w/v) SDS	Composition: - 200g/l - ddH2O Preparation: Under fume hood, SDS was carefully weighed and completely dissolved with heat and stirring bar.
Blocking solution for IF BSA/PBS/T	Composition: - 1% BSA - PBS - 0.1% Tween20 Preparation: Dilute BSA in PBS and add Tween20. Prepare freshly before use.
Blocking solution for WB BSA/TBS/T	Composition: - 5% BSA - TBS - 0.1% Tween20 Preparation: Dilute BSA in TBS and add Tween20. Prepare freshly before use.
Blocking solution for WB Milk/TBS/T	Composition: - 50g/l Milk - TBS - 0.1% Tween20 Preparation: Thoroughly dissolve milk in TBS and add Tween20 to the mix. Prepare freshly before use.

PBS	Composition: - 9.55g/l PBS Powder - ddH2O Preparation: Thoroughly dissolve and autoclave. Store at room temperature.
PBS/T	Composition: - 0.1% Tween20 - PBS Preparation: Dilute Tween20 in 1x PBS. Prepare freshly before use.
1x Stripping buffer	Composition: - 84 ml/l 1M Tris (pH 6.8) - 2% SDS - ddH2O - 0.7 % (v/v) β-mercaptoethanol Preparation: Dissolve TRIS thoroughly and add SDS. Store at room temperature. Add β-mercaptoethanol shortly before use.
TBS	Composition: - 20ml/l 1M TRIS pH 7.6 - 8.182g/l NaCl - ddH2O Preparation: Thoroughly dissolve and autoclave. Store at room temperature.
TBS/T	Composition: - 0.1% Tween20 - TBS Preparation: Dilute Tween20 in 1x TBS. Prepare freshly before use.
Towbin buffer	Composition: - 14.42g/l Glycine - 3g/l TRIS - ddH2O Preparation: Thoroughly dissolve and autoclave. Store at room temperature.
SDS-PAGE running buffer	Composition: - 18.8g/l Glycine - 3.02g/l TRIS - 0.1% SDS - ddH2O Preparation: Thoroughly dissolve glycine and TRIS in ddH2O. Add SDS and adjust final volume. Store at room temperature.
Western Blot transfer buffer	Composition: - 1x Towbin buffer - 20% (v/v) Methanol Preparation: Under a fume hood, mix Towbin and Methanol. Prepare freshly before use.

2.1.10 Softwares

- GraphPad Prism 9.5.0
- ImageJ2 version 2.14.0/1.54f, open-source image processing software
- Microsoft Excel version 16.77.1
- Microsoft PowerPoint version 16.77.1
- Microsoft Word version 16.77.1
- ZEISS ZEN 3.0 Software, blue edition

2.2 Methods

2.2.1 Cell culture methods

Thawing tumor cell lines

Cryovials were thawed with the hand warmth as quickly as possible. The content of each vial was pipetted up and down to ensure complete thawing and proper mixing, and immediately transferred to a pre-labeled 10cm dish (Thermo Scientific, 130182) containing full growth medium, which consisted of a mix of DMEM (Life Technologies, 31,966), 10% fetal bovine serum (FBS) (Life Technologies, 10270106), 100U/ml of penicillin and 100µg/ml of streptomycin (Life Technologies, 15140-122). Cells were kept at 37ºC and 5% CO2 and observed the next day. In general, culture media was replaced. However, if necessary, the cells were already split.

Preparation of G418

For the preparation of a 100mg/ml solution of G418, one should first check the information regarding the active fraction on the vial. It is necessary to calculate the active fraction contained in each LOT to reach the desired final concentration. For instance, in G418 with an active fraction of 721µg/mg, 3.605g represent the active fraction in 5g of G418 powder. To obtain a final concentration of 100mg/ml, one should therefore add 36.05ml of DPBS (Life Technologies, REF 14190-094).

Approximately 20 ml of DPBS were poured into a glass bottle containing a magnetic stirring bar, and the complete G418 powder was slowly added to the bottle while slowly stirring. The original G418 container was washed with 10ml DPBS, which were also transferred into the glass bottle. The solution was stirred for around 10 minutes at room temperature for complete dissolution. To adjust to the final volume, a measuring cylinder was used. In a sterile hood, the solution was filtered through a 0.45µm filter system (Roth, P667.1) and 1ml aliquots were prepared and stored in -20°C.

Culture of tumor cell lines

Human monoclonal U2OS and human monoclonal U2OS stably transfected cell lines cells were kept in culture at 37ºC and 5% CO2. U2OS were typically cultured in full growth medium. The medium for U2OS stably transfected cell lines, except for U2OS expressing NLS-M-Scarlet or MLS-EGFP-mCherry, also contained 0.6mg/ml G418 Sulfate (Life Technologies; 11811-098).

U2OS cells were subcultured every 2-3 days, in dilutions of 1:3 to 1:5, whereas U2OS stably transfected cell lines were diluted 1:2 to 1:3. Subculture was performed once the cells reached approximately 80% confluency. For this, the medium was aspirated, and cells were washed twice with DPBS. Then, 1ml of Trypsin-EDTA (0.05%) (Life Technologies, REF 25300-054) solution was added on top of cells for 5-10 minutes, until cells completely were detached from culture dish. Next, trypsinization was interrupted and full growth medium was used to resuspend and dilute cells, which were distributed into new culture dishes with fresh medium. U2OS cells were diluted in 1:3 to 1:5 proportions, and stable cell lines 1:2 to 1:3.

The human liver carcinoma cell line HuH-7 was also cultured in 10cm dishes at 37ºC and 5% CO2 in full growth medium, as described for U2OS. Human hepatic stellate cell line LX-2 was cultured in DMEM containing only 2% FBS, 100U/ml penicillin and 100µg/ml streptomycin, also in 10cm dishes at 5% CO2 and 37ºC. Liver cancer cell lines were subcultured every 2-3 days, with dilutions varying depending on the cell line. HuH-7 were split 1:4 to 1:7, whereas LX-2 cells were diluted 1:2 to 1:4.

Cryoconservation

Cells were regularly frozen in order to maintain stocks. For this, cells were trypsinized as described above. After being resuspended in at least 5ml of full growth medium, cells were transferred into a 15 ml tube, which was centrifuged (1100 rpm, 10 minutes; 800rpm, 5 minutes for LX-2 cells). Then, the supernatant was carefully aspirated, and the pelleted cells were resuspended and thoroughly mixed in 1ml of the appropriate freezing medium, according to the cell line. Finally, cryogenic vials were used to store cell suspension, which were frozen in a Freezing Container at -80ºC. On the following day, cells could be relocated to the liquid nitrogen tank for long term storage.

Sterilization of coverslips in 24-well plates

Cells were often seeded in 24-well plates for fluorescence microscopy. In a sterile hood, coverslips were distributed into the wells and sterilized with pure Ethanol (Honeywell, 603-002-00-5) prior to such experiments. Briefly, one coverslip was laid into each well. Each well was filled up with up to 1ml of Ethanol, and the plates were gently shaken to the sides. The Ethanol was aspirated off, and 0.5ml of Ethanol were distributed into each well three more times. On the last time, the plates were left to incubate with Ethanol for approximately 30 minutes. Then, the Ethanol was aspirated off and the plates were left to dry in the sterile hood

for about 15 minutes. Finally, the plates were either immediately used for the experiment or stored in sterile plastic bags until the moment of the experiment.

Co-culture (homo- and heterotypic)

Cell lines were washed and detached from culture plates as usual, followed by cell counting. If necessary for the experimental set-up, different cell populations were labelled with lipophilic DiO or DiI dyes (Thermo Scientific, V22889), according to the manufacturer's protocol. Briefly a cell suspension of 1 x 10^6/ml was incubated with 5µl of the desired lipophilic dye for 20 minutes at 37ºC. After the incubation, the cell suspensions were centrifuged at 1500 rpm for 5 minutes (800 rpm for LX-2). The supernatant was discarded, and cells were carefully and gently resuspended in pre-warmed medium. This step was repeated two more times. In the final wash, the cells were resuspended in the same volume as initially to maintain the original cell density. Finally, the cells were mixed in a 1:1 ratio and re-seeded either on top of sterilized coverslips for fluorescence microscopy or in 35mm dishes for live cell microscopy.

Stably transfected cell lines expressing fluorescently labeled proteins were counted and directly mixed in a 1:1 proportion for co-culture, then re-seeded.

Transient forward transfection of DNA

Approximately 16-18 hours after seeding, cells went through transient transfection with Lipofectamine 2000 (ThermoFischer Scientific, 11668-019), following the manufacture's protocol (Tables 11 and 12). In detail, firstly the DNA was pre-diluted to obtain 1µg/µl in autoclaved ddH2O. Then, DNA and Lipofectamine2000 were each diluted in OPTI.MEM (Thermo Fisher, 51985026) and incubated at room temperature for 10 minutes. Finally, the solution containing DNA was added into the mix with Lipofectamine2000, mixed by gently tapping, and further incubated at room temperature for 20 minutes. Finally, cells had their medium replaced for fresh pre-warmed DMEM/FCS and transfection mixes were distributed into the wells. Plates were gently rocked back and forth to ensure thorough mixing, and the cells were incubated for 48h with transfection mix.

Table 11. Transient forward transfection, mixes for 24-well plate

	sample	0.1 µg	0.25 µg	0.5 µg
DNA mix	OPTI.MEM, µl	25	25	25
	DNA (1 µg/µl), µl	0.1	0.25	0.5
Lipofectamine2000 mix	OPTI.MEM, µl	25	25	25
	Lipofectamine2000, µl	0.2	0.5	1
	Total DNA/Lipofectamine2000 mix/well	50	50	50

Table 12. Transient forward transfection in co-transfection set-up, mixes for 6-well plate

	sample	2.5 µg
DNA mix	OPTI.MEM, µl	125
	DNA (1 µg/µl), µl	2.5
Lipofectamine2000 mix	OPTI.MEM, µl	125
	Lipofectamine2000, µl	6.25
	Total DNA/Lipofectamine2000 mix/well	250

Transient reverse transfection of siRNA/esiRNA

Downregulation of NudC was achieved by reverse transfection with NudC Human siRNA Oligo Duplex (Origene, SR307310) (Table 13), whereas downregulation of WDR45 was mediated through reverse transfection of esiRNA (eHU023161) (Table 14). Controls from Origene and Sigma-Aldrich were, respectively siCtrl (Origene, SR30003) and esiFLUC (Sigma-Aldrich, eHU FLUC). In detail, OPTI.MEM, siRNA oligo duplexes or esiRNA and Lipofectamine™ RNAiMax Transfection Reagent (Thermo Fisher, 12778100) were mixed and incubated at room temperature for 20 minutes. After that, siRNA or esiRNA mix was transferred into its corresponding well and cell suspension in full nutrient medium without antibiotics was added dropwise onto esiRNA complexes (3ml final volume in 6-well plates or 1ml in 24-well plates). Cells were incubated at 37ºC in 5% CO2 for 48h.

Table 13. Reverse transfection with siRNA, mixes for 24-well plate

Components	siRNA control (µl/well)	Components	siNudC (µl/well)
OPTI.MEM	100	OPTI.MEM	100
siRNA	1.8	siRNA A	0.6
		siRNA B	0.6
		siRNA C	0.6
RNAiMax	1	RNAiMax	1
Total volume (µl/well)	102.8		102.8

Table 14. Reverse transfection with esiRNA, mixes for 6- and 24-well plates

Components	6-well plate (µl/well)	24-well plate (µl/well)
OPTI.MEM	500	100
esiRNA (FLUC or WDR45)	25	5
RNAiMax	5	1
Total volume (µl/well)	530	106

Co-transfection of esiRNA and DNA

For co-transfection of esiRNA followed by DNA, cells went through reverse transfection with esiRNA, as described above, for 8 hours. Then, forward transfection with DNA plasmids took place, as specified in Table 12, for the following 40 hours.

Autophagy and ferritinophagy assays

Generally, cells were seeded into 6- or 24-well plates, onto previously sterilized coverslips. In preparation for autophagy assay, cells were washed at least three times with pre-warmed DPBS. The media for autophagy assays consisted of full growth medium (DMEM/10%FBS; DMEM/2%FBS for LX-2), serum starvation medium (DMEM; DMEM/2.5%FBS), or starvation medium (EBSS). The assays took place for 24h.

Treatments with Sorafenib tosylate were combined with autophagy assays for the investigation in the field of liver cancer. In ferritinophagy assays, treatments with FAC and DFX were applied in DMEM/10%FCS for 24h, as specified below in Table 15.

Table 15. Cell culture supplements

Drug	Concentration	Treatment duration
Sorafenib tosylate	5μM	24h
Ammonium iron (III) citrate FAC	188.679245 μM	24h
Deferasirox	30μM	24h

2.2.3 Biochemical methods

Protein extraction

Protein extraction was accomplished with hot Laemmli buffer. Once the assay was completed, warm DPBS was used to wash the cells twice (Life Technologies, 14190-094) and the plates were quickly transferred into the fume hood, where 150μl hot 2x Laemmli buffer were added per well. Cells were thoroughly scrapped from the bottom of each well with a 1ml pipette tip and transferred into a 1.5 ml Eppendorf tube. Then, for shearing of chromatin, the extracts were pulled and forced back through a 23G needle into a 1ml syringe (maximum 4 times). Finally, the obtained extracts were boiled for approximately 5 minutes and stored at -20ºC until performing Western Blots.

SDS-PAGE electrophoresis

SDS-PAGE electrophoresis running gels in the percentages of 10 or 15% were casted with 5% stacking gel on top (Table 16). The percentage of the running gel depended on the molecular weight of the proteins of interest. In brief, running gels were casted in a casting chamber (glass plate sandwich), and overlaid with Isopropanol (Honneywell, 34863-2.5L) to obtain a straight

upper edge. Gel polymerization took place at room temperature for at least 45 minutes. Isopropanol was carefully poured out onto a paper towel and the gap on top of the running gel was thoroughly washed with ddH2O. Then, stacking gel was poured on top of the polymerized running gel, which was followed by gentle insertion of a comb. For this, the combs were carefully slid from one extremity to the other, pushing away any bubbles. After another 45 minutes of polymerization, either the gel was directly used or stored at 4ºC wrapped in wet paper and covered with clingfilm, to be used on the next day.

Table 16. Composition of electrophoresis gels

Running gels		
	10% (small)	15% (small)
ddH2O	4 ml	2.3 ml
30% Acrylamide mix	3.3 ml	5 ml
1.5M Tris buffer (pH 8.8)	2.5 ml	2.5 ml
10% SDS solution	100 µl	100 µl
10% APS solution	100 µl	100 µl
TEMED	10 µl	10 µl
Total volume	10 ml	10 ml
Stacking gels		
	5% (small)	5% (large)
ddH2O	3.4 ml	13.58 ml
30% Acrylamide mix	0.83 ml	3.4 ml
1.5M Tris buffer (pH 6.8)	0.63 ml	2.6 ml
10% SDS solution	50 µl	0.2 ml
10% APS solution	50 µl	0.2 ml
TEMED	5 µl	0.2 ml
Total volume	5 ml	20 ml

Once the run could be initiated, combs were delicately removed from each gel and the pockets were thoroughly washed with ddH2O. The gels were then assembled in the running chamber, which was filled up with 1x SDS-PAGE Running buffer (1l for small, 2l for large chambers). If stored over night at 4ºC, gels were allowed to warm up to room temperature. Meanwhile, all samples were boiled for around 5 minutes, followed by quick centrifugation at 14,000 rpm. At room temperature, the first pocket was loaded with 5µL of Color Protein Standard Broad Range (CellSignaling, 74124), and 30 to 50µL from each sample were loaded into each of the following pockets, according to loading plan. Loading uniformity was ensured by filling up marker or empty pockets with 2x Laemmli buffer, to match the loaded volume of samples. Electrophoresis run was carried out for circa 3,5 hours at 150V; small gels were run at 120V for approximately 2 hours.

Western Blotting

Proteins separated through SDS-PAGE electrophoresis were transferred onto PVDF membranes (Thermo Scientific, 88518). To achieve this, the membranes were activated with Methanol shortly before the procedure, submerged by it for 30 second. Meanwhile, Whatman paper pre-cut sheets were thoroughly soaked in Western Blot Buffer. Within the Trans-Blot Turbo Transfer System's cassette, paper, PVDF membrane, SDS-Page electrophoresis gel and paper were carefully assembled, in the described order from the bottom to the top. As paper, either one extra thick Western Blotting filter paper (ThermoFisher, 88605) or 3 sheets of Whatman 3MM Western Blotting paper (Whatman, 3030-917) were used on each side of the WB transfer assembly. Western blotting was performed at 25V and 1A and took 30 minutes.

Immunodetection

After Western Blotting, the membranes were blocked in incubation with Western Blot blocking solution at 4ºC, for a minimum of 1 hour. Once the blocking was complete, incubation with the appropriate primary antibody took place overnight, also at 4ºC. On the next day, fresh TBS/T was prepared and used for washing the membranes, which was done three times for at least 5 minutes each. Then, incubation with the required secondary antibody (depending on the primary antibody used) diluted in TBS/T took place for 1 hour. After this incubation, the membrane went through three more washes with fresh TBS/T buffer for 5 minutes, followed by one wash with TBS. Finally, membranes were stored in TBS prior to immunodetection. Incubation with anti-α-tubulin antibody as a loading control was done for 20 minutes at 4ºC, simultaneously with anti-mouse IgG, HRP-linked antibody as a secondary antibody.

Membrane imaging was performed using the iBright™ CL750 Imaging System (Invitrogen™), and detection was based on enhanced chemiluminescence (ECL) using SuperSignal West Femto Maximum Sensitivity Substrate (ThermoScientific, 34095). Each membrane was carefully placed in a metal box, had ECL-solution distributed over its surface and was incubated for 5 minutes in the dark. Then, the membranes were placed in an open plastic bag, which was closed and carefully rolled over with a small roll tool to remove excess liquid and potential air bubbles. Various exposure times were imaged, until saturation of protein bands was reached. Images of membrane, showing marker bands, and protein bands were also acquired in overlay. For temporary storage, the membranes were kept in boxes at 4ºC in TBS buffer.

Stripping

If different antibodies had to be probed on the same membrane, stripping was required. To achieve this, membranes were incubated in 100 ml of stripping buffer containing 700 µl of β-mercaptoethanol per membrane at 50ºC and 55rpm for 30 minutes. This was followed by three washes in TBS/T for 5 minutes each, as previously described. Once again, the membrane was blocked with blocking solution for Western Blot for a minimum of one hour at 4ºC in rotation. Finally, the membrane could be incubated one more time with the desired primary antibody.

2.2.4 Fluorescence microscopy and image processing methods

Immunofluorescence and fluorescent staining of TNTs

The traditional staining for investigation of TNTs in this thesis consisted of staining for plasma membrane, tubulin, and F-actin. In detail, once the treatment times were due, cells were washed 2 times with prewarmed DPBS and fixed with 3.7% paraformaldehyde for 20 minutes at room temperature, in the dark. Then, cells were washed 3 times with PBS (as there should be no permeabilization prior to WGA staining) and stained with WGA-AF488 (Thermo Fisher, W11261) or WGA-AF647 Conjugate (Thermo Fisher, W32466) for 20 minutes, at room temperature. This step was followed by 3 more washes with PBS/T. Next, the coverslips were blocked with blocking solution for immunofluorescence for at least 1 hour at 4ºC. After blocking, staining with primary antibodies took place in a metal box, with coverslips being laid on a drop of antibody solution in PBS/T overnight at 4ºC. On the next day, after the coverslips had been returned to their respective wells in the 24-well plate and washed 3 times with PBS/T, incubation with secondary antibodies could take place in combination with Phalloidin AF546 (Thermo Scientific, A22283) or AF647 (Thermo Scientific, A22287), as described for primary antibodies. If Phalloidin was not bound to indirect immunofluorescence, the staining could be performed at room temperature. DAPI (AppliChem, A4099) was applied for nuclear staining for 20 minutes at room temperature. Finally, coverslips were washed 3 times with PBS/T, once with PBS, and mounted on glass slides with Prolong™ Gold Antifade Reagent (Life Technologies, P36930). After drying overnight, coverslips were sealed with CoverGrip ™ Coverslip Sealant (Biotium, 23005).

Puncta assessment

Upon induction of autophagy, WIPI proteins localize to nascent phagophores and form fluorescent puncta. In this thesis, U2OS cells stably expressing GFP-WIPI1, GFP-WIPI2B,

mRFP-EGFP-WIPI4 were employed to assess puncta. For this, WIPI puncta positive cells were manually quantified over the total amount of cells, while using the fluorescence microscope Axiovert 200M with Axiovision Rel 4.7 Software (Carl Zeiss GmbH).

Quantification of TNT index and TNT transfer assays

Once the coverslips had been sealed, the fluorescence microscope Axiovert 200M described above was used for quantification of the TNT index and cargo positive TNTs. In order to be considered a TNT, a certain cellular structure should attend to the following criteria: 1. It should contain actin, 2. It should connect at least two cells, 3. It should not touch the substrate. If all criteria were fulfilled, the structure was counted as one TNT. These criteria are applied based on the first published observation of TNTs by Rustom, which led to the original definition of TNTs as "cell-to-cell interaction based on membrane continuity and intercellular transfer of organelles" (Rustom et al., 2004). The TNT index is defined by the number of TNTs per 100 cells, and at least 200 cells were counted per coverslip.

In general, cells were stained with at least Phalloidin to identify F-actin-labelled structures corresponding to TNTs. Importantly, F-actin should be labelled with a fluorophore observable according to the available filters in the microscope (in this case AF488, AF546 or AF647). If possible, depending on which channels had already been covered, fluorescent staining with WGA and/or endogenous tubulin was included. For confirmation whether a certain TNT connected at least two distinct cells, DAPI staining or brightfield microscopy was employed. To ensure that the potential TNT in question was above the substrate, the focal plane was constantly adjusted, allowing a full scan along the Z axis.

For the investigation of TNTs containing cargo, distinct experimental set ups were applied to identify target proteins. When investigating such aspect in U2OS cell lines stably expressing fluorescently tagged proteins, no further staining was necessary. For cargo such as mitochondria or ferritin, immunofluorescence was employed, respectively targeting TOM20 or ferritin itself. In the case of NCOA4 and FTH1, transient transfections of myc-NCOA4 variants or GFP-FTH1 were performed. All cargoes could thereby be identified through fluorescent microscopy.

TNTs were primarily identified according to the criteria above described, and the ones which contained a fluorescently tagged cargo co-localizing with the F-actin-stained structure were manually counted or simply imaged as a "cargo positive TNT". When quantifying puncta positive TNTs, the percentage of how many TNTs were counted as "puncta positive TNT" was calculated and is displayed in the results of this thesis.

Confocal laser scanning microscopy

Confocal laser scanning microscopy imaging was achieved with a Laser Scanning Microscope (LSM800, Carl Zeiss GmbH) using a 40x 1.3 DIC Plan-Apochromat Oil-Immersion Objective (Carl Zeiss GmbH) or 63x 1.4 DIC Plan-Apochromat Oil-Immersion Objective (Carl Zeiss GmbH). All confocal images were acquired using a 1024 x 1024 pixel format with a pixel dwell time of 2.06 µs and an averaging of 2 frames. Z-stacks were generally acquired with a section interval of 0.3 µm. Finally, CZI files were processed with ImageJ2 (Schindelin et al., 2012).

Colocalization profile

Colocalization profile was generated with the ZEN 3.0 Software (blue edition, Carl Zeiss GmbH). Briefly, once confocal images had been acquired, the tab "Profile" on the left of the visualization area allowed the assessment of a colocalization profile. After selecting two desired channels to investigate on a potential colocalization, a line could be manually drawn on top of a certain fluorescent puncta structure to be analyzed. Based on this, an intensity profile was generated, where pixel intensities corresponding the previously selected channels were plotted across a certain distance in µm, which is determined by the length of the drawn line. The obtained plots were exported for display along with the original images.

3D reconstruction and video rendering

To allow for 3D reconstruction, confocal images were acquired with Z stacks set for optimal slice distance, as automatically determined by the software. Reconstruction was mediated with the ZEN 3.0 Software.

In detail, once a confocal image had been successfully acquired, the tab "3D" on the left of the image opened up for 3D visualization. Among five different render modes for distinct appearances offered by the software, the option "Surface" was picked to display a 3D representation of the acquired image, where TNTs are visualized as continuous tubes. Cells were initially exhibited with scales in µm for X, Y and Z axes. Moving bars located on the corners of the visualization area allowed rotation of the image in all axes, as well as a zoom in or out tool. A "hand" tool allowed grabbing and freely moving the image across the visualization area, facilitating the desired positioning of the 3D reconstructed image. As for regular confocal images, the color of each channel could be manually adjusted, as needed. F-

actin was generally colored in grey for clearer visualization, whereas other fluorophores were usually kept at their traditional colors.

At first, 3D reconstructed images were manually adjusted into the desired position with the tools above described, and the zoom tool was used to focus on the TNT in question. For visualization of TNT content, a clipping tool was applied to place a sectional cut through the X or Y planes (depending on the orientation of the TNT in focus), across the Z axis. The clipping plane was set to be transparent, to allow visualization of TNT's interior and content. Based on the position of the TNT cargo to be exposed, the initial position of the cut through the X or Y axes was defined.

Render series were prepared by picking "Position List" and selecting a new position for the clipping tool while moving through the X or Y axes. Each zoom in, change of angle, or change in the clipping region corresponded to a new position in the "Position List", thereby producing a dynamic video. Most importantly, new positions were selected while gradually moving the clipping tool across the TNT containing a certain cargo, perpendicularly reconstructing the tube while visualizing its interior. For the rendering of the "Position List" into a video format, frames were set to "1000" when possible, to allow smooth motion once the model was exported as a video. Once the rendering was complete, the file was exported into .AVI format, with frame rate and frames per second settings individually adjusted for each video, to guarantee a smooth playback.

Live cell imaging and single-particle tracking

In the acquisition tab of the Zen 3.0 Software, the option "Time Series" was checked, opening up a section on the right of the visualization area for temperature and CO2 control settings. Once making sure the Definite focus was activated, the incubation chamber for live imaging was initiated at least 30 minutes prior to imaging to ensure that the cells were kept at 37ºC and 5% CO2 during time series image acquisition.

When the assay was completed, cells had their media aspirated and replaced by Live cell imaging solution (Invitrogen, A14291DJ) supplemented with Glucose (5mM after starvation or 20mM after full medium). Live cell microscopy was conducted with a 40x 1.3 DIC Plan-Apochromat Oil-Immersion Objective using the LSM800. The objective was placed in position and prepared with a drop of oil, followed by the attachment of the bottom part of the incubation chamber to the microscope stage. Then, a certain 35mm glass bottom dish containing the cells to be imaged was carefully attached to the chamber, without the lid, and the stage was brought down until the bottom of the dish gently touched the drop of oil on the

objective. After performing alignment for Koehler illumination, ESID (electronically switchable illumination and detection module) and Airyscan super-resolution were combined for image acquisition. Brightfield with ESID was necessary to distinguish different cells and identify TNT structures. Laser intensities, master and digital gain settings were specifically adjusted to each experiment, in order to avoid photobleaching as much as possible. Images were acquired with optimal frame size, a pixel dwell time of 2.11 µs and bidirectional scanning. Then, multiple positions could be selected to be imaged in one cycle with the "Tiles">"Positions" tool. The frame time, number of channels and number of selected positions determined the time intervals between each frame of the time series, which was in general between 30 and 60 seconds. At the bottom of the "Acquisition" tab, the final duration of the Time Series could be set. Once all positions had been manually selected, they were rechecked, allowing final readjustments of the focal plane before initiating the experiment.

Directly after acquisition, the obtained Airyscan projects were processed and exported with the ZEN software. The acquired stacks were processed to obtain videos in ImageJ2, where scale bars and time labeling were included.

Manual tracking of single particles was mediated with the open-source ImageJ2 Plug-in MTrackJ (Meijering et al., 2012). For this, each particle's position was manually tracked successively through each frame of the obtained time-lapse video. Once the tracking was concluded, one could adjust the track display settings. For this thesis, tracks were displayed in continuous and progressive lines, with each tracked position represented by a circle. The colour of tracking positions and tracks were chosen according to the fluorophores in question. Finally, the videos were exported exhibiting the track of each object in selection.

2.2.5 Statistical analysis

All data was analyzed with GraphPad PRISM 9.2.0. Data display mean and calculated standard deviation (SD) in bar graphs with individual data points. Gaussian distribution was assumed based on QQ plots, and the data was therefore further statistically analyzed with the following parametric tests: ordinary One Way-ANOVA, followed by Holm-Šidak's multiple comparisons post-hoc test, or ordinary Two Way-ANOVA, followed by Tukey's multiple comparisons post-hoc test. Datasets which did not follow a Gaussian distribution went through log-transformation and only then analyzed with the appropriate parametric test. P values below 0.05 were considered statistically significant, classifying p-values as n.s ($p > 0.05$), * ($p < 0.05$), ** ($p < 0.01$) or *** ($p < 0.001$).

CHAPTER 3. Autophagic membranes

3.1 Autophagic membranes in Tunneling Nanotubes

Autophagy is modulated by AMPK and mTORC1, with the important participation of WIPI proteins as PI3P effectors mediating autophagosome biogenesis. During the initiation of phagophore formation, WIPI1 and WIPI2 recruit the ATG16L1 complex, thereby promoting the localized lipidation of LC3, which leads to phagophore extension, maturation, fusion with lysosomes and cargo degradation (Proikas-Cezanne et al., 2015). WIPI4 also plays a crucial role in the initiation of autophagy and in phagophore formation, directly interacting with WIPI1 and WIPI2, and localizing to nascent autophagosomes (Bakula et al., 2017).

The intercellular transfer of several types of cargoes via TNTs has been under investigation by numerous research groups. The types of reported cargoes so far include small molecules as calcium ions, nucleic acid, plasma membrane elements, prion proteins and other protein aggregates. In addition, vesicles from lysosomes, Golgi complex, endoplasmic reticulum, and early endosomes, including double-membrane vesicles, and even whole organelles as mitochondria have been observed while travelling through TNTs (Abounit & Zurzolo, 2012; Sartori-Rupp et al., 2019). TNTs seem to offer an alternative path to cope with cellular stress, by allowing cells to receive support from neighboring cells, while diluting a certain burden by distributing it. For instance, lysosomes containing prion-like aggregates can hijack TNT-transport, thereby contributing to disease spreading in Parkinson (Abounit et al., 2016; Victoria & Zurzolo, 2017; Wu et al., 2013). An even better example is the spreading of protein aggregates and dysfunctional mitochondria by unhealthy cells, while simultaneously importing functional mitochondria via TNTs, as reported by Scheiblich (Scheiblich et al., 2021).

The mechanistic details concerning TNT biogenesis have not yet been fully deciphered. Several modulators of the actin cytoskeleton are involved in the biogenesis of TNTs, such as M-Sec, Cdc42, Eps8 and Myo10 (Ljubojevic et al., 2021). Recently, the Wnt pathway has been uncovered as yet another player in the formation of TNTs in primary neurons, via the Ca^{2+}/calmodulin-dependent protein kinase II (CaMKII) (Vargas et al., 2019). Interestingly, variations in Ca^{2+} levels are also connected with exosome and vesicle release (Victoria & Zurzolo, 2017), which may be induced either due to alterations in autophagic and lysosomal pathways (Caballero et al., 2021) or as a response to elevated Ca^{2+} levels (Medina, 2021). Finally, Ca^{2+} ions also act as an important signal for the regulation of autophagy, as they can induce AMPK and therefore autophagy itself (Hawley et al., 2005).

These observations, and specifically the presence of lysosomal and double-membrane vesicles within TNTs led to the hypothesis whether autophagic membranes could be intercellularly exported as well. This chapter aimed to investigate on the presence of WIPI1, WIPI2, WIPI4 and LC3 in TNTs. In (Sporbeck et al., 2023), it was revealed that autophagic membranes can travel through TNTs to nearby cells upon necessity. During my doctoral studies, my main contribution to this manuscript consisted of providing evidence that WIPI1 and LC3 puncta migrated from one cell to another via Tunneling Nanotubes, with the transfer of WIPI1 being enhanced upon starvation treatment.

3.1.1 WIPI1 puncta are intercellularly transferred via Tunneling Nanotubes

As previously introduced in this study, starvation leads to the initiation of autophagy, which is characterized by the accumulation of autophagy related proteins, such as WIPI1, at nascent phagophore membranes, forming punctate structures (Proikas-Cezanne et al., 2004). Here, a U2OS cell line stably expressing GFP-WIPI1 was employed as a tool for the investigation of TNTs in the context of autophagy. To facilitate visualization of WIPI1 marked membranes indicating phagophores, cells were subjected for 24 hours to the following conditions of nutrient availability: full medium, low serum or starvation. Identification of TNTs was facilitated by the fluorescent staining of the plasma membrane and filamentous actin (F-actin). As TNTs connect cells mediating membrane continuity, it becomes important to stain for plasma membrane, which was achieved with Wheat Germ Agglutinin (WGA) staining, a lectin which selectively binds to glycoproteins on the plasma membrane of cells. F-actin, the most important component of TNTs, was stained with Phalloidin, a peptide which binds F-actin with high specificity. WGA and Phalloidin staining allowed identification and manual quantification of TNTs per 100 cells (TNT index), as well as the percentage of puncta positive TNTs. Throughout this study, TNTs were identified following the three criteria before mentioned: 1. It contains actin; 2. It connects at least two cells; 3. It does not touch the substrate.

Indeed, GFP-WIPI1 puncta were identified within TNTs, based on the localization of GFP-WIPI1 puncta within F-actin and WGA-stained structures (representative images in Figure 9a). These cells were also quantitatively analyzed with regards to percentage of GFP-WIPI1 puncta positive cells, TNT index and percentage of GFP-WIPI1 puncta positive TNTs. As expected, starvation treatment significantly increased the percentage of GFP-WIPI1 puncta positive cells, compared to fed and low serum treatments (Figure 9b). Moreover, these results revealed that subjecting the cells to low serum barely induced the formation of TNTs, whereas

starvation strongly increased it (Figure 9c). Concerning the percentage of GFP-WIPI1 puncta positive TNTs, in comparison to fed conditions, low serum treatment resulted in a mild increase of GFP-WIPI1 puncta transfer via TNTs. In contrast to that, starved cells transferred significantly more GFP-WIPI1, indicated by the rise in the percentage of TNTs containing GFP-WIPI1 puncta (Figure 9d).

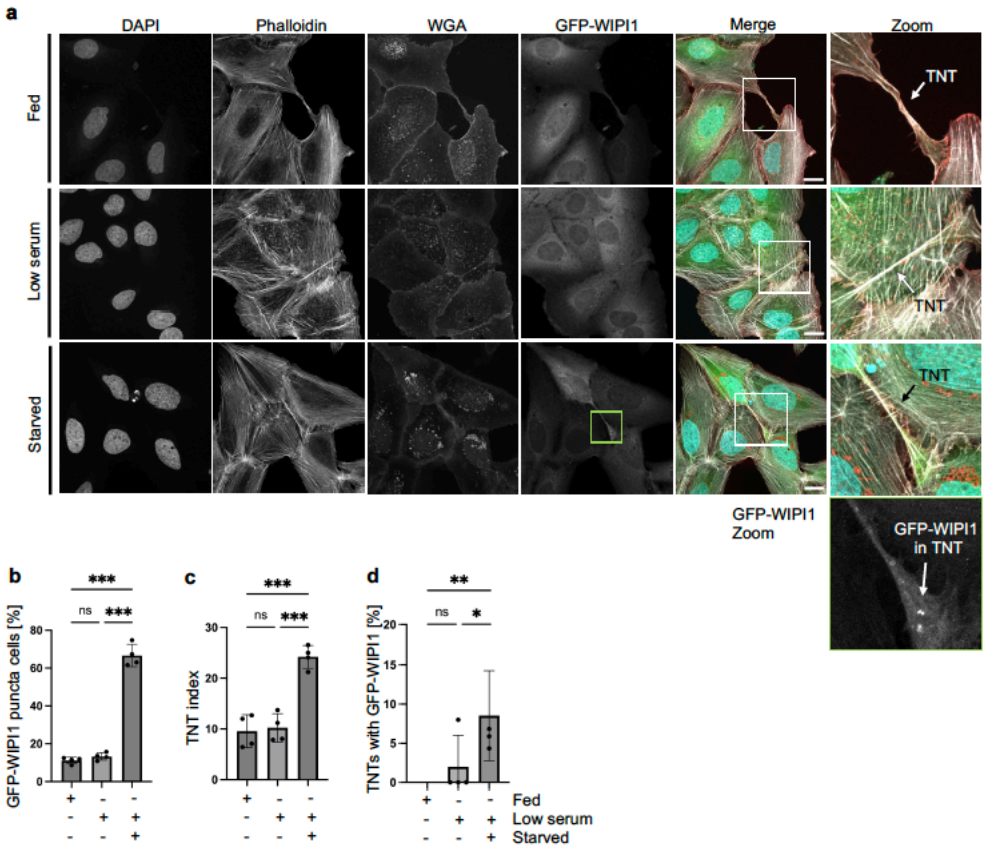

Figure 9. U2OS cells expressing GFP-WIPI1 form Tunneling Nanotubes, which mediate the intercellular transfer of GFP-WIPI1 puncta. a) U2OS GFP-WIPI1 cells were stained with Phalloidin for F-actin and WGA. Zoom in sections of a TNT in each condition are shown, including a zoom in image of the GFP channel in starved condition, exposing GFP-WIPI1 puncta in a TNT. **b)** U2OS GFP-WIPI1 cells cultured in fed, low serum, or starved conditions for 24 hours were manually quantified with regards to the percentage of GFP-WIPI1 puncta positive cells, **c)** TNT index and **d)** the percentage of TNTs containing GFP-WIPI1 puncta. Up to 952 cells were counted, in n = 4. The results were statistically analyzed with Ordinary One-Way ANOVA, Holm-Sidak's post-hoc test. "TNTs with GFP-WIPI1 [%]" data is displayed with original data points, however with significances obtained from log-transformation. P-values: <0.05: *; <0.01: **; <0.001: ***. Scale bars: 20µm.

Finally, the acquisition of confocal images with Z-stacks set with optimal distance allowed 3D reconstruction of the image with the ZEN software. Still images of a 3D

reconstructed TNT in U2OS cells stably expressing GFP-WIPI1 are shown in Figure 10. From sections 1 to 8, the observer is guided from the top view of the 3D model towards the interior of a certain TNT containing a GFP-WIPI1 puncta structure.

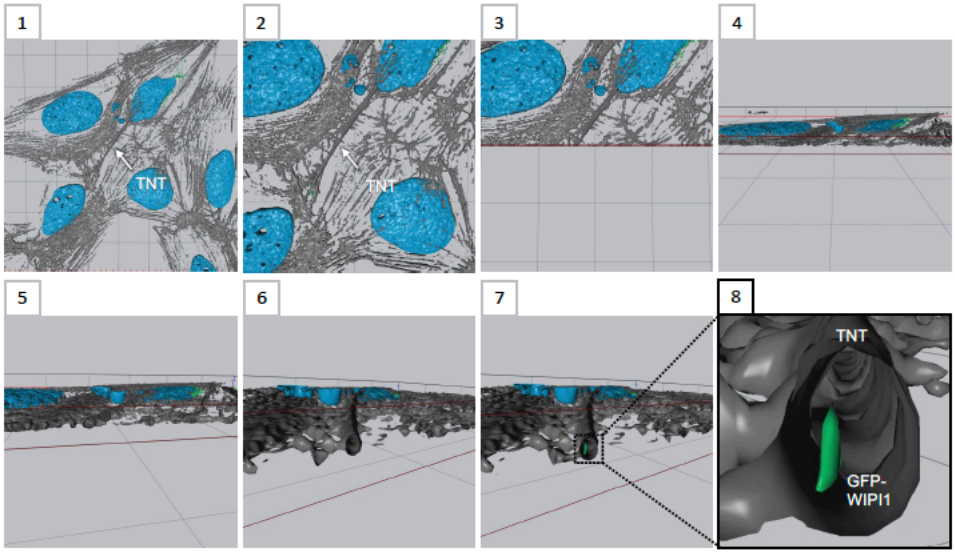

Figure 10. 3D reconstruction of Tunneling Nanotube containing GFP-WIPI1 puncta in U2OS cells stably expressing GFP-WIPI1. U2OS cells stably expressing GFP-WIPI1 were starved for 24 hours and stained with Phalloidin in gray and DAPI in light blue. **1)** Top view of the acquired 3D model. **2)** Zoom into the 3D model to show a TNT structure from a closer point of view. **3)** Activation of a clipping tool, with a cut placed through the Y- and Z-axes of the 3D model. **4**, **5** and **6)** The point of view is relocated and tilted towards the interior of the TNT in question, to reveal its content. **7)** As the TNT is reconstructed by moving the clipping tool along the Y-axis, a GFP-WIPI1 puncta is exposed. **8)** The frame is brought even closer into the TNT containing a GFP-WIPI1 puncta.

In addition, U2OS GFP-WIPI1 cells were seeded onto a 35mm glass bottom plate, and later treated with starvation medium for 24 hours. Once the assay was completed and the medium was replaced with live cell imaging solution, cells were imaged by live time lapse microscopy with Airyscan super resolution in combination with ESID, for approximately 45 minutes at 37ºC and 5% CO2. This live visualization presents five GFP-WIPI1 puncta in motion between neighboring cells under starved conditions, providing strong evidence of WIPI1 intercellular traffic through TNTs. The acquired images were processed into videos and manual single particle tracking with the MTrackJ open-source Plug-in for ImageJ2 allowed monitoring of traveling GFP-WIPI1 puncta (Figure 11).

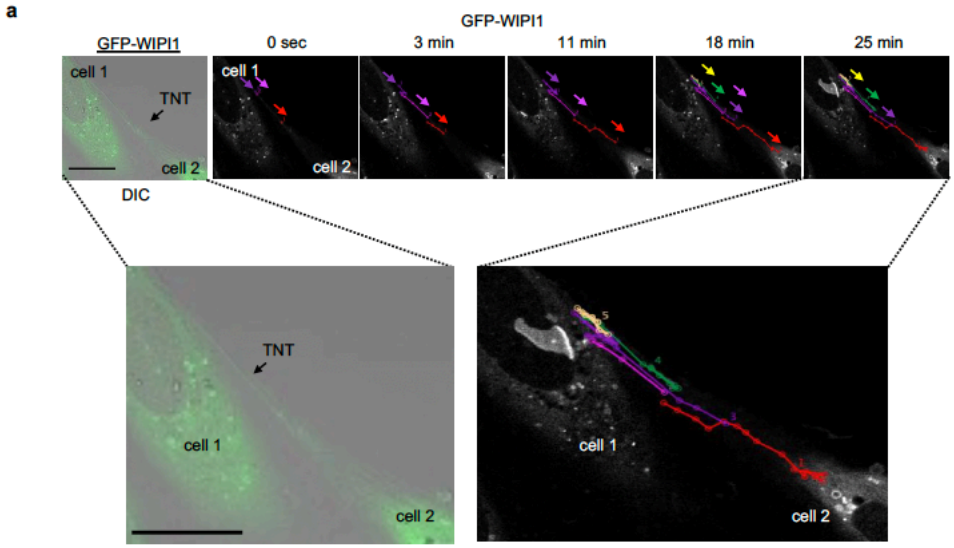

Figure 11. Live time lapse video of U2OS stably expressing GFP-WIPI1 after starvation treatment. U2OS stably expressing GFP-WIPI1 were starved for 24 hours and imaged through live time lapse microscopy over the course of 45 minutes. Manual single particle tracking allowed monitoring of GFP-WIPI1 puncta being trafficked from cell 1 to cell 2, with frames of five different time points showing tracks in distinct colors. Below, magnified images of the first time point with DIC and GFP channels merged, as well as the last displayed time point with GFP channel and tracks. Scale bars: 20µm.

3.1.2 WIPI2B puncta travel through Tunneling Nanotubes

As previously described, WIPI2, together with WIPI1, functions in phagophore formation, promoting membrane elongation by recruitment of the ATG16L1 complex (Proikas-Cezanne et al., 2015). Upon the observation that WIPI1 travels from cell to cell via TNTs and to reinforce the investigation on whether autophagic membranes are transferred via TNT to neighboring cells, it was questioned whether other well-known markers on autophagic membranes, such as WIPI2B, could also be identified within TNTs. This was achieved by using U2OS cells stably expressing GFP-WIPI2B, similarly to the experiments previously performed with U2OS GFP-WIPI1. Cells were treated in fed, serum starved or starved conditions for 24 hours, followed by staining of nuclei, F-actin cytoskeleton, and plasma membrane, respectively with DAPI, Phalloidin and WGA.

The presence of GFP-WIPI2B inside of TNTs was qualitatively confirmed (representative images in Figure 12a), leading the experiment to quantitative assessments. GFP-WIPI2B puncta positive cells were manually quantified, and the TNT index was assessed, as well as the percentage of GFP-WIPI2B puncta in TNTs. Low serum resulted in a gentle

increase in the percentage of GFP-WIPI2B puncta positive cells, in contrast to a remarkable increase caused by starvation. TNT index followed a similar tendency as seen in U2OS GFP-WIPI1, with a statistically significant rise in the formation of TNTs only upon starvation. With regards to cargo transfer through TNTs, low serum was not sufficient to induce the intercellular transfer of GFP-WIPI2B via TNTs, which was only observed in starved cells, where the percentage of TNTs with GFP-WIPI2B puncta was significantly enhanced.

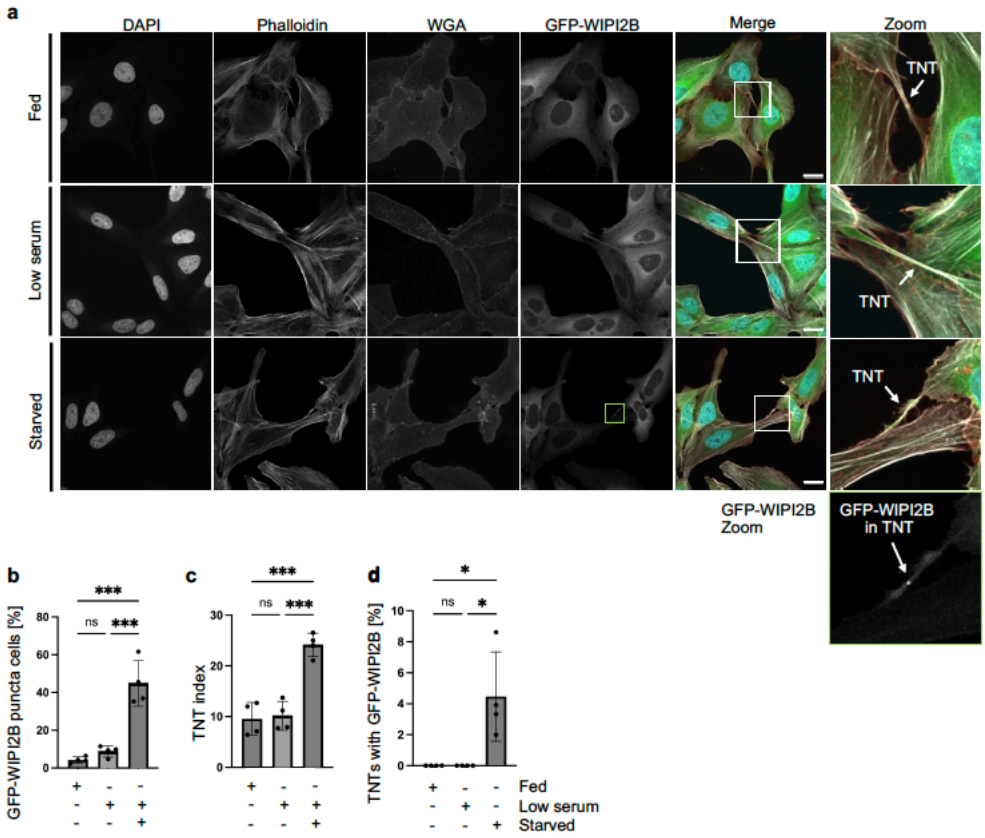

Figure 12. U2OS cells expressing GFP-WIPI2B build Tunneling Nanotubes, which promote the intercellular traffic of GFP-WIPI2B puncta. a) U2OS cell lines stably transfected with GFP-WIPI2B were treated with full medium, low serum or starved medium for 24 hours and stained with DAPI, Phalloidin and WGA. Zoom in sections show TNTs in all conditions, whereas an extra zoom in section of GFP channel in starved cells shows GFP-WIPI2B within a TNT. **b)** Results of quantitative assessment of the percentage of GFP-WIPI2B puncta positive cells, **c)** TNT index and **d)** percentage of GFP-WIPI2B puncta positive TNTs are shown. Up to 944 cells were counted per condition, n = 4. This data set was statistically analyzed with Ordinary One-Way ANOVA, Holm-Sidak's post-hoc test. P-values: <0.05: *; <0.01: **; <0.001: ***. Scale bars: 20µm.

A confocal image previously acquired of a TNT containing a GFP-WIPI2B puncta in U2OS cells stably expressing GFP-WIPI2B was reconstructed in a 3D model. Figure 13 shows

still images of the obtained 3D reconstruction, where one can observe a TNT, its interior and part of its content.

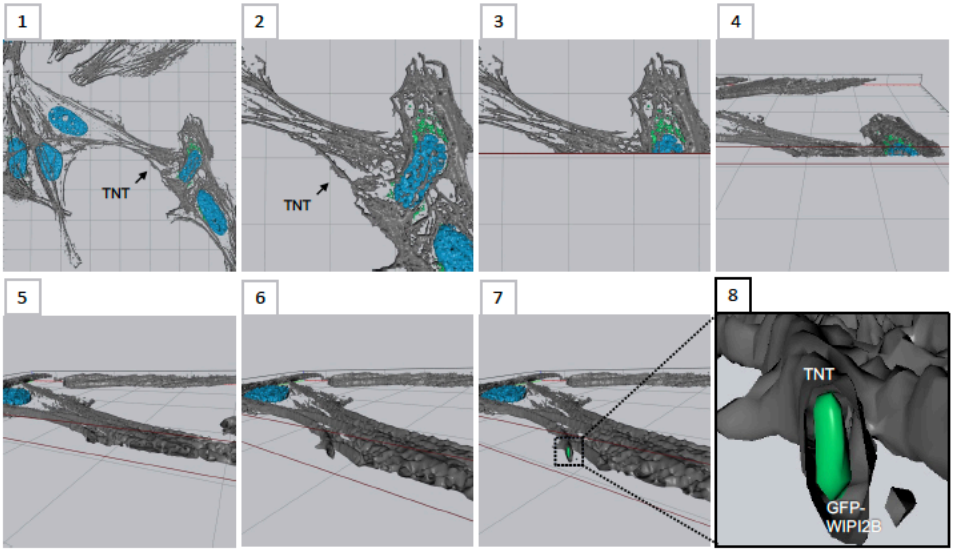

Figure 13. 3D model of a GFP-WIPI2B puncta in a Tunneling Nanotube. U2OS cells stably expressing GFP-WIPI2B starved for 24 hours, then stained with Phalloidin in gray and DAPI in light blue. **1)** 3D model visualized from the top. **2)** Zoom into the 3D model, showing a TNT structure. **3)** Clipping tool places a sectional cut through the Y- and Z-axes. **4**, **5** and **6)** Relocation of the frame guides the observer to visualize the interior of the TNT in question. **7)** The clipping tool is shifted along the Y-axis, thereby reconstructing the TNT and exposing a GFP-WIPI2B puncta inside of it. **8)** Further zoom in allows a closer point of view into the TNT containing a GFP-WIPI2B puncta.

3.1.3 WIPI4 puncta are trafficked via Tunneling Nanotubes

WIPI4 is yet another PI3P effector involved in phagophore formation, which interacts directly with both WIPI1 and WIPI2. Besides contributing to the double-membrane extension, WIPI4 determines phagophore size (Bakula et al., 2017). Considering the previous results presented in this thesis, it was next questioned whether WIPI4 could also travel intercellularly via TNTs.

To qualitatively assess whether WIPI4 could be intercellularly trafficked via TNTs, a U2OS cell line stably expressing mRFP-EGFP-WIPI4 was employed. Since several stress factors can induce the formation of TNTs (Rustom et al., 2004), and WIPI4 plays a role in iron metabolism through ferritinophagy (Aring et al., 2022), the cellular iron levels were modulated. Iron overload or iron chelation were respectively mediated by 188.68 µM Ferric ammonium citrate (FAC) treatment, or 30 µM Deferasirox (DFX), as previously described by (Mancias et

al., 2014). In addition, cells were starved with EBSS. All treatments were carried out for 24 hours, after which cells were stained with Phalloidin for the visualization of TNTs.

In a qualitative investigation, mRFP-WIPI4 puncta were only visualized within TNTs upon DFX treatment or starvation, but not in fed condition or iron overload with FAC (Figure 14a). mRFP-WIPI4 puncta positive cells were manually assessed, revealing that DFX and EBSS treatments considerably induced WIPI4 puncta formation, whereas FAC treatment did not seem to have an effect (Figure 14b).

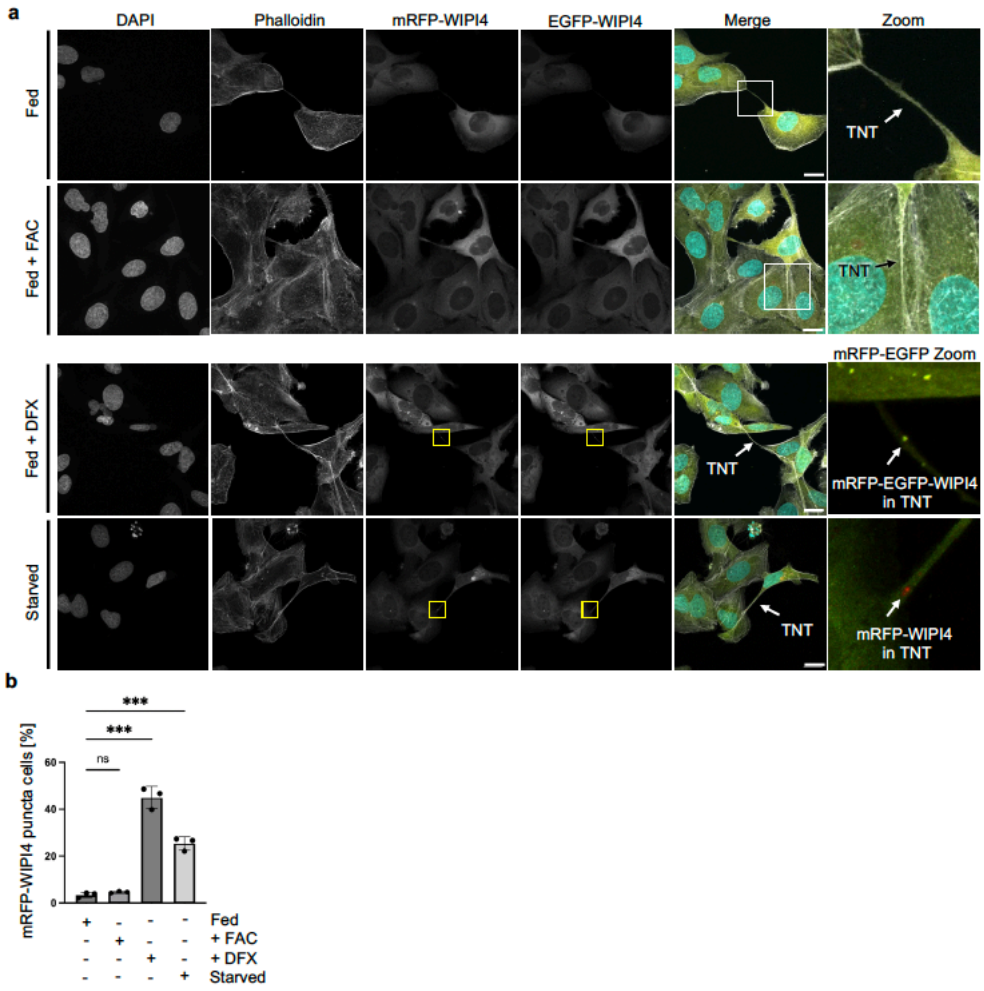

Figure 14. WIPI4 puncta are observed within Tunneling Nanotubes. a) Representative images of U2OS mRFP-EGFP-WIPI4 cells treated in fed, fed + FAC, fed + DFX or starved conditions for 24 hours, with zoom in sections depicting TNTs or mRFP-EGFP-WIPI4 puncta within TNTs. **b)** Manual quantification of mRFP-WIPI4 puncta in U2OS mRFP-EGFP-WIPI4 cells, treated as described in **a**. Data set analyzed with Ordinary One-Way ANOVA, Holm-Sidak's multiple comparison test. A maximum of 743 cells were counted per condition, in n=3. P-values: <0.05: *; <0.01: **; <0.001: ***. Scale bars: 20µm.

Once again, a 3D video was generated from acquired confocal images with Z-stacks of a U2OS stable cell line, in this case expressing mRFP-EGFP-WIPI4. Still images of a TNT containing a mRFP-EGFP-WIPI4 puncta when under DFX treatment are seen in Figure 15.

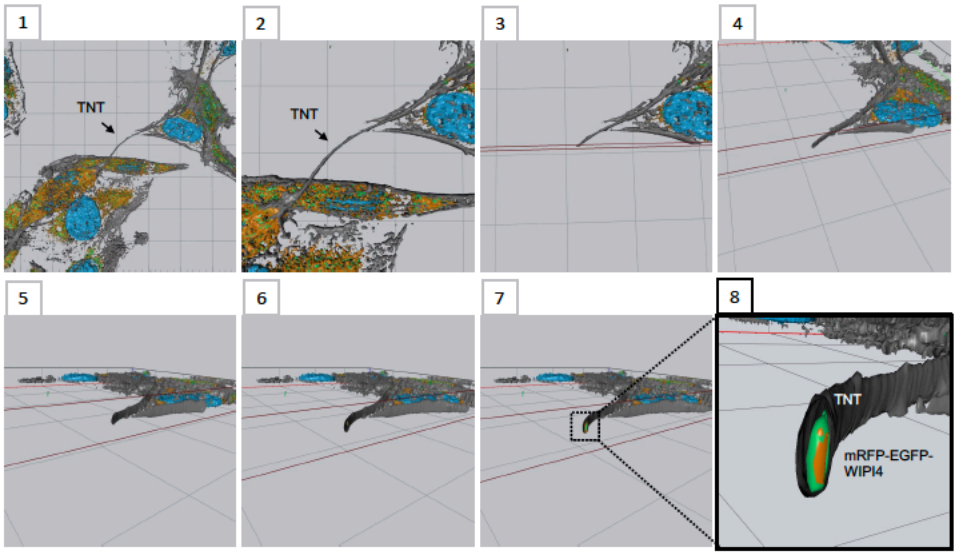

Figure 15. 3D reconstruction of WIPI4 puncta within a Tunneling Nanotube between U2OS cells stably expressing mRFP-EGFP-WIPI4. U2OS stably expressing mRFP-EGFP-WIPI4 were treated for 24 hours under iron chelation and stained with DAPI in light blue and Phalloidin in gray. Still images from 1 to 8 guide the observer from **1)** the top of the generated 3D model, **2)** zooming into a TNT structure through which **3)** a sectional cut is placed. **4, 5 and 6**) The point of view is relocated, and **7)** the TNT is reconstructed by moving the location of the section cut, revealing a mRFP-EGFP-WIPI4 puncta. **8)** Close up in the open TNT to show mRFP-EGFP-WIPI4 puncta inside of it.

3.1.4 In co-culture, the intercellular traffic of WIPI4 is enhanced towards WIPI4 deficient cells

TNTs are an important stress response mechanism and have been observed to promote the intercellular exchange of essential cellular content, thereby contributing to cellular survival (Chastagner et al., 2020). In (Sporbeck et al., 2023) it was reported that ATG16L1 deficient cells were supported by ATG16L1 competent cells by the enhanced delivery of WIPI1, WIPI2 and LC3. In light of this and knowing that TNTs can mediate the cell-to-cell transfer of WIPI4, it was hypothesized whether TNTs a similar mechanism could promote the transfer of WIPI4 from competent into WIPI4 deficient cells. To assess this, the U2OS cell line expressing mScarlet-tagged NLS (nuclear localization signal) provided by Prof. Anne Simonsen and Dr.

Chara Charsou, from the University of Oslo, was employed. Downregulation of WIPI4 was conducted in U2OS NLS-mScarlet cells (recipient) through the reverse transfection of esiWDR45. After 48 hours of downregulation, recipient cells were trypsinized and mixed in a 1:1 proportion with U2OS cells stably expressing mRFP-GFP-WIPI4 (donor) for co-culture. All cells were treated with fed, FAC iron loading, DFX iron chelation or starvation, as previously described. Finally, cells were stained with Phalloidin for TNT identification. Subsequently, representative confocal images were acquired (Figure 16a, Supplementary figure 1) and downregulation was confirmed with Western Blot (Figure 16b). Recipient cells containing mRFP-WIPI4 puncta were manually quantified (Figure 16c).

Quantification of mRFP-WIPI4 in recipient cells revealed that recipient cells lacking WIPI4 significantly received more WIPI4 from donor cells when subjected to iron chelation with DFX, in comparison to WIPI4 competent cells. Although DFX treatment increased the traffic of WIPI4 towards recipient cells, it was only significantly enhanced in cells lacking WIPI4. Furthermore, starvation treatment resulted in a remarkably higher transfer of WIPI4 into recipient cells independent on whether the cells had gone through WIPI4 downregulation or not. Representative images show WIPI4 deficient recipient cells with mRFP-EGFP-WIPI4 puncta, while images acquired from downregulation control are shown in Supplementary Figure 1.

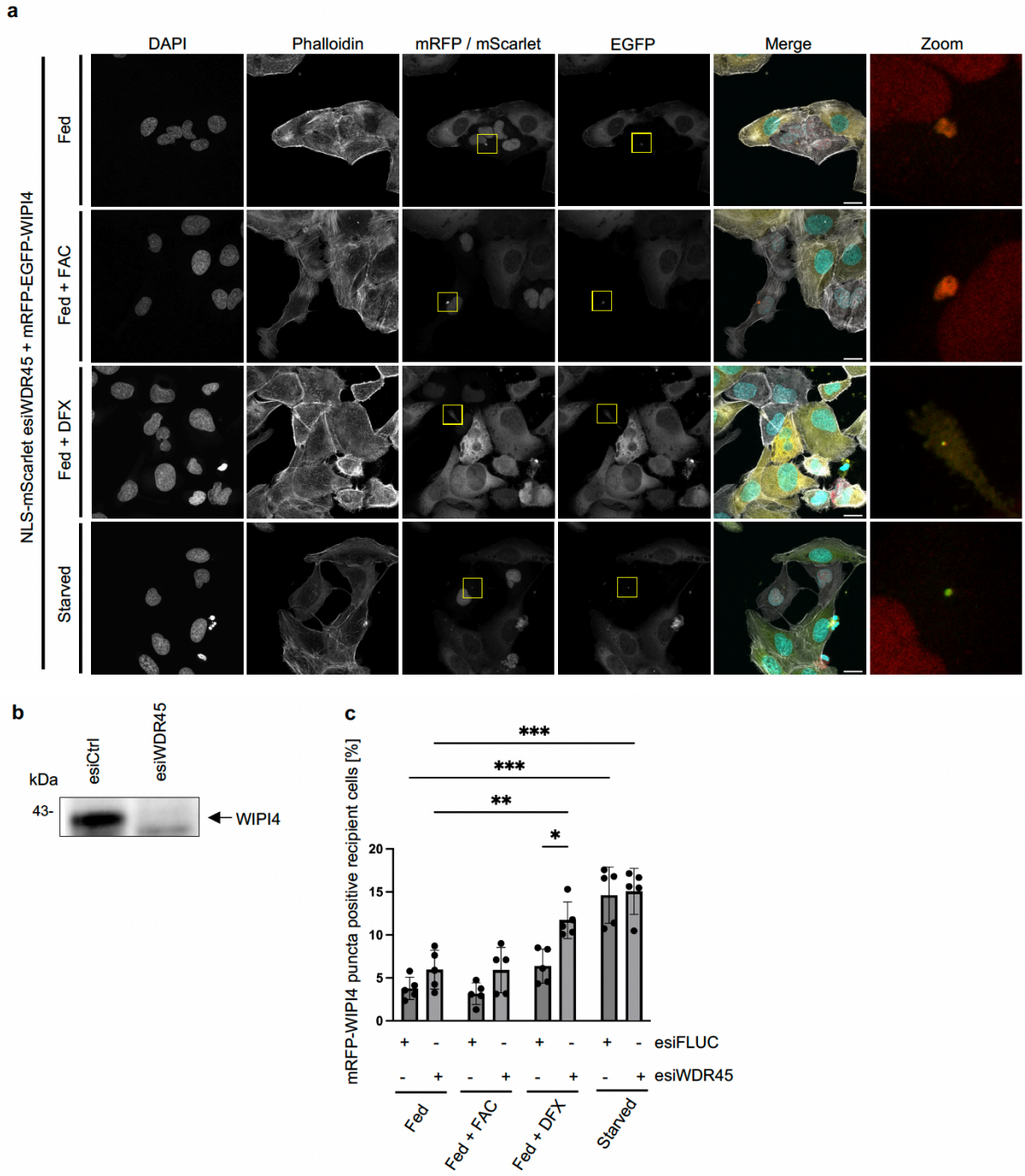

Figure 16. WIPI4 deficient U2OS cells receive WIPI4 from competent cells in co-culture. a) U2OS NLS-mScarlet cells lacking WIPI4 are co-cultured with U2OS mRFP-EGFP-WIPI4 cells and treated for 24 hours in fed, iron overload, iron chelation of starvation conditions. Representative images show WIPI4 deficient cells containing mRFP-EGFP-WIPI4 puncta. Zoom in sections of red-green overlay are shown. **b)** Western Blot confirming downregulation of WIPI4. **c)** Manual quantification of mRFP-WIPI4 puncta positive recipient cells. Statistical analysis was performed with Ordinary Two-Way ANOVA, Tukey's post-hoc test. Up to 1178 cells were counted for each condition, n = 5. P-values: <0.05: *; <0.01: **; <0.001: ***. Scale bars: 20µm.

Moreover, downregulation of WIPI4 was once again performed for a live assessment of the compensation mechanism. Employing the same cell lines, U2OS NLS-mScarlet downregulated for WIPI4 were co-cultured with U2OS mRFP-EGFP-WIPI4 and starved for 24 hours, after which cells were prepared for live time lapse imaging. Combining Airyscan super-resolution and ESID facilitated the visualization of mRFP-EGFP-WIPI4 puncta entering a recipient cell connected with a donor cell via a TNT. One mRFP-EGFP-WIPI4 punctate structure was manually tracked inside of the recipient cell with the MTrackJ plug-in for Fiji, as seen in Figure 17.

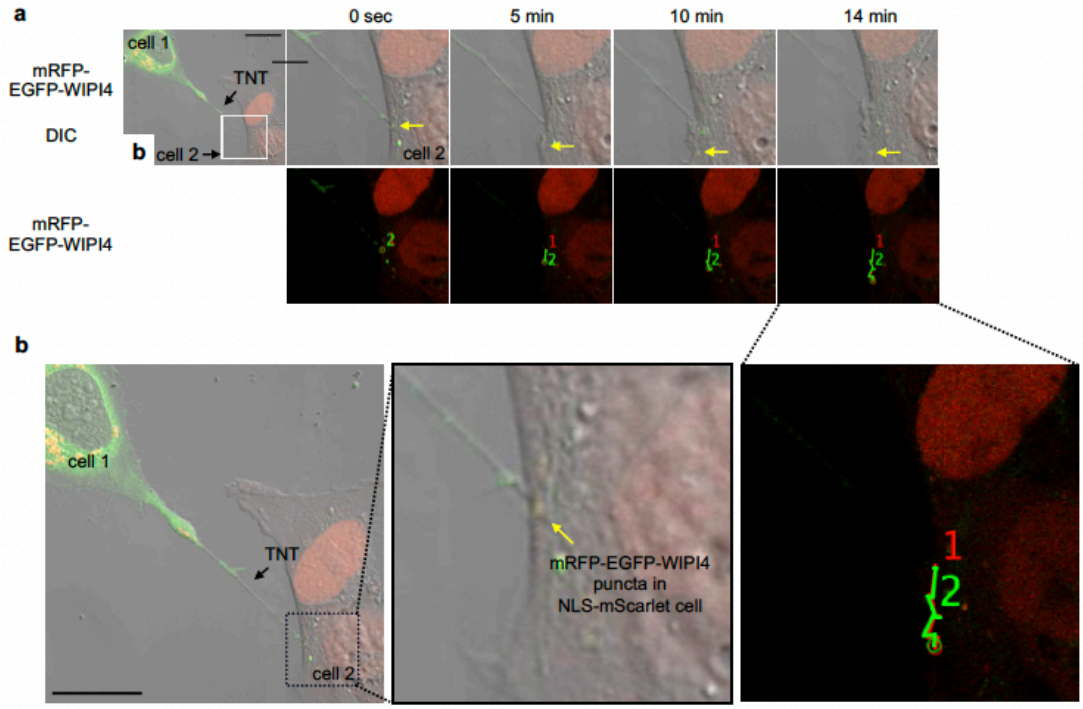

Figure 17. Live visualization of a WIPI4 deficient cell receiving compensation from WIPI4 competent cells in co-culture. In a live time lapse video, a mRFP-EGFP-WIPI4 puncta structure is observed and manually tracked within a NLS-mScarlet WIPI4 deficient recipient cell. Image acquisition was carried on for approximately 40 minutes. Track 1 corresponds to mRFP channel, whereas 2 represents EGFP. Scale bar: 20µm.

3.1.5 The autophagic marker LC3 is observed within Tunneling Nanotubes

The well-known autophagic marker LC3 localizes to forming phagophores and works on elongating their double-membranes (Kabeya et al., 2000), while co-localizing with other autophagy related proteins, such as WIPI1 (Proikas-Cezanne et al., 2004). Based on the previous results, where starvation enhanced autophagy, the formation of TNTs between

neighboring cells and the transfer of WIPI1 and WIPI2B, the next question was whether LC3 could also be observed within TNTs. In an experimental set-up as the ones previously described for U2OS GFP-WIPI1 and U2OS GFP-WIPI2B, U2OS cells stably expressing GFP-LC3 were subjected to full medium, serum starvation and starvation conditions for 24 hours, followed by Phalloidin and WGA staining for TNT visualization (Figure 18).

Manual quantification of the TNT index showed that the number of TNTs upon starvation significantly increased, consistent with previous results presented in this thesis (Figure 18b). However, in contrast to WIPI1 and WIPI2B, LC3 was trafficked via TNTs even in basal conditions. Although the percentage of TNTs containing GFP-LC3 puncta was the highest in starved cells, no statistically significant alteration was observed (Figure 18c).

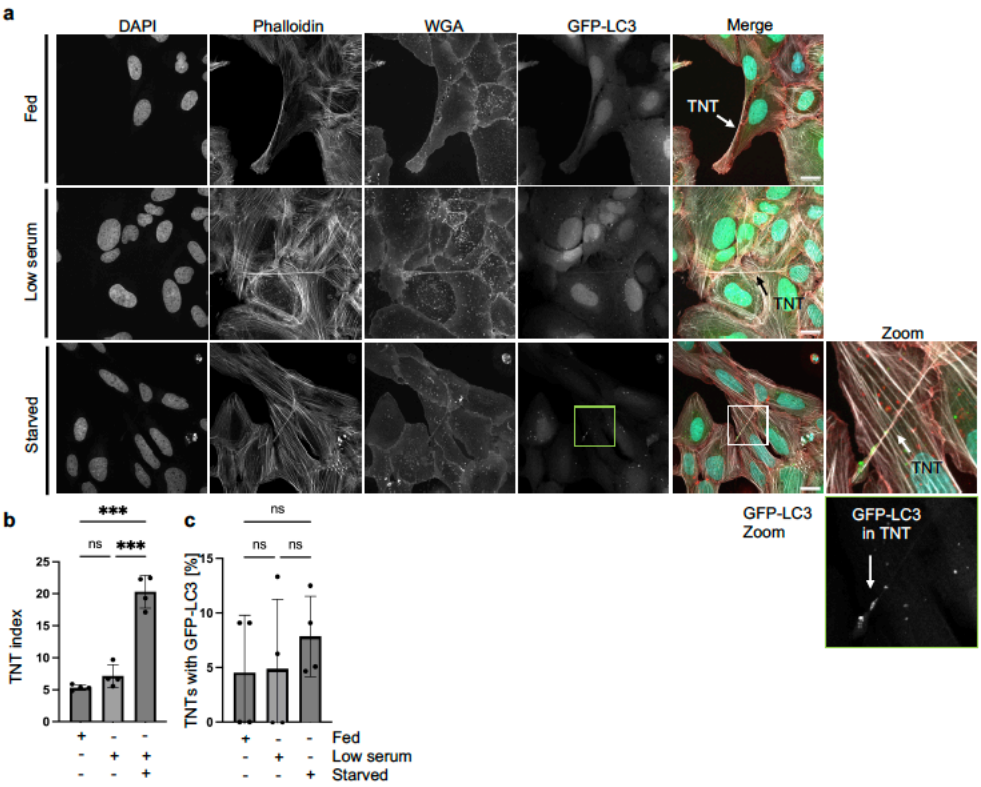

Figure 18. Starvation enhances the transfer of LC3 via Tunneling Nanotubes. U2OS GFP-LC3 cells were treated with full medium, serum starvation or starvation and subsequently stained with DAPI, Phalloidin and WGA. **a)** Representative images of U2OS GFP-LC3 cells, with zoom in sections of TNTs. In starved condition, an extra zoom in section of the GFP channel is included below, exhibiting a GFP-LC3 puncta in a TNT. **b)** Manual quantification of TNT index, as well as **(c)** GFP-LC3 puncta positive TNTs. Per condition, up to 982 cells were counted in n = 4. Data statistically analyzed with Ordinary One-Way ANOVA with Holm-Sidak's post-hoc test. P-values: <0.05: *; <0.01: **; <0.001: ***. Scale bars: 20µm.

Confocal images with Z-stacks of the U2OS cells stably expressing GFP-LC3 were acquired, allowing once again the generation of a 3D model, where two cells connected by a TNT exchange a GFP-LC3 puncta (Figure 19).

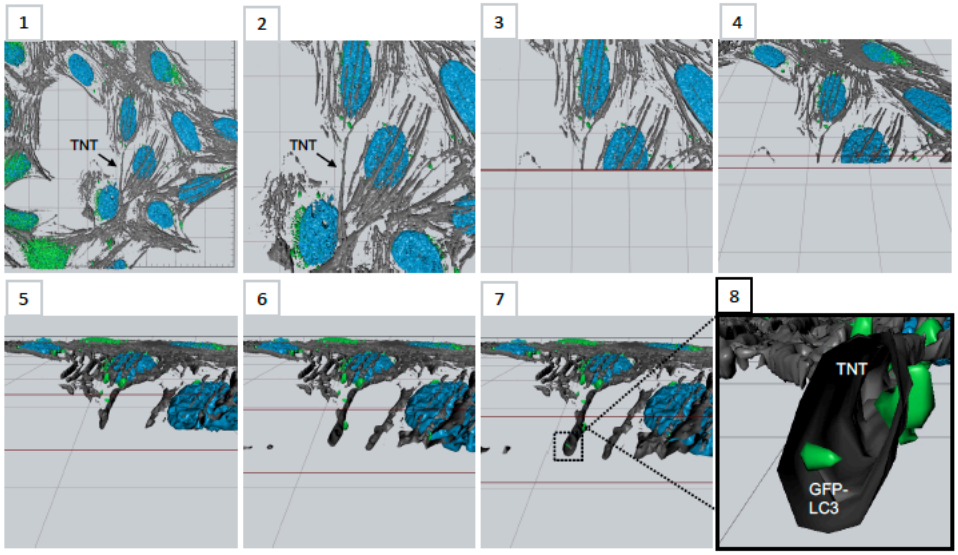

Figure 19. 3D reconstruction of LC3 puncta while in a Tunneling Nanotube connecting two U2OS GFP-LC3 cells. U2OS cells stably expressing GFP-LC3 were starved for 24 hours and stained with Phalloidin in gray and DAPI in light blue. **1)** Top view of the generated 3D model, with a TNT identified. **2)** Zoom in, coming closer to the TNT in question. **3)** Application of a clipping tool allows a sectional cut through the TNT. **4, 5, 6)** Reposition of the frame facilitates visualization of the TNT's interior. **7)** The TNT is reconstructed by adjusting the cut's position along the Y-axis, and a GFP-LC3 puncta is revealed. **8)** Zoom into the TNT, showing a GFP-LC3 puncta from up close.

In (Sporbeck et al., 2023), autophagic membranes were found in TNTs while being intercellularly transferred. Another part of my contribution to the manuscript was demonstrating this by the visualization of LC3 tagged with tandem mRFP-EGFP fluorescence within TNTs. As LC3 decorates autophagic membranes, it is therefore present in both autophagosomes and autolysosomes, once autophagosomes fuse with lysosomal vesicles. The application of LC3 tagged with tandem fluorescent constructs, such as mRFP-EGFP, facilitates the investigation of autophagic flux, since the quenching of EGFP in acidic compartments results in a shift from red-green to red-only fluorescence (Klionsky Abdel-Aziz, et al., 2021). Here, this property was applied to investigate the presence of autophagosomes or autolysosomes in TNTs. The identification of autophagic membranes within TNTs was facilitated by using a U2OS cell line stably expressing mRFP-EGFP-LC3. In basal conditions,

U2OS cells stably expressing mRFP-EGFP-LC3 and stained for F-actin were employed in a qualitative assessment for the presence of red-green (mRFP-EGFP) or red-only (mRFP) fluorescence signal within TNTs. In fact, both red-green and red-only signals were observed inside of TNT structures, indicating that TNTs mediate the intercellular transfer of autophagosomes as well as autolysosomes (Figure 20).

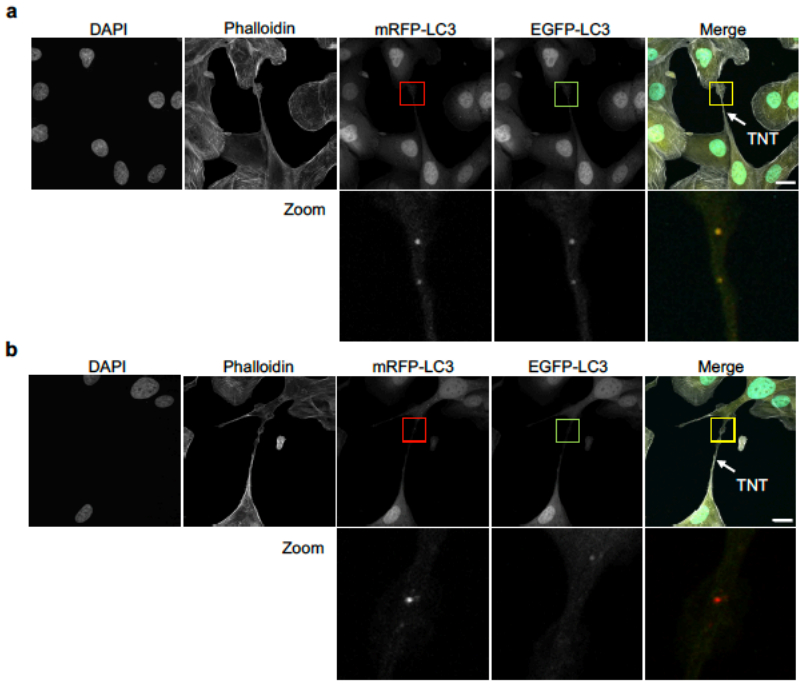

Figure 20. Both autophagosomes and autolysosomes are trafficked via Tunneling Nanotubes. U2OS cells stably expressing mRFP-EGFP-LC3 in basal conditions were stained with Phalloidin and DAPI. **a)** The presence of mRFP-EGFP-LC3 puncta within a TNT indicate the transfer of autophagosomes, whereas **b)** the presence of an mRFP-LC3 puncta inside a TNT represents the intercellular traffic of an autolysosome. Zoom in sections show mRFP, EGFP and mRFP-EGFP merged channels. Scale bars: 20μm.

U2OS stably expressing mRFP-EGFP-LC3 were imaged as previously described, for generation of a 3D model of a TNT connecting two cells. Within this TNT, an mRFP-EGFP-LC3 puncta is seen, as shown in Figure 21, indicating the presence of an autophagosome.

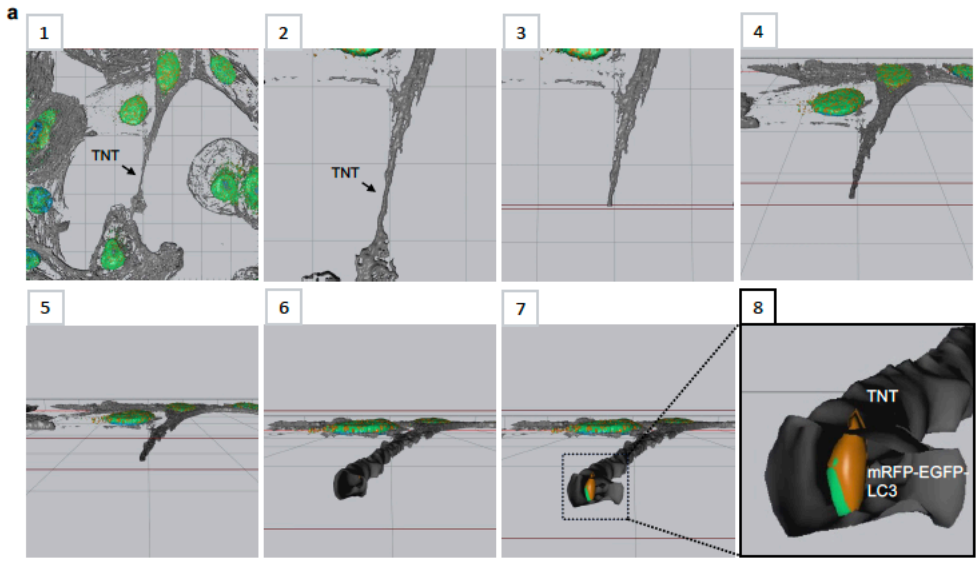

Figure 21. 3D representation of a TNT connecting cells exchanging an mRFP-EGFP-LC3 puncta. U2OS stably expressing mRFP-EGFP-LC3 were stained with Phalloidin in gray and DAPI in light blue. **1)** 3D model is displayed from a top-down perspective. **2)** Close up on the TNT structure in question. **3)** A cut is placed through the Y- and Z-axes and through the TNT. **4, 5, 6)** The frame is gradually adjusted to guide the observer through the interior of the TNT in question. **7)** Repositioning of the sectional cut allows reconstruction of the TNT, exposing a mRFP-EGFP-LC3 puncta. **8)** Further zooming in provides better visualization of a mRFP-EGFP-LC3 puncta within a TNT.

3.2 Conclusion

This chapter showed that autophagic membranes can travel intercellularly via TNTs. Specifically, the autophagy related proteins WIPI1, WIPI2, WIPI4 and LC3 were observed in TNT structures. Moreover, the transfer of WIPI1 and WIPI2 via TNTs was enhanced when cells were subjected to starvation. Furthermore, it was revealed that WIPI4 deficient cells received support from WIPI4 competent cells in co-culture conditions, and that the transfer of WIPI4 towards WIPI4 downregulated cells was significantly enhanced when compared to control cells.

To facilitate visualization, 3D reconstruction of confocal images allowed a more dynamic observation of WIPI proteins, as well as LC3 punctate structures within TNTs. Finally, time lapse videos offered live visualizations of WIPI1 and WIPI4 puncta while being transferred cell-to-cell, which were qualitatively assessed with manual single particle tracking.

3.3 Outlook

The observation of autophagy related proteins within TNTs confirming the transfer of autophagic membranes is an important remark, which paves the way for new research possibilities. TNTs had already been reported as a response to stress and to cellular metabolic alterations, such as extended serum starvation in neurons and astrocytes (Wang et al., 2011). Here it was shown how, not only starvation treatment can induce the formation of TNTs, but that it can also enhance the TNT-mediated transfer of WIPI1 and WIPI2, immediately sparking the question as to where exactly the intersection between the modulation of autophagy and the biogenesis of TNTs lies. Furthermore, the presence of both autophagosomes and autolysosomes in TNTs, observed with GFP-LC3 and mRFP-EGFP-LC3 signals, opens doors to the clarification as to what is the goal of trafficking autophagy related proteins or autophagic membranes. This could either represent the traffic of required cellular material for phagophore formation, the provision of recycled components resulting from mature autolysosomes, or simply a disposal system.

Another point that should be approached in further research concerns potential mechanical players involved in the transfer of autophagosomes and autolysosomes, such as motor proteins. Given WIPI1's and autophagosome's known movement along microtubules (Geeraert et al., 2010; Lorincz & Juhasz, 2020), it is possible that its traffic relies on a tubulin-dependent mechanism. Moreover, neuronal autophagosomal motility is fundamental for autophagosome maturation and is promoted by dynein, a motor protein which interacts with and moves along microtubules (Cason et al., 2021; Sweeney & Holzbaur, 2018). This also raises the question whether the other WIPI proteins and LC3 are transferred due to an indirect interaction while assembled in an autophagosome.

In Sporbeck et al., 2023 (Sporbeck et al., 2023), ATG16L1 deficient cells were supported with WIPI1, WIPI2 and LC3 from competent cells. Here it was shown that WIPI4 deficient cells can, similarly, receive WIPI4 from competent cells. WIPI4 is known to interact with ATG2 and determine autophagosomal size, with the accumulation of enlarged membranes in its absence (Bakula et al., 2017). Future research should address the point of how far WIPI4 deficiency could be restored in such a set-up. For instance, one could question whether WIPI4's activity could be fully reinstated in a rescue experiment. Nevertheless, there are also alternative ways to achieve the transfer of cellular components from cell-to-cell. Another important point which should be investigated is how much of this transfer is exclusively mediated by TNTs.

Finally, future research should apply sophisticated imaging techniques for providing improved visualization of autophagosomes within TNTs, for instance through correlative light

and electron microscopy (CLEM), correlative fluorescence and transmission electron microscopy (CF-TEM) or correlative light, fluorescence and cryo-electron microscopy (cryo-CLEM).

CHAPTER 4. Mitochondria

4.1 Mitochondria in Tunneling Nanotubes

Mitochondria are best known for their role in energy metabolism, through oxidative phosphorylation and the synthesis of ATP. Oxidative phosphorylation produces reactive oxygen species (ROS), generating a membrane potential which is essential for mitochondrial activity. However, over time, mitochondrial proteins themselves are subjected to oxidative damage, which is why mitochondria require constant quality control and maintenance. Importantly, one fundamental mechanism for the maintenance of mitochondrial and cellular homeostasis is mitophagy, the specific degradation of mitochondria by autophagy (Lemasters, 2005), which is the focus of one of the research projects conducted by the Proikas-Cezanne laboratory. Furthermore, excessive intracellular ROS is detrimental for homeostasis and causes damage to several cellular components, such as proteins, lipids and nucleic acids (Nunnari & Suomalainen, 2012). In summary, mitochondria are extremely important organelles for cell survival, which is likely the reason why their abnormal function has been linked to so many health conditions, including cancer and neurodegeneration (Fivenson et al., 2017; Pickrell et al., 2015).

Several studies have reported the cell-to-cell transfer of mitochondria via TNTs in cancer, which has a key participation in promoting cell survival, by restoring ATP production in unhealthy cells and potentially leading to the development of drug resistance, when under chemotherapy (Pasquier et al., 2013; Pinto et al., 2021). In the context of neurodegeneration, the traffic of healthy mitochondria via TNTs is also indicated as critical for survival, besides allowing the sharing of oxidative burden caused by damaged mitochondria (Chastagner et al., 2020; Scheiblich et al., 2021).

As already described in this thesis, varied types of cargoes have been observed to travel intercellularly via TNTs (Zurzolo, 2021). Furthermore, freeze-fracture electron microscopy has shown the transfer of several vesicles through TNTs, including double-membrane enclosed ones (Sartori-Rupp et al., 2019). In addition, the transfer of autophagic membranes has been reported in the previous chapter, specifically with recently published data on the transfer of WIPI1 and the well-known autophagic marker LC3 to neighboring cells (Sporbeck et al., 2023). However, the intercellular traffic of mitochondria as an autophagic cargo in mitophagosomes had not yet been confirmed. Taking that into consideration, it was here questioned whether cells would also export mitophagosomes to neighboring cells through TNTs.

4.1.1 Mitophagosomes are intercellularly trafficked via Tunneling Nanotubes

That TNTs facilitate the transfer of mitochondria has already been published. However, mitochondria while autophagic cargo had not yet been seen within TNTs, which was the aim of this investigation. To identify autophasogomes, the well-established LC3 marker was chosen as a target, as it is known to co-localize with autophagic membranes (Kabeya et al., 2000) and has previously been observed within TNTs (Sporbeck et al., 2023). For this qualitative assessment, U2OS cells stably expressing GFP-LC3 were employed as a model. Cells were stained with DAPI, for nuclei, Phalloidin, for the staining of F-actin, and endogenous TOM20, a known mitochondrial marker located in the mitochondrial outer membrane. Confocal images with Z stacks were acquired and qualitatively analysed by generating intensity profiles with the ZEN software, to assess potential co-localization of TOM20 and LC3 (Figure 22).

LC3, as an autophagic marker, forms punctate structures upon initiation of autophagy. Here, it was questioned whether LC3 puncta could be observed with the mitochondrial marker TOM20, while being intercellularly transferred via TNTs. Interestingly, TOM20 and LC3 were in fact seen together within TNTs. Qualitative analysis of confocal images was performed by generating intensity profiles, which revealed co-localization of pixel intensities for both proteins in three independent events. The obtained images, as well as the intensity profile plots are shown in Figure 22.

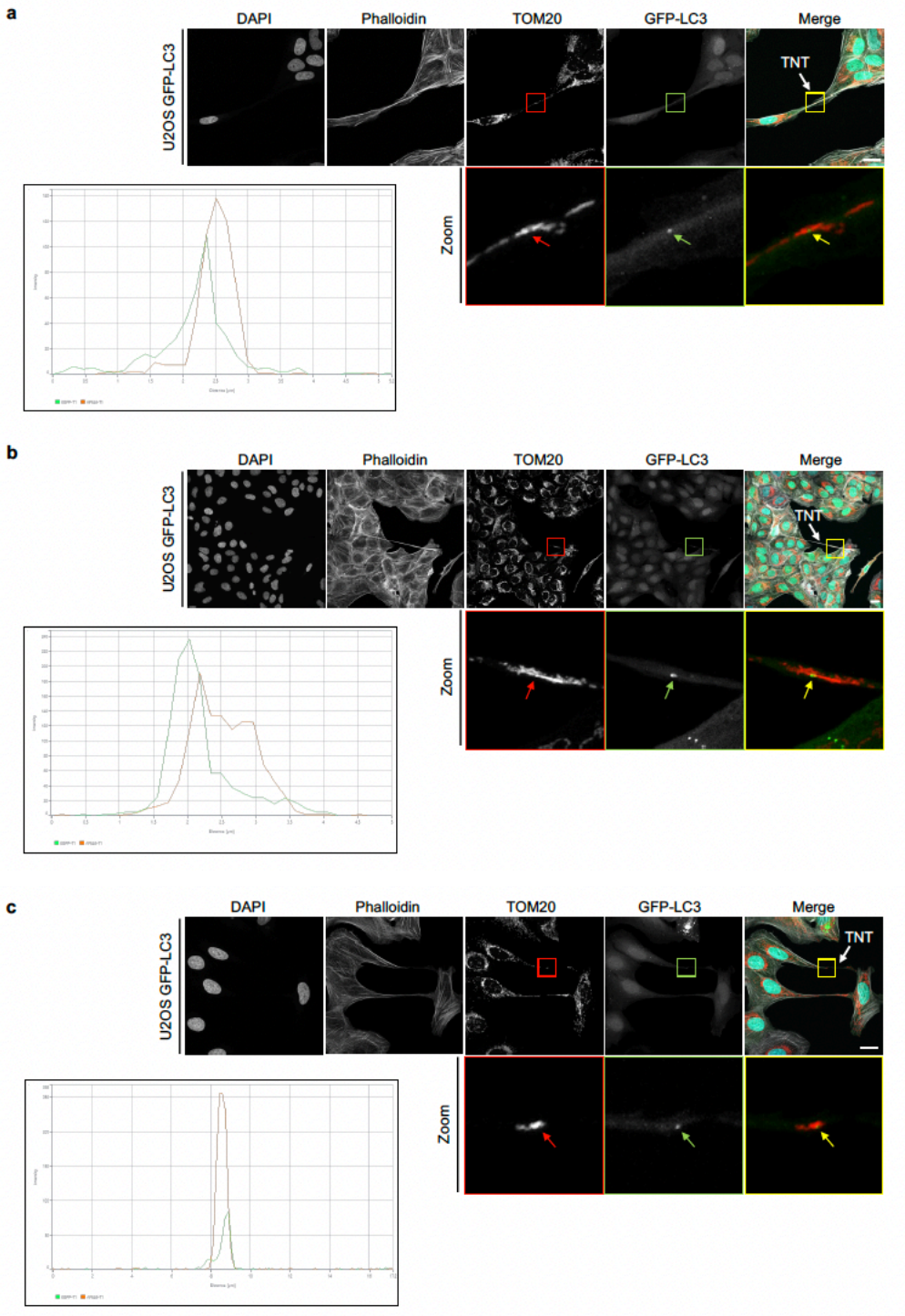

Figure 22. Tunneling Nanotubes mediate the traffic of mitophagosomes. U2OS GFP-LC3 cells stained with DAPI, Phalloidin and endogenous TOM20, with zoom in sections below depicting red and green channels, as well as red-green overlay. Below each set of representative images, intensity profile plot generated with ZEN software confirming co-localization of endogenous TOM20 and GFP-LC3. **a**, **b** and **c)** Depict three independent events where co-localization of TOM20 and LC3 was observed. Scale bars: 20µm.

In a different TNT, where TOM20 and GFP-LC3 are seen together, confocal images acquired in Z-stacks with optimal sectioning (Figure 23a) allowed image reconstruction in 3D, which was then processed into a video with pre-selected positions. A sectional cut through the depicted TNT was included, enabling visualization of the structure's interior containing TOM20 and LC3 structures (Figure 23b).

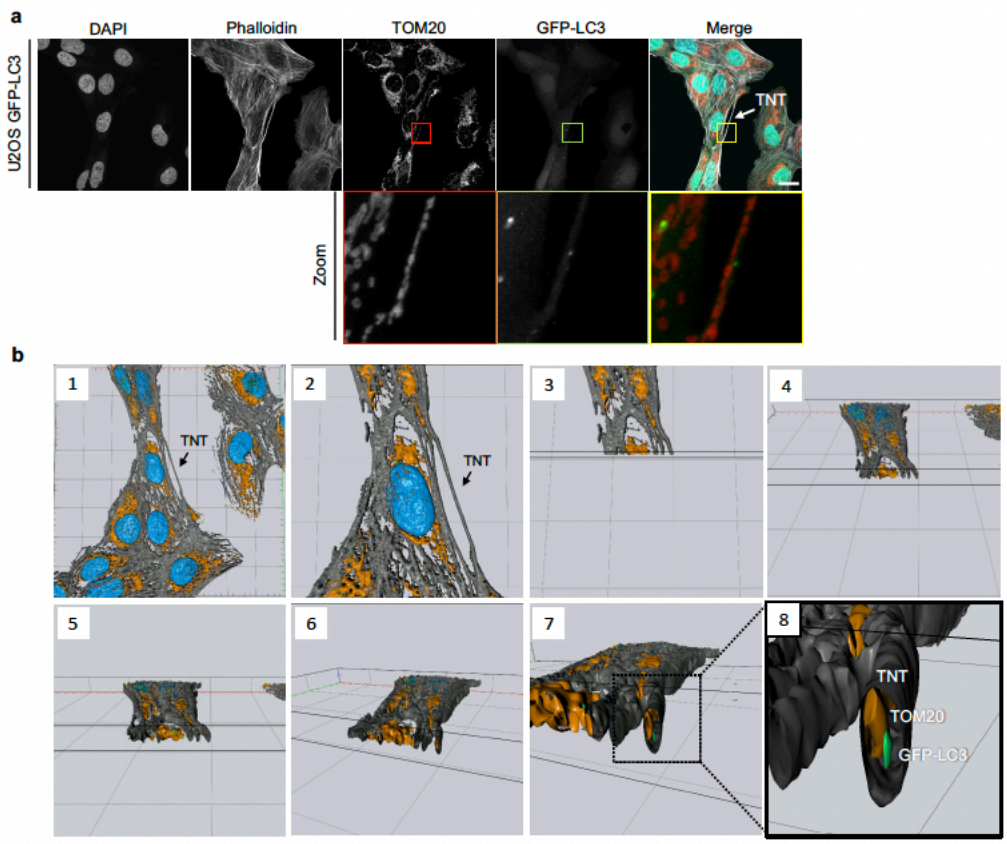

Figure 23. Tunneling Nanotubes mediate the traffic of mitochondria and LC3. U2OS cells stably expressing GFP-LC3 were stained with Phalloidin, DAPI and for endogenous TOM20, and confocal images were acquired with Z-stacks. **a)** Confocal images with zoom in sections of red, green and red-green channels on the bottom row, respectively showing mitochondria and LC3 puncta within a TNT. **b)** Still images of 3D-reconstructed model are shown in **a**. Phalloidin is shown in gray, DAPI in light blue and endogenous TOM20 in orange. **1)** 3D reconstructed model is observed from above, and **2)** zoom into the model shows TNT structure from up close. **3)** A sectional cut is placed in the Z- and Y-axes, cutting through the TNT in observation. **4**, **5** and **6)** The point of view is adjusted to show the interior of the TNT. **7)** As the tube is reconstructed, by shifting the sectional cut along the Y-axis, TOM20 and GFP-LC3 structures are exposed within the TNT. **8)** Further zoom in, showing TOM20 and GFP-LC3 from up close inside of TNT. Scale bar: 20µm.

4.1.2 Tunneling Nanotubes mediate the traffic of mitochondria under Sorafenib treatment

Several stress factors can induce TNT biogenesis, including drugs commonly used in cancer chemotherapy (Kretschmer et al., 2019). In light of this, Sorafenib, a multikinase inhibitor commonly used in liver cancer therapy (Gauthier & Ho, 2013), was chosen as an in vitro treatment to alter TNT formation while qualitatively assessing the TNT-mediated intercellular traffic of mitochondria. To investigate on this aspect, U2OS cells expressing mitochondrial localization signal (MLS)-EGFP-mCherry and U2OS cells expressing NLS-mScarlet, provided by Prof. Anne Simonsen and Dr. Chara Charsou from the University of Oslo, were utilized. U2OS cells stably expressing MLS-EGFP-mCherry (donor) were co-cultured with U2OS stably expressing NLS-mScarlet (recipient), in a 1 to 1 proportion. After 24 hours of treatment with 5μM Sorafenib, cells were imaged in a combination of Airyscan super resolution images and ESID, employed in live time lapse microscopy. Time lapse images were processed into a video with Fiji and qualitatively analyzed by manual single particle tracking of mitochondria, which was achieved with the open source MTrackJ plug-in.

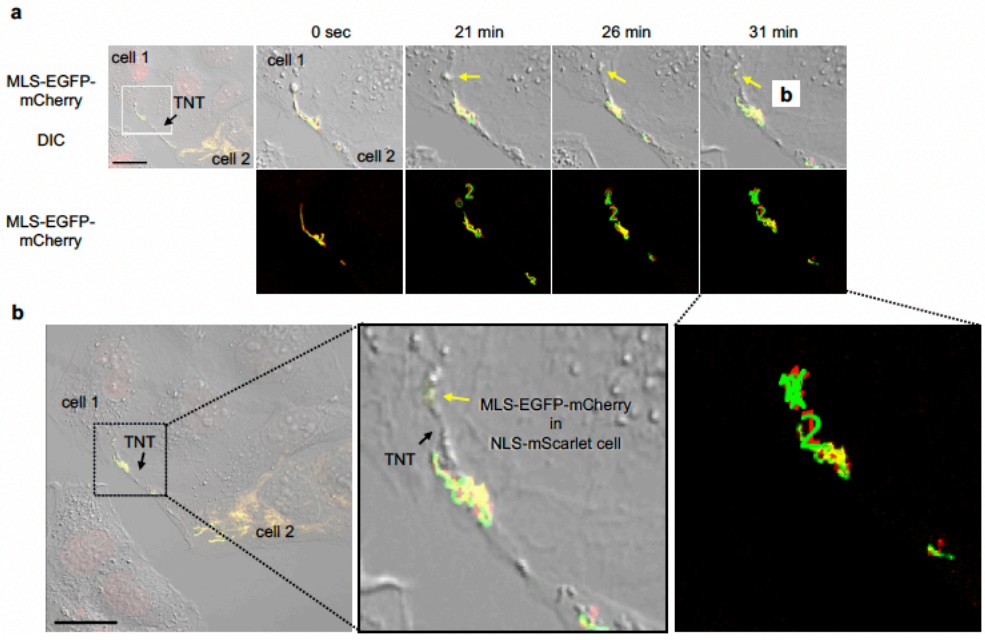

Figure 24. Mitochondrial intercellular traffic is observed live following Sorafenib treatment. Live time lapse imaging of U2OS NLS-mScarlet (cell 1) co-cultured with U2OS expressing MLS-EGFP-mCherry (cell 2). After 24 hours of Sorafenib treatment, cell 1 received labeled mitochondria from cell 2 via a TNT. **a)** Upper images show overlay red-green-DIC channels, whereas red-green overlay with manual tracking of mitochondria can be seen in the lower part. Track 1 in red corresponds to mCherry channel, while Track 2 in green corresponds to EGFP channel. **b)** Magnified version of the last frame showed in **a**, with further zoom in to show MLS-EGFP-

mCherry mitochondria from cell 2 in cell 1. On the far right, a magnified image of the last frame with tracks is shown. Scale bars: 20μm.

Following Sorafenib treatment, donor cells indeed transferred mitochondria into recipient cells via TNTs. Single particle tracking with MTrackJ allowed monitoring of the fluorescently marked mitochondria originated from the donor U2OS MLS-EGFP-mCherry cell inside of a recipient U2OS NLS-mScarlet cell. Frames of time lapse over the course of approximately 30 minutes are depicted in Figure 24.

4.2 Conclusion

Overall, this chapter shows that mitochondria are transferred to neighboring cells as autophagic cargo, which was confirmed by the co-localization of the mitochondrial marker TOM20 with the autophagic marker LC3 within TNT structures. Furthermore, the live intercellular transfer of mitochondria via a TNT was observed following treatment with Sorafenib, a chemotherapeutic drug commonly used in the treatment of liver cancer, here employed as a factor to potentially alter TNT formation.

4.3 Outlook

TNTs are indicated as an important stress coping mechanism, however the details concerning their functionality and how exactly they contribute to homeostasis and cell survival remain open questions. Mitochondrial transfer via TNTs is a highly important research topic, especially in the fields of cancer and neurodegeneration, due to their relevance in maintaining cellular homeostasis. In addition, mitophagy is deeply connected with the maintenance of a functional mitochondrial network itself.

In cancer, research has already shown that the TNT-mediated traffic of mitochondria can contribute to cell survival and the development of chemoresistance (Pasquier et al., 2013; Pinto et al., 2021). However, most studies so far consist of in vitro assays. Although TNTs have been shown in cancer in vivo, the potential of such cellular structures in promoting drug resistance in this context must still be assessed. Furthermore, TNTs mediate a two-way path, and it remains to be clarified whether the mechanism supporting cell survival consists of the supply of functional mitochondria or mitochondrial material, on the distribution of non-functional mitochondria as well as mitophagosomes, or on both. Specifically in the case of Sorafenib, a drug which commonly loses effect due to chemoresistance, future research should

evaluate to which extent it may alter the formation of TNTs and mitochondrial or mitophagosomes sharing. Furthermore, a deeper understanding of the molecular players involved in TNT biogenesis is of fundamental importance for its modulation. Understanding the biogenesis of TNTs in this context would provide further evidence concerning TNT's suitability as a potential therapeutic target, possibly leading to more effective treatment outcomes.

CHAPTER 5. Ferritin

5.1 Ferritinophagy related proteins in Tunneling Nanotubes

Iron is an essential element of most organisms' metabolism. In the human brain, iron is necessary for oxidative metabolism, neurotransmitter biosynthesis and energy production by mitochondria. However, intracellularly elevated concentrations of iron are detrimental due to oxidative stress and damage to cellular components, resulting in disease (Salvador, 2010; Uttara et al., 2009).

Interestingly, oxidative stress is one of many stress factors capable of triggering the formation of TNTs, along with serum deprivation and hypoxia (Desir et al., 2016; Wang et al., 2011; Zhu et al., 2005). As previously introduced in this thesis, TNTs are structures which allow the traffic of several cellular components between neighboring cells, among which are small ions, nucleic acids, proteins, vesicles and even whole organelles as lysosomes and mitochondria. TNTs have been shown to play a key role in human health and disease, and substantial research is currently being done to decipher their contribution in neurodegeneration (Zurzolo, 2021).

Recent research indicated a link between the WDR45 gene, which codes for WIPI4, and ferritinophagy. In addition, mutations in WDR45 have been shown to be causative of Beta-Propeller Associated-Protein Neurodegeneration (BPAN) (Aring et al., 2022; Haack et al., 2012). As the Proikas-Cezanne laboratory initiated to also evaluate the role of WIPI4 in ferritinophagy in the context of BPAN, it was next decided to investigate on the potential TNT-mediated transfer of ferritinophagy related proteins, namely ferritin and NCOA4, as autophagic cargoes. To our knowledge, no study has made a connection between TNTs and ferritinophagy so far.

5.1.1 Ferritin and its cargo receptor, NCOA4, travel through Tunneling Nanotubes

Initially, it was questioned whether the iron storage protein ferritin could be trafficked via TNTs. In the field of ferritinophagy, iron overload is commonly mediated with ammonium iron (III) citrate (FAC), whereas iron chelators promote, such as Deferasirox (DFX), are employed to counterbalance it (Mancias et al., 2014). To assess the presence of ferritin puncta within TNTs, U2OS cells were treated for 24 hours in fed, iron overload, iron chelation or starved conditions. Subsequently, cells were stained for endogenous ferritin, tubulin and with Phalloidin, for the staining of F-actin. The TNT index was quantified manually, as previously

described, as well as the percentage of TNTs containing ferritin puncta. In addition, representative confocal images were acquired, and Z-stacks processing allowed rendering of a 3D video of ferritin puncta within a TNT upon FAC treatment.

Representative images of all treatments are shown in Figure 25a, with zoom in sections of TNTs containing ferritin. Upon treatment with FAC, a small decrease in TNT index was observed, whereas DFX mildly increased it, in comparison to control treatment. In contrast to this, starvation treatment resulted in an increased in TNT index, as expected and previously demonstrated in this study (Figure 25b). Quantification of ferritin puncta positive TNTs revealed that some ferritin transfer already happens even in fed conditions. Increased ferritin transfer via TNTs upon FAC and starved treatments are observed, although only statistically significant in starved cells. DFX, on its turn, did not seem to influence the transfer of ferritin through TNTs (Figure 25c).

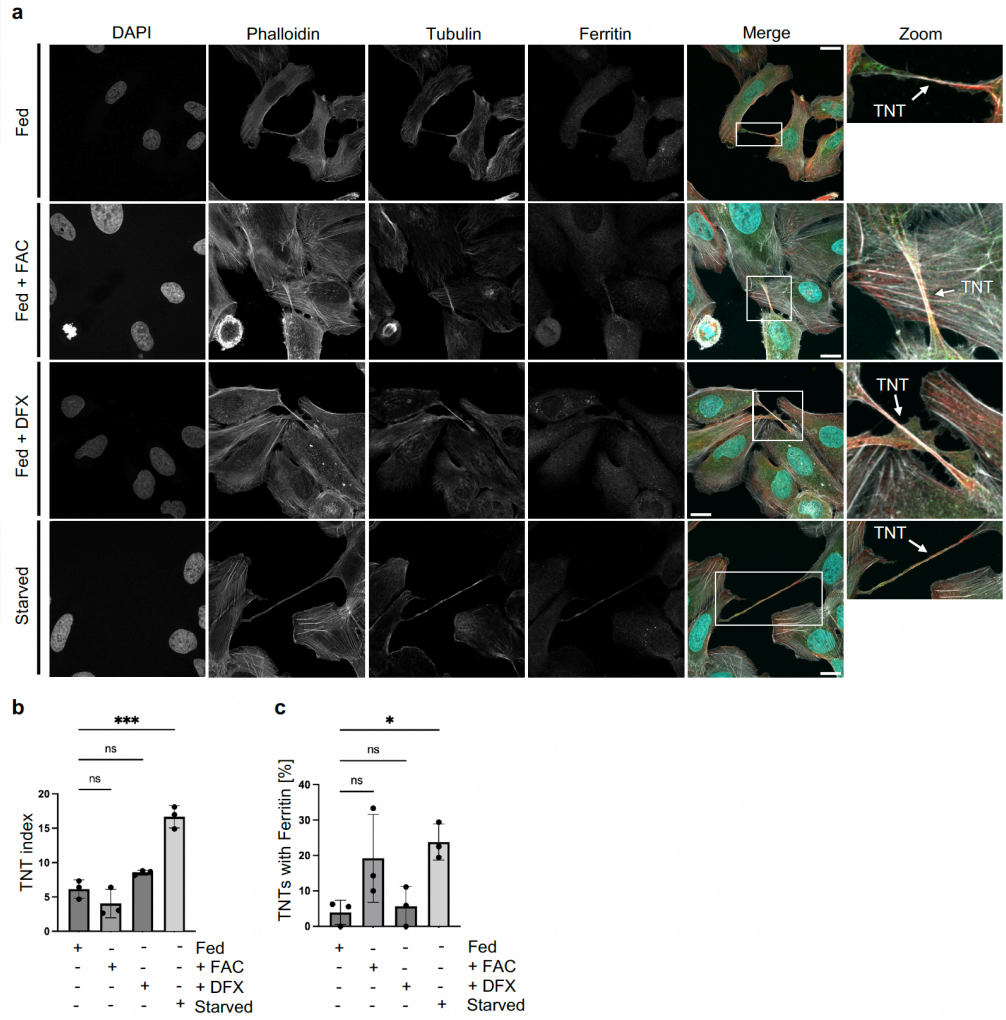

Figure 25. Tunneling Nanotubes mediate the intercellular traffic of ferritin. a) Representative images of ferritin within TNTs, with zoom in sections of TNTs containing ferritin. **b)** U2OS cells cultured in fed, fed + FAC,

fed + DFX or starved conditions were manually quantified with regards to TNT index. **c)** Upon the same treatments as in a, the percentage of TNTs containing ferritin puncta was quantified. Both quantifications were analyzed with Ordinary One-Way ANOVA, Holm-Sidak's multiple comparison test. Up to 759 cells were counted per condition, in n=3. P-values: <0.05: *; <0.01: **; <0.001: ***. Scale bars: 20µm.

Confocal images were acquired with Z-stacks set with optimal sectioning, which allowed 3D reconstruction and generation of a video, showing a TNT containing ferritin puncta. Still images of the video guide the observation of the TNT in question from the top, towards a sectional cut through the TNT, allowing visualization of its interior (Figure 26).

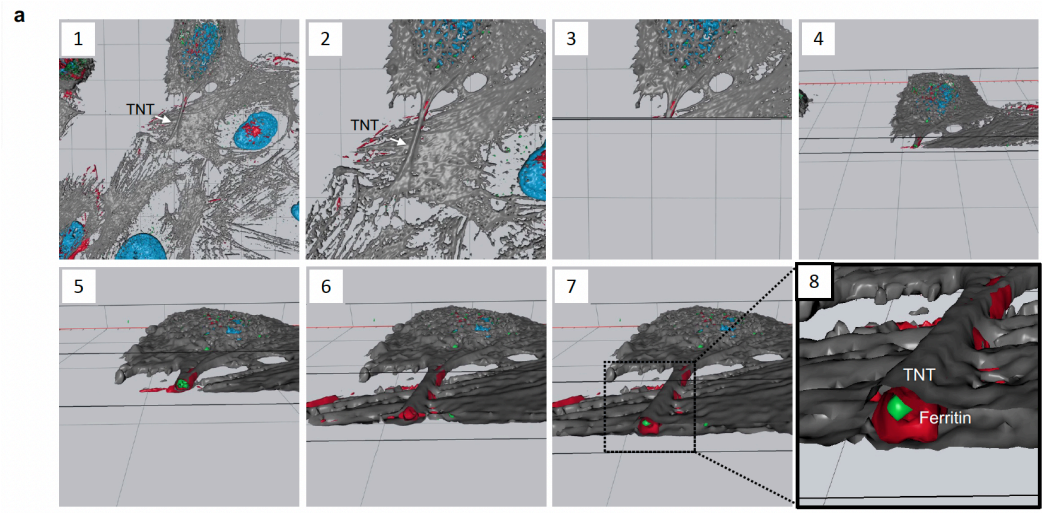

Figure 26. 3D model of a Tunneling Nanotube containing ferritin puncta. U2OS cells treated with FAC for 24 hours and stained with DAPI in light blue and Phalloidin in gray. **1)** 3D model visualized from the top, with TNT identified by a white arrow. **2)** Zoom into TNT in question. **3)** The clipping tool places a sectional cut across the Z- and Y-axes, cutting through the TNT. **4, 5, 6)** The frame position is adjusted, showing the content of the TNT in question. **7)** As the position of the clipping tool is shifted along the Y-axis, the TNT is visually reconstructed, exhibiting a ferritin puncta structure. **8)** Close up on the interior of the TNT containing ferritin puncta.

NCOA4 was identified in 2014 as a cargo receptor responsible for mediating the delivery of ferritin for autophagic degradation, therefore playing a crucial role in ferritinophagy (Mancias et al., 2014). Next, it was asked whether NCOA4 could also travel intercellularly via TNTs. For such, U2OS cells went through transient transfection with c-Myc tagged NCOA4 variants (isoforms 1, 2 or 4) for 48 hours, after which cells were trypsinized and re-seeded to ensure optimal cell density for the study of TNTs. Subsequently, cells were treated for 24 hours under iron chelation mediated by DFX. Finally, anti-c-Myc, DAPI and Phalloidin (for F-actin)

stainings took place, followed by confocal imaging. Indeed, all transfected variants of c-Myc-NCOA4 were visualized as punctate structures within TNTs (Figure 27a). Confocal images acquired with Z-stacks in optimal spacing setting allowed once more for the 3D reconstruction of a TNT, now containing a c-Myc-NCOA4 Variant 1 puncta (Figure 27b).

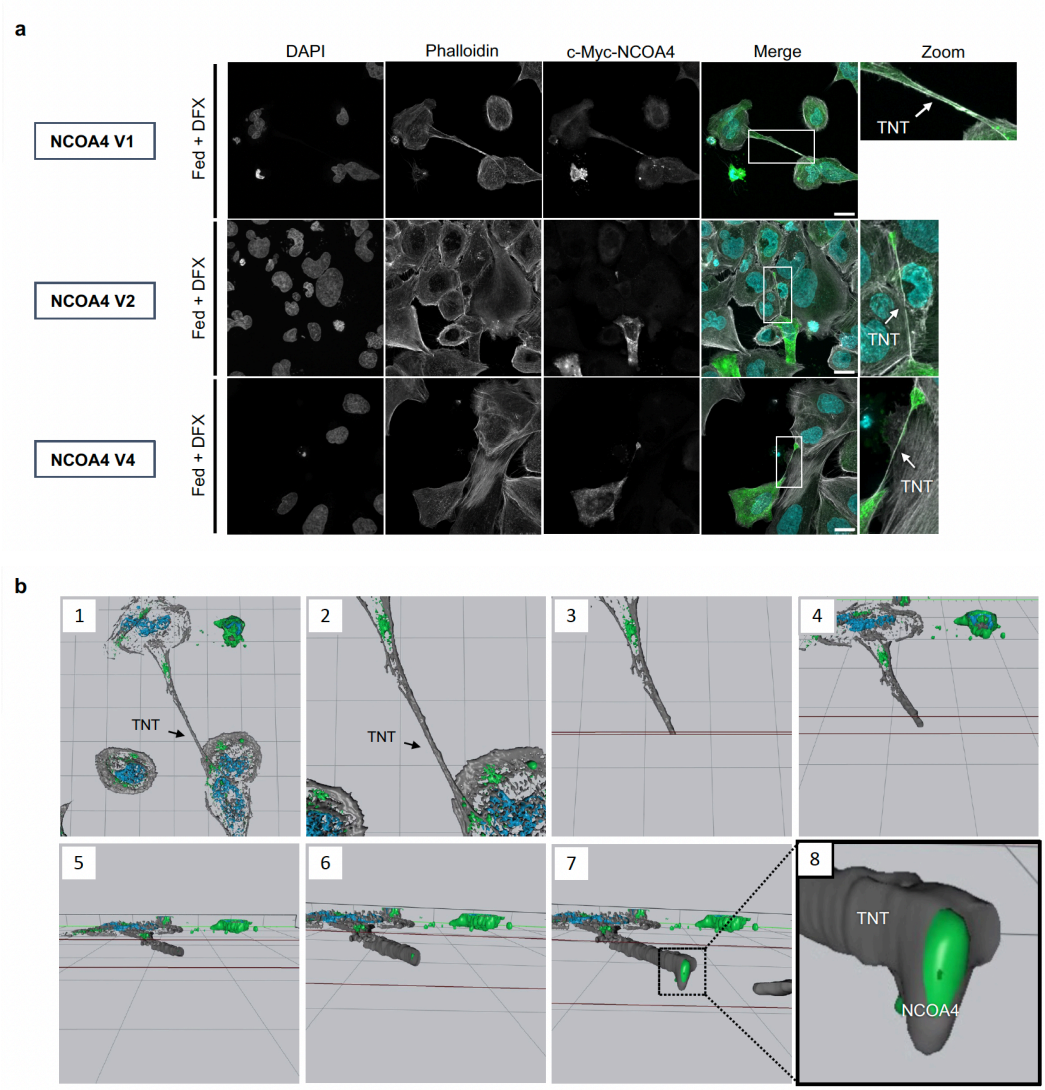

Figure 27. The ferritin cargo receptor NCOA4 travels from cell to cell through Tunneling Nanotubes. U2OS cells transfected with c-Myc-NCOA4 variants 1, 2 or 4, were subsequently treated with DFX iron chelation and stained for endogenous c-Myc, DAPI and Phalloidin. **a)** Representative images with zoom in sections of TNTs containing c-Myc-NCOA4 puncta. **b)** Still images of a 3D video obtained from confocal images, depicting c-Myc-NCOA4 Variant 1 within a TNT. **1)** 3D reconstructed cells are seen from above, with a TNT identified in the middle. **2)** Zoom into the 3D model, showing the TNT in question. **3)** Through the clipping tool, a sectional cut is placed through the TNT. **4, 5, 6)** The point of view is angled and adjusted to allow visualization of the TNT's interior. **7)** As the clipping tool's position is adjusted to move along the TNT, the tube is reconstructed and

eventually exposed an NCOA4 Variant 1 puncta. **8)** Further zoom in shows NCOA4 Variant 1 puncta from up close, while within a TNT. Scale bars: 20μm.

5.1.2 WIPI4 deficient cells redistribute GFP-FTH1 to neighboring cells

In Sporbeck et al., 2023 (Sporbeck et al., 2023), cells lacking ATG16L1 received increased WIPI1, WIPI2 and LC3 when compared to ATG16L1 competent cells. Similarly, previous results in this thesis showed the transfer of WIPI4 from competent to WIPI4 deficient cells. Having this in mind, the next step was to challenge WIPI4 deficient cells with regards to ferritinophagy, while questioning whether they would redistribute excess FTH1, a component of the ferritin cage. For this, a GFP tagged FTH1 construct was used, as a component of the ferritin cage for cellular iron storage. To achieve this, U2OS cells (donor) went through downregulation with esiWDR45 for 8 hours, followed by co-transfection with GFP-FTH1 for the following 40 hours. After this, donor cells were resuspended and combined with U2OS NLS-mScarlet cells (recipient) in equal proportions and re-seeded. Finally, cells were treated with fed, +FAC, +DFX or starvation conditions for 24 hours. Representative images of esiWDR45 cells are shown in Figure 28a (image panel with downregulation control transfected cells in Supplementary Figure 3). GFP-FTH1 puncta positive recipient cells were manually counted over the total amount of recipient cells (Figure 28b).

In fed condition, the transfer of GFP-FTH1 from WIPI4 deficient donor to recipient cells is mildly elevated, in comparison to WIPI4 competent cells. No considerable difference is observed upon iron loading treatment with FAC, when comparing the transfer between WIPI4 competent and incompetent cells. In contrast to that, a striking rise in the percentage of GFP-FTH1 puncta positive recipient cells is seen in cells co-cultured with WIPI4 incompetent cells and treated with DFX iron chelation, in relation to WIPI4 competent. Similarly, starvation treatment also significantly increased the redistribution of GFP-FTH1 from WIPI4 incompetent donor to WIPI4 competent recipient cells, although not as high as in DFX.

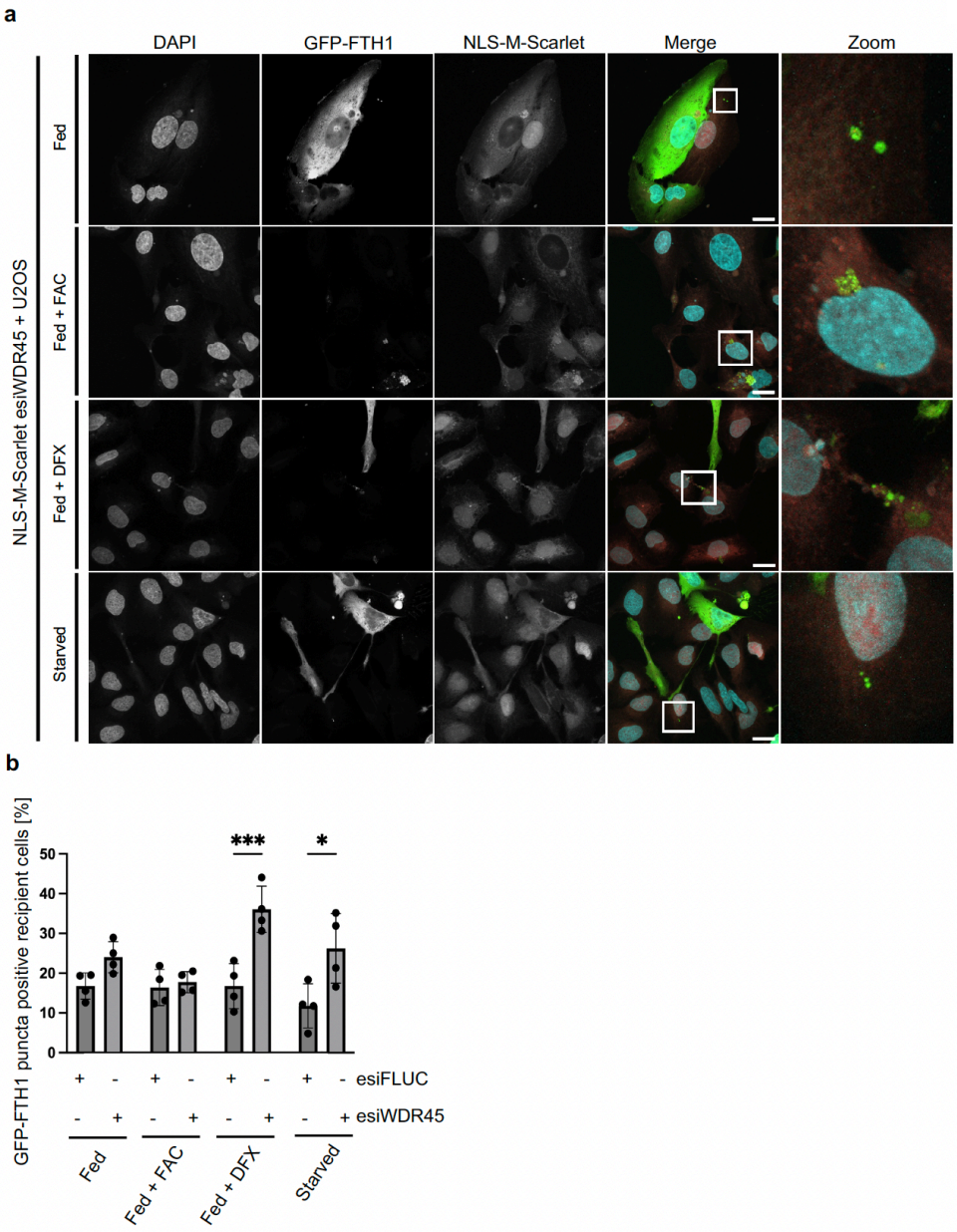

Figure 28. Cells lacking WIPI4 redistribute GFP-FTH1 to WIPI4 competent cells in co-culture. U2OS NLS-mScarlet (recipient) cells are co-cultured with U2OS (donor) cells, previously co-transfected with esiFLUC or esiWDR45 and GFP-FTH1, and cultured in fed, fed+FAC, fed+DFX or starved conditions for 24 hours. **a)** Representative images of GFP-FTH1 puncta in recipient U2OS NLS-mScarlet cells, with zoom in sections of red-green overlay. **b)** Manual quantification of U2OS NLS-mScarlet recipient cells containing GFP-FTH1. Results statistically analyzed with Ordinary Two-Way ANOVA, Tukey's multiple comparison test, with up to 860 cells counted in n = 4. P-values: <0.05: *; <0.01: **; <0.001: ***. Scale bars: 20µm.

5.2 Conclusion

In this chapter, the presence of the ferritinophagy players ferritin and NCOA4 within TNTs was investigated through qualitative and quantitative assays. While applying common modulators of ferritinophagy, it was observed that iron overload may induce the intercellular transfer of ferritin puncta via TNTs, whereas iron chelation did not seem to alter it. The presence of both players, ferritin and NCOA4, was demonstrated with 3D reconstruction of confocal images, where punctate structures of both proteins could be visualized within a TNT structure.

Finally, when challenged with iron chelation, WIPI4 deficient cells showed enhanced intercellular redistribution of FTH1, a component of the ferritin cage. This observation is in line with the result showed in Chapter 3, where WIPI4 deficient cells received more WIPI4 from competent cells when in co-culture.

5.3 Outlook

In this chapter, iron overload and iron chelation treatments were applied to modulate ferritinophagy, based on the literature (Mancias et al., 2014) and on previous studies performed in the Proikas-Cezanne group in the BPAN project. For a broader understanding of how this metabolic modulation can relate with TNT biogenesis and consequent TNT transfer of ferritinophagy players, these data should be integrated with TNT data in the near future.

Concerning the results here acquired, iron loading and starvation-promoted increases in ferritin transfer via TNTs indicate that ferritin might be involved in a bi-directional movement from cell-to-cell. Whereas iron overload apparently results in an export of excess ferritin, starvation seems to require a replenishment by importing ferritin from nearby cells. On the other hand, it remains an open question whether something similar would apply to NCOA4. Future experiments should quantitatively assess the TNT-mediated traffic of NCOA4 upon the modulation of ferritinophagy. Furthermore, another important point to be addressed is to confirm the presence of ferritin or NCOA4 within TNTs while as autophagic cargoes, by questioning whether they co-localize with each other or with autophagy markers, such as LC3.

Whereas free iron can be found in its ferrous form (Fe^{2+}), it has to be oxidized into ferric iron (Fe^{3+}) for ferritin storage (Rohrer et al., 1987). Excess free iron is detrimental for homeostasis, which is why iron is stored in ferritin. Here, only the transfer of ferritin, therefore containing ferric iron, through TNTs was observed. However, an important question would be whether TNTs could also mediate the traffic of ferrous iron.

Nevertheless, the results here obtained pave the way for future research on the intersection between ferritinophagy and TNTs. This link is particularly interesting, given the connection between ferritinophagy and the neurodegenerative disease BPAN, as will be further discussed in Chapter 7.

CHAPTER 6. Tunneling Nanotubes' biogenesis

6.1 The formation of Tunneling Nanotubes

Details concerning the molecular mechanism behind the biogenesis of TNTs remain to be clarified. Although several players have been uncovered, investigating on TNTs is still a challenge due to its high variability in several aspects, from distinct types of TNTs with high structural heterogeneity and varied cargoes, to its differential modulation depending on the cell type (Zurzolo, 2021). Among the so far uncovered players are M-Sec, Cdc42, Eps8, Myo10 and the Wnt pathway (Ljubojevic et al., 2021).

Understanding the formation of TNTs can represent a breakthrough in human health research, due to their important participation in immunity, infection, cancer, and neurodegeneration. The exchange of cellular content through TNTs in cancer has been suggested to assist the maintenance of the tumor microenvironment, supporting tumor cell survival, dissemination and angiogenesis, eventually leading to adaptation and the development of treatment resistance (Roehlecke & Schmidt, 2020). In the field of neurodegeneration, TNTs can act both facilitating the spread of protein aggregates and non-functional mitochondria, with consequent disease proliferation, and as a stress coping mechanism, by allowing the traffic of healthy mitochondria (Scheiblich et al., 2021; Victoria & Zurzolo, 2017).

However, before moving on to the clinical modulation of TNTs, additional basic research is necessary to identify further players and decipher TNT's differential modulation in varied contexts, cell types and tissues. Having this in mind, this chapter's goal was to investigate on TNT biogenesis in the cancer cell lines LX-2, HuH-7, and U2OS, as well as how this may be modulated, resulting in the discovery of two potential novel players.

6.1.1 Liver cell lines form Tunneling Nanotubes

So far TNTs have been observed in several cell lines, including many cancer cells in vitro, resected tumors, live pericytes and immune cells (Dubois et al., 2020; Errede et al., 2018). The formation of TNTs in U2OS cells was published by the Proikas-Cezanne group in 2023 (Sporbeck et al., 2023), and TNTs have also been observed in fibroblasts (Supplementary Figure 4). Still, to the time of this study, TNTs have not been reported in hepatic stellate cells (HSC) nor in hepatocellular carcinoma cells (HCC).

While the Proikas-Cezanne group investigated on mitophagy in the context of liver cancer, hepatic stellate (HSC) and hepatocellular carcinoma (HCC) cell lines were used as in vitro models. Inserting the investigation of TNTs in these cell lines could provide another perspective as to how cells might communicate in the tumor microenvironment and what this could represent in the development of chemoresistance.

To assess the presence of TNTs in human HSC and HCC cells, human hepatic stellate cell line (LX-2) and human liver carcinoma cell line (HuH-7) were employed. For the investigation of TNTs, cells were typically stained with DAPI, Wheat Germ Agglutinin (WGA), Phalloidin and for endogenous tubulin. As previously described, WGA stains the plasma membrane, whereas Phalloidin is employed for the staining of F-actin. Once again, confocal images were acquired for qualitative assessment, followed by the generation of 3D videos of TNTs.

Remarkably, qualitative analysis through fluorescence microscopy confirmed the presence of TNTs in both LX-2 (Figure 29a) and HuH-7 (Figure 29c) cell lines. Once again, the acquired confocal imaged allowed 3D reconstruction of TNT structures in both cell lines, with the generation of videos for a dynamic visualization. Still images of video frames are shown in Figures 29b and 29d, respectively of LX-2 and HuH-7.

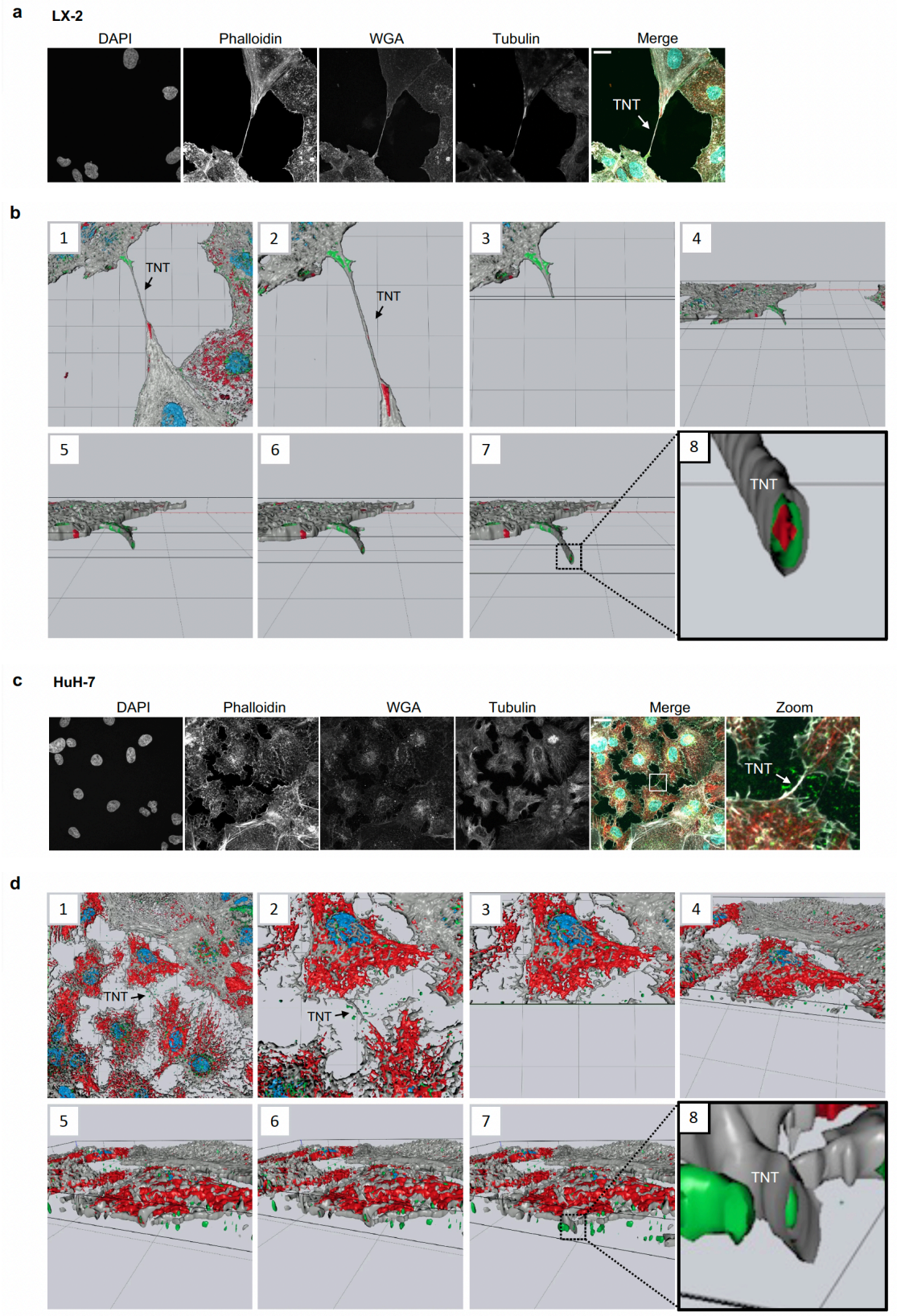

Figure 29. Hepatic stellate and hepatocellular carcinoma cell lines form Tunneling Nanotubes in homotypic cell culture. Representative images showing Hepatic stellate cell line LX-2 **(a)** and hepatocellular carcinoma cell line HuH-7 **(c)** connecting in homotypic cell culture via Tunneling Nanotubes. Zoom in sections show TNTs, which are identified with white arrows. All cells were labeled with DAPI, Phalloidin, WGA and endogenous

tubulin. **b) and d)** Still images of 3D reconstructed model of TNTs of LX-2 and HuH-7: **1)** 3D reconstructed image is observed from above, with a TNT identified by a black arrow. **2)** Zoom in to show TNT structure. **3)** Clipping tool places a sectional cut through the Y- and Z-axes, cutting through the TNT in question. **4, 5 and 6)** The point of view is adjusted, and the observer is guided to visualize TNT's interior. **7)** By moving the clipping tool along the Y-axis, the TNT is gradually reconstructed. **8)** Zoom in to show a close up of TNT's interior. Scale bars: 20μm.

6.1.2 Liver cells connect through Tunneling Nanotubes in heterotypical co-culture

The cellular composition of the liver is quite diverse, consisting of hepatocytes (which account for 60% to 80% of all liver cells), stellate cells and endothelial cells, fibroblasts, and stellate sinusoidal macrophages (Sia et al., 2017). In a healthy liver, stellate cells are normally found in an inactive state, and support the cellular microenvironment, as well as the liver's regeneration and integrity. Stellate cells possess high plasticity and can be activated into a proliferative state in response to a certain injury or stimuli, such as cancer. To meet such high energy demands, these cells can regulate a number of physiologic responses, going through metabolic changes, for instance by enhancing mitochondrial number and activity. In this case, stellate cells can drive hepatic fibrosis through the increased secretion of extracellular matrix, thereby contributing to tumor progression (Trivedi et al., 2021).

The cell-to-cell interaction between distinct cell types, also known as heterotypical interaction, has been shown as critical for cancer progression. In breast cancer, the formation of heterotypical TNTs has been linked to tumor invasion and disease progression (Hanna et al., 2019). Having this in mind, the next point to be addressed was whether the presence of heterotypical TNTs between hepatic stellate and hepatocellular carcinoma cells could be confirmed in an in vitro co-culture set-up.

Indeed, not only did LX-2 and HuH-7 connect to each other through TNTs in a homotypic culture set-up, but also in a heterotypical co-culture. This was observed by differentially labeling the cell lines with the lipophilic dyes DiO or DiI, followed by co-culture in a 1:1 proportion. Finally, once fixed, cells were stained with DAPI and Phalloidin to allow identification of TNTs. Figure 30 shows LX-2 and HuH-7 exchanging DiO while connected through a TNT, with zoom-in sections of DiI and DiO in a HuH-7 cell.

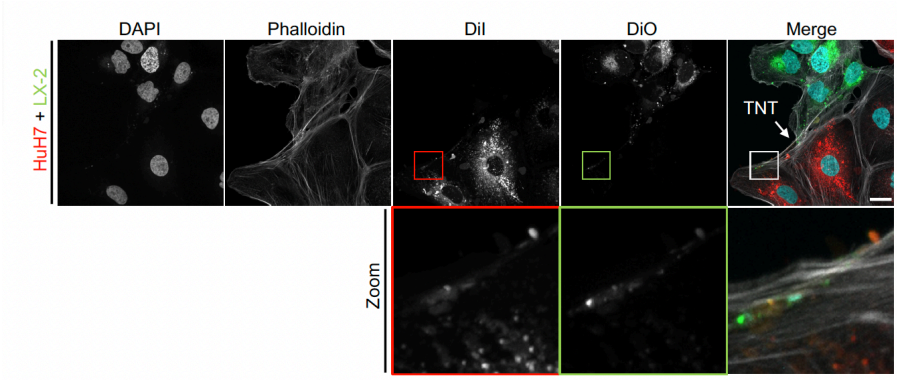

Figure 30. Hepatic stellate and hepatocellular carcinoma cell lines form Tunneling Nanotubes in co-culture. In a heterotypical co-culture set-up, LX-2 and HuH-7 respectively labeled with DiO and DiI, connect via TNTs and exchange the lypophilic dye DiO. Write arrow shows TNT structure. Zoom-in sections of red, green and red-green overlay are observed in the lower part of the image panel. Scale bars: 20μm.

6.2 NUDC and the formation of Tunneling Nanotubes

NUDC regulates actin and dynein dynamics (Zhang et al., 2016) and members of the NUDC family have been associated with cancer proliferation, invasion, and metastasis (Han et al., 2018; Suzuki et al., 2007). Additionally, according to the Human Protein Atlas, higher expression levels of NUDC in liver cancer have been suggested to lead to poor survival rates (Ponten et al., 2008). Taking this into consideration, the next question was whether NUDC could influence the biogenesis of TNTs. To investigate on this aspect, NUDC was downregulated through reverse transfection with siRNA in LX-2, HuH-7 and U2OS cells for 48 hours.

Following reverse transfection with siRNA, cells were treated for 24 hours with or without 5μM Sorafenib. As previously described, Sorafenib was chosen as a drug to alter TNT formation. Once the assay was completed, cells were fixed and stained with DAPI, WGA, Phalloidin and endogenous tubulin, respectively for the identification of nuclei, plasma membrane, F-actin and tubulin. The slides were analyzed for the manual quantification of TNT index.

Results corresponding to the LX-2 cell line are shown in Figure 31. Downregulation efficiency was confirmed with Western Blot, as presented in Figure 31a. In LX-2 cells treated with siCtrl, Sorafenib treatment remarkably increased the formation of TNTs, whereas the same treatment did not seem to have an effect upon NUDC downregulation. Overall, TNT index was reduced in the absence of NUDC, although the difference is only considered statistically significant when comparing downregulated control with NUDC downregulated

cells when treated with Sorafenib (Figure 31b). Representative images are shown in Figure 31c.

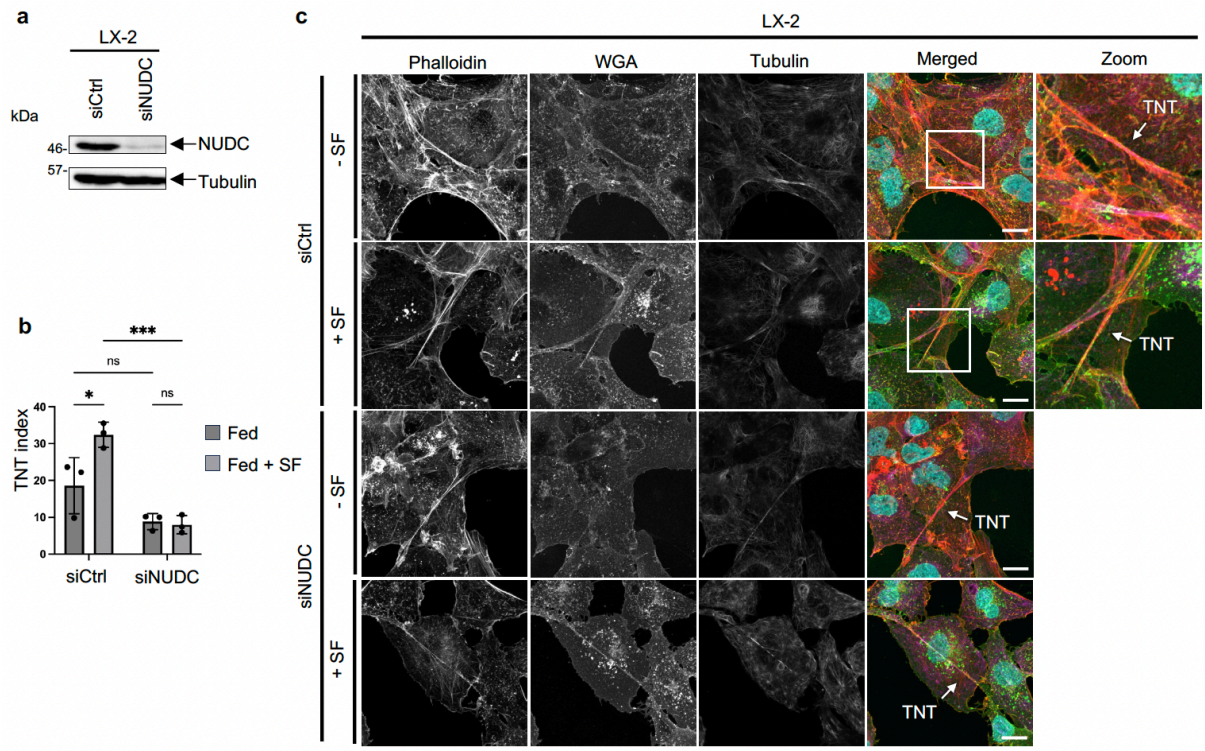

Figure 31. NUDC and the formation of Tunneling Nanotubes in LX-2. LX-2 cells reverse transfected with siCtrl or siNUDC for 48 hours, followed by 24 hours of Sorafenib treatment. Finally, cells stained with DAPI, Phalloidin, WGA and endogenous tubulin. **a)** Western Blot confirmed the efficiency of NUDC siRNA downregulation. **b)** Manual quantification of TNT index. **c)** Representative images are shown, with TNTs identified by white arrows, and zoom in sections when necessary for better visualization. Up to 717 cells were counted per condition, in n=3. Data set statistically analysed with Ordinary Two-Way ANOVA, Tukey's post-hoc test. P-values: <0.05: *; <0.01: **; <0.001: ***. Scale bars: 20µm.

Downregulation of HuH-7 cells was also confirmed with Western Blot, as in Figure 32a. Similarly, in HuH-7 cells transfected with control siRNA, Sorafenib treatment resulted in a significant increase in the TNT index. On the other hand, downregulation of NUDC resulted in a noticeable reduction of TNT index, which could not be induced upon Sorafenib treatment (Figure 32b). An image panel with representative images of HuH-7 cells is shown in Figure 32c.

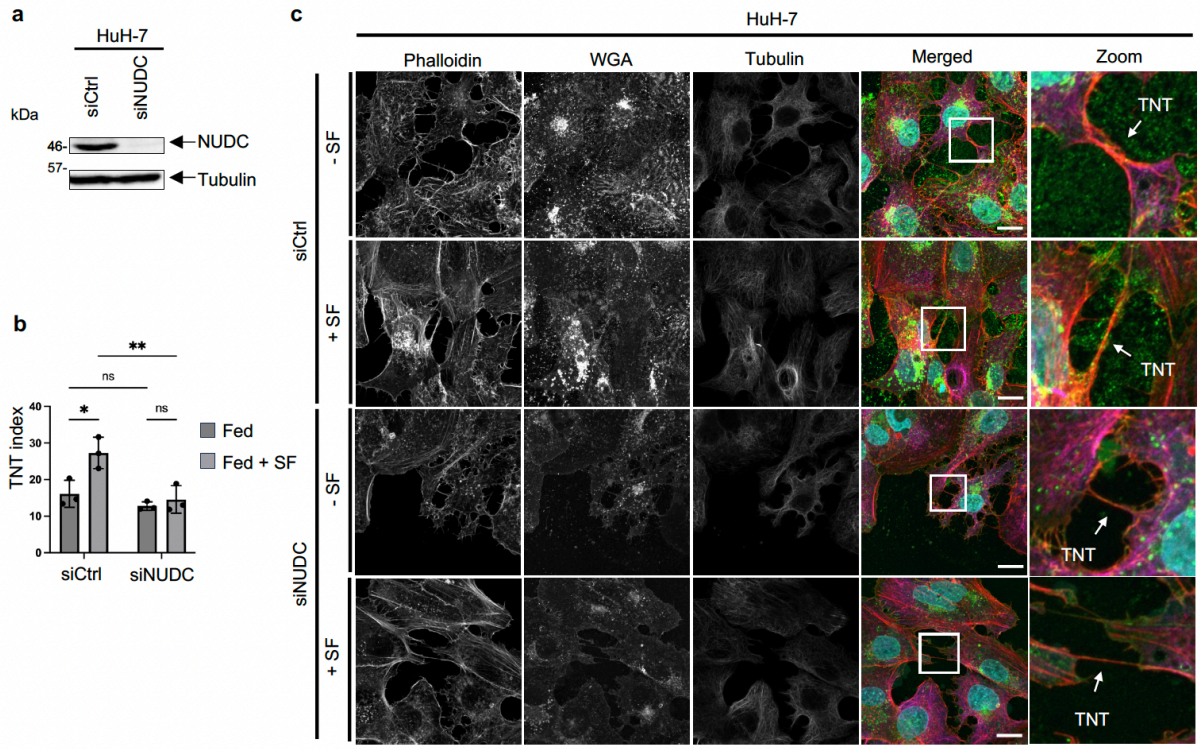

Figure 32. NUDC and the formation of Tunneling Nanotubes in HuH-7. HuH-7 cells went through reverse transfection of siCtrl or siNUDC for 48 hours, followed by 24 hours of Sorafenib treatment. Cells were stained with DAPI, Phalloidin, WGA and endogenous tubulin. **a)** Downregulation efficiency was confirmed through Western Blot. **b)** Results of manual quantification of TNT index. **c)** Image panels showing representative images, with zoom in sections and TNTs identified by white arrows. Up to 673 cells were counted per condition, in n=3. Data set statistically analysed with Ordinary Two-Way ANOVA, Tukey's post-hoc test. P-values: <0.05: *; <0.01: **; <0.001: ***. Scale bars: 20µm.

The downregulation of NUDC in U2OS was similarly confirmed with Western Blot, which is shown in Figure 33a. U2OS cells did not show significant alterations in the TNT index when treated with Sorafenib, independent on whether they had been transfected with downregulation control or with siNUDC. However, a mild increase in TNT index is observed in cells transfected with control downregulation treated with Sorafenib. Interestingly, upon downregulation of NUDC, U2OS actually formed a significantly higher number of TNTs in contrast to the other cell lines, LX-2 and HuH-7 (Figure 33b). Representative images are shown in Figure 33c.

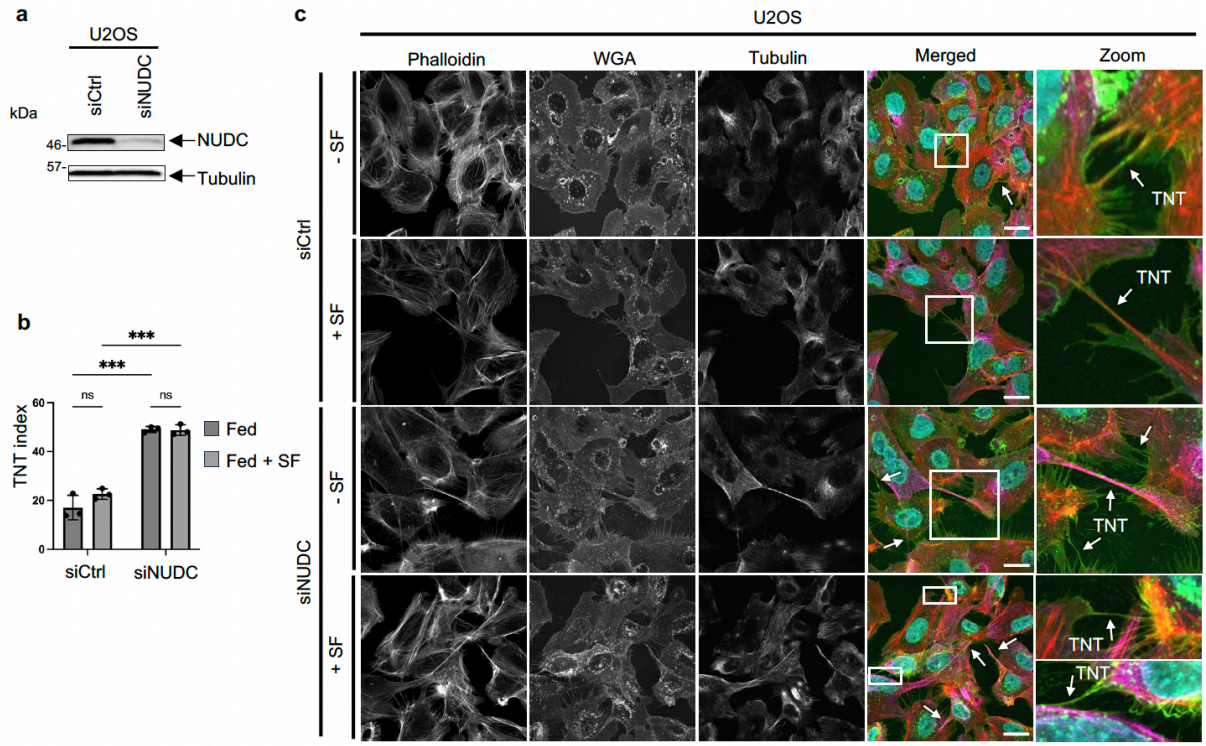

Figure 33. NUDC and the formation of Tunneling Nanotubes in U2OS. U2OS cells were reverse transfected with siCtrl or siNUDC, followed by Sorafenib treatment for 24 hours. Then, cells were stained with DAPI, Phalloidin, WGA and endogenous tubulin. **a)** Western Blot confirming NUDC downregulation efficiency. **b)** Graphs depicting results of TNT index manually quantified. **c)** Representative images are shown, with zoom in sections and white arrows identifying TNTs. Up to 783 cells were counted per condition, in n=3. Data set statistically analysed with Ordinary Two-Way ANOVA, Tukey's post-hoc test. P-values: <0.05: *; <0.01: **; <0.001: ***. Scale bars: 20µm.

6.3 WIPI1 and the formation of Tunneling Nanotubes

In Chapter 3 it was shown that U2OS cells formed more TNTs when in starvation, which mediated an enhanced intercellular transfer of WIPI1 under the same condition. This set of data was recently published in (Sporbeck et al., 2023). Another part of my contribution to this manuscript was investigating on the intersection between the initiation of autophagy and TNT biogenesis, by questioning whether WIPI1 itself could play a role in the formation of TNTs.

First, the effect of WIPI1 overexpression on TNT formation was evaluated. For such, U2OS were transiently transfected with EGFP or EGFP-WIPI1 plasmids in the concentrations of 0.1µg or 0.25µg for 48 hours, after which cells were re-seeded to ensure ideal confluency for the investigation of TNTs, and further cultured for the following 24 hours. After staining with DAPI, Phalloidin (for staining of F-actin), and for endogenous tubulin, the TNT index was manually quantified. Representative images are shown in Figure 34a. Manual

quantification of TNT index revealed that the overexpression of EGFP-WIPI1 enhanced the formation of TNTs, with a statistically significantly higher TNT index upon transfection with 0.25µg EGFP-WIPI1, in comparison to cells transfected with the same concentration of EGFP (Figure 34b).

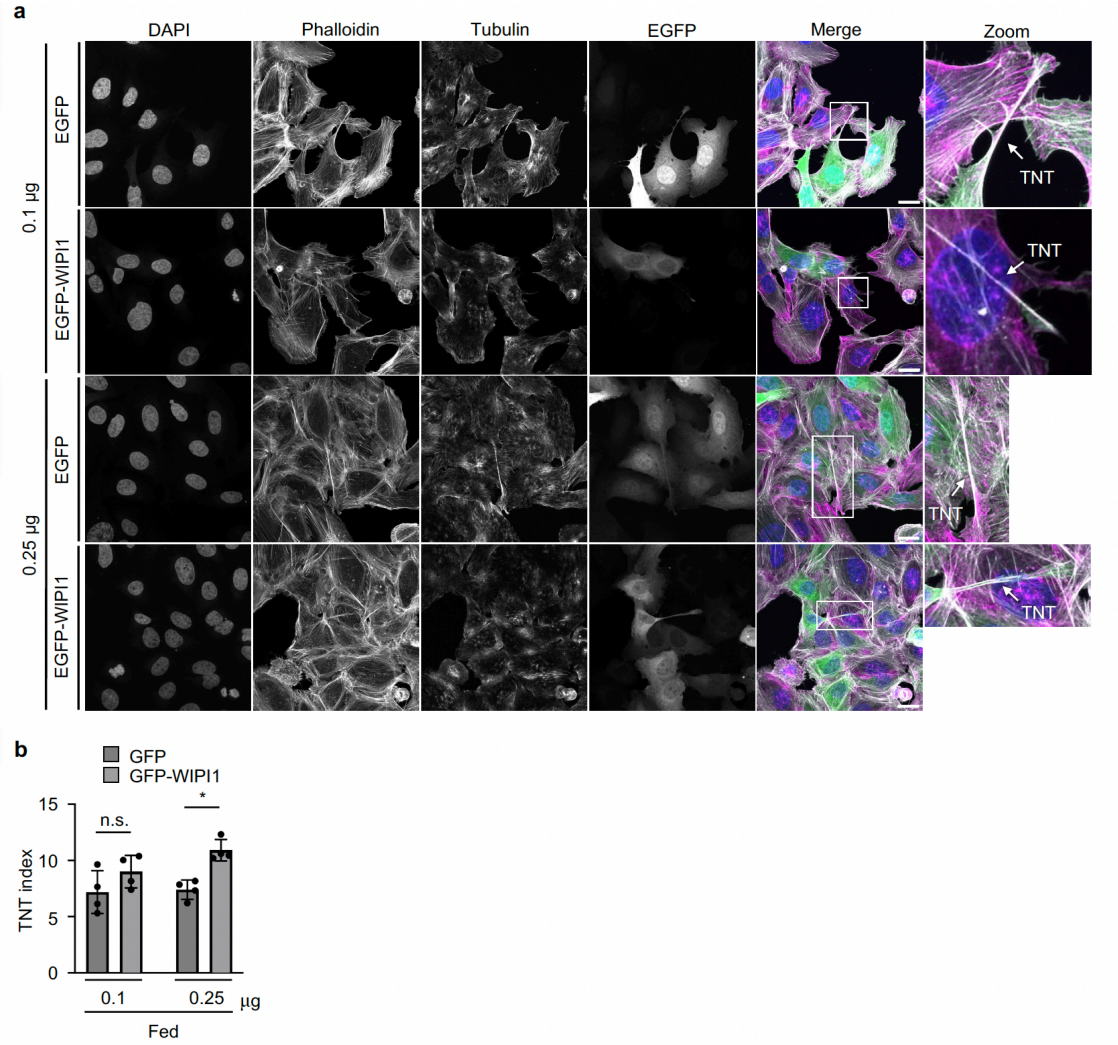

Figure 34. Overexpression of WIPI1 enhances the formation of Tunneling Nanotubes in U2OS cells. U2OS cells transfected with 0.1µg or 0.25µg EGFP or EGFP-WIPI1 for 48 hours and stained with DAPI, Phalloidin and endogenous tubulin. **a)** Image panel showing representative images with zoom in sections for better visualization of TNTs, which are indicated with white arrows. **b)** Manual quantification of TNT index in n = 4, with up to 1057 cells counted for each condition. Statistical analysis by Ordinary Two-Way ANOVA, with Tukey's test. P-values: <0.05: *; <0.01: **; <0.001: ***. Scale bars: 20µm.

Since WIPI1 overexpression enhanced TNT index, the next point to be addressed was whether the absence of WIPI1 could negatively affect TNT formation. For this assessment, U2OS CRISPR/Cas9 WIPI1 wild type and WIPI1 deficient cell lines were employed. The cells,

which were previously cultured by Carmen Julia Pastor Maldonado, were seeded, and on the following day subjected to low serum or starvation conditions for 24 hours. Once again, the TNT index was manually quantified once the cells went through nuclei, F-actin, plasma membrane and tubulin staining, respectively with DAPI, Phalloidin, WGA and endogenous tubulin. Representative images of this experiment are shown in Figure 35a. Here, the quantification revealed that both low serum and starvation treatments notably increased the TNT index in WIPI1 wild type cells. However, WIPI1 deficient cells formed less TNTs in all conditions, significantly in serum starvation and starvation conditions. Strikingly, none of the treatments could induce the formation of TNTs in WIPI1 deficient cells as seen in the wild type (Figure 35b).

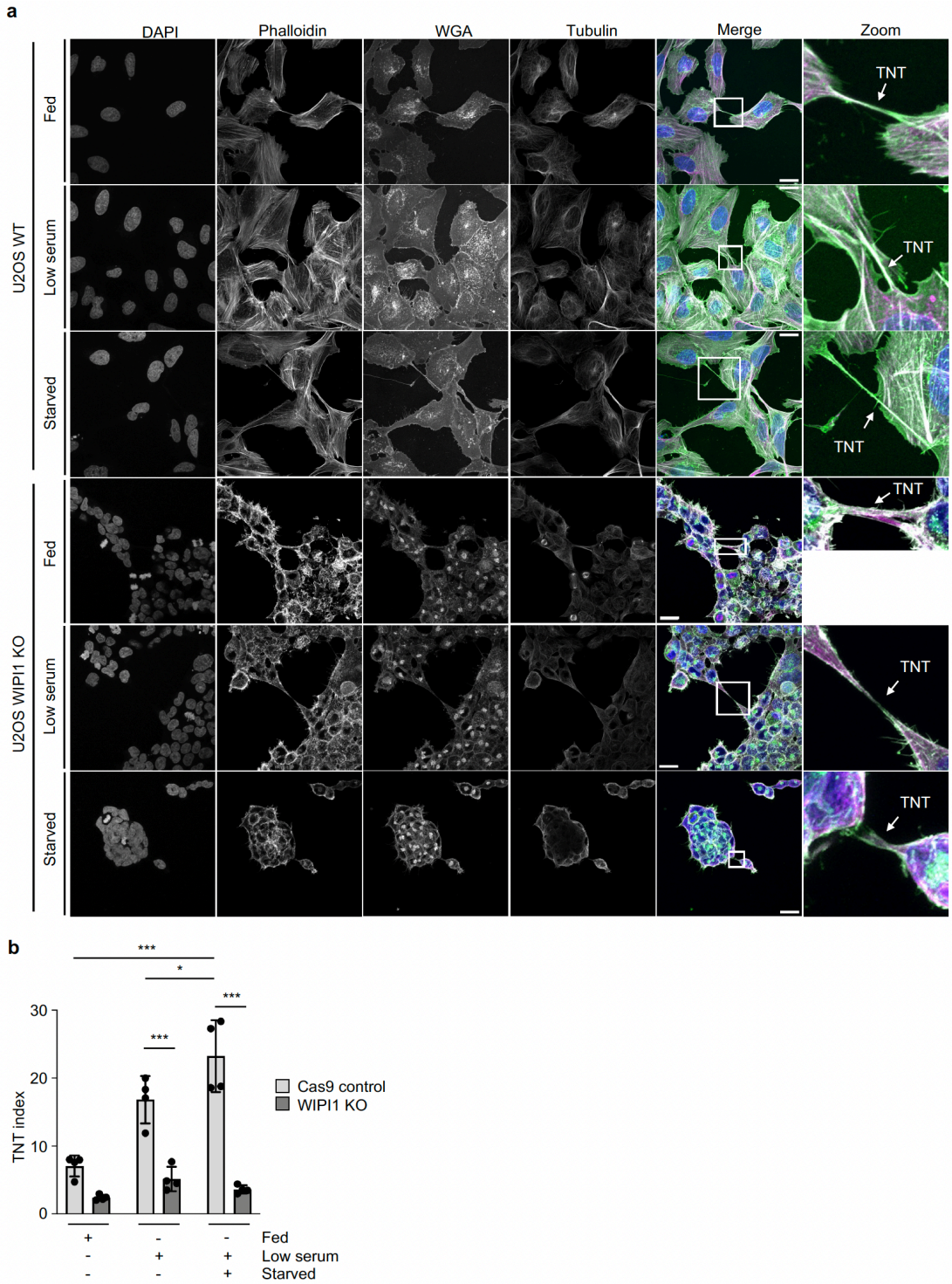

Figure 35. In the absence of WIPI1, U2OS cells form less Tunneling Nanotubes. U2OS CRISPR/Cas9 cells WIPI1 wild type or WIPI1 KO treated in full medium, low serum or starvation medium for 24 hours. Then, cells were stained with DAPI, Phalloidin, WGA and for endogenous tubulin, and the TNT index was manually quantified. **a)** Representative images with zoom in sections of TNTs, which are identified by white arrows. **b)** Graph corresponding to TNT index quantification, where a maximum of 1440 cells were counted per condition in n = 4. Data set was analyzed with Ordinary Two-Way ANOVA, Tukey's post-hoc test. P-values: <0.05: *; <0.01: **; <0.001: ***. Scale bars: 20µm.

6.4 Conclusion

The focus of this chapter was on investigating the biogenesis of TNTs in the liver cancer cell lines LX-2 and HuH-7, as well as on the osteosarcoma cell line U2OS.

Initially, qualitative analysis confirmed that the liver cell lines LX-2 and HuH-7 indeed form TNTs, both in homotypical and in heterotypical cell culture set-ups. Next, an important regulator of actin dynamics, namely NUDC, was identified as a potential player in the modulation of TNT formation. However, although NUDC seemed to positively regulate TNT biogenesis in LX-2 and HuH-7, the opposite effect was observed in U2OS cells. Lastly, WIPI1 was also identified as a potential player in TNT formation, since its overexpression resulted in increased TNT index, whereas its absence decreased it.

6.5 Outlook

The observation of homotypical and heterotypical TNTs in in vitro cell culture between the liver cell lines LX-2 and HuH-7 represent potential key features that should be further addressed in the context of liver cancer research. Future research should approach the point of whether heterotypical TNTs can also form in vivo in liver cancer, potentially supporting the tumor microenvironment.

Furthermore, the next point to be addressed should consider the known poor survival rates upon overexpression of NUDC in liver cancer, as stated in the Human Genome Atlas (Ponten et al., 2008). Knowing that TNTs are positively modulated by NUDC in LX-2 and HuH-7 raises questions as to how exactly this feature could be related to the above-mentioned poor survival rates and if it could contribute to the development of chemoresistance. Thorough investigation should establish, in vivo, how the modulation of NUDC can influence survival rates in liver cancer. This is a relevant point, as the modulation of TNTs via NUDC regulation combined with chemotherapy could potentially result in improved treatment efficiency, revealing NUDC as a novel therapeutic target.

Concerning WIPI1, further investigation is necessary to clarify the connection between autophagy regulation and the biogenesis of TNTs. Perhaps, one initial step would be evaluating whether the TNT index can be restored in an assessment combining downregulation followed by rescue.

CHAPTER 7. Discussion

7.1 Cells support each other by sharing autophagic membranes via Tunneling Nanotubes

TNTs are important intercellular connections which play a fundamental role in the preservation of physiological balance, immunity, inflammation, and diseases such as cancer and neurodegeneration. Although considered a relatively new research topic, TNTs already present great potential for future research in human health. TNTs are currently under intense investigation in several research groups worldwide, and substantial research is still necessary for a broader understanding of their modulation, structure, and function. So far, what is clear is that the mere existence of cellular structures such as TNTs questions the dogmatic concept of what a cell is, initially thought to function as isolated units (Zurzolo, 2021). Coined by Rustom in 2016, the term "supercellularity" now defines a key feature of the cellular microenvironment, which supports homeostasis conservation under constantly fluctuating circumstances (Rustom, 2016). In addition to environmental or external changes, such as nutrition or infection, there are also internal variations that must be overcome, such as differential gene expression (Squair et al., 2021).

One of the ways TNTs act on maintaining homeostasis, which was investigated in this study, might by exchanging autophagic membranes, autophagy related proteins and even autophagic cargo. Autophagy itself has been long known to fundamentally maintain cellular homeostasis, keeping a constant clearance mechanism even under basal conditions (Dikic & Elazar, 2018).

Chapter 3 begins with results from Manuscript 1, where it is shown that autophagic membranes containing GFP-WIPI1 can travel to neighboring cells through TNTs (Figure 9). Further in the chapter, evidence of the presence of GFP-WIPI2B, mRFP-EGFP-WIPI4, GFP-LC3 and mRFP-EGFP-LC3 in TNTs is also provided. As expected, based on what was described by Thost et al. (Thost et al., 2015), starvation enhanced the numbers of GFP-WIPI1 and GFP-WIPI2B puncta positive cells (Figures 9b and 12b). These initial results were considered as positive controls of autophagy induction, relevant for the following steps of this study.

In the stable cell lines U2OS GFP-WIPI1, U2OS GFP-WIPI2B and U2OS GFP-LC3, TNT formation was notably induced by amino acid and serum starvation (Figures 9c, 12c and 18b). This was in line with previous research, as the formation of TNTs is induced in response to numerous stress factors, including starvation (Abounit & Zurzolo, 2012). However, in this study, 24 hours of serum depletion were not sufficient to enhance TNT index in U2OS cells,

in contrast to what was reported by Wang et al., where astrocytes and neurons showed an increase in TNT index when serum starved over the course of 7 days (Wang et al., 2011).

Interestingly, starvation not only simultaneously induced puncta positive cells and the formation of TNTs, but also led to more intercellular transfer of GFP-WIPI1 and GFP-WIPI2B via TNTs (Figures 9d and 12d). In U2OS GFP-WIPI1 cells, a mild increase in GFP-WIPI1 transfer is already observed in low serum, although not significantly altered in comparison to fed condition. One may raise the question about the necessity for similar cells placed in the same conditions to engage in material exchange. This phenomenon could be attributed to differential gene expression, as well as metabolic variations, and the requirement to maintain homeostasis in an unbalanced microenvironment. Starvation imposes a challenge that needs to be overcome, and the results here shown indicate that cells may achieve that by forming more TNTs and exchanging cellular content, which includes autophagy related proteins.

Moreover, even though GFP-LC3 was also seen in transit between TNT connected cells in all applied conditions, no striking differences were perceived in the number of TNTs containing GFP-LC3 puncta between treatments (Figure 18c). Nevertheless, one should have in mind that although autophagy can be assessed by quantifying WIPI1 or WIPI2 puncta positive cells, the appropriate way to quantify LC3 for the investigation of autophagy would rather be the abundance of puncta per cell (Klionsky Abdel-Aziz, et al., 2021). Perhaps the quantification of LC3 puncta per TNT would have been more robust in this case. However, obtaining accurate data on LC3 puncta per cell requires automated quantification, and the high variability in TNT morphology combined with automated puncta quantification is a considerable technical limitation.

During autophagy initiation, LC3 co-localizes with WIPI1 at the nascent phagophore (Proikas-Cezanne et al., 2004). In addition, cryo-transmission electron microscopy (TEM) revealed the presence of several vesicles within TNTs, some in fact surrounded by a double-membrane (Sartori-Rupp et al., 2019). Considering this and previous results, where GFP-WIPI1, GFP-WIPI2 and GFP-LC3 puncta were observed travelling via TNTs, indicating the transfer of autophagic membranes, it was asked whether early or late autophagosomes could be observed in TNTs. The use of U2OS cells stably expressing mRFP-EGFP-LC3 facilitated the distinction between autophagosomes and autolysosomes, since the latter ones only appear with red signal once EGFP is no longer stable in acidic environments. In fact, both early and late autophagosomes can travel via TNTs even under basal conditions, indicating TNTs' and autophagy's importance in the maintenance of a physiological balance (Figure 20).

As described in the literature, WIPI4 plays a role in ferritinophagy (Aring et al., 2022), which mediates the degradation of ferritin with release of free intracellular iron, when needed (Dowdle et al., 2014; Mancias et al., 2014). To investigate on the presence of mRFP-EGFP-WIPI4 in TNTs, a ferritinophagy assay was performed with iron loading, mediated by FAC treatment, and iron chelation, promoted by DFX treatment. For the quantification of WIPI4 puncta, mRFP signal was chosen for its stability in acidic environments. The presence of mRFP-WIPI4 in TNTs only upon DFX or starvation treatments indicates that when challenged, cells tend to exchange material to maintain a metabolically balanced cellular microenvironment (Figure 14a). In this case, the absence of free iron or starvation promoted not only WIPI4 mediated-ferritinophagy, but also the transfer of WIPI4 to balance ferritinophagy in neighboring cells in need. Unfortunately, quantification of TNT index and WIPI4 puncta positive TNTs was not possible due to staining incompatibility.

Here once again, starvation treatment was applied as a standard positive control of the initiation of autophagy. Remarkable increases in the percentages of mRFP-WIPI4 puncta positive cells treated with DFX and in starvation were observed, with approximately 40x increase in DFX treatment and 20x when starved (Figure 14b). Upon iron chelation, the free iron is no longer available for cellular storage, calling for ferritin degradation, and therefore enhancing WIPI4-mediated ferritinophagy. Furthermore, FAC treatment resulted in a very low percentage of puncta positive cells, which was comparable with normal fed condition, once iron overload did not require iron turnover.

The enhanced transfer of WIPI4 from competent towards deficient cells will be discussed later on in this thesis.

As to the qualitative assessments in this study, the processing of confocal images acquired with Z-stacks in optimal sectioning enabled image rendering of 3D videos, which offered a more dynamic, enriching, and clearer picturing of TNT structures and its contents (Figures 10, 13, 15, 19 and 21). Furthermore, the combination of ESID detection and Airyscan super-resolution in a live time lapse imaging offered a lively visualization of GFP-WIPI1 and mRFP-EGFP-WIPI4 in motion travelling through TNTs from one cell to another. In 30 minutes, 5 punctate GFP-WIPI1 structures were observed in transit and later tracked with the open-source plug-in MTrackJ for Fiji, revealing how transient and potent the process of intercellular transfer can be (Figure 11). Both image acquision methods mentioned, namely confocal imaging with Z-stacks and live time lapse, represent robust tools in the investigation of TNTs (Dubois et al., 2020).

7.2 Tunneling Nanotubes mediate the transfer of mitochondria and mitophagosomes

Mitochondria are essential organelles in eukaryotic cells, responsible for critical steps in the cellular metabolism. Importantly, mitochondrial disfunctions are linked to several health conditions, including cancer and neurodegeneration (Nunnari & Suomalainen, 2012). Mitochondria are quite dynamic, constantly going through fission and fusion to maintain organelle renewal and homeostasis. A crucial player in mitochondrial network maintenance is mitophagy, a specific category of autophagy which promptly acts in the clearance of non-functional mitochondria (Ashrafi & Schwarz, 2013). Importantly, when combining the fields of cancer and TNTs, mitochondria have been indicated as the culprit of cell survival and development of drug resistance, as they have been reported to use TNTs to migrate from cell to cell (Pasquier et al., 2013; Pinto et al., 2021).

The transfer of mitochondria via TNTs has been extensively reported by several research groups so far. However, here it is shown not only that mitochondria travel from cell to cell through TNTs even under basal conditions, but also that mitophagosomes can be exported in the same way, indicated by the co-localization of TOM20 and GFP-LC3 shown in Figure 22. Once again, the concept of super-cellularity coined by Rustom (Rustom, 2016) is reinforced.

Live imaging set up facilitated the lively observation of mitochondria being transferred from donor to recipient cell following 24 hours of Sorafenib treatment (Figure 24). Curiously, the live images were acquired over the course of approximately 40 minutes, with MLS-EGFP-mCherry signal tracked in a recipient cell from 21 to 31 minutes. This once more emphasizes how transient cell-to-cell communication can be, especially once the cells are metabolically challenged. Here, Sorafenib was applied as a chemotherapy drug to alter TNT biogenesis. However, it is already known that Sorafenib can disrupt the mitochondrial membrane potential and mitochondrial network while also stimulating AMPK phosphorylation and autophagy (Ross et al., 2017; Ullen et al., 2010), besides interfering with autophagy through the PI3K/Akt/mTOR signaling cascade (Shimizu et al., 2012; Zhai et al., 2014). Sorafenib treatment in liver cancer has been commonly associated with treatment adaptation and the development of chemoresistance (Gauthier & Ho, 2013). Taking this into consideration, this preliminary result suggests that the development of chemoresistance resulting from Sorafenib treatment might be associated with increased formation of TNTs and consequent enhancement of mitochondrial traffic, as well as the export of mitophagosomes, between neighboring cells. Uncovering the molecular players acting on TNT biogenesis could represent a breakthrough in improving cancer treatment efficiency.

7.3 The transfer of ferritinophagy related proteins through Tunneling Nanotubes and the potential behind it

In a ferritinophagy experimental set up, the TNT index was assessed (Figure 25b), and ferritin staining facilitated the quantification of ferritin puncta positive TNTs (Figure 25c). Curiously, while only starvation significantly enhanced the formation of TNTs, both FAC and starved treatments resulted in higher percentages of ferritin puncta within TNTs (although only statistically significant upon starvation). These results suggest that cells could overcome iron overload by increasing ferritin storage, which was then gradually redistributed into neighboring cells without the need to form more TNTs. In contrast to that, starvation imposes a greater challenge than iron loading or iron chelation alone, resulting in both increases in the formation of TNTs and the transfer of ferritin via TNTs. In addition to that, the presence of ferritinophagy's cargo receptor NCOA4 was qualitatively confirmed within TNTs, potentially indicating the transfer of ferritinophagy cargo (Figure 27).

These observations, along with the finding of WIPI4 intercellular transfer, indicate that cells not only share autophagic membranes via TNTs, but also members of the ferritinophagy machinery. Most importantly, the modulation of ferritinophagy itself can influence how the traffic takes place, as cells face the need to restore homeostasis upon a metabolic challenge.

Altered ferritinophagy has been observed in two BPAN patients and was linked to mutations in the WDR45 gene (Aring et al., 2022; Diaw et al., 2022). In line with this, WIPI4 has been shown to play an important role in iron metabolism, where the absence of WDR45 resulted in defective ferritinophagy in a neuroblastoma cell line (Aring et al., 2022). BPAN is a neurodegeneration with brain iron accumulation (NBIA), caused by a de novo mutation in the WDR45 gene. The condition is characterized by cognitive and motor developmental delay, followed by further neurological degradation resulting in dementia and parkinsonism. Morphologically, patients present iron deposition in the substantia nigra and globus pallidus regions (Haack et al., 2012; Hayflick et al., 2013; Saitsu et al., 2013). Altered ferritinophagy can lead to increased intracellular iron levels, resulting in elevated ROS levels and oxidative stress, and causing cellular damage. Ultimately, this can lead to ferroptosis, a type of programmed cell death caused by the intracellular accumulation of iron. Mutations in the WDR45 gene reportedly resulted in alterations in both ferritinophagy and ferroptosis (Diaw et al., 2022).

The detailed mechanism behind brain iron accumulation and how this relates to defective iron metabolism in BPAN patients remains unclear. Once cells go through ferroptosis, the fate of the resulting free iron in the cellular microenvironment is not well-documented in the literature. Furthermore, it has been observed in other neurodegenerative diseases that even before cell death, defective autophagic and lysosomal pathways can result in exosome and vesicle release, promoting the spread of protein aggregates (Caballero et al., 2021). Importantly, although extracellular vesicles and TNTs are distinct forms of intercellular communication, some of their regulatory pathways do overlap, as both involve players of the exocyst complex (Nawaz & Fatima, 2017). Moreover, TNTs can be induced by several stress factors, as inflammation and oxidative stress, the latter a common feature of BPAN. Taking this into consideration and given TNTs' already known relevance in neurodegenerative diseases, investigating on TNTs in the context of BPAN research presents great potential for future investigations.

7.4 In co-culture, healthy cells rescue neighboring cells when hardship strikes

In (Sporbeck et al., 2023) it was shown that, in a co-culture experimental set-up, ATG16L1 deficient cells received more GFP-WIPI1, GFP-WIPI2B and GFP-LC3 than ATG16L1 competent cells. Considering this, it was hypothesized whether a similar mechanism could be observed in cells lacking other autophagy proteins. This was first achieved by suppressing WIPI4 in U2OS expressing NLS-mScarlet, which were co-cultured with U2OS mRFP-EGFP-WIPI4. Subsequently, all cells were treated with the established ferritinophagy assay previously described. Only recipient cells were manually counted with regards to mRFP-WIPI4 puncta positive (Figure 16).

Here, fed and iron overload conditions in control cells resulted in comparable percentages of mRFP-WIPI4 puncta positive recipient cells, which was expected, as in this case iron turnover was not required. Still in downregulated control cells, iron chelation, on the other hand, mildly increased the transfer of mRFP-WIPI4 towards recipient cells, whereas starvation remarkably enhanced mRFP-WIPI4 traffic. Although the mean of mRFP-WIPI4 puncta positive recipient cells upon WIPI4-downregulation was higher in all conditions, in comparison to control, only DFX showed a notable rise within the different treatments. This result matched our hypothesis, indicating that WIPI4 deficient cells were supported by their neighboring WIPI4 competent cells when challenged with iron chelation, to assist ferritin degradation by WIPI4. Furthermore, starvation already significantly enhanced the sharing of

WIPI4 from donor to recipient cells even in downregulation control, with no further increase upon downregulation.

In addition to mRFP-WIPI4 puncta quantification in recipient cells and the acquirement of representative images, the traffic of mRFP-WIPI4 into WIPI4 deficient recipient cells was also visualized in a live time lapse imaging. In a similar experimental set-up to the one previously described, a U2OS NLS-mScarlet was observed connected via a TNT to a U2OS mRFP-EGFP-WIPI4 cell, which had just delivered a mRFP-EGFP-WIPI4 puncta. At 0 seconds, the mRFP-EGFP-WIPI4 is seen at the connection of the TNT to the recipient cell, and as time progresses, the punctate structure was tracked in motion inside of the recipient cell. Other puncta can also be spotted in the recipient cell, although only the one depicted in Figure 17 was manually tracked, as it was the one seen leaving a TNT.

In the second TNT-rescue experiment shown in this thesis, it was questioned if WIPI4 deficient cells would also try to alleviate the burden of excess FTH1 by redistributing it. To achieve this, cells initially transfected with esiFLUC or esiWDR45 were co-transfected with GFP-FTH1 (donor cells) and then co-cultured with WIPI4 competent cells (in this case U2OS NLS-mScarlet, as recipient cells). Once again, all cells were subjected to a ferritinophagy assay. In this assay, only recipient cells were counted as GFP-FTH1 puncta positive or not (Figure 28).

Remarkably, cells lacking WIPI4 exported more GFP-FTH1 to WIPI4 competent cells in all treatment conditions, and significantly more upon iron chelation and starvation. Although more GFP-FTH1 puncta were transferred from WIPI4 incompetent into WIPI4 competent recipient cells in fed conditions, the difference was not statistically significant. Interestingly, the amount of GFP-FTH1 transfer in iron overloaded cells was hardly increased in WIPI4 downregulation in comparison to esiFLUC.

Together these observations indicate that when challenged with iron starvation, cells can support each other by providing WIPI4, while simultaneously redistributing excess material which they cannot process, in this case FTH1. However, the molecular details behind this mechanism remain unknown, and further research is necessary. Knowing of iron's importance in the brain, above all tissues, makes this a discovery with great potential. Brain iron accumulation is a common feature in several neurodegenerative diseases, including BPAN, a disease caused by *de novo* mutations in WDR45 which has been linked to deficient ferritinophagy (Aring et al., 2022). Furthermore, TNTs' potential dual role in neurodegeneration is currently under intense investigation by several research groups. Indeed, it has already been shown that TNTs play a part in both disease spread by propagating protein

aggregates (Chastagner et al., 2020; Scheiblich et al., 2021), and in a rescue mechanism mediating bidirectional transfer of functional and non-functional mitochondria (Scheiblich et al., 2021). Moreover, there is evidence of protein aggregates being rerouted to extracellular export via late endosomes, multivesicular bodies or TNTs when autophagy fails (Caballero et al., 2021; Chastagner et al., 2020). Considering all of this, TNTs represent a great potential target for future studies in BPAN and other neurodegenerative diseases.

7.5 Homo- and heterotypical interactions via Tunneling Nanotubes are observed between the liver cells LX-2 and HuH-7

TNTs have already been identified in numerous cell types so far, including many cancer cells (Dubois et al., 2020). However, TNTs had not yet been observed in hepatic stellate or hepatocellular carcinoma cells. As introduced in this thesis, liver cancer can be formed by distinct types of cells, with stellate cell lines playing a crucial role due to their high plasticity and support to hepatic cells (Sia et al., 2017; Trivedi et al., 2021).

Confirming the presence of TNTs in the HSC (LX-2) and HCC (HuH-7) (Figure 29) cell lines, and most importantly, that these cells could also connect in a heterotypical co-culture set-up (Figure 30), provided important insights concerning cell-to-cell communication in the tumor microenvironment. This heterotypical intercellular communication is highly relevant, not only for LX-2 to perform its role promoting hepatic fibrosis and supporting the tumor microenvironment, but also for the development of chemoresistance (Trivedi et al., 2021).

Furthermore, heterotypical interactions are not only important in cancer, as neurons connect to astrocytes through TNTs for the exchange of calcium ions, a fundamental step for neuronal development (Wang & Gerdes, 2012). Overall, distinct cell types must interact in tissues, exchanging cellular materials and chemical signals necessary for the maintenance of the organismal health. TNTs have been observed in numerous cell types, and it is likely that they play an important role in many more different contexts.

7.6 NUDC differentially modulates Tunneling Nanotubes' biogenesis

The nuclear distribution C or nuclear migration protein NUDC is a ubiquitously expressed regulator of dynein and actin dynamics (Zhang et al., 2016). Importantly, NUDC is as well known for its detrimental role in cancer, due to its association with proliferation, cancer invasion and metastasis (Han et al., 2018; Suzuki et al., 2007).

To investigate on the potential connection between NUDC and the biogenesis of TNTs, NUDC was downregulated in the cell lines LX-2, HuH-7 and U2OS. This was followed by staining with Phalloidin, WGA and endogenous tubulin allowed manual quantification of TNT index. Strikingly, the downregulation of NUDC in LX-2 and HuH-7 significantly reduced the number of TNTs per 100 cells (respectively in Figures 31b and 32b). In these cell lines, even though Sorafenib treatment was observed to increase the TNT index in control cells, it failed to do the same once NUDC was downregulated. This result indicates that NUDC is in fact involved in TNT biogenesis, although not exclusively required for it. Furthermore, LX-2, as stellate cells, are known to be responsible for supporting liver regeneration (Roskams, 2008).

Particularly interesting is the observation that the stellate cell line LX-2 forms more TNTs in comparison to the hepatocellular carcinoma cell line HuH-7. This is a probable key feature for their role as stellate cells, supporting hepatic cells, which potentially indicates their crucial part in the development of chemoresistance.

In contrast to the observations in LX-2 and HuH-7 cells, NUDC seems to negatively modulate the formation of TNTs in U2OS (Figure 33b). There are several reported cases where TNT biogenesis is differentially modulated by the same factor in distinct cell lines. Importantly, the overexpression of NUDC in liver cancer presents an unfavorable prognostic, with associated lower survival rates, according to the Human Protein Atlas (Ponten et al., 2008). Moreover, knowing that NUDC has been linked to tumor proliferation and metastasis (Han et al., 2018; Suzuki et al., 2007), and since NUDC was here revealed as a positive regulator of TNT biogenesis, it can be suggested that TNTs might play a role in the development of drug resistance, specifically in the context of liver cancer. This may be achieved by mediating the intercellular transfer of mitochondria and other cellular components in the tumor microenvironment, a mechanism facilitated by NUDC's induced formation of TNTs. Cell-to-cell communication in liver cancer promotes the rescue of cancer cells when under chemotherapy, resulting in cellular survival, tumor proliferation and disease progression (Llovet et al., 2021). Nonetheless, further studies are necessary to unravel the molecular details behind the complex interaction between autophagy, TNTs and NUDC, and to potentially reveal novel therapy targets in the context of liver cancer.

7.7 A link between the initiation of autophagy and Tunneling Nanotube formation

The observation of a connection between increased WIPI1 puncta formation and the formation of TNTs raised the question as to how the biogenesis of TNTs might be modulated by WIPI1.

To investigate on this aspect, EGFP-WIPI1 was overexpressed, followed by manual quantification of the TNT index. Strikingly, a statistically significant increase in the number of TNTs per 100 cells was observed upon transfection of 0.25μg of EGFP-WIPI1 when compared to cells transfected with EGFP-vector in the same concentration (Figure 34b).

Since the presence of more WIPI1 led to an increase in TNTs, it was next questioned whether less WIPI1 would hinder TNT biogenesis. This was indeed observed, once WIPI1 deficient cells failed to form more TNTs even when challenged with serum starvation or serum and amino acid starvation for 24 hours (Figure 35b). Although the presence of WIPI1 seems to play a significant role in the formation of TNTs, it does not seem to be required for it, as its absence decreased but did not abolish TNTs.

Several proteins acting in cytoskeleton remodeling have been pointed out as important players in TNT biogenesis. However, the detailed molecular mechanism behind it remains to be clarified, and further studies are necessary to reveal details concerning the role played by WIPI1 in the building of TNTs. Nevertheless, the connection between autophagy and cytoskeleton dynamics is already well-known, and microtubule's dynamics has been reported to play a key role in the recruitment of specific actors in autophagosome formation, with mature autophagosomes interacting with stable microtubules (Geeraert et al., 2010). However, the interaction between autophagy and cytoskeleton components is mostly responsible for the intracellular trafficking of vesicular cargoes, as well as for phagophore biogenesis and its maturation (Cason et al., 2021; Kast & Dominguez, 2017).

Knowing that TNTs contain F-actin, and may or may not contain tubulin, raises the question whether the transfer of autophagosomes via TNTs could be dependent on the presence of tubulin. It may be hypothesized that the cytoskeleton affects the traffic of WIPI1, but this does not answer how WIPI1 could simultaneously modulate TNT biogenesis. Different types of TNTs have been observed, and it is speculated that distinct types of cargo can determine which type of TNTs should be built (Zurzolo, 2021). On this note, one may hypothesize whether WIPI1 could induce the formation of its own category of TNTs. In line with this, the significant drop in TNT index in WIPI1 KO cells could indicate a preferential transfer of WIPI1 and autophagosomes via TNTs, since less WIPI1 would require less TNTs. This, of course, requires for further investigation. Additionally, the Wnt/Ca^{2+} pathway has been previously linked to the formation of TNTs, via the *β isoform of* calmodulin-dependent protein kinase II (CAMKII), a known F-actin interactor involved in actin cytoskeleton remodeling (Vargas et al., 2019). Interestingly, the Wnt pathway also acts in the regulation of autophagy via both mTORC1 and AMPK (Inoki et al., 2006; Pfisterer et al., 2011).

In addition, a previous study has reported an interaction between WIPI1 and NUDC (Bakula et al., 2017), also shown to play a role in the formation of TNTs in this thesis. Certainly, further research is necessary to uncover the mechanistic of WIPI1's role in TNT formation. Notwithstanding, the preliminary evidence provided in this study indicates great potential for discoveries in both the autophagy and TNT fields.

Conclusion

This study investigated on the potential of TNTs as a cellular rescue mechanism, due to their property of promoting the exchange of cellular components. The aims of this thesis were assessing the presence of autophagic membranes, as well as of the autophagic cargoes mitochondria and ferritin, within TNTs.

Initially in Chapter 3, it was discovered that autophagic membranes can travel intercellularly via TNTs, which was achieved with the assessment of WIPI1, WIPI2 and LC3 puncta, and that this feature can be stimulated by starvation. In addition, the transfer of WIPI4 via TNTs was witnessed, and could only be observed upon iron chelation or starvation. This was an interesting discovery, once WIPI4 has been linked to iron metabolism due to its role in ferritinophagy. Furthermore, the traffic of both autophagosomes and autolysosomes was confirmed and qualitatively assessed, by the visualization of LC3 bound to tandem mRFP-EGFP constructs inside of TNTs.

Chapter 4 focused on an already known feature of TNTs: mitochondrial transfer. However, here it was questioned whether mitophagosomes could be also transferred via TNTs, which was indeed confirmed by the co-localization of TOM20 and LC3 within TNTs. This was followed by the investigation on the transfer of mitochondria between cells subjected to Sorafenib, a drug commonly used in the treatment of liver cancer and a known mitophagy disruptor.

Next, in Chapter 5, TNTs were investigated in the context of ferritinophagy. Here, ferritin and its cargo receptor, NCOA4, were observed inside of TNTs, while being intercellularly transferred between neighboring cells. Iron loading and iron chelation were used to modulate ferritinophagy, which did not seem to significantly influence the formation of TNTs. Nevertheless, iron overload and starvation promoted the transfer of ferritin, assessed by the manual quantification of TNT index combined with the quantification of ferritin puncta positive TNTs.

Results in Chapters 3 and 5 provided evidence of TNTs most important feature as a cellular rescue mechanism, where, strikingly, WIPI4 deficient cells could be supported by WIPI4 competent cells in co-culture in two ways: compensation of deficiency and redistribution of undegraded material.

Finally, Chapter 6 investigated on the biogenesis of TNTs in cancer cell lines. In liver cancer cells, the presence of TNTs was confirmed in both homotypic and heterotypic cultures. As to the modulation of TNT formation, NUDC was identified as a potential player,

differentially regulating the TNT biogenesis in different cell types. In addition, the study revealed WIPI1 as another potential player in the biogenesis of TNTs, in which its overexpression increased TNT index, whereas its absence remarkably decreased it.

Regarding TNT biogenesis and its two potential regulators identified in this thesis, WIPI1 and NUDC, it is worth pointing out that previous research already reported a connection between them. Proteomics studies revealed that WIPI1 and NUDC directly interact (Bakula et al., 2017), although this interaction has not yet been studied in detail. These observations when put together open many doors to further investigation on the potential role of NUDC in autophagy, as well as autophagy's and NUDC's roles in determining the formation of TNTs.

Figure 36 shows a graphical abstract of the discoveries presented in this thesis.

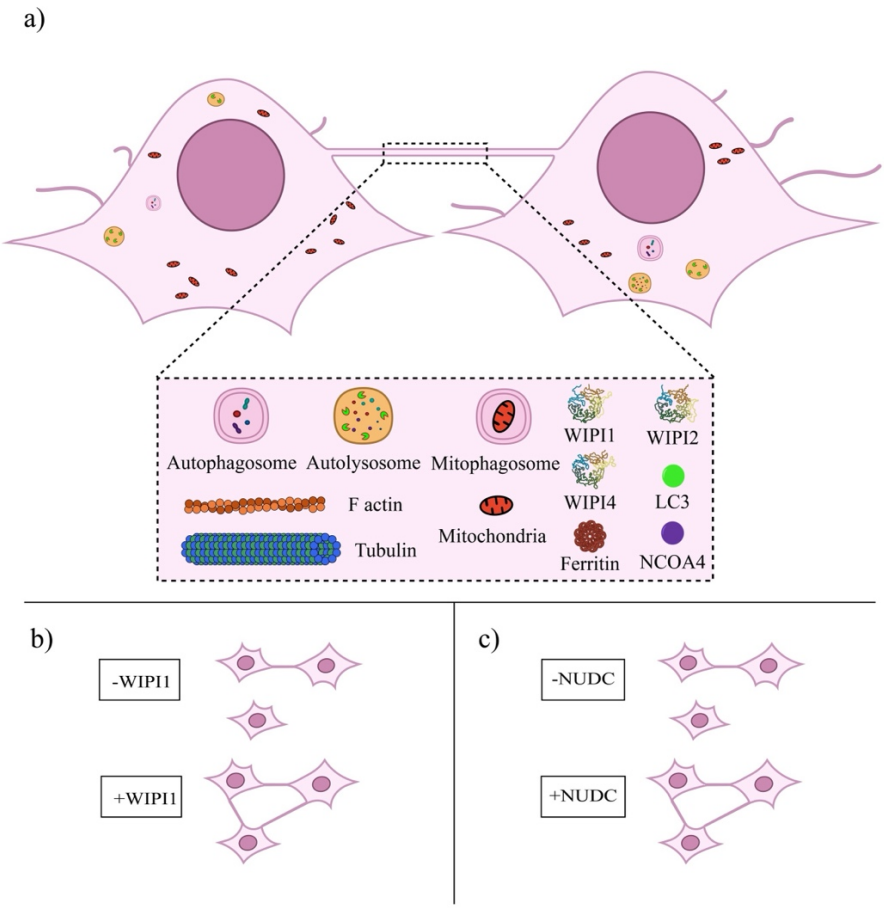

Figure 36. Distribution of cellular content over long-distance via TNTs. a) Cells connect via TNTs, which contain F actin and tubulin, and facilitate the sharing of autophagosomes, autolysosomes, and mitophagosomes, as well as ferritin, NCOA4, WIPI1, WIPI2, WIPI4 and LC3. **b)** WIPI1 positively modulates TNT biogenesis, as well as **c)** NUDC.

How these observations translate *in vivo* remains to be further studied. For instance, it is well-known that treatment options for hepatocellular carcinoma remain limited, and the development of chemoresistance is a common obstacle. On another note, the inevitability of protein aggregates spreading and disease progression in neurodegeneration imposes a significant challenge for positive treatment outcomes. TNTs are related to both cancer and neurodegenerative diseases. Thereby, investigating on the modulation of TNTs *in vivo* could reveal novel therapy targets to improve treatment efficiency and survival rates.

Moreover, a large part of this thesis were qualitative assessments on TNTs, providing enlightening visualization of these structures via the 3D reconstruction of confocal images. In addition, time lapse imaging combining transmitted light illumination and Airyscan microscopy provided dynamic observation of live TNTs while connecting cells and promoting the exchange of cellular content, which was complemented with the manual tracking of single particles.

This was a rewarding study, for being so unique in its observations. Most importantly, the novel results shown in this thesis open several doors for future research in the fields of autophagy and TNTs, and especially pave the way for the further research in the contexts of cancer and neurodegeneration.

Literature

Abounit, S., Bousset, L., Loria, F., Zhu, S., de Chaumont, F., Pieri, L., Olivo-Marin, J. C., Melki, R., & Zurzolo, C. (2016). Tunneling nanotubes spread fibrillar alpha-synuclein by intercellular trafficking of lysosomes. *EMBO J*, *35*(19), 2120-2138. https://doi.org/10.15252/embj.201593411

Abounit, S., & Zurzolo, C. (2012). Wiring through tunneling nanotubes--from electrical signals to organelle transfer. *J Cell Sci*, *125*(Pt 5), 1089-1098. https://doi.org/10.1242/jcs.083279

Almannai, M., Marafi, D., Abdel-Salam, G. M. H., Zaki, M. S., Duan, R., Calame, D., Herman, I., Levesque, F., Elbendary, H. M., Hegazy, I., Chung, W. K., Kavus, H., Saeidi, K., Maroofian, R., AlHashim, A., Al-Otaibi, A., Al Madhi, A., Abou Al-Seood, H. M., Alasmari, A., . . . El-Hattab, A. W. (2022). El-Hattab-Alkuraya syndrome caused by biallelic WDR45B pathogenic variants: Further delineation of the phenotype and genotype. *Clin Genet*, *101*(5-6), 530-540. https://doi.org/10.1111/cge.14132

Antanaviciute, I., Rysevaite, K., Liutkevicius, V., Marandykina, A., Rimkute, L., Sveikatiene, R., Uloza, V., & Skeberdis, V. A. (2014). Long-distance communication between laryngeal carcinoma cells. *PLoS One*, *9*(6), e99196. https://doi.org/10.1371/journal.pone.0099196

Apel, A., Herr, I., Schwarz, H., Rodemann, H. P., & Mayer, A. (2008). Blocked autophagy sensitizes resistant carcinoma cells to radiation therapy. *Cancer Res*, *68*(5), 1485-1494. https://doi.org/10.1158/0008-5472.CAN-07-0562

Aring, L., Choi, E. K., Kopera, H., Lanigan, T., Iwase, S., Klionsky, D. J., & Seo, Y. A. (2022). A neurodegeneration gene, WDR45, links impaired ferritinophagy to iron accumulation. *J Neurochem*, *160*(3), 356-375. https://doi.org/10.1111/jnc.15548

Ashrafi, G., & Schwarz, T. L. (2013). The pathways of mitophagy for quality control and clearance of mitochondria. *Cell Death Differ*, *20*(1), 31-42. https://doi.org/10.1038/cdd.2012.81

Aumais, J. P., Tunstead, J. R., McNeil, R. S., Schaar, B. T., McConnell, S. K., Lin, S. H., Clark, G. D., & Yu-Lee, L. Y. (2001). NudC associates with Lis1 and the dynein motor at the leading pole of neurons. *J Neurosci*, *21*(24), RC187. https://doi.org/10.1523/JNEUROSCI.21-24-j0002.2001

Aumais, J. P., Williams, S. N., Luo, W., Nishino, M., Caldwell, K. A., Caldwell, G. A., Lin, S.-H., & Yu-Lee, L.-y. (2003). Role for NudC, a dynein-associated nuclear movement protein, in mitosis and cytokinesis. *Journal of Cell Science*, *116*(10), 1991-2003.

Bakula, D., Muller, A. J., Zuleger, T., Takacs, Z., Franz-Wachtel, M., Thost, A. K., Brigger, D., Tschan, M. P., Frickey, T., Robenek, H., Macek, B., & Proikas-Cezanne, T. (2017). WIPI3 and WIPI4 beta-propellers are scaffolds for LKB1-AMPK-TSC signalling circuits in the control of autophagy. *Nat Commun*, *8*, 15637. https://doi.org/10.1038/ncomms15637

Baskaran, S., Ragusa, M. J., Boura, E., & Hurley, J. H. (2012). Two-site recognition of phosphatidylinositol 3-phosphate by PROPPINs in autophagy. *Mol Cell*, *47*(3), 339-348. https://doi.org/10.1016/j.molcel.2012.05.027

Caballero, B., Bourdenx, M., Luengo, E., Diaz, A., Sohn, P. D., Chen, X., Wang, C., Juste, Y. R., Wegmann, S., Patel, B., Young, Z. T., Kuo, S. Y., Rodriguez-Navarro, J. A., Shao, H., Lopez, M. G., Karch, C. M., Goate, A. M., Gestwicki, J. E., Hyman, B. T., . . . Cuervo, A. M. (2021). Acetylated tau inhibits chaperone-mediated autophagy and promotes tau pathology propagation in mice. *Nat Commun*, *12*(1), 2238. https://doi.org/10.1038/s41467-021-22501-9

Caldas, L. A., Carneiro, F. A., Higa, L. M., Monteiro, F. L., da Silva, G. P., da Costa, L. J., Durigon, E. L., Tanuri, A., & de Souza, W. (2020). Ultrastructural analysis of SARS-CoV-2 interactions with the host cell via high resolution scanning electron microscopy. *Sci Rep*, *10*(1), 16099. https://doi.org/10.1038/s41598-020-73162-5

Cason, S. E., Carman, P. J., Van Duyne, C., Goldsmith, J., Dominguez, R., & Holzbaur, E. L. F. (2021). Sequential dynein effectors regulate axonal autophagosome motility in a maturation-dependent pathway. *J Cell Biol*, *220*(7). https://doi.org/10.1083/jcb.202010179

Chastagner, P., Loria, F., Vargas, J. Y., Tois, J., M, I. D., Okafo, G., Brou, C., & Zurzolo, C. (2020). Fate and propagation of endogenously formed Tau aggregates in neuronal cells. *EMBO Mol Med*, *12*(12), e12025. https://doi.org/10.15252/emmm.202012025

Codogno, P., Mehrpour, M., & Proikas-Cezanne, T. (2012). Canonical and non-canonical autophagy: variations on a common theme of self-eating? *Nature reviews Molecular cell biology*, *13*(1), 7-12.

Cong, Y., So, V., Tijssen, M. A. J., Verbeek, D. S., Reggiori, F., & Mauthe, M. (2021). WDR45, one gene associated with multiple neurodevelopmental disorders. *Autophagy*, *17*(12), 3908-3923. https://doi.org/10.1080/15548627.2021.1899669

Cordero Cervantes, D., & Zurzolo, C. (2021). Peering into tunneling nanotubes-The path forward. *EMBO J*, *40*(8), e105789. https://doi.org/10.15252/embj.2020105789

Costanzo, M., Abounit, S., Marzo, L., Danckaert, A., Chamoun, Z., Roux, P., & Zurzolo, C. (2013). Transfer of polyglutamine aggregates in neuronal cells occurs in tunneling nanotubes. *Journal of Cell Science*, *126*(16), 3678-3685. https://doi.org/10.1242/jcs.126086

Davies, S. P., Helps, N. R., Cohen, P. T., & Hardie, D. G. (1995). 5'-AMP inhibits dephosphorylation, as well as promoting phosphorylation, of the AMP-activated protein kinase. Studies using bacterially expressed human protein phosphatase-2C alpha and native bovine protein phosphatase-2AC. *FEBS Lett*, *377*(3), 421-425. https://doi.org/10.1016/0014-5793(95)01368-7

De Domenico, I., Vaughn, M. B., Li, L., Bagley, D., Musci, G., Ward, D. M., & Kaplan, J. (2006). Ferroportin-mediated mobilization of ferritin iron precedes ferritin degradation by the proteasome. *EMBO J*, *25*(22), 5396-5404. https://doi.org/10.1038/sj.emboj.7601409

De Duve, C. (1963). Ciba Foundation Symposium on Lysosomes,(AVS de Reuck and MPL Cameron, editors). In: Boston, Little, Brown and Company.

de Duve, D. (1969). The peroxisome: a new cytoplasmic organelle. *Proc R Soc Lond B Biol Sci*, *173*(1030), 71-83. https://www.ncbi.nlm.nih.gov/pubmed/4389354

Delage, E., Cervantes, D. C., Penard, E., Schmitt, C., Syan, S., Disanza, A., Scita, G., & Zurzolo, C. (2016). Differential identity of Filopodia and Tunneling Nanotubes revealed by the opposite functions of actin regulatory complexes. *Sci Rep*, *6*, 39632. https://doi.org/10.1038/srep39632

Desir, S., Dickson, E. L., Vogel, R. I., Thayanithy, V., Wong, P., Teoh, D., Geller, M. A., Steer, C. J., Subramanian, S., & Lou, E. (2016). Tunneling nanotube formation is stimulated by hypoxia in ovarian cancer cells. *Oncotarget*, *7*(28), 43150-43161. https://doi.org/10.18632/oncotarget.9504

Dettmann, A., Heilig, Y., Valerius, O., Ludwig, S., & Seiler, S. (2014). Fungal communication requires the MAK-2 pathway elements STE-20 and RAS-2, the NRC-1 adapter STE-50 and the MAP kinase scaffold HAM-5. *PLoS Genet*, *10*(11), e1004762. https://doi.org/10.1371/journal.pgen.1004762

Diaw, S. H., Ganos, C., Zittel, S., Plotze-Martin, K., Kulikovskaja, L., Vos, M., Westenberger, A., Rakovic, A., Lohmann, K., & Dulovic-Mahlow, M. (2022). Mutant

WDR45 Leads to Altered Ferritinophagy and Ferroptosis in beta-Propeller Protein-Associated Neurodegeneration. *Int J Mol Sci*, *23*(17). https://doi.org/10.3390/ijms23179524

Dikic, I., & Elazar, Z. (2018). Mechanism and medical implications of mammalian autophagy. *Nat Rev Mol Cell Biol*, *19*(6), 349-364. https://doi.org/10.1038/s41580-018-0003-4

Dilsizoglu Senol, A., Samarani, M., Syan, S., Guardia, C. M., Nonaka, T., Liv, N., Latour-Lambert, P., Hasegawa, M., Klumperman, J., & Bonifacino, J. S. (2021). α-Synuclein fibrils subvert lysosome structure and function for the propagation of protein misfolding between cells through tunneling nanotubes. *PLoS biology*, *19*(7), e3001287.

Dooley, H. C., Razi, M., Polson, H. E., Girardin, S. E., Wilson, M. I., & Tooze, S. A. (2014). WIPI2 links LC3 conjugation with PI3P, autophagosome formation, and pathogen clearance by recruiting Atg12-5-16L1. *Mol Cell*, *55*(2), 238-252. https://doi.org/10.1016/j.molcel.2014.05.021

Dowdle, W. E., Nyfeler, B., Nagel, J., Elling, R. A., Liu, S., Triantafellow, E., Menon, S., Wang, Z., Honda, A., Pardee, G., Cantwell, J., Luu, C., Cornella-Taracido, I., Harrington, E., Fekkes, P., Lei, H., Fang, Q., Digan, M. E., Burdick, D., . . . Murphy, L. O. (2014). Selective VPS34 inhibitor blocks autophagy and uncovers a role for NCOA4 in ferritin degradation and iron homeostasis in vivo. *Nat Cell Biol*, *16*(11), 1069-1079. https://doi.org/10.1038/ncb3053

Dubey, G. P., & Ben-Yehuda, S. (2011). Intercellular nanotubes mediate bacterial communication. *Cell*, *144*(4), 590-600. https://doi.org/10.1016/j.cell.2011.01.015

Dubois, F., Benard, M., Jean-Jacques, B., Schapman, D., Roberge, H., Lebon, A., Goux, D., Monterroso, B., Elie, N., Komuro, H., Bazille, C., Levallet, J., Bergot, E., Levallet, G., & Galas, L. (2020). Investigating Tunneling Nanotubes in Cancer Cells: Guidelines for Structural and Functional Studies through Cell Imaging. *Biomed Res Int*, *2020*, 2701345. https://doi.org/10.1155/2020/2701345

Dupont, M., Souriant, S., Lugo-Villarino, G., Maridonneau-Parini, I., & Verollet, C. (2018). Tunneling Nanotubes: Intimate Communication between Myeloid Cells. *Front Immunol*, *9*, 43. https://doi.org/10.3389/fimmu.2018.00043

Errede, M., Mangieri, D., Longo, G., Girolamo, F., de Trizio, I., Vimercati, A., Serio, G., Frei, K., Perris, R., & Virgintino, D. (2018). Tunneling nanotubes evoke pericyte/endothelial communication during normal and tumoral angiogenesis. *Fluids Barriers CNS*, *15*(1), 28. https://doi.org/10.1186/s12987-018-0114-5

Fivenson, E. M., Lautrup, S., Sun, N., Scheibye-Knudsen, M., Stevnsner, T., Nilsen, H., Bohr, V. A., & Fang, E. F. (2017). Mitophagy in neurodegeneration and aging. *Neurochem Int*, *109*, 202-209. https://doi.org/10.1016/j.neuint.2017.02.007

Gan-Or, Z., Dion, P. A., & Rouleau, G. A. (2015). Genetic perspective on the role of the autophagy-lysosome pathway in Parkinson disease. *Autophagy*, *11*(9), 1443-1457. https://doi.org/10.1080/15548627.2015.1067364

Ganti, K., Han, J., Manicassamy, B., & Lowen, A. C. (2021). Rab11a mediates cell-cell spread and reassortment of influenza A virus genomes via tunneling nanotubes. *PLoS Pathog*, *17*(9), e1009321. https://doi.org/10.1371/journal.ppat.1009321

Gatica, D., Lahiri, V., & Klionsky, D. J. (2018). Cargo recognition and degradation by selective autophagy. *Nat Cell Biol*, *20*(3), 233-242. https://doi.org/10.1038/s41556-018-0037-z

Gaugel, A., Bakula, D., Hoffmann, A., & Proikas-Cezanne, T. (2012). Defining regulatory and phosphoinositide-binding sites in the human WIPI-1 beta-propeller responsible

for autophagosomal membrane localization downstream of mTORC1 inhibition. *J Mol Signal*, *7*(1), 16. https://doi.org/10.1186/1750-2187-7-16
Gauthier, A., & Ho, M. (2013). Role of sorafenib in the treatment of advanced hepatocellular carcinoma: An update. *Hepatol Res*, *43*(2), 147-154. https://doi.org/10.1111/j.1872-034X.2012.01113.x
Geeraert, C., Ratier, A., Pfisterer, S. G., Perdiz, D., Cantaloube, I., Rouault, A., Pattingre, S., Proikas-Cezanne, T., Codogno, P., & Pous, C. (2010). Starvation-induced hyperacetylation of tubulin is required for the stimulation of autophagy by nutrient deprivation. *J Biol Chem*, *285*(31), 24184-24194. https://doi.org/10.1074/jbc.M109.091553
Geng, J., & Klionsky, D. J. (2008). The Atg8 and Atg12 ubiquitin-like conjugation systems in macroautophagy. 'Protein modifications: beyond the usual suspects' review series. *EMBO Rep*, *9*(9), 859-864. https://doi.org/10.1038/embor.2008.163
González, A., & Hall, M. N. (2017). Nutrient sensing and TOR signaling in yeast and mammals. *The EMBO Journal*, *36*(4), 397-408. https://doi.org/https://doi.org/10.15252/embj.201696010
Gousset, K., Marzo, L., Commere, P. H., & Zurzolo, C. (2013). Myo10 is a key regulator of TNT formation in neuronal cells. *J Cell Sci*, *126*(Pt 19), 4424-4435. https://doi.org/10.1242/jcs.129239
Grotemeier, A., Alers, S., Pfisterer, S. G., Paasch, F., Daubrawa, M., Dieterle, A., Viollet, B., Wesselborg, S., Proikas-Cezanne, T., & Stork, B. (2010). AMPK-independent induction of autophagy by cytosolic Ca2+ increase. *Cell Signal*, *22*(6), 914-925. https://doi.org/10.1016/j.cellsig.2010.01.015
Gwinn, D. M., Shackelford, D. B., Egan, D. F., Mihaylova, M. M., Mery, A., Vasquez, D. S., Turk, B. E., & Shaw, R. J. (2008). AMPK phosphorylation of raptor mediates a metabolic checkpoint. *Mol Cell*, *30*(2), 214-226. https://doi.org/10.1016/j.molcel.2008.03.003
Haack, T. B., Hogarth, P., Kruer, M. C., Gregory, A., Wieland, T., Schwarzmayr, T., Graf, E., Sanford, L., Meyer, E., Kara, E., Cuno, S. M., Harik, S. I., Dandu, V. H., Nardocci, N., Zorzi, G., Dunaway, T., Tarnopolsky, M., Skinner, S., Frucht, S., . . . Hayflick, S. J. (2012). Exome sequencing reveals de novo WDR45 mutations causing a phenotypically distinct, X-linked dominant form of NBIA. *Am J Hum Genet*, *91*(6), 1144-1149. https://doi.org/10.1016/j.ajhg.2012.10.019
Hahn-Windgassen, A., Nogueira, V., Chen, C. C., Skeen, J. E., Sonenberg, N., & Hay, N. (2005). Akt activates the mammalian target of rapamycin by regulating cellular ATP level and AMPK activity. *J Biol Chem*, *280*(37), 32081-32089. https://doi.org/10.1074/jbc.M502876200
Han, B., Zhang, Y. Y., Xu, K., Bai, Y., Wan, L. H., Miao, S. K., Zhang, K. X., Zhang, H. W., Liu, Y., & Zhou, L. M. (2018). NUDCD1 promotes metastasis through inducing EMT and inhibiting apoptosis in colorectal cancer. *Am J Cancer Res*, *8*(5), 810-823. https://www.ncbi.nlm.nih.gov/pubmed/29888104
Hanna, S. J., McCoy-Simandle, K., Leung, E., Genna, A., Condeelis, J., & Cox, D. (2019). Tunneling nanotubes, a novel mode of tumor cell-macrophage communication in tumor cell invasion. *J Cell Sci*, *132*(3). https://doi.org/10.1242/jcs.223321
Hanna, S. J., McCoy-Simandle, K., Miskolci, V., Guo, P., Cammer, M., Hodgson, L., & Cox, D. (2017). The Role of Rho-GTPases and actin polymerization during Macrophage Tunneling Nanotube Biogenesis. *Sci Rep*, *7*(1), 8547. https://doi.org/10.1038/s41598-017-08950-7
Hardie, D. G. (2007). AMP-activated/SNF1 protein kinases: conserved guardians of cellular energy. *Nat Rev Mol Cell Biol*, *8*(10), 774-785. https://doi.org/10.1038/nrm2249

Harding, T. M., Morano, K. A., Scott, S. V., & Klionsky, D. J. (1995). Isolation and characterization of yeast mutants in the cytoplasm to vacuole protein targeting pathway. *J Cell Biol*, *131*(3), 591-602. https://doi.org/10.1083/jcb.131.3.591

Hase, K., Kimura, S., Takatsu, H., Ohmae, M., Kawano, S., Kitamura, H., Ito, M., Watarai, H., Hazelett, C. C., Yeaman, C., & Ohno, H. (2009). M-Sec promotes membrane nanotube formation by interacting with Ral and the exocyst complex. *Nat Cell Biol*, *11*(12), 1427-1432. https://doi.org/10.1038/ncb1990

Hawley, S. A., Pan, D. A., Mustard, K. J., Ross, L., Bain, J., Edelman, A. M., Frenguelli, B. G., & Hardie, D. G. (2005). Calmodulin-dependent protein kinase kinase-beta is an alternative upstream kinase for AMP-activated protein kinase. *Cell Metab*, *2*(1), 9-19. https://doi.org/10.1016/j.cmet.2005.05.009

Hayflick, S. J., Kruer, M. C., Gregory, A., Haack, T. B., Kurian, M. A., Houlden, H. H., Anderson, J., Boddaert, N., Sanford, L., Harik, S. I., Dandu, V. H., Nardocci, N., Zorzi, G., Dunaway, T., Tarnopolsky, M., Skinner, S., Holden, K. R., Frucht, S., Hanspal, E., . . . Hogarth, P. (2013). beta-Propeller protein-associated neurodegeneration: a new X-linked dominant disorder with brain iron accumulation. *Brain*, *136*(Pt 6), 1708-1717. https://doi.org/10.1093/brain/awt095

Hosokawa, N., Hara, T., Kaizuka, T., Kishi, C., Takamura, A., Miura, Y., Iemura, S., Natsume, T., Takehana, K., Yamada, N., Guan, J. L., Oshiro, N., & Mizushima, N. (2009). Nutrient-dependent mTORC1 association with the ULK1-Atg13-FIP200 complex required for autophagy. *Mol Biol Cell*, *20*(7), 1981-1991. https://doi.org/10.1091/mbc.e08-12-1248

Hoyer-Hansen, M., Bastholm, L., Szyniarowski, P., Campanella, M., Szabadkai, G., Farkas, T., Bianchi, K., Fehrenbacher, N., Elling, F., Rizzuto, R., Mathiasen, I. S., & Jaattela, M. (2007). Control of macroautophagy by calcium, calmodulin-dependent kinase kinase-beta, and Bcl-2. *Mol Cell*, *25*(2), 193-205. https://doi.org/10.1016/j.molcel.2006.12.009

Inoki, K., Ouyang, H., Zhu, T., Lindvall, C., Wang, Y., Zhang, X., Yang, Q., Bennett, C., Harada, Y., Stankunas, K., Wang, C. Y., He, X., MacDougald, O. A., You, M., Williams, B. O., & Guan, K. L. (2006). TSC2 integrates Wnt and energy signals via a coordinated phosphorylation by AMPK and GSK3 to regulate cell growth. *Cell*, *126*(5), 955-968. https://doi.org/10.1016/j.cell.2006.06.055

Itakura, E., & Mizushima, N. (2010). Characterization of autophagosome formation site by a hierarchical analysis of mammalian Atg proteins. *Autophagy*, *6*(6), 764-776. https://doi.org/10.4161/auto.6.6.12709

Jackson, K. L., Lin, W. L., Miriyala, S., Dayton, R. D., Panchatcharam, M., McCarthy, K. J., Castanedes-Casey, M., Dickson, D. W., & Klein, R. L. (2017). p62 Pathology Model in the Rat Substantia Nigra with Filamentous Inclusions and Progressive Neurodegeneration. *PLoS One*, *12*(1), e0169291. https://doi.org/10.1371/journal.pone.0169291

Jahnke, R., Matthiesen, S., Zaeck, L. M., Finke, S., & Knittler, M. R. (2022). Chlamydia trachomatis Cell-to-Cell Spread through Tunneling Nanotubes. *Microbiol Spectr*, *10*(6), e0281722. https://doi.org/10.1128/spectrum.02817-22

Jelani, M., Dooley, H. C., Gubas, A., Mohamoud, H. S. A., Khan, M. T. M., Ali, Z., Kang, C., Rahim, F., Jan, A., Vadgama, N., Khan, M. I., Al-Aama, J. Y., Khan, A., Tooze, S. A., & Nasir, J. (2019). A mutation in the major autophagy gene, WIPI2, associated with global developmental abnormalities. *Brain*, *142*(5), 1242-1254. https://doi.org/10.1093/brain/awz075

Ji, C., Zhao, H., Chen, D., Zhang, H., & Zhao, Y. G. (2021). beta-propeller proteins WDR45 and WDR45B regulate autophagosome maturation into autolysosomes in neural cells. *Curr Biol*, *31*(8), 1666-1677 e1666. https://doi.org/10.1016/j.cub.2021.01.081

Ji, C., Zhao, H., Li, D., Sun, H., Hao, J., Chen, R., Wang, X., Zhang, H., & Zhao, Y. G. (2020). Role of Wdr45b in maintaining neural autophagy and cognitive function. *Autophagy*, *16*(4), 615-625.

Johansen, T., & Lamark, T. (2020). Selective Autophagy: ATG8 Family Proteins, LIR Motifs and Cargo Receptors. *J Mol Biol*, *432*(1), 80-103. https://doi.org/10.1016/j.jmb.2019.07.016

Kabeya, Y., Mizushima, N., Ueno, T., Yamamoto, A., Kirisako, T., Noda, T., Kominami, E., Ohsumi, Y., & Yoshimori, T. (2000). LC3, a mammalian homologue of yeast Apg8p, is localized in autophagosome membranes after processing. *EMBO J*, *19*(21), 5720-5728. https://doi.org/10.1093/emboj/19.21.5720

Kabeya, Y., Mizushima, N., Yamamoto, A., Oshitani-Okamoto, S., Ohsumi, Y., & Yoshimori, T. (2004). LC3, GABARAP and GATE16 localize to autophagosomal membrane depending on form-II formation. *J Cell Sci*, *117*(Pt 13), 2805-2812. https://doi.org/10.1242/jcs.01131

Karanasios, E., & Ktistakis, N. T. (2016). *Autophagy at the cell, tissue and organismal level*. Springer.

Karanasios, E., Stapleton, E., Manifava, M., Kaizuka, T., Mizushima, N., Walker, S. A., & Ktistakis, N. T. (2013). Dynamic association of the ULK1 complex with omegasomes during autophagy induction. *J Cell Sci*, *126*(Pt 22), 5224-5238. https://doi.org/10.1242/jcs.132415

Karsli-Uzunbas, G., Guo, J. Y., Price, S., Teng, X., Laddha, S. V., Khor, S., Kalaany, N. Y., Jacks, T., Chan, C. S., & Rabinowitz, J. D. (2014). Autophagy Is Required for Glucose Homeostasis and Lung Tumor MaintenanceAcute Autophagy Ablation Selectively Impairs NSCLC. *Cancer discovery*, *4*(8), 914-927.

Kast, D. J., & Dominguez, R. (2017). The Cytoskeleton-Autophagy Connection. *Curr Biol*, *27*(8), R318-R326. https://doi.org/10.1016/j.cub.2017.02.061

Kim, J., Kundu, M., Viollet, B., & Guan, K. L. (2011). AMPK and mTOR regulate autophagy through direct phosphorylation of Ulk1. *Nat Cell Biol*, *13*(2), 132-141. https://doi.org/10.1038/ncb2152

Kirisako, T., Ichimura, Y., Okada, H., Kabeya, Y., Mizushima, N., Yoshimori, T., Ohsumi, M., Takao, T., Noda, T., & Ohsumi, Y. (2000). The reversible modification regulates the membrane-binding state of Apg8/Aut7 essential for autophagy and the cytoplasm to vacuole targeting pathway. *J Cell Biol*, *151*(2), 263-276. https://doi.org/10.1083/jcb.151.2.263

Klionsky, D. J. (2005). The molecular machinery of autophagy: unanswered questions. *J Cell Sci*, *118*(Pt 1), 7-18. https://doi.org/10.1242/jcs.01620

Klionsky, D. J., Abdel-Aziz, A. K., Abdelfatah, S., Abdellatif, M., Abdoli, A., Abel, S., Abeliovich, H., Abildgaard, M. H., Abudu, Y. P., Acevedo-Arozena, A., Adamopoulos, I. E., Adeli, K., Adolph, T. E., Adornetto, A., Aflaki, E., Agam, G., Agarwal, A., Aggarwal, B. B., Agnello, M., . . . Tong, C. K. (2021). Guidelines for the use and interpretation of assays for monitoring autophagy (4th edition)(1). *Autophagy*, *17*(1), 1-382. https://doi.org/10.1080/15548627.2020.1797280

Klionsky, D. J., Cregg, J. M., Dunn, W. A., Jr., Emr, S. D., Sakai, Y., Sandoval, I. V., Sibirny, A., Subramani, S., Thumm, M., Veenhuis, M., & Ohsumi, Y. (2003). A unified nomenclature for yeast autophagy-related genes. *Dev Cell*, *5*(4), 539-545. https://doi.org/10.1016/s1534-5807(03)00296-x

Klionsky, D. J., Petroni, G., Amaravadi, R. K., Baehrecke, E. H., Ballabio, A., Boya, P., Bravo-San Pedro, J. M., Cadwell, K., Cecconi, F., Choi, A. M. K., Choi, M. E., Chu, C. T., Codogno, P., Colombo, M. I., Cuervo, A. M., Deretic, V., Dikic, I., Elazar, Z., Eskelinen, E. L., . . . Pietrocola, F. (2021). Autophagy in major human diseases. *EMBO J*, *40*(19), e108863. https://doi.org/10.15252/embj.2021108863

Komatsu, M., Waguri, S., Chiba, T., Murata, S., Iwata, J.-i., Tanida, I., Ueno, T., Koike, M., Uchiyama, Y., Kominami, E., & Tanaka, K. (2006). Loss of autophagy in the central nervous system causes neurodegeneration in mice. *Nature*, *441*(7095), 880-884. https://doi.org/10.1038/nature04723

Kretschmer, A., Zhang, F., Somasekharan, S. P., Tse, C., Leachman, L., Gleave, A., Li, B., Asmaro, I., Huang, T., Kotula, L., Sorensen, P. H., & Gleave, M. E. (2019). Stress-induced tunneling nanotubes support treatment adaptation in prostate cancer. *Sci Rep*, *9*(1), 7826. https://doi.org/10.1038/s41598-019-44346-5

Krick, R., Busse, R. A., Scacioc, A., Stephan, M., Janshoff, A., Thumm, M., & Kuhnel, K. (2012). Structural and functional characterization of the two phosphoinositide binding sites of PROPPINs, a beta-propeller protein family. *Proc Natl Acad Sci U S A*, *109*(30), E2042-2049. https://doi.org/10.1073/pnas.1205128109

Kuma, A., Mizushima, N., Ishihara, N., & Ohsumi, Y. (2002). Formation of the approximately 350-kDa Apg12-Apg5.Apg16 multimeric complex, mediated by Apg16 oligomerization, is essential for autophagy in yeast. *J Biol Chem*, *277*(21), 18619-18625. https://doi.org/10.1074/jbc.M111889200

Lee, N. K., Cho, S., & Kim, I. S. (2022). Ferritin - a multifaceted protein scaffold for biotherapeutics. *Exp Mol Med*, *54*(10), 1652-1657. https://doi.org/10.1038/s12276-022-00859-0

Lemasters, J. J. (2005). Selective mitochondrial autophagy, or mitophagy, as a targeted defense against oxidative stress, mitochondrial dysfunction, and aging. *Rejuvenation Res*, *8*(1), 3-5. https://doi.org/10.1089/rej.2005.8.3

Liang, X. H., Jackson, S., Seaman, M., Brown, K., Kempkes, B., Hibshoosh, H., & Levine, B. (1999). Induction of autophagy and inhibition of tumorigenesis by beclin 1. *Nature*, *402*(6762), 672-676. https://doi.org/10.1038/45257

Liu, D., Yang, Y., Liu, Q., & Wang, J. (2011). Inhibition of autophagy by 3-MA potentiates cisplatin-induced apoptosis in esophageal squamous cell carcinoma cells. *Med Oncol*, *28*(1), 105-111. https://doi.org/10.1007/s12032-009-9397-3

Liu, W., Shen, J., Li, Y., Wu, J., Luo, X., Yu, Y., Zhang, Y., Gu, L., Zhang, X., Jiang, C., & Li, J. (2021). Pyroptosis inhibition improves the symptom of acute myocardial infarction. *Cell Death Dis*, *12*(10), 852. https://doi.org/10.1038/s41419-021-04143-3

Ljubojevic, N., Henderson, J. M., & Zurzolo, C. (2021). The Ways of Actin: Why Tunneling Nanotubes Are Unique Cell Protrusions. *Trends Cell Biol*, *31*(2), 130-142. https://doi.org/10.1016/j.tcb.2020.11.008

Llovet, J. M., Kelley, R. K., Villanueva, A., Singal, A. G., Pikarsky, E., Roayaie, S., Lencioni, R., Koike, K., Zucman-Rossi, J., & Finn, R. S. (2021). Hepatocellular carcinoma. *Nat Rev Dis Primers*, *7*(1), 6. https://doi.org/10.1038/s41572-020-00240-3

Lorincz, P., & Juhasz, G. (2020). Autophagosome-Lysosome Fusion. *J Mol Biol*, *432*(8), 2462-2482. https://doi.org/10.1016/j.jmb.2019.10.028

Lou, E., Fujisawa, S., Morozov, A., Barlas, A., Romin, Y., Dogan, Y., Gholami, S., Moreira, A. L., Manova-Todorova, K., & Moore, M. A. (2012). Tunneling nanotubes provide a unique conduit for intercellular transfer of cellular contents in human malignant pleural mesothelioma. *PLoS One*, *7*(3), e33093. https://doi.org/10.1371/journal.pone.0033093

Ma, L., Chen, Z., Erdjument-Bromage, H., Tempst, P., & Pandolfi, P. P. (2005). Phosphorylation and functional inactivation of TSC2 by Erk implications for tuberous sclerosis and cancer pathogenesis. *Cell*, *121*(2), 179-193. https://doi.org/10.1016/j.cell.2005.02.031

Mancias, J. D., Pontano Vaites, L., Nissim, S., Biancur, D. E., Kim, A. J., Wang, X., Liu, Y., Goessling, W., Kimmelman, A. C., & Harper, J. W. (2015). Ferritinophagy via NCOA4 is required for erythropoiesis and is regulated by iron dependent HERC2-mediated proteolysis. *Elife*, *4*. https://doi.org/10.7554/eLife.10308

Mancias, J. D., Wang, X., Gygi, S. P., Harper, J. W., & Kimmelman, A. C. (2014). Quantitative proteomics identifies NCOA4 as the cargo receptor mediating ferritinophagy. *Nature*, *509*(7498), 105-109. https://doi.org/10.1038/nature13148

Manning, B. D. (2004). Balancing Akt with S6K: implications for both metabolic diseases and tumorigenesis. *J Cell Biol*, *167*(3), 399-403. https://doi.org/10.1083/jcb.200408161

Manzoni, C., Mamais, A., Dihanich, S., Abeti, R., Soutar, M. P. M., Plun-Favreau, H., Giunti, P., Tooze, S. A., Bandopadhyay, R., & Lewis, P. A. (2013). Inhibition of LRRK2 kinase activity stimulates macroautophagy. *Biochim Biophys Acta*, *1833*(12), 2900-2910. https://doi.org/10.1016/j.bbamcr.2013.07.020

Maroofian, R., Gubas, A., Kaiyrzhanov, R., Scala, M., Hundallah, K., Severino, M., Abdel-Hamid, M. S., Rosenfeld, J. A., Ebrahimi-Fakhari, D., Ali, Z., Rahim, F., Houlden, H., Tooze, S. A., Alsaleh, N. S., & Zaki, M. S. (2021). Homozygous missense WIPI2 variants cause a congenital disorder of autophagy with neurodevelopmental impairments of variable clinical severity and disease course. *Brain Commun*, *3*(3), fcab183. https://doi.org/10.1093/braincomms/fcab183

Massey, A. C., Zhang, C., & Cuervo, A. M. (2006). Chaperone-mediated autophagy in aging and disease. *Current topics in developmental biology*, *73*, 205-235.

Mauthe, M., Jacob, A., Freiberger, S., Hentschel, K., Stierhof, Y. D., Codogno, P., & Proikas-Cezanne, T. (2011). Resveratrol-mediated autophagy requires WIPI-1-regulated LC3 lipidation in the absence of induced phagophore formation. *Autophagy*, *7*(12), 1448-1461. https://doi.org/10.4161/auto.7.12.17802

McAlpine, F., Williamson, L. E., Tooze, S. A., & Chan, E. Y. (2013). Regulation of nutrient-sensitive autophagy by uncoordinated 51-like kinases 1 and 2. *Autophagy*, *9*(3), 361-373. https://doi.org/10.4161/auto.23066

Medina, D. L. (2021). Lysosomal calcium and autophagy. *Int Rev Cell Mol Biol*, *362*, 141-170. https://doi.org/10.1016/bs.ircmb.2021.03.002

Meijering, E., Dzyubachyk, O., & Smal, I. (2012). Methods for cell and particle tracking. *Methods Enzymol*, *504*, 183-200. https://doi.org/10.1016/B978-0-12-391857-4.00009-4

Mihaylova, M. M., & Shaw, R. J. (2011). The AMPK signalling pathway coordinates cell growth, autophagy and metabolism. *Nat Cell Biol*, *13*(9), 1016-1023. https://doi.org/10.1038/ncb2329

Mizushima, N., & Komatsu, M. (2011). Autophagy: renovation of cells and tissues. *Cell*, *147*(4), 728-741. https://doi.org/10.1016/j.cell.2011.10.026

Mizushima, N., Levine, B., Cuervo, A. M., & Klionsky, D. J. (2008). Autophagy fights disease through cellular self-digestion. *Nature*, *451*(7182), 1069-1075.

Mizushima, N., Noda, T., & Ohsumi, Y. (1999). Apg16p is required for the function of the Apg12p-Apg5p conjugate in the yeast autophagy pathway. *EMBO J*, *18*(14), 3888-3896. https://doi.org/10.1093/emboj/18.14.3888

Mizushima, N., Noda, T., Yoshimori, T., Tanaka, Y., Ishii, T., George, M. D., Klionsky, D. J., Ohsumi, M., & Ohsumi, Y. (1998). A protein conjugation system essential for autophagy. *Nature*, *395*(6700), 395-398. https://doi.org/10.1038/26506

Mukaiyama, H., Oku, M., Baba, M., Samizo, T., Hammond, A. T., Glick, B. S., Kato, N., & Sakai, Y. (2002). Paz2 and 13 other PAZ gene products regulate vacuolar engulfment of peroxisomes during micropexophagy. *Genes Cells*, *7*(1), 75-90. https://doi.org/10.1046/j.1356-9597.2001.00499.x

Najmabadi, H., Hu, H., Garshasbi, M., Zemojtel, T., Abedini, S. S., Chen, W., Hosseini, M., Behjati, F., Haas, S., & Jamali, P. (2011). Deep sequencing reveals 50 novel genes for recessive cognitive disorders. *Nature*, *478*(7367), 57-63.

Nawaz, M., & Fatima, F. (2017). Extracellular Vesicles, Tunneling Nanotubes, and Cellular Interplay: Synergies and Missing Links. *Front Mol Biosci*, *4*, 50. https://doi.org/10.3389/fmolb.2017.00050

Noda, M., Ito, H., & Nagata, K. I. (2021). Physiological significance of WDR45, a responsible gene for beta-propeller protein associated neurodegeneration (BPAN), in brain development. *Sci Rep*, *11*(1), 22568. https://doi.org/10.1038/s41598-021-02123-3

Nunnari, J., & Suomalainen, A. (2012). Mitochondria: in sickness and in health. *Cell*, *148*(6), 1145-1159. https://doi.org/10.1016/j.cell.2012.02.035

Oakhill, J. S., Steel, R., Chen, Z. P., Scott, J. W., Ling, N., Tam, S., & Kemp, B. E. (2011). AMPK is a direct adenylate charge-regulated protein kinase. *Science*, *332*(6036), 1433-1435. https://doi.org/10.1126/science.1200094

Ogawa, M., Yoshikawa, Y., Kobayashi, T., Mimuro, H., Fukumatsu, M., Kiga, K., Piao, Z., Ashida, H., Yoshida, M., Kakuta, S., Koyama, T., Goto, Y., Nagatake, T., Nagai, S., Kiyono, H., Kawalec, M., Reichhart, J. M., & Sasakawa, C. (2011). A Tecpr1-dependent selective autophagy pathway targets bacterial pathogens. *Cell Host Microbe*, *9*(5), 376-389. https://doi.org/10.1016/j.chom.2011.04.010

Onfelt, B., Nedvetzki, S., Benninger, R. K., Purbhoo, M. A., Sowinski, S., Hume, A. N., Seabra, M. C., Neil, M. A., French, P. M., & Davis, D. M. (2006). Structurally distinct membrane nanotubes between human macrophages support long-distance vesicular traffic or surfing of bacteria. *J Immunol*, *177*(12), 8476-8483. https://doi.org/10.4049/jimmunol.177.12.8476

Osawa, T., Kotani, T., Kawaoka, T., Hirata, E., Suzuki, K., Nakatogawa, H., Ohsumi, Y., & Noda, N. N. (2019). Atg2 mediates direct lipid transfer between membranes for autophagosome formation. *Nat Struct Mol Biol*, *26*(4), 281-288. https://doi.org/10.1038/s41594-019-0203-4

Osmani, A. H., Osmani, S. A., & Morris, N. R. (1990). The molecular cloning and identification of a gene product specifically required for nuclear movement in Aspergillus nidulans. *J Cell Biol*, *111*(2), 543-551. https://doi.org/10.1083/jcb.111.2.543

Osswald, M., Jung, E., Sahm, F., Solecki, G., Venkataramani, V., Blaes, J., Weil, S., Horstmann, H., Wiestler, B., Syed, M., Huang, L., Ratliff, M., Karimian Jazi, K., Kurz, F. T., Schmenger, T., Lemke, D., Gommel, M., Pauli, M., Liao, Y., . . . Winkler, F. (2015). Brain tumour cells interconnect to a functional and resistant network. *Nature*, *528*(7580), 93-98. https://doi.org/10.1038/nature16071

Palikaras, K., Lionaki, E., & Tavernarakis, N. (2018). Mechanisms of mitophagy in cellular homeostasis, physiology and pathology. *Nat Cell Biol*, *20*(9), 1013-1022. https://doi.org/10.1038/s41556-018-0176-2

Panasiuk, M., Rychlowski, M., Derewonko, N., & Bienkowska-Szewczyk, K. (2018). Tunneling Nanotubes as a Novel Route of Cell-to-Cell Spread of Herpesviruses. *J Virol*, *92*(10). https://doi.org/10.1128/JVI.00090-18

Pande, S., Shitut, S., Freund, L., Westermann, M., Bertels, F., Colesie, C., Bischofs, I. B., & Kost, C. (2015). Metabolic cross-feeding via intercellular nanotubes among bacteria. *Nat Commun*, *6*, 6238. https://doi.org/10.1038/ncomms7238

Pantopoulos, K., Porwal, S. K., Tartakoff, A., & Devireddy, L. (2012). Mechanisms of mammalian iron homeostasis. *Biochemistry*, *51*(29), 5705-5724. https://doi.org/10.1021/bi300752r

Pasquier, J., Guerrouahen, B. S., Al Thawadi, H., Ghiabi, P., Maleki, M., Abu-Kaoud, N., Jacob, A., Mirshahi, M., Galas, L., Rafii, S., Le Foll, F., & Rafii, A. (2013). Preferential transfer of mitochondria from endothelial to cancer cells through tunneling nanotubes modulates chemoresistance. *J Transl Med*, *11*, 94. https://doi.org/10.1186/1479-5876-11-94

Pepe, A., Pietropaoli, S., Vos, M., Barba-Spaeth, G., & Zurzolo, C. (2022). Tunneling nanotubes provide a route for SARS-CoV-2 spreading. *Sci Adv*, *8*(29), eabo0171. https://doi.org/10.1126/sciadv.abo0171

Pfisterer, S. G., Bakula, D., Frickey, T., Cezanne, A., Brigger, D., Tschan, M. P., Robenek, H., & Proikas-Cezanne, T. (2014). Lipid droplet and early autophagosomal membrane targeting of Atg2A and Atg14L in human tumor cells. *J Lipid Res*, *55*(7), 1267-1278. https://doi.org/10.1194/jlr.M046359

Pfisterer, S. G., Mauthe, M., Codogno, P., & Proikas-Cezanne, T. (2011). Ca2+/calmodulin-dependent kinase (CaMK) signaling via CaMKI and AMP-activated protein kinase contributes to the regulation of WIPI-1 at the onset of autophagy. *Mol Pharmacol*, *80*(6), 1066-1075. https://doi.org/10.1124/mol.111.071761

Pickrell, A. M., Huang, C. H., Kennedy, S. R., Ordureau, A., Sideris, D. P., Hoekstra, J. G., Harper, J. W., & Youle, R. J. (2015). Endogenous Parkin Preserves Dopaminergic Substantia Nigral Neurons following Mitochondrial DNA Mutagenic Stress. *Neuron*, *87*(2), 371-381. https://doi.org/10.1016/j.neuron.2015.06.034

Pinto, G., Saenz-de-Santa-Maria, I., Chastagner, P., Perthame, E., Delmas, C., Toulas, C., Moyal-Jonathan-Cohen, E., Brou, C., & Zurzolo, C. (2021). Patient-derived glioblastoma stem cells transfer mitochondria through tunneling nanotubes in tumor organoids. *Biochem J*, *478*(1), 21-39. https://doi.org/10.1042/BCJ20200710

Polson, H. E., de Lartigue, J., Rigden, D. J., Reedijk, M., Urbe, S., Clague, M. J., & Tooze, S. A. (2010). Mammalian Atg18 (WIPI2) localizes to omegasome-anchored phagophores and positively regulates LC3 lipidation. *Autophagy*, *6*(4), 506-522. https://doi.org/10.4161/auto.6.4.11863

Ponten, F., Jirstrom, K., & Uhlen, M. (2008). The Human Protein Atlas--a tool for pathology. *J Pathol*, *216*(4), 387-393. https://doi.org/10.1002/path.2440

Poole, L. P., & Macleod, K. F. (2021). Mitophagy in tumorigenesis and metastasis. *Cell Mol Life Sci*, *78*(8), 3817-3851. https://doi.org/10.1007/s00018-021-03774-1

Proikas-Cezanne, T., & Robenek, H. (2011). Freeze-fracture replica immunolabelling reveals human WIPI-1 and WIPI-2 as membrane proteins of autophagosomes. *J Cell Mol Med*, *15*(9), 2007-2010. https://doi.org/10.1111/j.1582-4934.2011.01339.x

Proikas-Cezanne, T., Ruckerbauer, S., Stierhof, Y. D., Berg, C., & Nordheim, A. (2007). Human WIPI-1 puncta-formation: a novel assay to assess mammalian autophagy. *FEBS Lett*, *581*(18), 3396-3404. https://doi.org/10.1016/j.febslet.2007.06.040

Proikas-Cezanne, T., Takacs, Z., Donnes, P., & Kohlbacher, O. (2015). WIPI proteins: essential PtdIns3P effectors at the nascent autophagosome. *J Cell Sci*, *128*(2), 207-217. https://doi.org/10.1242/jcs.146258

Proikas-Cezanne, T., Waddell, S., Gaugel, A., Frickey, T., Lupas, A., & Nordheim, A. (2004). WIPI-1α (WIPI49), a member of the novel 7-bladed WIPI protein family, is aberrantly expressed in human cancer and is linked to starvation-induced autophagy. *Oncogene*, *23*(58), 9314-9325.

Reid, S. E., Kolapalli, S. P., Nielsen, T. M., & Frankel, L. B. (2022). Canonical and non-canonical roles for ATG8 proteins in autophagy and beyond. *Front Mol Biosci*, *9*, 1074701. https://doi.org/10.3389/fmolb.2022.1074701

Ren, J., Liang, R., Wang, W., Zhang, D., Yu, L., & Feng, W. (2020). Multi-site-mediated entwining of the linear WIR-motif around WIPI beta-propellers for autophagy. *Nat Commun*, *11*(1), 2702. https://doi.org/10.1038/s41467-020-16523-y

Riera, J., & Lazo, P. S. (2009). The mammalian NudC-like genes: a family with functions other than regulating nuclear distribution. *Cell Mol Life Sci*, *66*(14), 2383-2390. https://doi.org/10.1007/s00018-009-0025-3

Roehlecke, C., & Schmidt, M. H. H. (2020). Tunneling Nanotubes and Tumor Microtubes in Cancer. *Cancers (Basel)*, *12*(4). https://doi.org/10.3390/cancers12040857

Rohrer, J., Joo, M., Dartyge, E., Sayers, D. E., Fontaine, A., & Theil, E. (1987). Stabilization of iron in a ferrous form by ferritin. A study using dispersive and conventional x-ray absorption spectroscopy. *Journal of Biological Chemistry*, *262*(28), 13385-13387.

Roskams, T. (2008). Relationships among stellate cell activation, progenitor cells, and hepatic regeneration. *Clin Liver Dis*, *12*(4), 853-860, ix. https://doi.org/10.1016/j.cld.2008.07.014

Ross, F. A., Hawley, S. A., Auciello, F. R., Gowans, G. J., Atrih, A., Lamont, D. J., & Hardie, D. G. (2017). Mechanisms of Paradoxical Activation of AMPK by the Kinase Inhibitors SU6656 and Sorafenib. *Cell Chem Biol*, *24*(7), 813-824 e814. https://doi.org/10.1016/j.chembiol.2017.05.021

Rupp, I., Sologub, L., Williamson, K. C., Scheuermayer, M., Reininger, L., Doerig, C., Eksi, S., Kombila, D. U., Frank, M., & Pradel, G. (2011). Malaria parasites form filamentous cell-to-cell connections during reproduction in the mosquito midgut. *Cell Res*, *21*(4), 683-696. https://doi.org/10.1038/cr.2010.176

Rustom, A. (2016). The missing link: does tunnelling nanotube-based supercellularity provide a new understanding of chronic and lifestyle diseases? *Open Biol*, *6*(6). https://doi.org/10.1098/rsob.160057

Rustom, A., Saffrich, R., Markovic, I., Walther, P., & Gerdes, H. H. (2004). Nanotubular highways for intercellular organelle transport. *Science*, *303*(5660), 1007-1010. https://doi.org/10.1126/science.1093133

Saha, T., Dash, C., Jayabalan, R., Khiste, S., Kulkarni, A., Kurmi, K., Mondal, J., Majumder, P. K., Bardia, A., Jang, H. L., & Sengupta, S. (2022). Intercellular nanotubes mediate mitochondrial trafficking between cancer and immune cells. *Nat Nanotechnol*, *17*(1), 98-106. https://doi.org/10.1038/s41565-021-01000-4

Saitsu, H., Nishimura, T., Muramatsu, K., Kodera, H., Kumada, S., Sugai, K., Kasai-Yoshida, E., Sawaura, N., Nishida, H., Hoshino, A., Ryujin, F., Yoshioka, S., Nishiyama, K., Kondo, Y., Tsurusaki, Y., Nakashima, M., Miyake, N., Arakawa, H., Kato, M., . . . Matsumoto, N. (2013). De novo mutations in the autophagy gene WDR45 cause static encephalopathy of childhood with neurodegeneration in adulthood. *Nat Genet*, *45*(4), 445-449, 449e441. https://doi.org/10.1038/ng.2562

Sakai, Y., Koller, A., Rangell, L. K., Keller, G. A., & Subramani, S. (1998). Peroxisome degradation by microautophagy in Pichia pastoris: identification of specific steps and morphological intermediates. *J Cell Biol*, *141*(3), 625-636. https://doi.org/10.1083/jcb.141.3.625

Salvador, G. A. (2010). Iron in neuronal function and dysfunction. *Biofactors*, *36*(2), 103-110. https://doi.org/10.1002/biof.80

Sartori-Rupp, A., Cordero Cervantes, D., Pepe, A., Gousset, K., Delage, E., Corroyer-Dulmont, S., Schmitt, C., Krijnse-Locker, J., & Zurzolo, C. (2019). Correlative cryo-electron microscopy reveals the structure of TNTs in neuronal cells. *Nat Commun*, *10*(1), 342. https://doi.org/10.1038/s41467-018-08178-7

Scheiblich, H., Dansokho, C., Mercan, D., Schmidt, S. V., Bousset, L., Wischhof, L., Eikens, F., Odainic, A., Spitzer, J., Griep, A., Schwartz, S., Bano, D., Latz, E., Melki, R., & Heneka, M. T. (2021). Microglia jointly degrade fibrillar alpha-synuclein cargo by distribution through tunneling nanotubes. *Cell*, *184*(20), 5089-5106 e5021. https://doi.org/10.1016/j.cell.2021.09.007

Schussele, D. S., Haller, P. K., Haas, M. L., Hunter, C., Sporbeck, K., & Proikas-Cezanne, T. (2022). Autophagy profiling in single cells with open source CellProfiler-based image analysis. *Autophagy*, 1-14. https://doi.org/10.1080/15548627.2022.2065617

Shimizu, S., Takehara, T., Hikita, H., Kodama, T., Tsunematsu, H., Miyagi, T., Hosui, A., Ishida, H., Tatsumi, T., Kanto, T., Hiramatsu, N., Fujita, N., Yoshimori, T., & Hayashi, N. (2012). Inhibition of autophagy potentiates the antitumor effect of the multikinase inhibitor sorafenib in hepatocellular carcinoma. *Int J Cancer*, *131*(3), 548-557. https://doi.org/10.1002/ijc.26374

Sia, D., Villanueva, A., Friedman, S. L., & Llovet, J. M. (2017). Liver Cancer Cell of Origin, Molecular Class, and Effects on Patient Prognosis. *Gastroenterology*, *152*(4), 745-761. https://doi.org/10.1053/j.gastro.2016.11.048

Sowinski, S., Jolly, C., Berninghausen, O., Purbhoo, M. A., Chauveau, A., Kohler, K., Oddos, S., Eissmann, P., Brodsky, F. M., Hopkins, C., Onfelt, B., Sattentau, Q., & Davis, D. M. (2008). Membrane nanotubes physically connect T cells over long distances presenting a novel route for HIV-1 transmission. *Nat Cell Biol*, *10*(2), 211-219. https://doi.org/10.1038/ncb1682

Sporbeck, K., Haas, M. L., Pastor-Maldonado, C. J., Schussele, D. S., Hunter, C., Takacs, Z., Diogo de Oliveira, A. L., Franz-Wachtel, M., Charsou, C., Pfisterer, S. G., Gubas, A., Haller, P. K., Knorr, R. L., Kaulich, M., Macek, B., Eskelinen, E. L., Simonsen, A., & Proikas-Cezanne, T. (2023). The ABL-MYC axis controls WIPI1-enhanced autophagy in lifespan extension. *Commun Biol*, *6*(1), 872. https://doi.org/10.1038/s42003-023-05236-9

Squair, J. W., Gautier, M., Kathe, C., Anderson, M. A., James, N. D., Hutson, T. H., Hudelle, R., Qaiser, T., Matson, K. J. E., Barraud, Q., Levine, A. J., La Manno, G., Skinnider, M. A., & Courtine, G. (2021). Confronting false discoveries in single-cell differential expression. *Nat Commun*, *12*(1), 5692. https://doi.org/10.1038/s41467-021-25960-2

Stavoe, A. K., Gopal, P. P., Gubas, A., Tooze, S. A., & Holzbaur, E. L. (2019). Expression of WIPI2B counteracts age-related decline in autophagosome biogenesis in neurons. *Elife*, *8*. https://doi.org/10.7554/eLife.44219

Stein, S. C., Woods, A., Jones, N. A., Davison, M. D., & Carling, D. (2000). The regulation of AMP-activated protein kinase by phosphorylation. *Biochem J*, *345 Pt 3*(Pt 3), 437-443. https://www.ncbi.nlm.nih.gov/pubmed/10642499

Stonebloom, S., Brunkard, J. O., Cheung, A. C., Jiang, K., Feldman, L., & Zambryski, P. (2012). Redox states of plastids and mitochondria differentially regulate intercellular transport via plasmodesmata. *Plant Physiol*, *158*(1), 190-199. https://doi.org/10.1104/pp.111.186130

Stotland, A., & Gottlieb, R. A. (2015). Mitochondrial quality control: Easy come, easy go. *Biochim Biophys Acta*, *1853*(10 Pt B), 2802-2811. https://doi.org/10.1016/j.bbamcr.2014.12.041

Strong, L. M., Chang, C., Riley, J. F., Boecker, C. A., Flower, T. G., Buffalo, C. Z., Ren, X., Stavoe, A. K., Holzbaur, E. L., & Hurley, J. H. (2021). Structural basis for membrane recruitment of ATG16L1 by WIPI2 in autophagy. *Elife*, *10*. https://doi.org/10.7554/eLife.70372

Suleiman, J., Allingham-Hawkins, D., Hashem, M., Shamseldin, H. E., Alkuraya, F. S., & El-Hattab, A. W. (2018). WDR45B-related intellectual disability, spastic quadriplegia, epilepsy, and cerebral hypoplasia: A consistent neurodevelopmental syndrome. *Clin Genet*, *93*(2), 360-364. https://doi.org/10.1111/cge.13054

Sun, Y., Shen, W., Hu, S., Lyu, Q., Wang, Q., Wei, T., Zhu, W., & Zhang, J. (2023). METTL3 promotes chemoresistance in small cell lung cancer by inducing mitophagy. *J Exp Clin Cancer Res*, *42*(1), 65. https://doi.org/10.1186/s13046-023-02638-9

Suter, M., Riek, U., Tuerk, R., Schlattner, U., Wallimann, T., & Neumann, D. (2006). Dissecting the role of 5'-AMP for allosteric stimulation, activation, and deactivation of AMP-activated protein kinase. *J Biol Chem*, *281*(43), 32207-32216. https://doi.org/10.1074/jbc.M606357200

Suzuki, S. O., McKenney, R. J., Mawatari, S. Y., Mizuguchi, M., Mikami, A., Iwaki, T., Goldman, J. E., Canoll, P., & Vallee, R. B. (2007). Expression patterns of LIS1, dynein and their interaction partners dynactin, NudE, NudEL and NudC in human gliomas suggest roles in invasion and proliferation. *Acta Neuropathol*, *113*(5), 591-599. https://doi.org/10.1007/s00401-006-0180-7

Sweeney, H. L., & Holzbaur, E. L. F. (2018). Motor Proteins. *Cold Spring Harb Perspect Biol*, *10*(5). https://doi.org/10.1101/cshperspect.a021931

Thost, A. K., Donnes, P., Kohlbacher, O., & Proikas-Cezanne, T. (2015). Fluorescence-based imaging of autophagy progression by human WIPI protein detection. *Methods*, *75*, 69-78. https://doi.org/10.1016/j.ymeth.2014.11.011

Thumm, M., Egner, R., Koch, B., Schlumpberger, M., Straub, M., Veenhuis, M., & Wolf, D. H. (1994). Isolation of autophagocytosis mutants of Saccharomyces cerevisiae. *FEBS Lett*, *349*(2), 275-280. https://doi.org/10.1016/0014-5793(94)00672-5

Titorenko, V. I., Keizer, I., Harder, W., & Veenhuis, M. (1995). Isolation and characterization of mutants impaired in the selective degradation of peroxisomes in the yeast Hansenula polymorpha. *J Bacteriol*, *177*(2), 357-363. https://doi.org/10.1128/jb.177.2.357-363.1995

Trivedi, P., Wang, S., & Friedman, S. L. (2021). The Power of Plasticity-Metabolic Regulation of Hepatic Stellate Cells. *Cell Metab*, *33*(2), 242-257. https://doi.org/10.1016/j.cmet.2020.10.026

Tsukada, M., & Ohsumi, Y. (1993). Isolation and characterization of autophagy-defective mutants of Saccharomyces cerevisiae. *FEBS Lett*, *333*(1-2), 169-174. https://doi.org/10.1016/0014-5793(93)80398-e

Ullen, A., Farnebo, M., Thyrell, L., Mahmoudi, S., Kharaziha, P., Lennartsson, L., Grander, D., Panaretakis, T., & Nilsson, S. (2010). Sorafenib induces apoptosis and autophagy in prostate cancer cells in vitro. *Int J Oncol*, *37*(1), 15-20. https://doi.org/10.3892/ijo_00000648

Uttara, B., Singh, A. V., Zamboni, P., & Mahajan, R. T. (2009). Oxidative stress and neurodegenerative diseases: a review of upstream and downstream antioxidant therapeutic options. *Curr Neuropharmacol*, *7*(1), 65-74. https://doi.org/10.2174/157015909787602823

Valverde, D. P., Yu, S., Boggavarapu, V., Kumar, N., Lees, J. A., Walz, T., Reinisch, K. M., & Melia, T. J. (2019). ATG2 transports lipids to promote autophagosome biogenesis. *J Cell Biol*, *218*(6), 1787-1798. https://doi.org/10.1083/jcb.201811139

Vargas, J. Y., Loria, F., Wu, Y. J., Cordova, G., Nonaka, T., Bellow, S., Syan, S., Hasegawa, M., van Woerden, G. M., Trollet, C., & Zurzolo, C. (2019). The Wnt/Ca(2+) pathway is involved in interneuronal communication mediated by tunneling nanotubes. *EMBO J*, *38*(23), e101230. https://doi.org/10.15252/embj.2018101230

Vergne, I., Roberts, E., Elmaoued, R. A., Tosch, V., Delgado, M. A., Proikas-Cezanne, T., Laporte, J., & Deretic, V. (2009). Control of autophagy initiation by phosphoinositide 3-phosphatase Jumpy. *EMBO J*, *28*(15), 2244-2258. https://doi.org/10.1038/emboj.2009.159

Victoria, G. S., & Zurzolo, C. (2017). The spread of prion-like proteins by lysosomes and tunneling nanotubes: Implications for neurodegenerative diseases. *J Cell Biol*, *216*(9), 2633-2644. https://doi.org/10.1083/jcb.201701047

Waddell, S., Jenkins, J. R., & Proikas-Cezanne, T. (2001). A "no-hybrids" screen for functional antagonizers of human p53 transactivator function: dominant negativity in fission yeast. *Oncogene*, *20*(42), 6001-6008. https://doi.org/10.1038/sj.onc.1204702

Walker, S., Chandra, P., Manifava, M., Axe, E., & Ktistakis, N. T. (2008). Making autophagosomes: localized synthesis of phosphatidylinositol 3-phosphate holds the clue. *Autophagy*, *4*(8), 1093-1096. https://doi.org/10.4161/auto.7141

Wang, L., Ren, A., Tian, T., Li, N., Cao, X., Zhang, P., Jin, L., Li, Z., Shen, Y., Zhang, B., Finnell, R. H., & Lei, Y. (2019). Whole-Exome Sequencing Identifies Damaging de novo Variants in Anencephalic Cases. *Front Neurosci*, *13*, 1285. https://doi.org/10.3389/fnins.2019.01285

Wang, X., & Gerdes, H. H. (2012). Long-distance electrical coupling via tunneling nanotubes. *Biochim Biophys Acta*, *1818*(8), 2082-2086. https://doi.org/10.1016/j.bbamem.2011.09.002

Wang, Y., Cui, J., Sun, X., & Zhang, Y. (2011). Tunneling-nanotube development in astrocytes depends on p53 activation. *Cell Death Differ*, *18*(4), 732-742. https://doi.org/10.1038/cdd.2010.147

Woods, A., Johnstone, S. R., Dickerson, K., Leiper, F. C., Fryer, L. G., Neumann, D., Schlattner, U., Wallimann, T., Carlson, M., & Carling, D. (2003). LKB1 is the upstream kinase in the AMP-activated protein kinase cascade. *Curr Biol*, *13*(22), 2004-2008. https://doi.org/10.1016/j.cub.2003.10.031

Wu, J. W., Herman, M., Liu, L., Simoes, S., Acker, C. M., Figueroa, H., Steinberg, J. I., Margittai, M., Kayed, R., Zurzolo, C., Di Paolo, G., & Duff, K. E. (2013). Small misfolded Tau species are internalized via bulk endocytosis and anterogradely and retrogradely transported in neurons. *J Biol Chem*, *288*(3), 1856-1870. https://doi.org/10.1074/jbc.M112.394528

Wullschleger, S., Loewith, R., & Hall, M. N. (2006). TOR signaling in growth and metabolism. *Cell*, *124*(3), 471-484.

Xiao, B., Sanders, M. J., Underwood, E., Heath, R., Mayer, F. V., Carmena, D., Jing, C., Walker, P. A., Eccleston, J. F., Haire, L. F., Saiu, P., Howell, S. A., Aasland, R., Martin, S. R., Carling, D., & Gamblin, S. J. (2011). Structure of mammalian AMPK and its regulation by ADP. *Nature*, *472*(7342), 230-233. https://doi.org/10.1038/nature09932

Xiao, F. H., Chen, X. Q., Yu, Q., Ye, Y., Liu, Y. W., Yan, D., Yang, L. Q., Chen, G., Lin, R., Yang, L., Liao, X., Zhang, W., Zhang, W., Tang, N. L., Wang, X. F., Zhou, J., Cai, W. W., He, Y. H., & Kong, Q. P. (2018). Transcriptome evidence reveals enhanced autophagy-lysosomal function in centenarians. *Genome Res*, *28*(11), 1601-1610. https://doi.org/10.1101/gr.220780.117

Yuan, W., Tuttle, D. L., Shi, Y. J., Ralph, G. S., & Dunn, W. A., Jr. (1997). Glucose-induced microautophagy in Pichia pastoris requires the alpha-subunit of phosphofructokinase. *J Cell Sci*, *110 (Pt 16)*, 1935-1945. https://doi.org/10.1242/jcs.110.16.1935

Zhai, B., Hu, F., Jiang, X., Xu, J., Zhao, D., Liu, B., Pan, S., Dong, X., Tan, G., Wei, Z., Qiao, H., Jiang, H., & Sun, X. (2014). Inhibition of Akt reverses the acquired resistance to sorafenib by switching protective autophagy to autophagic cell death in hepatocellular carcinoma. *Mol Cancer Ther*, *13*(6), 1589-1598. https://doi.org/10.1158/1535-7163.MCT-13-1043

Zhang, C. (2014). Essential functions of iron-requiring proteins in DNA replication, repair and cell cycle control. *Protein Cell*, *5*(10), 750-760. https://doi.org/10.1007/s13238-014-0083-7

Zhang, C., Zhang, W., Lu, Y., Yan, X., Yan, X., Zhu, X., Liu, W., Yang, Y., & Zhou, T. (2016). NudC regulates actin dynamics and ciliogenesis by stabilizing cofilin 1. *Cell Res*, *26*(2), 239-253. https://doi.org/10.1038/cr.2015.152

Zheng, J. X., Li, Y., Ding, Y. H., Liu, J. J., Zhang, M. J., Dong, M. Q., Wang, H. W., & Yu, L. (2017). Architecture of the ATG2B-WDR45 complex and an aromatic Y/HF motif crucial for complex formation. *Autophagy*, *13*(11), 1870-1883. https://doi.org/10.1080/15548627.2017.1359381

Zhou, C., Wu, Z., Du, W., Que, H., Wang, Y., Ouyang, Q., Jian, F., Yuan, W., Zhao, Y., Tian, R., Li, Y., Chen, Y., Gao, S., Wong, C. C. L., & Rong, Y. (2022). Recycling of autophagosomal components from autolysosomes by the recycler complex. *Nat Cell Biol*, *24*(4), 497-512. https://doi.org/10.1038/s41556-022-00861-8

Zhou, T., Aumais, J. P., Liu, X., Yu-Lee, L. Y., & Erikson, R. L. (2003). A role for Plk1 phosphorylation of NudC in cytokinesis. *Dev Cell*, *5*(1), 127-138. https://doi.org/10.1016/s1534-5807(03)00186-2

Zhu, D., Tan, K. S., Zhang, X., Sun, A. Y., Sun, G. Y., & Lee, J. C.-M. (2005). Hydrogen peroxide alters membrane and cytoskeleton properties and increases intercellular connections in astrocytes. *Journal of Cell Science*, *118*(16), 3695-3703.

Zurzolo, C. (2021). Tunneling nanotubes: Reshaping connectivity. *Curr Opin Cell Biol*, *71*, 139-147. https://doi.org/10.1016/j.ceb.2021.03.003

Supplements

The following supplement section contains complementary material to the data presented in this thesis, such as supplementary figures, uncropped images of Western Blot membranes and tables with raw data of manual quantifications of cells and TNTs. Finally, the last part of this supplement section consists of the manuscript “The ABL-MYC axis controls WIPI1-enhanced autophagy in lifespan extension” (Sporbeck et al., 2023), from which part of the data was included in this thesis.

Each supplementary figure or table has been labelled according to the Figure and/or data set it corresponds to.

Supplementary figures

Supplementary tables

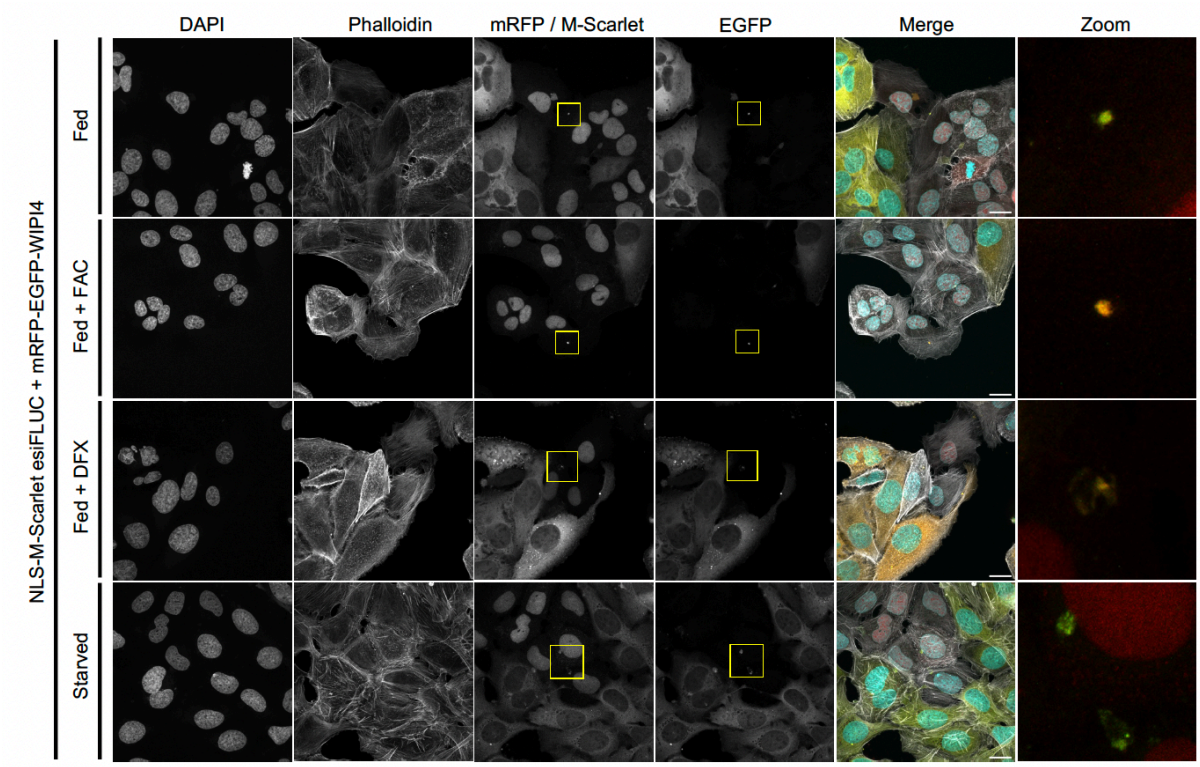

Supplementary Figure 1, referring to Figure 16. U2OS NLS-mScarlet cells reverse transfected with esiFLUC and co-cultured with U2OS mRFP-EGFP-WIPI4. In addition, cells were treated with DMEM + 10% FCS, DMEM + 10% FCS + FAC, DMEM + 10% FCS + DFX or EBSS for 24 hours and stained with DAPI and Phalloidin. Zoom in sections show mRFP-EGFP-WIPI4 puncta inside of U2OS NLS-mScarlet cells. Scale bars: 20µm.

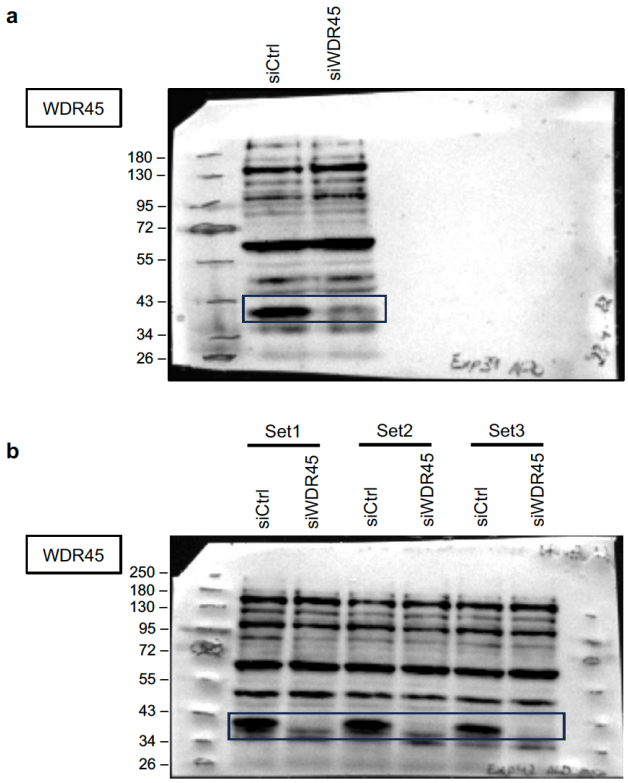

Supplementary Figure 2, referring to Figure 16. Uncropped original images of Western Blot membranes confirming the downregulation of WDR45.

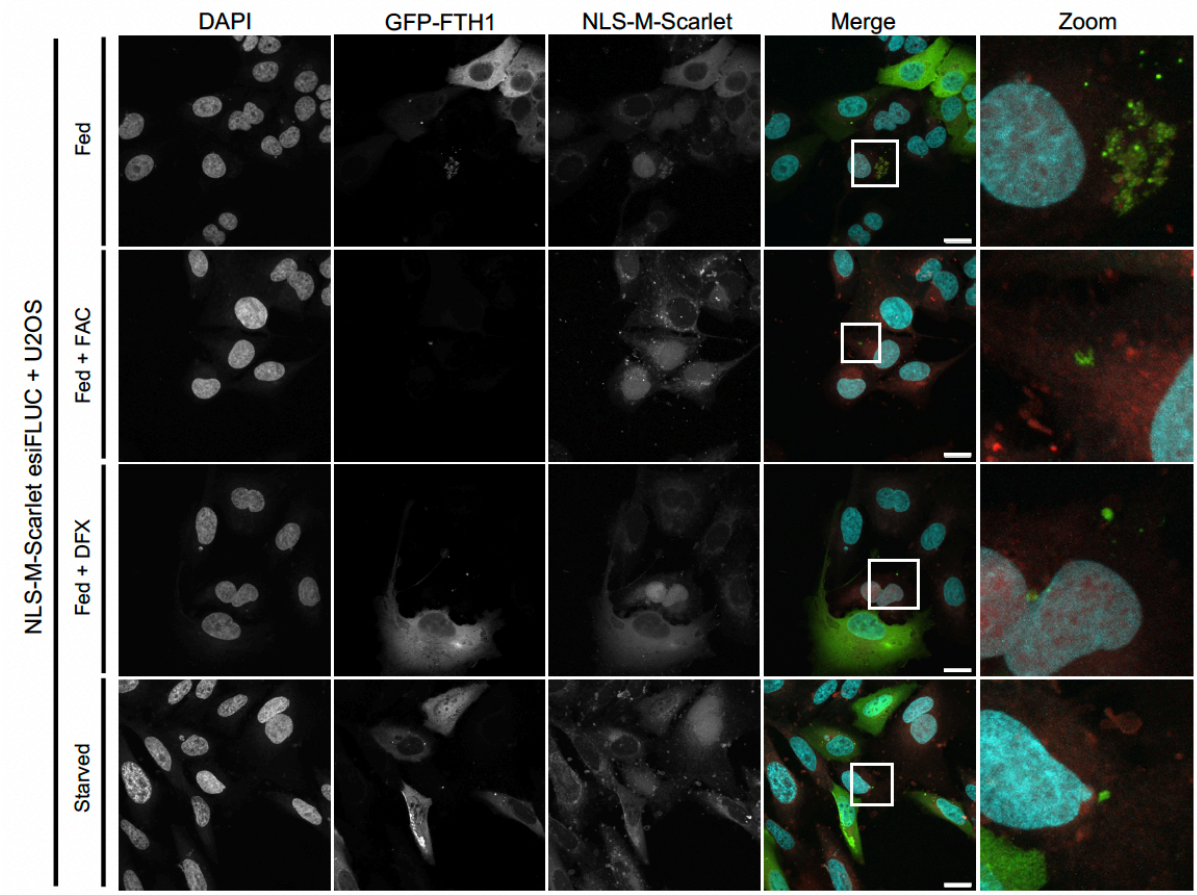

Supplementary Figure 3, referring to Figure 28. U2OS cells reverse transfected with esiFLUC and co-transfected with GFP or GFP-FTH1. Then, co-cultured with U2OS NLS-mScarlet. In addition, cells were treated with DMEM + 10% FCS, DMEM + 10% FCS + FAC, DMEM + 10% FCS + DFX or EBSS for 24 hours and stained with DAPI. Zoom in sections show GFP-FTH1 puncta inside of U2OS NLS-mScarlet cells. Scale bars: 20µm.

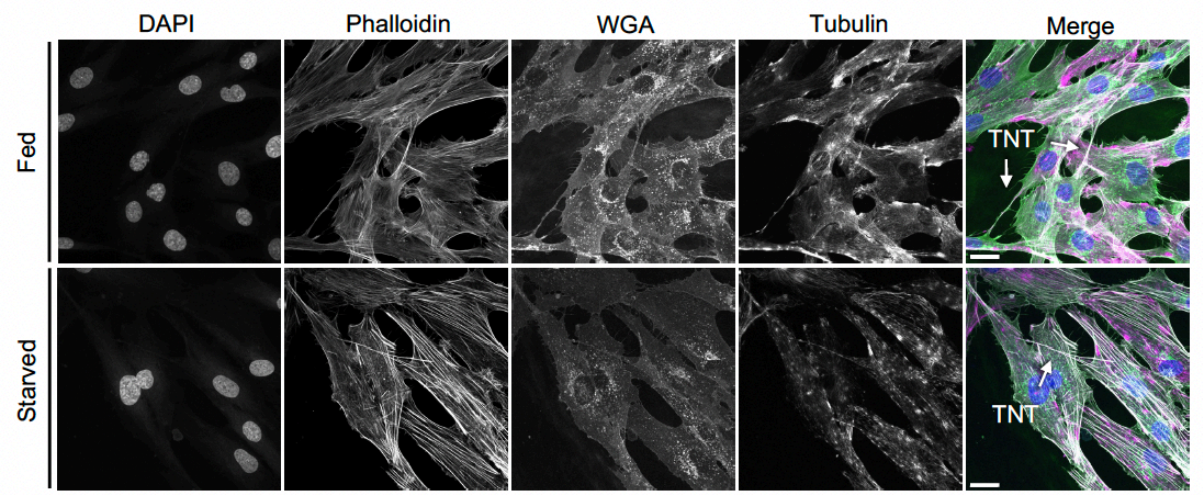

Supplementary Figure 4, Fibroblasts form TNTs. Fibroblasts were cultured in DMEM + 10% FCS, DMEM + 10% FCS + FAC, DMEM + 10% FCS + DFX or EBSS for 24 hours and stained with DAPI. Zoom in sections show GFP-FTH1 puncta inside of U2OS NLS-mScarlet cells. Scale bars: 20µm.

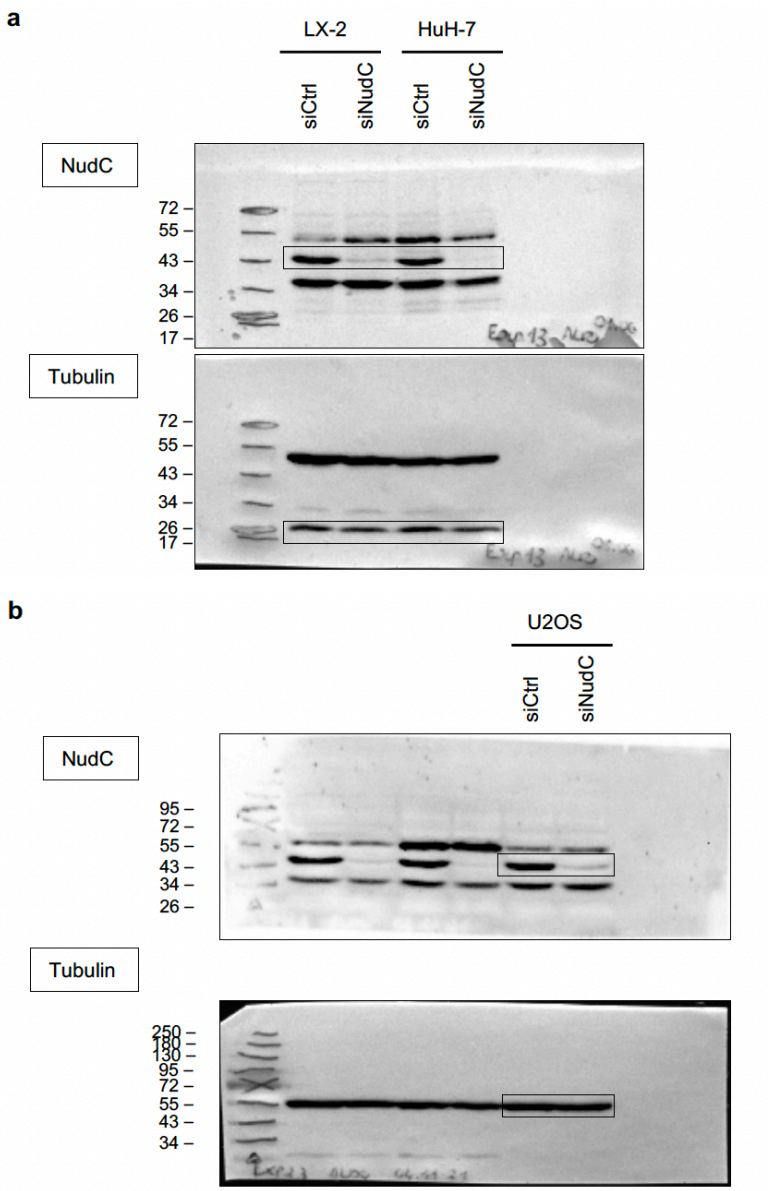

Supplementary Figure 5, referring to Figure 31, 32 and 33. Uncropped original image of Western Blot membranes confirming the downregulation of NudC in **a)** LX-2 and HuH-7, and **b)** U2OS cells.

Supplementary table 1. Summary of manually quantified U2OS GFP-WIPI1 puncta positive cells, referring to Figure 9b.

U2OS GFP-WIPI1				
Condition	**Independent experiment (n = 4)**	**Number of counted cells**	**WIPI1 puncta positive cells (%)**	**Mean (± SD) of WIPI1 puncta positive cells (%)**
DMEM + 10% FCS	**#1**	243	11.9341564	11.162782 (± 1.7121397)
	#2	225	11.5555556	
	#3	254	8.66141732	
	#4	224	12.5	
DMEM + 2.5% FCS	**#1**	258	13.5658915	13.217437 (± 2.0803651)
	#2	240	12.9166667	
	#3	229	15.720524	
	#4	225	10.6666667	
EBSS	**#1**	215	62.7906977	66.553887 (± 6.0680244)
	#2	239	67.3640167	
	#3	204	61.2745098	
	#4	234	74.7863248	

Supplementary table 2. Calculated p-values of manual quantification of U2OS GFP-WIPI1 puncta positive cells referring to Figure 9b.

Ordinary One-Way ANOVA				
Holm-Sidak's multiple comparisons test	**Mean Diff.**	**Below threshold?**	**Summary**	**Adjusted P value**
DMEM + 10% FCS vs. DMEM + 2.5% FCS	-2.054654895	No	ns	0.47
DMEM + 10% FCS vs. EBSS	-55.39110492	Yes	***	<0.001
DMEM + 2.5% FCS vs. EBSS	-53.33645003	Yes	***	<0.001

Supplementary table 3. Summary of manually quantified TNT index and WIPI1 positive TNTs in U2OS GFP-WIPI1, referring to Figures 9c, 9d.

U2OS GFP-WIPI1								
Condition	**Independent experiment (n = 4)**	**Number of counted cells**	**Number of counted TNTs**	**TNTs per 100 cells**	**Mean (± SD) of TNTs per 100 cells**	**WIPI1 positive TNTs**	**WIPI1 positive TNTs (%)**	**Mean (± SD) of WIPI1 positive TNTs (%)**
DMEM + 10%FCS	**#1**	220	13	5.909090909	9.02298469 (± 2.75774971)	0	0	0 (± 0)
	#2	230	18	7.826086957		0	0	
	#3	238	24	10.08403361		0	0	
	#4	220	27	12.27272727		0	0	
DMEM + 2.5%FCS	**#1**	225	21	9.333333333	10.7950558 (± 0.99591411)	0	0	2 (± 4)
	#2	200	22	11		0	0	
	#3	209	24	11.48325359		0	0	
	#4	220	25	11.36363636		2	8	
EBSS	**#1**	207	46	22.22222222	21.4723033 (± 1.05659567)	2	4.34782609	8.51740936 (± 5.75997914)
	#2	214	47	21.96261682		8	17.0212766	
	#3	221	44	19.90950226		3	6.81818182	
	#4	234	51	21.79487179		3	5.88235294	

Supplementary table 4. Transformed data of % of WIPI1 positive TNTs (log+1), referring to Figure 9d.

DMEM/FCS	DMEM+2.5% FCS	EBSS
0	0	0.728177276
0	0	1.255785552
0	0	0.893105766
0	0.954242509	0.83773694
0	0.238560627	0.928701384
0	0.477121255	0.228572052

Supplementary table 5. Calculated p-values of manual quantification of TNT index and GFP-WIPI1 puncta positive TNTs in U2OS GFP-WIPI1 cells, referring to Figures 9c and 9d.

TNT index				
Ordinary One-Way ANOVA				
Holm-Sidak's multiple comparisons test	**Mean Diff.**	**Below threshold?**	**Summary**	**Adjusted P value**
DMEM + 10% FCS vs. DMEM + 2.5% FCS	-1.77207	No	ns	0.2
DMEM + 10% FCS vs. EBSS	-12.4493	Yes	***	<0.001
DMEM + 2.5% FCS vs. EBSS	-10.6772	Yes	***	<0.001
WIPI1 puncta positive TNTs				
Ordinary One-Way ANOVA				
Holm-Sidak's multiple comparisons test	**Mean Diff.**	**Below threshold?**	**Summary**	**Adjusted P value**
DMEM + 10% FCS vs. DMEM + 2.5% FCS	-0.238560627	No	ns	0.3
DMEM + 10% FCS vs. EBSS	-0.928701384	Yes	**	0.006
DMEM + 2.5% FCS vs. EBSS	-0.690140756	Yes	*	0.02

Supplementary table 6. Summary of manually quantified U2OS GFP-WIPI2B puncta positive cells, referring to Figure 12b.

U2OS GFP-WIPI2B				
Condition	**Independent experiment (n = 4)**	**Number of counted cells**	**WIPI2B puncta positive cells (%)**	**Mean (± SD) of WIPI2B puncta positive cells (%)**
DMEM + 10% FCS	**#1**	205	3.90243902	4.2360177 (± 1.7079471)
	#2	206	4.36893204	
	#3	234	6.41025641	
	#4	221	2.26244344	
DMEM + 2.5% FCS	**#1**	220	5.45454545	9.0719448 (± 2.5666271)
	#2	222	9.90990991	
	#3	235	11.4893617	
	#4	212	9.43396226	
EBSS	**#1**	202	45.5445545	45.124377 (± 0.7627818)
	#2	200	37.5	
	#3	206	61.6504854	
	#4	243	35.8024691	

Supplementary table 7. Calculated p-values of manual quantification of U2OS GFP-WIPI2B puncta positive cells, referring to Figure 12b.

Ordinary One-Way ANOVA				
Holm-Sidak's multiple comparisons test	**Mean Diff.**	**Below threshold?**	**Summary**	**Adjusted P value**
DMEM + 10% FCS vs. DMEM + 2.5 FCS	-4.8359271025	No	ns	0.36
DMEM + 10% FCS vs. EBSS	-40.8883595225	Yes	***	<0.001
DMEM + 2.5% FCS vs. EBSS	-36.05243242	Yes	***	<0.001

Supplementary table 8. Summary of manually quantified TNT index and WIPI2B positive TNTs in U2OS GFP-WIPI2B, referring to Figures 12c and 12d.

U2OS GFP-WIPI2B								
Condition	**Independent experiment (n = 4)**	**Number of counted cells**	**Number of counted TNTs**	**TNTs per 100 cells**	**Mean (± SD) of TNTs per 100 cells**	**WIPI2B positive TNTs**	**WIPI2B positive TNTs (%)**	**Mean (± SD) of WIPI2B positive TNTs (%)**
DMEM + 10%FCS	**#1**	233	28	12.01716738	9.558248585 (± 3.255138531)	0	0	0 (± 0)
	#2	252	32	12.6984127		0	0	
	#3	226	16	7.079646018		0	0	
	#4	233	15	6.43776824		0	0	
DMEM + 2.5%FCS	**#1**	226	31	13.71681416	10.22588848 (± 2.778857972)	0	0	0 (± 0)
	#2	232	26	11.20689655		0	0	
	#3	228	18	7.894736842		0	0	
	#4	235	19	8.085106383		0	0	
EBSS	**#1**	204	51	25	24.20037582 (± 2.255042769)	2	3.92156863	4.4688979 (± 2.88223917)
	#2	226	60	26.54867257		2	3.33333333	
	#3	241	58	24.06639004		5	8.62068966	
	#4	236	50	21.18644068		1	2	

Supplementary table 9. Calculated p-values of manual quantification of TNT index and GFP-WIPI2B puncta positive TNTs in U2OS GFP-WIPI2B cells, referring to Figures 12c and 12d.

TNT index				
Ordinary One-Way ANOVA				
Holm-Sidak's multiple comparisons test	**Mean Diff.**	**Below threshold?**	**Summary**	**Adjusted P value**
DMEM + 10% FCS vs. DMEM + 2.5% FCS	-0.6676398993	No	ns	0.74
DMEM + 10% FCS vs. EBSS	-14.64212724	Yes	***	<0.001
DMEM + 2.5% FCS vs. EBSS	-13.97448734	Yes	***	<0.001
WIPI2B puncta positive TNTs				
Ordinary One-Way ANOVA				
Holm-Sidak's multiple comparisons test	**Mean Diff.**	**Below threshold?**	**Summary**	**Adjusted P value**
DMEM + 10% FCS vs. DMEM + 2.5% FCS	0.000000000	No	ns	>0.99
DMEM + 10% FCS vs. EBSS	-4.468897905	Yes	*	0.01
DMEM + 2.5% FCS vs. EBSS	-4.468897905	Yes	*	0.01

Supplementary table 10. Summary of manually quantified mRFP-WIPI4 puncta positive cells, referring to Figure 14b.

U2OS mRFP-WIPI4				
Condition	**Independent experiment (n = 4)**	**Number of counted cells**	**WIPI4 Puncta positive cells (%)**	**Mean (± SD) of WIPI4 puncta positive cells (%)**
DMEM + 10%FCS	**#1**	226	2.21238938	3.4334675 (± 1.0729213)
	#2	284	4.22535211	
	#3	233	3.86266094	
DMEM + 10%FCS + FAC	**#1**	221	4.07239819	4.5010037 (± 0.4268659)
	#2	203	4.92610837	
	#3	222	4.5045045	
DMEM + 10%FCS + DFX	**#1**	203	39.408867	44.882321 (± 4.8348786)
	#2	210	48.5714286	
	#3	225	46.6666667	
EBSS	**#1**	234	21.7948718	25.281988 (± 3.0377686)
	#2	221	26.6968326	
	#3	223	27.3542601	

Supplementary table 11. Calculated p-values of manual quantification of U2OS mRFP-WIPI4 puncta positive cells, referring to Figure 14b.

Ordinary One-Way ANOVA				
Holm-Sidak's multiple comparisons test	**Mean Diff.**	**Below threshold?**	**Summary**	**Adjusted P value**
DMEM + 10% FCS vs. DMEM + 10%FCS + FAC	-1.067536210	No	Ns	0.67
DMEM + 10% FCS vs. DMEM + 10%FCS + DFX	-41.44885329	Yes	***	<0.001
DMEM + 10% FCS vs. EBSS	-21.84852069	Yes	***	<0.001

Supplementary table 12. Summary of manually quantified mRFP-WIPI4 puncta positive U2OS NLS-mScarlet cells, referring to Figure 16c.

esiFLUC U2OS NLS-M-Scarlet					
Condition	**Independent experiment (n = 5)**	**Number of NLS-M-Scarlet cells**	**Number of WIPI4 Puncta positive NLS-M-Scarlet cells**	**Number of WIPI4 Puncta positive NLS-M-Scarlet cells (%)**	**Mean (± SD) of WIPI4 puncta positive cells (%)**
DMEM + 10%FCS	**#1**	218	9	4.12844037	3.7791302 (± 1.302556284)
	#2	227	7	3.08370044	
	#3	259	15	5.79150579	
	#4	225	8	3.55555556	
	#5	214	5	2.3364486	
DMEM + 10%FCS + FAC	**#1**	214	8	3.73831776	3.163532 (± 1.257002969)
	#2	226	7	3.09734513	
	#3	253	12	4.743083	
	#4	239	7	2.92887029	
	#5	229	3	1.31004367	
DMEM + 10%FCS + DFX	**#1**	240	20	8.33333333	6.3701284 (± 1.99565808)
	#2	229	14	6.11353712	
	#3	282	24	8.5106383	
	#4	219	10	4.56621005	
	#5	208	9	4.32692308	
EBSS	**#1**	222	39	17.5675676	14.617929 (± 3.27708391)
	#2	238	40	16.8067227	
	#3	241	40	16.5975104	
	#4	202	23	11.3861386	
	#5	205	22	10.7317073	
esiWDR45 U2OS NLS-M-Scarlet					
Condition	**Independent experiment (n = 5)**	**Number of NLS-M-Scarlet cells**	**Number of WIPI4 Puncta positive NLS-M-Scarlet cells**	**Number of WIPI4 Puncta positive NLS-M-Scarlet cells (%)**	**Mean (± SD) of WIPI4 puncta positive cells (%)**

DMEM + 10%FCS	**#1**	236	18	7.62711864	5.9783325 (± 2.23517111)
	#2	237	14	5.907173	
	#3	241	21	8.71369295	
	#4	210	7	3.33333333	
	#5	232	10	4.31034483	
DMEM + 10%FCS + FAC	**#1**	225	16	7.11111111	5.9259569 (± 2.60978435)
	#2	233	21	9.01287554	
	#3	239	17	7.11297071	
	#4	218	7	3.21100917	
	#5	220	7	3.18181818	
DMEM + 10%FCS + DFX	**#1**	246	29	11.7886179	11.733827 (± 2.10172594)
	#2	244	27	11.0655738	
	#3	237	24	10.1265823	
	#4	212	22	10.3773585	
	#5	209	32	15.3110048	
EBSS	**#1**	246	41	16.6666667	15.090974 (± 2.64482867)
	#2	243	38	15.6378601	
	#3	239	37	15.4811715	
	#4	210	36	17.1428571	
	#5	228	24	10.5263158	

Supplementary table 13. Calculated p-values of manual quantification of mRFP-WIPI4 puncta positive U2OS NLS-mScarlet, referring to Figure 16c.

Ordinary Two-Way ANOVA				
mRFP-WIPI4 puncta positive U2OS NLS-mScarlet				
Tukey's multiple comparisons test	**Mean Diff.**	**Below threshold?**	**Summary**	**Adjusted P-value**
Ctrl:esiFLUC vs. Ctrl:esiWDR45	-2.199202398	No	ns	0.78
Ctrl:esiFLUC vs. DMEM/FCS + FAC:esiFLUC	0.6155981819	No	ns	>0.99
Ctrl:esiFLUC vs. DMEM/FCS + DFX:esiFLUC	-2.590998224	No	ns	0.62
Ctrl:esiFLUC vs. EBSS:esiFLUC	-10.838799168	Yes	***	<0.001
Ctrl:esiWDR45 vs. DMEM/FCS + FAC:esiWDR45	0.052375608	No	ns	>0.99
Ctrl:esiWDR45 vs. DMEM/FCS + DFX:esiWDR45	-5.755494910	Yes	**	0.007
Ctrl:esiWDR45 vs. EBSS:esiWDR45	-9.11264169	Yes	***	<0.001
DMEM/FCS + FAC:esiFLUC vs. DMEM/FCS + FAC:esiWDR45	-2.762424972	No	ns	0.55
DMEM/FCS + DFX:esiFLUC vs. DMEM/FCS + DFX:esiWDR45	-5.363699084	Yes	*	0.01
EBSS:esiFLUC vs. EBSS:esiWDR45	-0.473044919	No	ns	>0.99

Supplementary table 14. Summary of manually quantified TNT index and LC3 positive TNTs in U2OS GFP-LC3, referring to Figures 18b and 18c.

U2OS GFP-LC3								
Conditions	**Independent experiment (n = 4)**	**Number of counted cells**	**Number of counted TNTs**	**TNTs per 100 cells**	**Mean (± SD) of TNTs per 100 cells**	**LC3 positive TNTs**	**LC3 positive TNTs (%)**	**Mean (± SD) of LC3 positive TNTs (%)**
DMEM + 10%FCS	**#1**	227	12	5.286343612	5.351667099 (± 0.425605612)	0	0	4.545454545 (± 5.248638811)
	#2	204	11	5.392156863		1	9.090909091	
	#3	227	11	4.845814978		1	9.090909091	
	#4	255	15	5.882352941		0	0	
DMEM + 2.5%FCS	**#1**	240	16	6.666666667	7.181832251 (± 1.750779908)	0	0	4.895833333 (± 6.349896106)
	#2	267	15	5.617977528		2	13.33333333	
	#3	237	16	6.751054852		1	6.25	
	#4	227	22	9.691629956		0	0	
EBSS	**#1**	228	44	19.29824561	20.30811997 (± 2.567037657)	4	9.090909091	7.881306911 (± 3.645281652)
	#2	245	42	17.14285714		2	4.761904762	
	#3	258	58	22.48062016		3	5.172413793	
	#4	251	56	22.31075697		7	12.5	

Supplementary table 15. Calculated p-values of manual quantification of TNT index and GFP-LC3 puncta positive TNTs in U2OS GFP-LC3 cells, referring to Figures 18b and 18c.

TNT index				
Ordinary One-Way ANOVA				
Holm-Sidak's multiple comparisons test	**Mean Diff.**	**Below threshold?**	**Summary**	**Adjusted P value**
DMEM + 10% FCS vs. DMEM + 2.5% FCS	-1.830165152	No	ns	0.19
DMEM + 10% FCS vs. EBSS	-14.95645287	Yes	***	<0.001
DMEM + 2.5% FCS vs. EBSS	-13.12628772	Yes	***	<0.001
LC3 puncta positive TNTs				
Ordinary One-Way ANOVA				
Holm-Sidak's multiple comparisons test	**Mean Diff.**	**Below threshold?**	**Summary**	**Adjusted P value**
DMEM + 10% FCS vs. DMEM + 2.5% FCS	-0.35037878	No	ns	0.93
DMEM + 10% FCS vs. EBSS	-3.335852365	No	ns	0.77
DMEM + 2.5% FCS vs. EBSS	-2.985473585	No	ns	0.77

Supplementary table 16. Summary of manually quantified TNT index and ferritin puncta positive TNTs in U2OS cells, referring to Figures 25b and 25c.

U2OS – Ferritin 488								
Condition	**Independent experiment (n = 4)**	**Number of counted cells**	**Number of counted of TNTs**	**TNTs per 100 cells**	**Mean (± SD) of TNTs per 100 cells**	**Ferritin positive TNTs**	**Ferritin positive TNTs (%)**	**Mean (± SD) of Ferritin positive TNTs (%)**
DMEM + 10%FCS	**#1**	250	16	6.4	6.14725815 (± 1.34399462)	1	6.25	0.269387755 (± 0.233332342)
	#2	245	18	7.346938776		1	5.555555556	
	#3	213	10	4.694835681		0	0	
DMEM + 10%FCS + FAC	**#1**	312	20	6.41025641	4.07469007 (± 2.0329417)	2	10	0.662123662 (± 0.228958444)
	#2	222	6	2.702702703		2	33.33333333	
	#3	225	7	3.111111111		1	14.28571429	
DMEM + 10%FCS + DFX	**#1**	219	19	8.675799087	8.57062963 (± 0.31877304)	0	0	0.487827981 (± 0.490213238)
	#2	204	18	8.823529412		2	11.11111111	
	#3	207	17	8.212560386		1	5.882352941	
EBSS	**#1**	221	40	18.09954751	16.6862177 (± 1.58154571)	9	22.5	3.926523775 (± 0.565978932)
	#2	212	36	16.98113208		7	19.44444444	
	#3	227	34	14.97797357		10	29.41176471	

Supplementary table 17. Calculated p-values of manual quantification of TNT index and ferritin puncta positive TNTs, referring to Figures 25b and 25c.

TNT index				
Ordinary One-Way ANOVA				
Holm-Sidak's multiple comparisons test	**Mean Diff.**	**Below threshold?**	**Summary**	**Adjusted P value**
DMEM + 10% FCS vs. DMEM + 10% FCS + FAC	2.07256807	No	ns	0.15
DMEM + 10% FCS vs. DMEM + 10% FCS + DFX	-2.42337147	No	ns	0.15
DMEM + 10% FCS vs. EBSS	-10.53895956	Yes	***	<0.001
Ferritin puncta positive TNTs (%)				
Ordinary One-Way ANOVA				
Holm-Sidak's multiple comparisons test	**Mean Diff.**	**Below threshold?**	**Summary**	**Adjusted P value**
DMEM + 10% FCS vs. DMEM + 10% FCS + FAC	-15.2711640	No	ns	0.07
DMEM + 10% FCS vs. DMEM + 10% FCS + DFX	-1.72930283	No	ns	0.78
DMEM + 10% FCS vs. EBSS	-19.8502178	Yes	*	0.03

Supplementary table 18. Summary of manually quantified GFP-FTH1 puncta positive U2OS NLS-mScarlet cells, referring to Figure 28b.

esiFLUC U2OS GFP-FTH1 + U2OS NLS-M-Scarlet					
Condition	**Independent experiment (n = 4)**	**Number of NLS-M-Scarlet cells**	**Number of GFP-FTH1 puncta positive NLS-mScarlet cells**	**Number of GFP-FTH1 puncta positive NLS-mScarlet cells (%)**	**Mean (± SD) of GFP-FTH1 puncta positive NLS-mScarlet cells (%)**
DMEM + 10%FCS	**#1**	214	27	12.6168224	16.74539 (± 3.309182304)
	#2	219	34	15.5251142	
	#3	200	39	19.5	
	#4	212	41	19.3396226	
DMEM + 10%FCS + FAC	**#1**	203	25	12.3152709	16.409147 (± 4.536116527)
	#2	207	27	13.0434783	
	#3	206	45	21.8446602	
	#4	217	40	18.4331797	
DMEM + 10%FCS + DFX	**#1**	212	30	14.1509434	16.729772 (± 5.664273017)
	#2	214	22	10.2803738	
	#3	216	50	23.1481481	
	#4	212	41	19.3396226	
EBSS	**#1**	208	10	4.80769231	11.766108 (± 5.538457644)
	#2	213	25	11.7370892	
	#3	207	38	18.3574879	
	#4	222	27	12.1621622	
esiWDR45 U2OS GFP-FTH1 + U2OS NLS-M-Scarlet					
Condition	**Independent experiment (n = 4)**	**Number of NLS-M-Scarlet cells**	**Number of GFP-FTH1 puncta positive NLS-mScarlet cells**	**Number of GFP-FTH1 puncta positive NLS-mScarlet cells (%)**	**Mean (± SD) of GFP-FTH1 puncta positive NLS-mScarlet cells (%)**
DMEM + 10%FCS	**#1**	172	43	25	24.011072 (± 3.881054919)
	#2	216	48	22.2222222	
	#3	204	59	28.9215686	
	#4	201	40	19.9004975	

DMEM + 10%FCS + FAC	**#1**	210	41	19.5238095	17.750411 (± 2.635284673)
	#2	203	32	15.7635468	
	#3	210	43	20.4761905	
	#4	210	32	15.2380952	
DMEM + 10%FCS + DFX	**#1**	204	68	33.3333333	36.047933 (± 5.790415323)
	#2	202	73	36.1386139	
	#3	202	89	44.0594059	
	#4	212	65	30.6603774	
EBSS	**#1**	207	66	31.884058	26.247489 (± 8.719384901)
	#2	234	50	21.3675214	
	#3	202	71	35.1485149	
	#4	217	36	16.5898618	

Supplementary table 19. Calculated p-values of manual quantification of GFP-FTH1 puncta positive U2OS NLS-mScarlet, referring to Figure 28b.

Ordinary Two-Way ANOVA				
GFP-FTH1 puncta positive U2OS NLS-mScarlet cells				
Tukey's multiple comparisons test	**Mean Diff.**	**Below threshold?**	**Summary**	**Adjusted P-value**
DMEM + FCS:esiFLUC vs. DMEM + FCS:esiWDR45	-7.265682275	No	ns	0.54
DMEM + FCS:esiFLUC vs. DMEM/FCS + FAC:esiFLUC	0.3362425249	No	ns	>0.99
DMEM + FCS:esiFLUC vs. DMEM/FCS + DFX:esiFLUC	0.0156178249	No	ns	>0.99
DMEM + FCS:esiFLUC vs. EBSS:esiFLUC	4.9792818975	No	ns	0.88
DMEM + FCS:esiWDR45 vs. DMEM/FCS + FAC:esiWDR45	6.260661575	No	ns	0.71
DMEM + FCS:esiWDR45 vs. DMEM/FCS + DFX:esiWDR45	-12.03686055	No	ns	0.06
DMEM + FCS:esiWDR45 vs. EBSS:esiWDR45	-2.23641695	No	ns	>0.99
DMEM/FCS + FAC:esiFLUC vs. DMEM/FCS + FAC:esiWDR45	-1.341263225	No	ns	>0.99
DMEM/FCS + DFX:esiFLUC vs. DMEM/FCS + DFX:esiWDR45	-19.31816065	Yes	***	<0.001
EBSS:esiFLUC vs. EBSS:esiWDR45	-14.4813811225	Yes	*	0.01

Supplementary table 20. Summary of manually quantified TNT index in LX-2 cells, referring to Figure 31b.

LX-2						
siRNA	**Condition**	**Independent experiment (n = 4)**	**Number of counted cells**	**Number of counted TNTs**	**TNTs per 100 cells**	**Mean (± SD) of TNTs per 100 cells**
siCtrl	**DMEM + 2%FCS**	**#1**	204	20	9.803921569	18.57626227 (± 7.629093542)
		#2	265	59	22.26415094	
		#3	224	53	23.66071429	
	DMEM + 2%FCS + SF	**#1**	231	76	32.9004329	32.39720688 (± 3.437697779)
		#2	225	80	35.55555556	
		#3	261	75	28.73563218	
siNudC	**DMEM + 2%FCS**	**#1**	237	15	6.329113924	8.838099703 (± 2.174817376)
		#2	216	22	10.18518519	
		#3	230	23	10	
	DMEM + 2%FCS + SF	**#1**	203	15	7.389162562	7.960408685 (± 0.2.51734369)
		#2	225	13	5.777777778	
		#3	224	24	10.71428571	

Supplementary table 21. Calculated p-values of manual quantification of TNT index in LX-2 cells, referring to Figure 31b.

Ordinary Two-Way ANOVA				
TNTs per 100 cells (TNT index) – LX-2				
Tukey's multiple comparisons test	**Mean Diff.**	**Below threshold?**	**Summary**	**Adjusted P-value**
siCtrl:DMEM + 2%FCS vs. siCtrl:DMEM + 2%FCS + SF	-13.82094461	Yes	*	0.02
siCtrl:DMEM + 2%FCS vs. siNudC:DMEM + 2%FCS	9.738162561	No	ns	0.11
siCtrl:DMEM + 2%FCS + SF vs. siNudC:DMEM + 2%FCS + SF	24.43679819	Yes	***	<0.001
siNudC:DMEM + 2%FCS vs. siNudC:DMEM + 2%FCS + SF	0.8776910212	No	ns	>0.99

Supplementary table 22. Summary of manually quantified TNT index in HuH-7 cells, referring to Figure 32b.

HuH-7						
			cells	**TNTs**	**TNTs/100 cells**	**Mean**
siCtrl	**DMEM + 10%FCS**	**1**	205	30	14.63414634	16.1188263 (± 3.6949639)
		2	246	50	20.32520325	
		3	209	28	13.39712919	
	DMEM + 10%FCS + SF	**1**	237	75	31.64556962	27.2799859 (± 4.3045343)
		2	232	63	27.15517241	
		3	204	47	23.03921569	
siNudC	**DMEM + 10%FCS**	**1**	217	26	11.98156682	12.7757926 (± 1.1470948)
		2	204	25	12.25490196	
		3	220	31	14.09090909	
	DMEM + 10%FCS + SF	**1**	200	26	13	14.5635282 (± 3.7739108)
		2	212	40	18.86792453	
		3	203	24	11.8226601	

Supplementary table 23. Calculated p-values of manual quantification of TNT index in HuH-7 cells, referring to Figure 32b.

Ordinary Two-Way ANOVA				
TNTs per 100 cells (TNT index) – HuH-7				
Tukey's multiple comparisons test	**Mean Diff.**	**Below threshold?**	**Summary**	**Adjusted P-value**
siCtrl:DMEM + 10%FCS vs. siCtrl:DMEM + 10%FCS + SF	-11.16115963	Yes	*	0.02
siCtrl:DMEM + 10%FCS vs. siNudC:DMEM + 10%FCS	3.34303363	No	ns	0.65
siCtrl:DMEM + 10%FCS + SF vs. siNudC:DMEM + 10%FCS + SF	12.7164577	Yes	**	0.009
siNudC:DMEM + 10%FCS vs. siNudC:DMEM + 10%FCS + SF	-1.78773556	No	ns	0.92

Supplementary table 24. Summary of manually quantified TNT index in U2OS cells, referring to Figure 33b.

U2OS						
			cells	**TNTs**	**TNTs/100 cells**	**Mean**
siCtrl	**DMEM + 10%FCS**	**1**	276	63	22.82608696	17.0767068 (± 4.99700171)
		2	253	37	14.62450593	
		3	254	35	13.77952756	
	DMEM + 10%FCS + SF	**1**	237	53	22.3628692	22.6188105 (± 2.15733954)
		2	233	58	24.89270386	
		3	233	48	20.60085837	
siNudC	**DMEM + 10%FCS**	**1**	204	102	50	49.0678984 (± 1.21128229)
		2	239	114	47.69874477	
		3	202	100	49.5049505	
	DMEM + 10%FCS + SF	**1**	234	120	51.28205128	48.7588022 (± 2.22329139)
		2	206	97	47.08737864	
		3	215	103	47.90697674	

Supplementary table 25. Calculated p-values of manual quantification of TNT index in U2OS cells, referring to Figure 33b.

Ordinary Two-Way ANOVA				
TNTs per 100 cells (TNT index) – U2OS				
Tukey's multiple comparisons test	**Mean Diff.**	**Below threshold?**	**Summary**	**Adjusted P-value**
siCtrl:DMEM + 10%FCS vs. siCtrl:DMEM + 10%FCS + SF	-5.54210366	No	***	0.19
siCtrl:DMEM + 10%FCS vs. siNudC:DMEM + 10%FCS	-31.99119160	Yes	ns	<0.001
siCtrl:DMEM + 10%FCS + SF vs. siNudC:DMEM + 10%FCS + SF	-26.13999174	Yes	***	<0.001
siNudC:DMEM + 10%FCS vs. siNudC:DMEM + 10%FCS + SF	0.309096203	No	ns	>0.99

Supplementary table 26. Summary of manually quantified TNT index upon EGFP and EGFP-WIPI1 transfection, referring to Figure 34b.

EGFP					
DNA concentration	**Independent experiment (n = 4)**	**Number of counted cells**	**Number of counted TNTs**	**TNTs per cells**	**Mean (± SD) of TNTs per 100 cells**
0.1 µg	**#1**	277	17	6.13718412	7.18578778 (± 1.90393253)
	#2	248	19	7.66129032	
	#3	249	24	9.63855422	
	#4	245	13	5.30612245	
0.25 µg	**#1**	229	18	7.86026201	7.39214624 (± 0.85953459)
	#2	245	20	8.16326531	
	#3	306	19	6.20915033	
	#4	259	19	7.33590734	
EGFP-WIPI1					
DNA concentration	**Independent experiment (n = 4)**	**Number of counted cells**	**Number of counted TNTs**	**TNTs per cells**	**Mean (± SD) of TNTs per 100 cells**
0.1 µg	**#1**	260	27	10.3846154	9.01480043 (± 1.42116078)
	#2	299	30	10.0334448	
	#3	256	21	8.203125	
	#4	242	18	7.43801653	
0.25 µg	**#1**	268	33	12.3134328	10.9190368 (± 0.94300737)
	#2	244	25	10.2459016	
	#3	267	28	10.4868914	
	#4	254	27	10.6299213	

Supplementary table 27. Calculated p-values of manual quantification of TNT index upon EGFP-WIPI1 transfection, referring to Figure 34b.

Ordinary Two-Way ANOVA		
TNTs per 100 cells (TNT index)		
Tukey's multiple comparisons test	**Significant?**	**Adjusted P-value**
0.1 µg EGFP vs. 0.25 µg EGFP	ns	>0.99
0.1 µg EGFP-WIPI1 vs. 0.25 µg EGFP-WIPI1	ns	0.24
0.1 µg EGFP vs. 0.1 µg EGFP-WIPI1	ns	0.27
0.25 µg EGFP vs. 0.25 µg EGFP-WIPI1	yes	0.01

Supplementary table 28. Summary of manually quantified TNT index in U2OS Cas9 and U2OS Cas9 WIPI1 KO, referring to Figure 35b.

Cell line	Condition	Independent experiment (n = 4)	Number of counted cells	Number of counted TNTs	TNTs per 100 cells	Mean (± SD) of TNTs per 100 cells
U2OS Cas9	DMEM + 10% FCS	#1	274	13	4.74452555	7.07007461 (± 1.56167704)
		#2	277	21	7.58122744	
		#3	264	21	7.95454545	
		#4	275	22	8	
	DMEM + 2.5% FCS	#1	218	40	18.3486239	16.8265973 (± 3.5009994)
		#2	252	43	17.0634921	
		#3	227	27	11.8942731	
		#4	250	50	20	
	EBSS	#1	213	40	18.7793427	23.2555264 (± 5.28883776)
		#2	215	40	18.6046512	
		#3	208	59	28.3653846	
		#4	231	63	27.2727273	
U2OS Cas9 WIPI1 KO	DMEM + 10% FCS	#1	272	6	2.20588235	2.43044653 (± 0.40218782)
		#2	241	5	2.0746888	
		#3	285	7	2.45614035	
		#4	268	8	2.98507463	
	DMEM + 2.5% FCS	#1	265	12	4.52830189	5.15854844 (± 1.78738644)
		#2	256	9	3.515625	
		#3	490	24	4.89795918	
		#4	429	33	7.69230769	
	EBSS	#1	269	8	2.9739777	3.61716059 (± 0.59779081)
		#2	317	14	4.41640379	
		#3	250	9	3.6	
		#4	230	8	3.47826087	

Supplementary table 29. Calculated p-values of manual quantification of TNT index in U2OS Cas9 WT and U2OS Cas9 WIPI1 KO, referring to Figures 35b.

Ordinary Two-Way ANOVA			
TNTs per 100 cells (TNT index)			
Tukey's multiple comparisons test		Significant?	Adjusted P-value
U2OS Cas9	DMEM + 10% FCS vs DMEM + 2.5% FCS	yes	0.001
	DMEM + 10% FCS vs EBSS	yes	<0.001
	DMEM + 2.5% FCS vs EBSS	yes	0.04
U2OS WIPI1 KO	DMEM + 10% FCS vs DMEM + 2.5% FCS	ns	0.73
	DMEM + 10% FCS vs EBSS	ns	0.99
	DMEM + 2.5% FCS vs EBSS	ns	0.97
U2OS Cas9 vs U2OS WIPI1 KO	DMEM + 10% FCS	ns	0.22
U2OS Cas9 vs U2OS WIPI1 KO	DMEM + 2.5% FCS	yes	<0.001
U2OS Cas9 vs U2OS WIPI1 KO	EBSS	yes	<0.001

Manuscript 1 - The ABL-MYC axis controls WIPI1-enhanced autophagy in lifespan extension

Katharina Sporbeck[1,2], Maximilian L. Haas[1,#], Carmen J. Pastor-Maldonado[1,#], David S. Schüssele[1,#], Catherine Hunter[1,2], Zsuzsanna Takacs[1,2,†], Ana L. Diogo de Oliveira[1], Mirita Franz-Wachtel[3], Chara Charsou[4,5], Simon G. Pfisterer[1,§], Andrea Gubas[6], Patricia K. Haller[1,2], Roland L. Knorr[7,8,9], Manuel Kaulich[6], Boris Macek[2,3], Eeva-Liisa Eskelinen[10,11], Anne Simonsen[4,5], Tassula Proikas-Cezanne[1,2,*]

[1]Interfaculty Institute of Cell Biology, Eberhard Karls University Tübingen, 72076 Tübingen, Germany.
[2]International Max Planck Research School 'From Molecules to Organisms', Max Planck Institute for Biology and Eberhard Karls University Tubingen, 72076 Tübingen, Germany.
[3]Proteome Center Tübingen, Interfaculty Institute of Cell Biology, Eberhard Karls University Tübingen, 72076 Tübingen, Germany.
[4]Institute of Basic Medical Sciences, University of Oslo, 0372 Oslo, Norway.
[5]Centre for Cancer Cell Reprogramming, Institute of Clinical Medicine, University of Oslo, 0316 Oslo, Norway.
[6]Institute of Biochemistry II, Frankfurt Cancer Institute, Goethe University Medical School, 60590 Frankfurt, Germany.
[7]Humboldt University of Berlin, Institute of Biology, 10115 Berlin, Germany.
[8]Graduate School and Faculty of Medicine, The University of Tokyo, Tokyo 113-0033, Japan.
[9]International Research Frontiers Initiative, Institute of Innovative Research, Tokyo Institute of Technology, Yokohama 226-8503, Japan.
[10]Department of Biosciences, University of Helsinki, Fl-00790 Helsinki, Finland.
[11]Institute of Biomedicine, University of Turku, FI-20520 Turku, Finland.
[†]Present address: Institute of Molecular Biotechnology, A-1030 Vienna, Austria.
[§]Present address: Department of Anatomy, Faculty of Medicine, University of Helsinki, FI-00290 Helsinki, Finland.
[#]Equal contribution (alphabetical order).
Commun Biol **6**, 872 (2023). https://doi.org/10.1038/s42003-023-05236-9

communications biology

ARTICLE

https://doi.org/10.1038/s42003-023-05236-9 OPEN

The ABL-MYC axis controls WIPI1-enhanced autophagy in lifespan extension

Katharina Sporbeck[1,2], Maximilian L. Haas[1,14], Carmen J. Pastor-Maldonado[1,14], David S. Schüssele[1,14], Catherine Hunter[1,2], Zsuzsanna Takacs[1,2,12], Ana L. Diogo de Oliveira[1], Mirita Franz-Wachtel[3], Chara Charsou[4,5], Simon G. Pfisterer[1,13], Andrea Gubas[6], Patricia K. Haller[1,2], Roland L. Knorr[7,8,9], Manuel Kaulich[6], Boris Macek[2,3], Eeva-Liisa Eskelinen[10,11], Anne Simonsen[4,5] & Tassula Proikas-Cezanne[1,2]✉

Human WIPI β-propellers function as PI3P effectors in autophagy, with WIPI4 and WIPI3 being able to link autophagy control by AMPK and TORC1 to the formation of autophagosomes. WIPI1, instead, assists WIPI2 in efficiently recruiting the ATG16L1 complex at the nascent autophagosome, which in turn promotes lipidation of LC3/GABARAP and autophagosome maturation. However, the specific role of WIPI1 and its regulation are unknown. Here, we discovered the ABL-ERK-MYC signalling axis controlling WIPI1. As a result of this signalling, MYC binds to the WIPI1 promoter and represses WIPI1 gene expression. When ABL-ERK-MYC signalling is counteracted, increased WIPI1 gene expression enhances the formation of autophagic membranes capable of migrating through tunnelling nanotubes to neighbouring cells with low autophagic activity. ABL-regulated WIPI1 function is relevant to lifespan control, as ABL deficiency in *C. elegans* increased gene expression of the WIPI1 orthologue ATG-18 and prolonged lifespan in a manner dependent on ATG-18. We propose that WIPI1 acts as an enhancer of autophagy that is physiologically relevant for regulating the level of autophagic activity over the lifespan.

[1] Interfaculty Institute of Cell Biology, Eberhard Karls University Tübingen, D-72076 Tübingen, Germany. [2] International Max Planck Research School 'From Molecules to Organisms', Max Planck Institute for Biology and Eberhard Karls University Tübingen, D-72076 Tübingen, Germany. [3] Proteome Center Tübingen, Interfaculty Institute of Cell Biology, Eberhard Karls University Tübingen, D-72076 Tübingen, Germany. [4] Institute of Basic Medical Sciences, University of Oslo, 0372 Oslo, Norway. [5] Centre for Cancer Cell Reprogramming, Institute of Clinical Medicine, University of Oslo, 0316 Oslo, Norway. [6] Institute of Biochemistry II, Frankfurt Cancer Institute, Goethe University Medical School, D-60590 Frankfurt, Germany. [7] Humboldt University of Berlin, Institute of Biology, D-10115 Berlin, Germany. [8] Graduate School and Faculty of Medicine, The University of Tokyo, Tokyo 113-0033, Japan. [9] International Research Frontiers Initiative, Institute of Innovative Research, Tokyo Institute of Technology, Yokohama 226-8503, Japan. [10] Department of Biosciences, University of Helsinki, FI-00790 Helsinki, Finland. [11] Institute of Biomedicine, University of Turku, FI-20520 Turku, Finland. [12] Present address: Institute of Molecular Biotechnology, A-1030 Vienna, Austria. [13] Present address: Department of Anatomy, Faculty of Medicine, University of Helsinki, FI-00290 Helsinki, Finland. [14] These authors contributed equally: Maximilian L. Haas, Carmen J. Pastor-Maldonado, David S. Schüssele. ✉email: tassula.proikas-cezanne@uni-tuebingen.de

Macroautophagy (hereinafter referred to as autophagy)[1] plays a critical role in controlling the lifespan of eukaryotic organisms by maintaining cellular integrity and breaking down intracellular proteins, lipids, and organelles for recycling purposes[2,3]. Loss of autophagy control and dysfunctional autophagy are closely associated with the development of age-related pathologies, including various types of cancer and neurodegenerative diseases[4–6]. In this context, the complexity of regulatory signalling networks that control the function of autophagy related (ATG) proteins in certain phases of the autophagy process is still insufficiently understood.

In previous studies, we identified four human WIPI proteins (WIPI1 to WIPI4)[7,8] that fold into 7-bladed β-propellers[7,9–12], specifically bind phosphoinositides[9,13,14], and function as PI3P effectors on the nascent autophagosome[8], also known as the phagophore[15]. Through their specific interactions with critical autophagy regulators, WIPI proteins can perform nonredundant functions in autophagy, with WIPI1 and WIPI2 acting upstream and WIPI3 and WIPI4 acting downstream of LC3/GABARAP lipidation at the phagophore[9]. After autophagy initiation via AMPK activation[16] and TORC1 inhibition[17,18], the ULK1 complex[19–21] promotes activation of the PI3KC3 complex[22], which produces PI3P and initiates phagophore formation at the omegasome structures of the endoplasmic reticulum (ER)[4,23–25]. Here, WIPI1 and WIPI2 can heterodimerize and act as lipid sensors by specifically binding to this pool of newly produced PI3P and mediating subsequent steps in autophagosome maturation[26,27]. It is believed that, mechanistically, WIPI1 assists WIPI2 in efficiently recruiting the ATG16L1 complex, which in turn promotes lipidation of LC3/GABARAP[9,27,28]. However, cells lacking WIPI1 can still undergo autophagosome formation[9] since having WIPI2 is sufficient to enable recruitment of the ATG16L1 complex to the phagophore[29]. Therefore, the specific function of WIPI1 and its regulation remain unknown.

Here, we set out to identify upstream regulators of WIPI1 and performed an automated, image-based, high-throughput screening that targeted human kinases with lentiviral-delivered small hairpin RNAs (shRNAs) while assessing for the presence of WIPI1-decorated autophagic membranes, hereinafter referred to as WIPI1 puncta[30]. We identified ABL1, previously reported to control late stages of autophagy by regulating lysosomal acquisition of hydrolytic enzymes[31], as a novel inhibitor of WIPI1 puncta formation and confirmed our finding by subsequent quantitative autophagy assessments using WIPI1, WIPI2, LC3/GABARAP[32,33] and p62[34,35]. Furthermore, stable isotope labeling by amino acids in cell culture (SILAC)-based quantitative phosphoproteomics suggested the possibility that WIPI1 might be under the control of an ABL-ERK2-MYC axis[36,37], an idea confirmed by (i) an unbiased approach using human autophagy pathway-focused gene expression profiling that revealed WIPI1 gene expression under the control of ABL and (ii) a targeted approach in which we showed that ERK-controlled MYC binds to the WIPI1 promoter and represses WIPI1 mRNA synthesis. To investigate the physiological relevance of ABL1-mediated gene expression control of WIPI1, we used *C. elegans* as a model organism and found that ABL deficiency promotes gene expression of ATG-18, the orthologue of WIPI1, and promotes autophagic flux and lifespan extension. To determine whether elevated WIPI1 protein levels can affect autophagy, we overexpressed WIPI1 in human cells and found evidence that WIPI1 can enhance phagophore formation, as determined by correlative light electron microscopy (CLEM) and by analysis of WIPI2 and LC3. In this context, we discovered that autophagic membranes positive for WIPI1, WIPI2, or LC3 are present in tunnelling nanotubes (TNTs), which are bridges for intercellular transport[38], and we discovered that autophagic membranes are transported through TNTs to cells lacking sufficient autophagy, as assessed by coculture setups with ATG16 L-deficient human cells[39].

Results

Human kinome screening revealed an inhibitory role for ABL kinases and DDR1 in initiating autophagy. In the present study, our primary goal was to define the function of WIPI1 in autophagy, and we hypothesized that understanding the regulation of WIPI1 should represent a crucial step towards this goal. Therefore, using an automated fluorescence-based imaging platform with human U2OS cells stably expressing green fluorescent protein (GFP)-WIPI1[30], we screened a lentiviral-based human shRNA library targeting human kinases[9] under starvation conditions while measuring the translocation of GFP-WIPI1 to autophagic membranes, hereafter referred to as puncta (Fig. 1a). The results from targeting 250 human kinases, each with multiple shRNAs applied individually, enabled us to identify 29 candidate kinases whose knockdown led to a significant increase (Fig. 1b; Supplementary Fig. 1a) and 22 candidate kinases whose knockdown led to a significant decrease in the numbers of WIPI1 puncta cells (Fig. 1b; Supplementary Fig. 1b). Among the candidate kinases identified in this unbiased manner (Fig. 1b; Supplementary Fig. 1a, b), we identified known protein kinases, such as ULK2 and EGFR, that activate or inhibit autophagy, respectively, and that modulated the number of WIPI1 puncta cells as expected[40–42]. Pathway enrichment using all candidate kinases indicated involvement of MAPK signalling pathways (Supplementary Fig. 1c, d), and we decided to further analyse ABL1 and DDR1, as both were shown to be involved in MAPK signalling[43,44] and because 9 (ABL1) or 12 (DDR1) individually applied shRNAs resulted in a consistent increase in WIPI1 puncta cells (Supplementary Data 1).

First, we used alternative small interfering RNA (siRNA) sources to transiently knockdown (KD) ABL1 or DDR1, and at this point, we included siRNAs targeting ABL2 (Supplementary Fig. 2a, b), an ABL1 paralogue that works in tandem with ABL1[45,46]. It is noted here that shRNAs targeting ABL2 were absent in the initial kinome screen. Further, we extended the treatment conditions from the initial starvation screening to also include fed conditions and serum deprivation, both in the absence and presence of bafilomycin A1 (Fig. 1c; Supplementary Fig. 2c). Automated imaging assessment confirmed that ABL1 KD as well as DDR1 KD significantly increased the number of GFP-WIPI1 puncta cells, and we extended this observation to ABL2 KD (Fig. 1c; Supplementary Fig. 2c). Since ABL1 and ABL2 have been shown to heterodimerize to regulate overlapping cellular processes but also to have distinguishable cellular functions[45], we compared single ABL1 KD and ABL2 KD settings to double ABL1/2 KD settings in relation to autophagy (Fig. 1d). Using automated single-cell analysis to assess GFP-WIPI1 puncta per cell, we confirmed that both ABL kinases are involved in autophagy regulation and that their influence on autophagy inhibition is stronger when both ABL1/2 are downregulated (Fig. 1d). Based on this result, which suggests a nonredundant effect of ABL1 and ABL2 on autophagy, we downregulated ABL1 and ABL2 together in follow-up experiments. This is consistent with the approach taken by Pendergast's study, which shows that the late stages of autophagy control in the course of lysosomal acquisition of hydrolytic enzymes depend on both ABL1 and ABL2[31].

Second, we employed the bona fide autophagy markers LC3 and GABARAPL1[32,33], functioning downstream from WIPI1[9], as well as the autophagic receptor SQSTM1/p62, which targets ubiquitinated cargo for autophagic degradation[34,35]. Automated imaging assessments of GFP-LC3 showed that ABL1 KD, ABL2

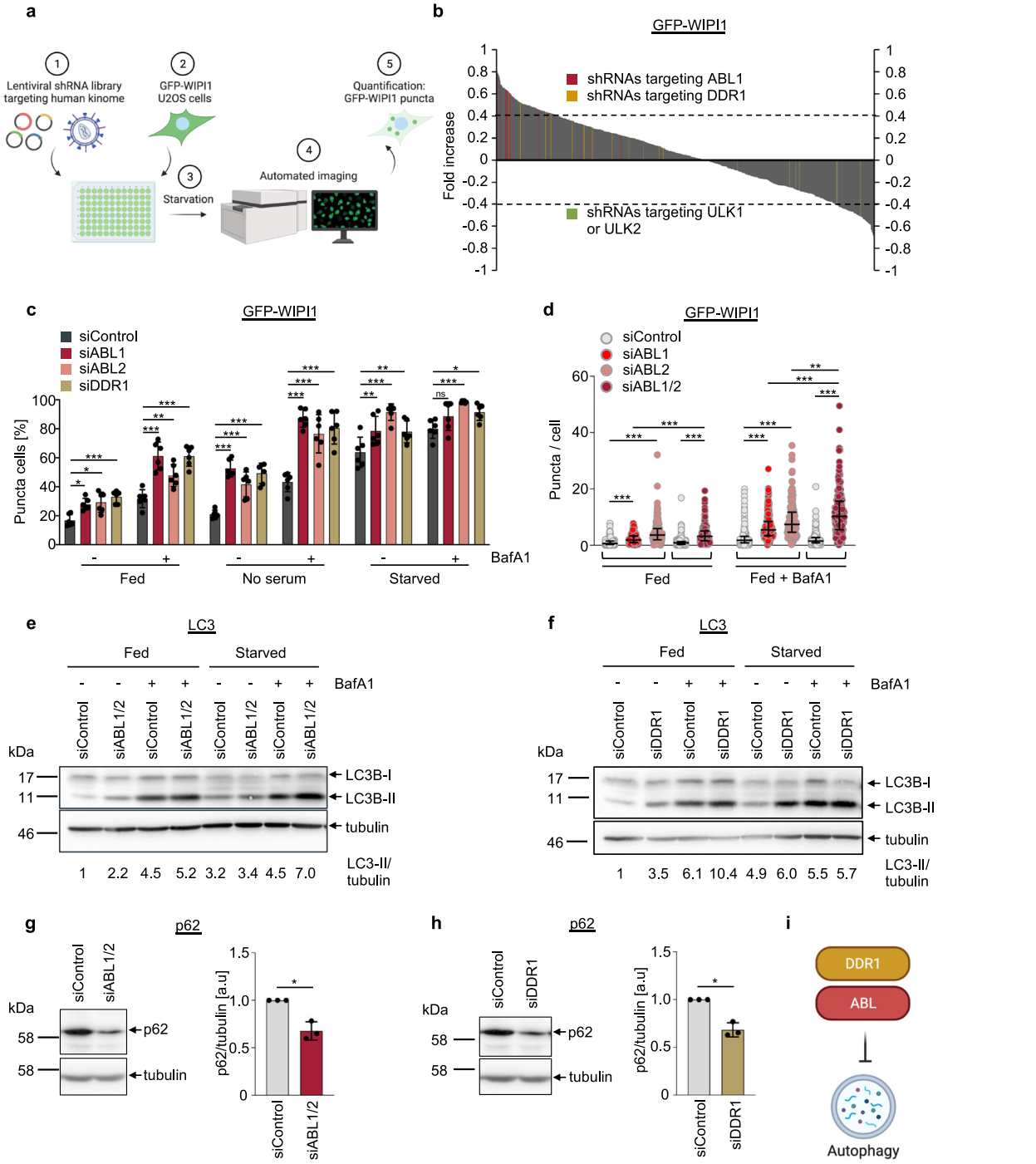

KD and DDR1 KD (Supplementary Fig. 2d, e) as well as ABL1/2 KD (Supplementary Fig. 2f), elicited a significant increase in the GFP-LC3 puncta per single cell, which was most evident in the presence of bafilomycin A1 (Supplementary Fig. 2d–f), indicating increased autophagic flux. Alternatively, we also used U2OS cells stably expressing tandem fluorescent-tagged LC3[47] and found that ABL1/2 KD provoked a significant increase in both autophagosomes and autolysosomes (Supplementary Fig. 2g, left panel), further indicating that autophagic flux is increased when ABL kinases are depleted. However, this elevation was less pronounced in DDR1 KD settings, where we observed an increase in autophagosomes in fed conditions and an increase in autolysosomes in starved conditions (Supplementary Fig. 2g, right panel). For this reason, we also performed Western blotting to assess LC3/GABARAPL1 lipidation and p62 protein abundances. We observed an increase in LC3-II (Fig. 1e; Supplementary Fig. 2h) and GAPARAPL1-II (Supplementary Fig. 2i) in both the absence and presence of bafilomycin A1 in ABL1/2 KD, and in DDR1 KD settings (Fig. 1f; Supplementary Fig. 2j). This evidence of increased autophagic flux in both ABL1/2 KD and DDR1 KD settings was further confirmed by p62 Western blotting, which showed that ABL1/2 KD (Fig. 1g) as well as DDR1 KD (Fig. 1h) produced a significant decrease in p62 protein abundance, indicating increased autophagic degradation. Finally, due to the availability of the dasatinib (Supplementary Fig. 2k) and imatinib (Supplementary Fig. 2l, m), pharmacological inhibitors of ABL[48], we found that, in agreement with the results described above, ABL inhibition led to a significant increase in

Fig. 1 Lentiviral-based GFP-WIPI1 image-based kinome screen reveals a role for ABL kinases and DDR1 in the control of autophagy. a U2OS cells stably expressing GFP-WIPI1 were seeded in 96-well plates containing the shRNA library followed by 3 h of starvation, fixation and automated GFP-WIPI1 puncta image acquisition and analysis using the InCell Analyzer 1000. Created with BioRender.com. **b** The difference in the fold increase in GFP-WIPI1 puncta cells after transfection with 1103 single target shRNAs compared to control shRNAs is shown. All shRNAs targeting ABL1 (red), DDR1 (yellow) or ULK1/2 (green) are highlighted. Kinases with a difference in fold increase >0.4 were considered candidates. **c** U2OS cells stably expressing GFP-WIPI1 were transfected with siRNAs targeting ABL1 (siABL1), ABL2 (siABL2), DDR1 (siDDR1) or nontargeting control siRNAs (siControl) for 48 h. Prior to automated GFP-WIPI1 image acquisition and analysis using the InCell Analyzer 1000, cells were incubated in control medium (fed), control medium lacking serum (no serum) or starved for 3 h in the presence (+) or absence (−) of bafilomycin A1 (BafA1). The percentages of GFP-WIPI1 puncta cells are displayed. Puncta were defined by automated threshold-based segmentation in terms of intensity and size of the puncta. Two-way ANOVA with Dunnett's post-hoc test, mean ± SD, up to 2758 analysed cells from $n = 6$ for each condition. Representative images are shown in Supplementary Fig. 2c. **d** Using CellProfiler-based single cell analysis of images acquired with automated confocal laser-scanning microscopy (LSM), the number of GFP-WIPI1 puncta per cell (threshold-based puncta segmentation) was determined with single knockdown of either ABL1 or ABL2, or double knockdown of ABL1/2 in fed conditions in the presence or absence of BafA1 as indicated. A two-way ANOVA with Tukey's multiple comparisons test was performed (up to 1241 cells from $n = 3$ for each condition) and error bars show the mean ± SD deviation. **e**, **f** U2OS cells were transfected with siRNAs targeting ABL1/2 (siABL1/2), DDR1 (siDDR1) or nontargeting control siRNAs (siControl) as indicated for 48 h. Protein extracts were analysed by immunoblotting against LC3B and tubulin, and a representative result is shown ($n = 3$, additional immunoblots presented in Supplementary Fig. 2g, i). Numbers indicate LC3-II/tubulin ratios [a.u.]. **g**, **h** Likewise, protein extracts were analysed by immunoblotting against p62 and tubulin (left panels) and relative quantification of p62 protein abundance normalized over tubulin is presented (right panels). Welch's *t* test, mean ± SD, $n = 3$. **i** The kinome screening results with subsequent confirmation are summarized graphically. Created with BioRender.com. Supplementary material is available (Supplementary Figs. 1, 2; Supplementary Data 1). *P* values: $^{*}p < 0.05$; $^{**}p < 0.01$; $^{***}p < 0.001$; ns not significant.

both GFP-WIPI1 and endogenous WIPI2 puncta cells (Supplementary Fig. 2k–l). We also used DPH, a small-molecule allosteric activator of ABL[49], and confirmed its mode of action in U2OS cells by using phosphospecific antibodies for CRKL, a bona fide ABL substrate (Supplementary Fig. 2n). Upon subsequent use of DPH to treat U2OS cells, we found that the number of GFP-WIPI1 puncta per single cell decreased significantly under starved conditions (Supplementary Fig. 2o), further confirming our kinome screening results (Fig. 1i).

ABL kinases and DDR1 inhibit WIPI1 gene expression. Both ABL and DDR1 have been reported to regulate TORC1[50,51], and the TORC1-TFEB pathway affects WIPI1 gene expression[52]. Furthermore, it has been found that increased WIPI1 gene expression is a response to autophagy initiation when TORC1 is inactive[53,54]. Therefore, the question arose whether the gene expression of WIPI1 could change depending on the status of ABL kinases and DDR1. Since GFP-WIPI1 homodimerizes with endogenous WIPI1[9], we first assessed GFP-WIPI1 localization to autophagic membranes (puncta) in the presence or absence of cycloheximide (CHX), an inhibitor of eukaryotic translation, and observed that the increase in GFP-WIPI1 puncta cells evoked by ABL1/2 KD (Supplementary Fig. 3a) and DDR1 KD (Supplementary Fig. 3b) was blunted in the presence of CHX. To assess whether ABL kinases and DDR1 actually have an effect, we approached this point in an unbiased fashion by using a human autophagy pathway-focused gene expression array with 84 genes containing WIPI1 ($n = 3$ in duplicate). Indeed, WIPI1 mRNA was significantly upregulated by 3-fold upon ABL1/2 KD, which we also demonstrated using standard TaqMan assessments (Supplementary Fig. 3c–e). Similarly, DDR1 KD also provoked a significant increase in WIPI1 mRNA abundance, albeit to a lesser extent (Supplementary Fig. 3f–h). In addition, we examined the gene expression of all four WIPI genes, as only WIPI1 was part of the ATG array (Supplementary Fig. 3e, h). In both ABL1/2 KD (Supplementary Fig. 3d) and DDR1 KD (Supplementary Fig. 3g) conditions, additional ATG genes were significantly upregulated, including WIPI4 under ABL1/2 KD conditions (Supplementary Fig. 3e).

ABL kinases and DDR1 inhibit autophagy initiation via MAPK signalling towards MYC. Since we also found additional ATG genes upregulated in the settings of ABL KD (Supplementary Fig. 3c–e, Supplementary Data 1) and DDR1 KD (Supplementary Fig. 3f, g; Supplementary Data 1), we further considered whether the TORC1-TFEB route downstream of ABL and DDR1 could be the reason for our results. To address this question, we decided to perform an unbiased quantitative SILAC-based phospho-proteomics approach, assessing specific and overlapping changes in phosphoproteins of U2OS cells with KD of ABL1/2 and DDR1 (Supplementary Data 1). The rationale for using the KD of ABL1/2 and DDR1 to look for overlapping proteins that showed a changed phospho-status in both KD situations was based on the following initial experiment (Fig. 2a, b). While ABL1/2 KD resulted in the expected significant decrease in phosphorylation of its bona fide target CRKL at Y207 (Fig. 2a), we found that DDR1 KD also resulted in a significant decrease in CRKL phosphorylation (Fig. 2b), suggesting that ABL1/2 and DDR1 could operate on the same signalling axis. When we then turned to the phospho-proteome and compared the ABL1/2 KD and DDR1 KD settings, instead of pointing to the TORC1-TFEB route, our results led us to the ERK signalling axis (Fig. 2c, d; Supplementary Data 1). An increased level of ERK2 phosphorylation at Y187 was revealed in both the ABL1/2 KD and DDR1 KD settings (Fig. 2d; Supplementary Data 1). Y187 is part of the threonine–glutamic acid–tyrosine residue (TEY) motif within the ERK2 activation loop, and activation requires dual phosphorylation at T185 and Y187[55]. Since we observed an unequal phospho-status with more phosphorylation at Y187 but not at T185, ERK2 was in its inactive state, consistent with the established paradigm where ABL and DDR1 activate ERK signalling[43,44]. Notably, we also confirmed a significant increase in ERK2 Y187 phosphorylation by Western blotting in the ABL1/2 KD setting (Fig. 2e) as well as in DDR1 KD settings (Supplementary Fig. 4a).

In agreement with our initial finding concerning CRKL phosphorylation (Fig. 2a, b), our phosphoproteomics analysis further suggested that DDR1 should function upstream of ABL since DDR1 deficiency altered the phospho-status at S290 of ABI1 (Fig. 2d; Supplementary Data 1), an interaction partner and regulator of ABL kinases[56]. Interestingly, in both ABL1/2 KD and DDR1 KD settings, phosphorylation of MAX—a DNA-binding protein that heterodimerizes with MYC to transcriptionally control target gene expression involved in various cellular behaviours ranging from proliferation to lifespan control[57]—at S2 and S11[58] was significantly altered (Fig. 2d, f; Supplementary Data 1). That this is relevant in this context to the heteromeric function of MYC-MAX downstream of ERK and dependent on

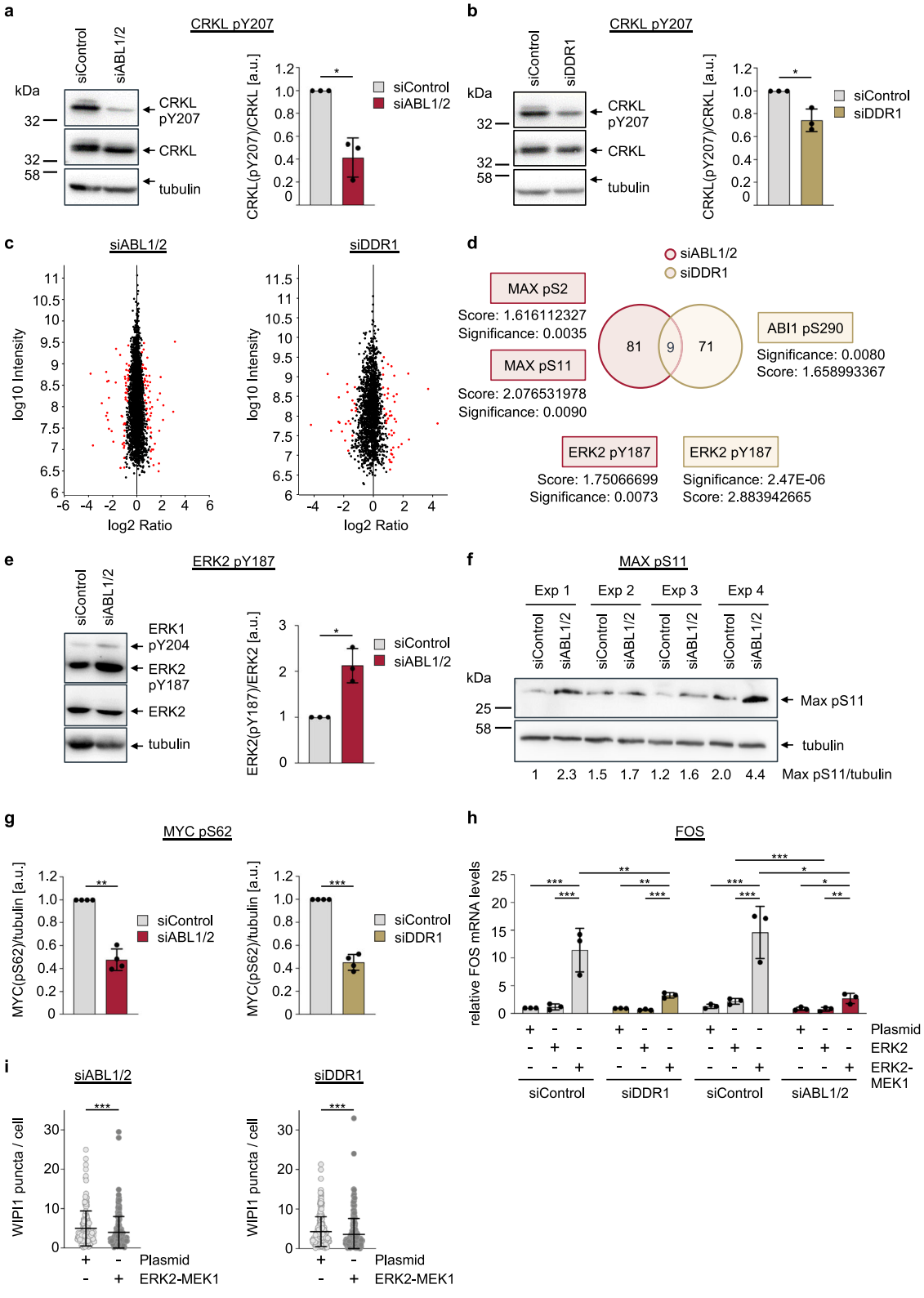

ABL and DDR1 was then indicated when we assessed S62 phosphorylation of MYC, a bona fide target site for ERK[37], required for transcriptional transactivation[59]. We found that both ABL1/2 KD and DDR1 KD (Fig. 2g) significantly decreased the abundance of phospho-S62 MYC, in line with ERK being inactive in this context. That ERK2 is inactive in the absence of ABL1/2 or DDR1 is also shown by employing a construct expressing constitutively active ERK as a myc-ERK2-MEK1 fusion protein[60] and scoring for FOS gene expression upon ABL1/2 KD and DDR1 KD (Fig. 2h). Consistent with this result, in both ABL1/2 KD and DDR1 KD settings, GFP-WIPI1 puncta counts decreased significantly when the ERK2-MEK1 fusion protein was over-expressed, as shown in automated single-cell image analysis (Fig. 2i).

In addition, although our phospho-proteomics analysis showed no change in the TORC1-TFEB route, we analysed several mTOR

Fig. 2 DDR1 and ABL1/2 signal via ERK2-MYC in the control of autophagy. a, **b** U2OS cells stably expressing GFP-WIPI1 were transfected with siRNAs targeting ABL1/2 (siABL1/2), DDR1 (siDDR1) or nontargeting control siRNAs (siControl) for 48 h as indicated. Cell extracts were analysed by immunoblotting against CRKL pTyr207, CRKL or tubulin. Representative immunoblots (left panels) and quantifications are presented (right panels). Welch's *t* test, mean ± SD, $n = 3$. **c** SILAC-based quantitative phosphoproteomics comparing siControl, siABL1/2 and siDDR1 settings. Scatterplot of all phosphosites detected in phospho-SILAC upon downregulation of ABL1/2 (left) or DDR1 (right). Phosphorylation ratios of target siRNA/control siRNA (log(2) versus log(10)) signal intensity are plotted. Significant changes ($p < 0.05$) are highlighted in red. **d** Venn diagram of significantly changed phosphosites along with overlaps. **e** Changes in ERK2 phosphorylation following ABL1/2 knockdown were confirmed by Western blotting. U2OS cells were transfected with siABL1/2 or nontargeting siRNA (siControl) for 48 h, and cell extracts were analysed by immunoblotting against ERK1/2 p-Y204/Y187, ERK2 and tubulin. Quantification of protein abundance was conducted by Welch's *t* test, mean ± SD, $n = 3$. **f** Confirmation of increased MAX p-Ser11 phosphorylation is displayed ($n = 4$, indicated as Exp 1 through Exp 4). **g** U2OS cells were transfected with siABL1/2 or siDDR1 and the corresponding nontarget control (siControl) for 48 h and then treated with 10 μM MG132 for 3 h to prevent proteasomal MYC degradation. Protein extracts were analysed by immunoblotting against MYC p-Ser62, MYC or tubulin. Welch's *t* test, mean ± SD, $n = 4$. **h** U2OS cells were treated with siRNAs targeting ABL1/2 or DDR1 for 16 h prior to transfection with empty control plasmids or with plasmids encoding myc-tagged ERK2 or myc-tagged ERK2-MEK1 for 48 h. Total RNA was extracted, and relative FOS gene expression was analysed by qPCR. Two-way ANOVA with Tukey's multiple comparison's test, mean ± SD, $n = 3$ in triplicates. **i** Using CellProfiler-based single cell analysis of images acquired with automated confocal laser-scanning microscopy (LSM), the number of GFP-WIPI1 puncta per cell (threshold-based puncta segmentation) was determined in ABL1/2 KD (left panel) or DDR1 KD (right panel) U2OS cells overexpressing empty control plasmids or myc-tagged ERK2-MEK1 for 48 h in fed conditions. Welch's *t* testing was performed (up to 1496 cells from $n = 3$ for each condition) and error bars show the mean ± SD deviation. Supplementary material is available (Supplementary Data 1). *P* values: $^{*}p < 0.05$; $^{**}p < 0.01$; $^{***}p < 0.001$; ns not significant.

targets by quantitative Western blotting, including TFEB, in the settings ABL1/2 KD, DDR1 KD, ERK2 KD and MYC KD (Supplementary Fig. 4b–l). Down-regulation of neither ABL1/2 nor DDR1 altered TFEB phosphorylation at the mTOR target site S211 (Supplementary Fig. 4b), and ABL/DDR1 KD had no additive effect on TFEB pS211 either (Supplementary Fig. 4b). It is also worth noting in this context that ABL1/2 KD and DDR1 KD also had no effect on the mTOR target site ULK1 pS758, which serves as a switch for autophagy initiation, while treatment with the specific mTOR inhibitor Torin 1, as expected, resulted in a significantly reduced level of ULK1 pS758 (Supplementary Fig. 4c, d). Likewise, the phosphostatus of S6K pT389 remained unchanged in the ABL1/2 KD and DDR1 KD settings (Supplementary Fig. 4c, e). In line with these results, down-regulation of neither ERK2 nor c-MYC altered the phosphostatus of ULK1 pS758 or S6K pT389 (Supplementary Fig. 4g–k). The significant changes in the ABL-ERK-MYC axis detected by our phosphoproteome analysis are therefore not to be classified in the context of the TORC1 signaling pathway and therefore the following experiment is also to be understood in full agreement with this hypothesis. When we downregulated ABL1/2 or DDR1, we showed that the autophagic flux was increased, as indicated by decreased p62 levels (Fig. 1g, h). Now, when we performed this experiment in the presence of Torin 1, p62 levels decreased significantly further (Supplementary Fig. 4f), suggesting that ABL-ERK-MYC and TORC1 signalling are additive pathways in controlling the autophagic flux. In this context, we confirmed that ABL1/2 and DDR1 do not display an additive effect on p62 degradation (Supplementary Fig. 4l).

MYC binds to the WIPI1 promoter and represses WIPI1 gene expression. Since unbiased analysis of ATG gene expression in both ABL1/2 KD and DDR1 KD settings revealed that WIPI1 gene expression increased in this context (Supplementary Fig. 3), and our proteomic analysis pointed towards the transcription factor MYC/MAX, we now asked whether MYC-MAX deficiency affects WIPI1 gene expression. Indeed, we were able to show through qPCR assessments that the absence of MYC or MAX significantly increased WIPI1 gene expression (Fig. 3a). Furthermore, we also pursued this question in an unbiased manner using the human autophagy pathway-focused gene expression array with 84 genes containing WIPI1 that we already used for ABL1/2 KD and DDR1 KD settings (Supplementary Fig. 3). Again, WIPI1 mRNA was significantly up-regulated and scored as a positive hit on MYC KD (Supplementary Fig. 5a). Likewise, as in ABL1/2 KD and DDR1 KD settings, additional ATG genes were upregulated after downregulation of MYC (Supplementary Fig. 5a), and in overlap with the ABL1/2 KD phenotype, WIPI4 was upregulated, albeit to a much lesser degree compared to WIPI1 (Supplementary Figs. 3e, 5b). As in the ABL1/2 KD and DDR1 KD settings, WIPI2 and WIPI3 are not significantly upregulated (Supplementary Figs. 3e, h, 5b). Since the upregulation of WIPI1 was an overlapping result after ABL1/2 KD, DDR1 KD and MYC KD (Supplementary Fig. 3, Fig. 3a; Supplementary Fig. 5a, b), and this being most pronounced compared to the other WIPI genes (Supplementary Figs. 3e, h, 5b), we subsequently focused on further characterizing WIPI1 gene expression in the context of the ABL-MYC signalling axis.

In this context, we wanted to assess whether ERK2 inactivation would also increase WIPI1 gene expression. To this end, we treated U2OS cells with AZD0364, an ERK2 inhibitor, which significantly reduced ERK-mediated phosphorylation of S62 in MYC (Fig. 3b), phenocopying the effect of ABL1/2 KD and DDR1 KD on ERK phosphorylation at Y187. Clearly, administration of AZD0364 over time elicited a significant upregulation of WIPI1 mRNA levels, showing that ERK inhibition also provoked an increase in WIPI1 gene expression (Fig. 3c). Furthermore, the AZD0364-mediated increase in WIPI1 gene expression was significantly reduced when c-MYC was simultaneously overexpressed in the siControl, and in siABL1/2 settings the AZD0364-mediated increase in WIPI1 expression was attenuated (Supplementary Fig. 5c). To verify that AZD0364 impacts ERK2-mediated changes in gene expression, we used FOS as a bona fide read-out for ERK-mediated transcription control and demonstrated that ERK inhibition by AZD0364 inhibited FOS gene expression as expected (Fig. 3d).

To investigate further, we next asked if MYC-MAX could directly control WIPI1 gene expression by binding to the WIPI1 promoter. For this purpose, we used the ConTra v3 webserver[61] to predict E-boxes (Fig. 3e; Supplementary Fig. 5d-f), classic MYC-MAX binding sites[62] (Fig. 3e, upper left panel) in the human WIPI1 promoter and identified candidate E-boxes termed M19, M11 and M + 1 hereafter (Fig. 3e, upper right panel, lower panel). In this context, we recognized that M + 1 is positioned at a specific site in the WIPI1 promoter previously shown to be occupied by histone methyltransferase G9a/EHMT2[63] (Fig. 3e, lower panel). Since the heterodimer MYC-MAX interacts with G9a to repress transcription of target genes[64], we tested whether MYC could bind to the predicted E-boxes (M11, M19) as well to

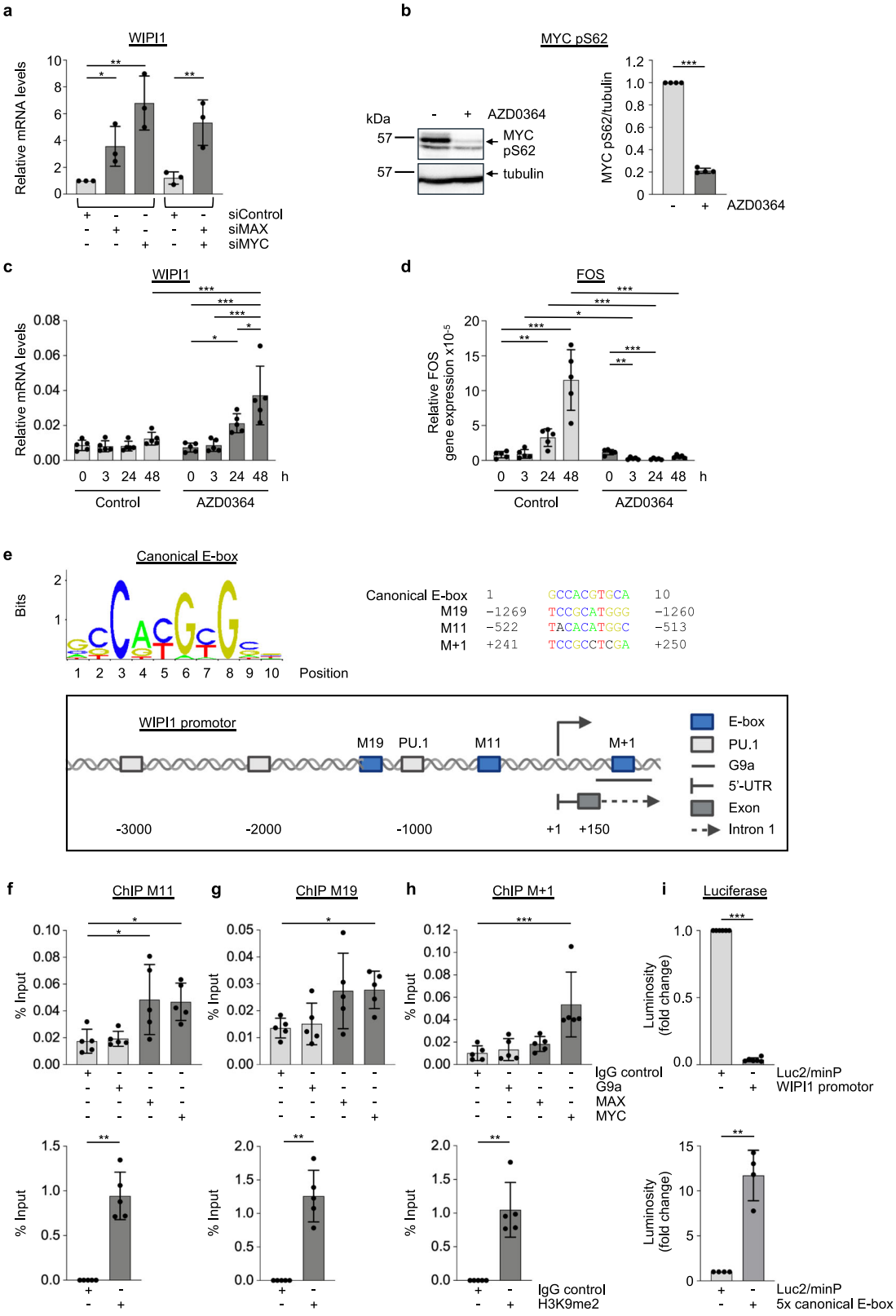

the region occupied by G9a (M + 1) in the WIPI1 promoter by conducting chromatin immunoprecipitation (ChIP). In addition, we performed ChIPs with anti-H3K9me2 antibodies as repressive marks since MYC-MAX in complex with G9a regulates H3K9me2 dimethylation[64]. This evaluation revealed that MYC and MAX bind to the WIPI1 promoter at the M11 E-box (Fig. 3f, upper panel) and MYC further to the M19 E-box (Fig. 3g, upper panel), located upstream of the transcription initiation site (+1) (Fig. 3e, lower panel), marked as repressive sites by H3K9me2 occupancy (Fig. 3f, g; lower panels). Likewise, MYC could also bind to the M + 1 E-box in the WIPI1 promoter downstream of the transcription initiation site (Fig. 3h, e; lower panel). Based on these results, we performed luciferase reporter assays and confirmed that a partial WIPI1 promoter sequence, including

Fig. 3 MYC represses WIPI1 gene expression. a MAX, MYC or both were transiently downregulated using siRNAs in U2OS cells for 72 h, and total RNA was extracted, followed by assessing WIPI1 mRNA levels by RT–qPCR. One-way ANOVA with Holm-Sidak post-hoc testing, mean ± SD, $n = 3$. **b** U2OS cells were treated with 10 μM AZD0364 for 48 h, and during the last 3 h, 10 μM MG132 was added to prevent proteasomal MYC degradation. Cell extracts were analysed by immunoblotting against MYC p-Ser62, MYC or tubulin, (left panel: representative Western blot, right panel: quantification). Welch's t test, mean ± SD, $n = 4$. **c**, **d** U2OS cells were treated with or without 10 μM AZD0364 for 0, 3, 24 or 48 h. Total RNA was extracted, and relative WIPI1 (**c**) or FOS (**d**) gene expression was analysed by RT–qPCR. Two-way ANOVA with Tukey's post hoc testing, mean ± SD, $n = 5$. **e** Canonical E-box sequence used to identify potential E-boxes in the human WIPI1 promoter (left upper panel) using ConTra v3. Clustal Omega-based multiple nucleotide sequence alignment using a canonical E-box sequence along with putative E-boxes (M + 1, M11, M19) in the human WIPI1 promoter (upper right panel, indicated are the positions relative to the transcription start site (+1) according to Ensembl Release 109 (Feb 2023), transcript ID ENST00000262139.10 WIPI1-201). A schematic WIPI1 promoter overview with putative E-boxes was created with BioRender.com. Published binding sites for PU.1 are additionally indicated. **f–h** U2OS cells were crosslinked, and chromatin immunoprecipitation against G9A, MAX, MYC or negative control IgG was performed. qPCR against M11 (**f**), M19 (**g**) or M + 1 (**h**) binding sites was conducted, the %input was calculated and analysed with one-way ANOVA followed by Dunnett's post-hoc testing (mean ± SD, $n = 5$) (upper panels). Alternatively, chromatin immunoprecipitation was performed against H2K9me2 (lower panels). Welch's *t* test, mean ± SD, $n = 5$. **i** Dual-luciferase reporter assays were conducted using U2OS co-transfected for 24 h with pGL4.73[hRluc/SV40] expressing Renilla luciferase together with plasmids with the potential to drive firefly luciferase from a minimal promotor: empty pGL4.23[luc2/minP] plasmid (Luc2/minP), pGL4.23-WIPI1promotor (WIPI1 promotor, upper panel, $n = 6$) or pGL4.23-5xE-box (5x canonical E-box, lower panel, $n = 4$). Firefly- and Renilla luciferase activities were measured via luminosity and firefly luminosity normalized to Renilla luminosity for each sample. For statistical analysis, an unpaired *t*-test with Welch's correction was performed. Error bars show the mean ± Standard deviation. Supplementary material is available (Supplementary Fig. 4a–c; Supplementary Data 1). *P* values: $^{*}p < 0.05$; $^{**}p < 0.01$; $^{***}p < 0.001$; ns not significant.

E-boxes M19, M11, and M + 1 (Supplementary Fig. 5g), represses the minimal promoter activity driving firefly luciferase (Fig. 3i, upper panel). As a positive control for MYC-mediated activation, we used a sequence with five canonical E-boxes (Supplementary Fig. 5h), which activated minimal promoter activity on firefly luciferase (Fig. 3i, lower panel). Our analysis is consistent with the result from a global genome mapping approach that found that MYC can bind to the WIPI1 promoter, although this interaction had not yet been further characterized at the time[65]. Our results further support the idea that MYC represses WIPI1 gene expression, and when we then performed a WIPI1/MYC gene expression correlation meta-analysis with Genevestigator, a large-scale microarray reference database and analysis tool, we indeed found that high MYC expression correlates with low WIPI1 gene expression in various human cell lines (Supplementary Fig. 5i).

Elevated WIPI1 protein levels enhance autophagy initiation across cell boundaries. Combined, our results obtained up to this point provided evidence that the ABL-ERK-MYC axis negatively controls WIPI1 gene expression and that DDR1 may act upstream of ABL in this context. We committed at this stage to analyse the potential signalling pathway from DDR1 to ABL with an additional approach and here to focus more on effects resulting from increased WIPI1 levels. Because WIPI1, in contrast to WIPI2, is expressed at extremely low levels[30], we transiently overexpressed 9E10-tagged WIPI1 using increasing concentrations of plasmids and observed that an increased level of overexpressed WIPI1 correlated with an increase in lipidated LC3 (Fig. 4a; Supplementary Fig. 6a). Consistent with this result, quantification of LC3 lipidation in fed conditions in the presence or absence of lysosomal inhibitor upon overexpression of 9E10-WIPI1 demonstrated significantly increased autophagic flux (Fig. 4b, Cas9 control). The autophagic flux was less pronounced in WIPI1 KO cells (Fig. 4b; Supplementary Fig. 6b, c) as seen under fed conditions comparing minus and plus BafA1 settings, when overexpressing the empty 9E10 vector control (Fig. 4b). However, this deficiency was rescued by overexpression of 9E10-WIPI1 (Fig. 4b). Likewise, we also found that the number of GFP-WIPI2B puncta cells increased significantly when mCherry-WIPI1 was overexpressed (Fig. 4c), and conversely, that the absence of WIPI1 decreased the number of endogenous WIPI2 puncta in both ABL1/2 KD and DDR1 KD settings, as shown by automated single-cell image analysis (Fig. 4d). As WIPI1 is the interaction partner of WIPI2 and is expected to support WIPI2-mediated LC3 lipidation, we have detailed the WIPI2 response in terms of its localization to autophagic membranes. To this end, we overexpressed GFP-WIPI1 under both fed and starved conditions and in the absence or presence of bafilomycin A1 and immunostained endogenous WIPI2. Again, we observed that an increase in WIPI1 protein caused an increase in WIPI2 puncta cells, particularly under starved conditions (Fig. 4e, left panel; Supplementary Fig. 6d). In this context, we observed that typical WIPI1 structures, elongated puncta mainly in the perinuclear region[7], became visible for WIPI2 only when WIPI1 was overexpressed (Fig. 4e, right panel; Supplementary Fig. 6d), suggesting that WIPI1 can promote WIPI2 localization towards autophagic membranes. If this is the case, we hypothesized that treatments that counteract the ABL-ERK-MYC axis and induce WIPI1 gene expression should also affect WIPI2 localization to autophagic membranes. Indeed, both ABL inhibition by the pharmacologically selective inhibitor dasatinib and MYC inhibition by 10058-F4 or 10074-G5, specific compounds that prevent MYC-MAX heterodimerization and inhibit the regulation of MYC target genes, resulted in an increase in WIPI2 puncta cells (Supplementary Fig. 2k). Likewise, ERK inhibition by AZD0364 resulted in an increase in WIPI2 puncta over time (Supplementary Fig. 6e) as well as an increased p62 degradation (Supplementary Fig. 6f), a response that correlates with an increase in WIPI1 gene expression (Fig. 3c) and that was blunted by inhibiting gene expression using CHX (Supplementary Fig. 3a, b). These assessments suggest that increasing WIPI1 levels can increase autophagy levels to a certain extent. This idea was further supported by correlative light electron microscopy observations, which revealed that perinuclear, elongated WIPI1 puncta represent multiple formed phagophores at the same site (Fig. 5a). Moreover, such multiple phagophore production sites were found to develop with prolonged starvation (Fig. 5b). Since multiple phagophore formation sites should be associated with omegasomes, we evaluated GFP-WIPI1 puncta by live cell microscopy and indeed showed that elongated GFP-WIPI1 puncta are highly dynamic and resemble omegasomes (Fig. 5c, Supplementary Video 1), at which WIPI2 is located, as previously shown[27]. Next, we confirmed that elongated GFP-WIPI1 puncta are not a result of a blockage downstream in the pathway of forming productive autophagosomes by performing the following live-cell microscopy experiment. First, we starved cells and then treated these starved cells with the PI3P inhibitor LY2940002, resulting in cells lacking any GFP-WIPI1 puncta (Fig. 5d, left upper panels). Importantly,

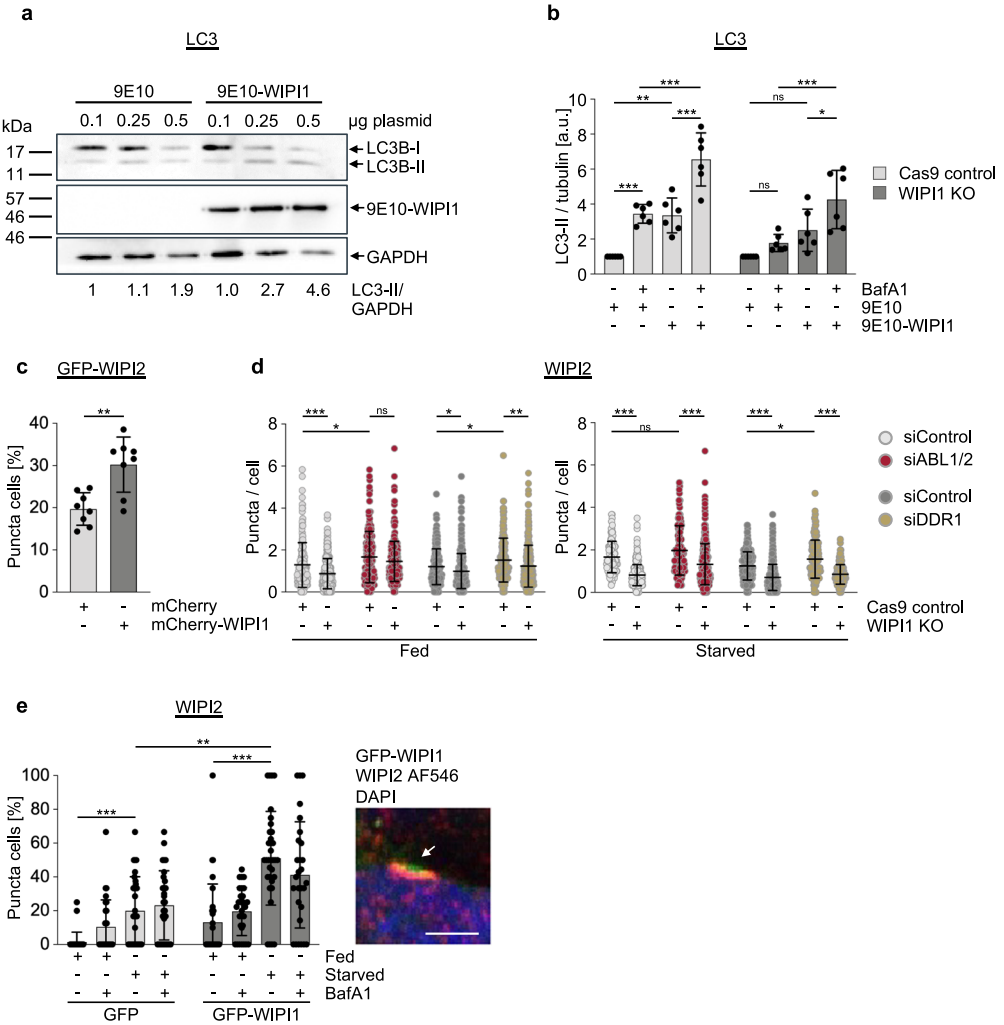

Fig. 4 Increase of WIPI1 protein enhances autophagic flux. a Immunoblot analysis of LC3B lipidation in U2OS cells after transfection with control plasmids (9E10) or plasmids encoding 9E10-tagged WIPI1. U2OS cells were transfected with the indicated amounts of plasmids for 48 h before protein extraction and immunoblotting against LC3B, 9E10-tagged WIPI1 or GAPDH, $n = 3$. Additional immunoblots provided in Supplementary Fig. 5a. **b** U2OS Cas9 control or U2OS WIPI1 KO cells were transfected with control plasmids (9E10) or plasmids encoding 9E10-tagged WIPI1 for 48 h, followed by treatment with bafilomycin A1 (BafA1) in fed conditions for 3 h. Immunoblotting was conducted against LC3B, 9E10 and tubulin ($n = 6$, mean ± SD, Two-way ANOVA with Tukey's multiple comparisons test). WIPI1 deficiency control Taqman qPCR is presented in Supplementary Fig. 6b, and representative Western blots in Supplementary Fig. 6c. **c** U2OS cells stably expressing GFP-WIPI2 were transfected with control plasmids or plasmids encoding mCherry-tagged WIPI1 for 48 h. The numbers of GFP-WIPI2 puncta cells were assessed by fluorescence microscopy in transfected cells. Welch's t test, mean ± SD, up to 1272 analysed cells from $n = 4$ in duplicates. **d** U2OS Cas9 control or U2-OS WIPI1-KO cells were seeded into 96-well glass bottom plates and transfected with siABL1/2, siDDR1 or nontargeting siRNA (siControl) for 48 h, followed by treatment with either DMEM/FBS (fed) or EBSS (starved) for 3 h. After fixation, cells were stained with DAPI and anti-WIPI2/AF488. By automated confocal LSM, 20 images per well were acquired and between 621 to 2563 single cells (from $n = 3$) subjected to automated CellProfiler-based image analysis (threshold-based puncta segmentation). For statistical analysis, a two-way ANOVA with Tukey's multiple comparisons test was performed (mean ± SD). **e** G361 cells were transfected with plasmids encoding GFP or GFP-WIPI1 and were fed or starved for 3 h in the presence or absence of bafilomycin A1, followed by anti-WIPI2/AF546 immunofluorescence staining. Confocal LSM stacks were acquired, and the numbers of WIPI2 puncta-positive cells per acquired image (individual data points represent the result derived from each image) were counted (left panel: two-way ANOVA with Tukey's post-hoc test, mean ± SD, up to 215 single cells from $n = 3$ for each condition). Indicative of the presence of overexpressed GFP-WIPI1 are elongated, perinuclear autophagic membranes found to colocalize with WIPI2 (right panel: Scale bar: 5 µm, extended image presentation in Supplementary Fig. 5b). Supplementary material is available (Supplementary Fig. 6d; Supplementary Data 1). *P* values: $^{*}p < 0.05$; $^{**}p < 0.01$; $^{***}p < 0.001$; ns not significant.

we conducted the same experiment but in the presence of bafilomycin A1, blocking the autophagic pathway at the lysosome level (Fig. 5d, left lower panels). This demonstrated that elongated GFP-WIPI1 puncta (marked with arrows) disappeared in starved cells that were first treated with bafilomycin A1 and afterwards with the PI3P inhibitor LY2940002, indicating that elongated GFP-WIPI1 puncta formation is the result of newly formed autophagic membranes and not the result of a block in autophagic flux. This idea was further supported by measuring the disappearance time of perinuclear elongated GFP-WIPI1 puncta in cells treated with LY2940002 after starvation (3 h) in the presence or absence of bafilomycin, with the disappearance time being similar in both conditions (Fig. 5d, right panel). Finally, we confirmed that GFP-WIPI1 preferentially binds to PI3P over $PI(3,5)P_2$[9,14] by generating giant unilamellar vesicles (GUVs) containing either PI3P or $PI(3,5)P_2$ and then quantifying

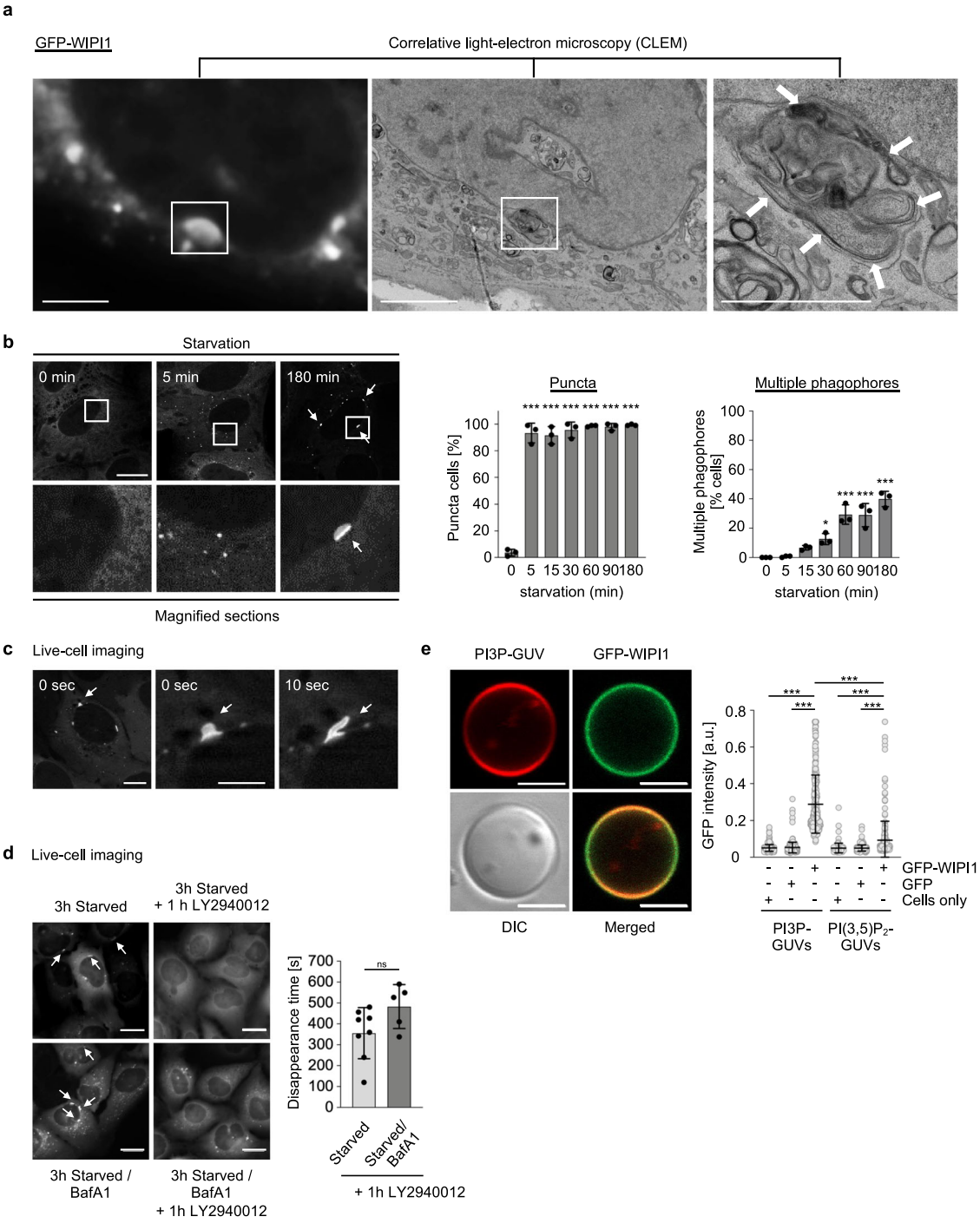

the binding efficiency of GFP-WIPI1 derived from native cell extracts (Fig. 5e; Supplementary Fig. 7a–c). Taken together, these data suggest that WIPI1 should act as an enhancer of autophagy.

While assessing the intracellular WIPI1 localization, we observed that the formation of WIPI1 puncta was not uniform in cell monolayers and that cells with high puncta content sometimes lie adjacent to cells with little or no puncta content, even though all cells were starved. We hypothesized that there might be a compensatory mechanism that allows sufficient autophagy in all cells and assessed whether autophagic membranes positive for WIPI1, WIPI2, or LC3 could reach neighbouring cells, perhaps through tunnelling nanotubes (TNTs), intercellular bridges (Fig. 6a) through which cells exchange organelles, such as lysosomes[66–69]. In fact, we found that U2OS cells can form TNTs, stained here with phalloidin to detect F-actin and with wheat germ agglutinin (WGA) to visualize the plasma membrane (Fig. 6b). Alternatively, we stained cells with phalloidin and an anti-tubulin antibody and confirmed that TNTs in U2OS cells could also contain both F-actin and tubulin (Supplementary Fig. 8a) according to previous observations in different cell types[66]. In line with this, TNTs did not form in the presence of latrunculin A, an F-actin inhibitor, or nocodazole, a tubulin inhibitor (Supplementary Fig. 8b). Since it has been found that lysosomes can move through TNTs[70], we asked if autophagic membranes could be observed in TNTs. For this aim we used a stable GFP-WIPI1 U2OS cell line as well as a stable tandem fluorescent RFP-GFP-LC3 U2OS cell line (Fig. 6c) and observed that, indeed, autophagic membranes are

Fig. 5 Elevation of WIPI1 protein abundance enhances phagophore formation. a Correlative light (left panel) electron microscopy (middle, right panel) of U2OS cells stably expressing GFP-WIPI1. Elongated, perinuclear autophagic membranes decorated with WIPI1 (left panel) were found to represent the presence of multiple phagophore-like membranes (indicated with white arrows, right panel). Scale bars: 20 μm (left panel), 5 μm (middle panel), 2 μm (right panel). **b** Time-course analyses of WIPI1 puncta formation after transient inhibition of PI3P synthesis. Stable U2OS GFP-WIPI1 cells were pretreated with LY294002 (100 μM) for 3 h, followed by starvation for 5, 15, 30, 60, 90 min as indicated. Representative images were acquired by confocal LSM (scale bar: 20 μm). The numbers of WIPI1 puncta cells (middle panel) and the numbers of cells harbouring elongated, perinuclear autophagic membranes decorated with GFP-WIPI1 (right panel) were quantified by fluorescence microscopy (one-way ANOVA with Dunnett's post-hoc test, mean ± SD, 300 cells from $n = 3$). **c** Stable U2OS GFP-WIPI1 cells were starved and analysed by live-cell microscopy. Still images from Supplementary Video 1 displaying omegasome-like structures decorated with GFP-WIPI1 are displayed. **d** GFP-WIPI1-positive phagophores are sensitive to the inhibition of PI3P synthesis. U2OS cells stably expressing GFP-WIPI1 were starved with or without bafilomycin A1 (BafA1) and subjected to live-cell microscopy. Approximately 3 h after autophagy induction by starvation, LY294002 (100 μM) was added. The disappearance of WIPI1-positive perinuclear phagophores after LY294002 treatment was determined by live-cell microscopy and representative still images are shown (left panels, scale bar: 20 μm). Quantifications are provided in the right panels (Welch's t test, mean ± SD, $n = 8$ videos for starved conditions, $n = 5$ videos for starved/BafA1 conditions). **e** Rhodamine-PE GUVs containing PI(3)P (representative images, left panels, scale bar: 5 μm) or PI(3,5)P_2 (images shown with controls in Supplementary Fig. 7) were incubated with native protein extracts from U2OS cells stably expressing GFP-WIPI1 or GFP, along with parental U2OS cells, followed by confocal LSM imaging. CellProfiler-based image analysis was used to measure the GFP intensity on GUV edges (right panels, Kruskal–Wallis with Dunn's post-hoc testing, up to 404 GUVs analysed from $n = 3$ for each condition). Supplementary material is available (Supplementary Fig. 7; Supplementary Video 1; Supplementary Data 1). P values: $^{*}p < 0.05$; $^{**}p < 0.01$; $^{***}p < 0.001$; ns not significant.

present in TNTs, and such GFP-WIPI1-harbouring TNTs are exemplified using a 3D video reconstruction from confocal laser-scanning microscopy (Supplementary Video 2), and a still image from this video displaying GFP-WIPI1 puncta in a TNT is shown (Fig. 6c, left panel). That autophagosomes are also found in TNTs is indicated by the identification of RFP-GFP-LC3 puncta in TNTs (Fig. 6c, right panel; Supplementary Video 3).

On this basis, we extended TNT assessment in U2OS cells stably expressing GFP-WIPI1 using fed and starved conditions (Fig. 6d). While the number of puncta-positive GFP-WIPI1 cells increased significantly during starvation-induced autophagy, as expected (Fig. 6d, left panel), the number of TNTs also increased (Fig. 6d, middle panel), as did the number of TNTs containing GFP-WIPI1 puncta (Fig. 6d, right panel). Furthermore, we found that the presence or absence of WIPI1 affects TNT formation (Fig. 6e, f). Transient overexpression of GFP-WIPI1 significantly increased the number of TNTs (Fig. 6e), while WIPI1 deficiency significantly decreased the number of TNTs and starvation-induced TNT formation was significantly attenuated in U2OS cells (Fig. 6f; Supplementary Fig. 8c, d). Importantly, using live-cell microscopy, we tracked GFP-WIPI1 puncta through the TNTs (Fig. 6g; Supplementary Video 4, 5). These results demonstrate that starvation-induced autophagy is accompanied by the formation of TNTs and the transport of autophagic membranes to neighbouring cells via the TNTs. To investigate further, asking if autophagic membranes can indeed invade neighbouring cells and whether such a scenario could represent a compensatory response to certain cells with low autophagic activity, we developed the following experimental design. We used cocultures of U2OS cells stably expressing GFP-WIPI1, GFP-WIPI2B or GFP-LC3[9], which were defined as donor cells, along with U2OS containing labelled mitochondria[39], which were defined as recipient cells. U2OS cells with labelled mitochondria expressed ATG16L1 (U2OS WT), were ATG16L1 deficient (U2OS ATG16L1 KO), or expressed ATG16L1 in an ATG16L1 deficient background (U2OS ATG16L1 KO + ATG16L1)[39]. Using this approach, we quantified the number of recipient cells with GFP puncta and showed that trafficking of autophagic membranes positive for GFP-WIPI1 (Fig. 6h), GFP-WIPI2B (Fig. 6i) and GFP-LC3 (Fig. 6j) was significantly increased towards autophagy-incompetent recipient cells (U2OS ATG16L1 KO). Representative images of recipient cells containing GFP-WIPI1, GFP-WIPI2B or GFP-LC3 puncta are shown (Fig. 6k; Supplementary Fig. 8e). Our results suggest that low levels of autophagy in single cells may be compensated for by cell-to-cell communication, with cells with a higher proportion of formed autophagic membranes or autophagosomes spreading a subfraction thereof to cells with low autophagic activity. In this context, it is conceivable that an enhancing role of WIPI1 in the formation of autophagic membranes should therefore also influence the extent of autophagic membrane transport by TNTs. This assumption turned out to be relevant since the transfer of GFP-LC3 positive autophagosomes was significantly increased when WIPI1 was overexpressed (Fig. 6l, m).

ABL deficiency elevates autophagy and extends lifespan in *C. elegans*. In our final component of this study, we wanted to address the role of WIPI1 as an autophagy enhancer in a physiological context. We predicted that if ABL signalling negatively affects WIPI1 expression and autophagy in human cells, this level of autophagy control should also play an important role in lower eukaryotes such as *C. elegans* because the autophagy pathway is evolutionarily conserved. Furthermore, since a large number of previous studies reported that key signalling pathways that control autophagy are important in controlling lifespan through their effect on autophagy[2,71,72], we speculated that ABL deficiency would not only increase autophagy but could therefore also prolong lifespan. In *C. elegans*, ABL1 and ABL2 have a single homologue, ABL-1, and for our studies, we used the *C. elegans* strain XR1 expressing a nonfunctional ABL-1 mutant (*abl-1(ok171)*[73]. In addition, we employed the VC893 strain (*atg-18(gk378)*), lacking ATG-18[74,75], the orthologue for human WIPI1/WIPI2[7,76], and generated an *abl-1(ok171);atg-18(gk378)* double mutant (*abl1;atg-18*). Initially, we assessed the viability of these strains and observed no significant differences in terms of egg-laying capacity (Fig. 7a, left panel), while the progeny that reached the fourth larval (L4) stage were significantly reduced to 10% in the *C. elegans* strain lacking ATG-18 (*atg-18(gk378)*), as previously reported[74,75,77] (Fig. 7a, right panel). This was also observed for the *C. elegans* strain lacking both ABL-1 and ATG-18 function (*abl1;atg-18*) but not when ABL1 function alone was missing (*abl-1(ok171)*) (Fig. 7a, right panel). Next, we assessed the recovery of first-stage (L1) larvae after prolonged starvation followed by unrestricted feeding (Fig. 7b), indicating autophagy-mediated compensation for nutrient deficiencies in early life[75]. In a time course experiment, we starved L1 larvae for extended periods of time (days of starvation) and then unrestrictedly subjected larvae to food and counted the number of larvae able to survive and progress beyond the L2 larvae stage (Fig. 7b). As

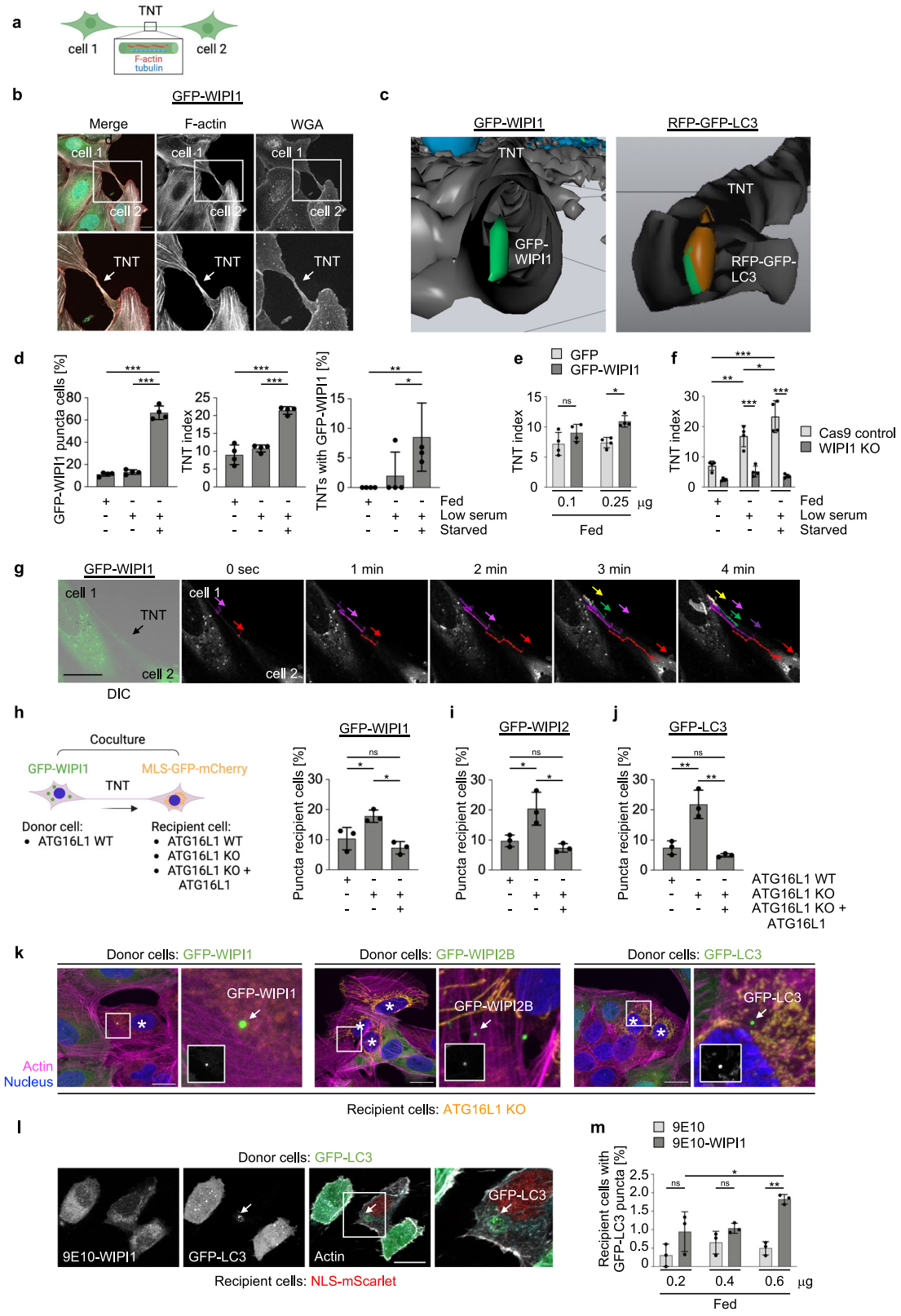

expected, *atg-18(gk378)* larvae were unable to recover from starvation of more than one day[75]. Only 5% of the *abl-1;atg-18* double mutant larvae were able to recover from up to 3 days of starvation, but not beyond 3 days (Fig. 7b). In contrast, *abl-1(ok171)* larvae were able to survive and recover from prolonged starvation of up to 29 days, as were wild-type larvae (Fig. 7b). Further, we demonstrate that in this context, autophagy is indeed more active in L1 larvae without ABL-1 function (*abl-1(ok171)*) by measuring the level of cleaved GFP in *abl-1(ok171)* nematodes carrying a GFP::LGG1 reporter transgene. Compared to wild-type nematodes, *abl-1(ok171)* nematodes showed significantly increased levels of cleaved GFP, indicating an increase in autophagic flux (Fig. 7c). In line with this result, both the number and size of GFP-LGG1 puncta increased significantly in

Fig. 6 WIPI1-, WIPI2- and LC3-decorated autophagic membranes migrate through tunnelling nanotubes (TNTs) to neighbouring cells with limited autophagic activity. a Scheme displaying a TNT connecting two cells. Created with BioRender.com. **b** U2OS cells stably expressing GFP-WIPI1 form TNTs. U2OS GFP-WIPI1 cells were costained with phalloidin-AF546 to visualize F-actin and with WGA-AF647 to visualize the plasma membrane. Merged channels (left panels) are shown as well as split channels displaying F-actin (middle panels) and WGA only (right panels). Boxes (upper panels) indicate magnified sections (lower panels), and arrows point at a TNT connecting two cells. Scale bar: 20 µm. **c** Starved (24 h) U2OS cells stably expressing GFP-WIPI1 were stained with phalloidin-AF546 and DAPI and imaged by confocal LSM. A video was generated from the 3D reconstruction of confocal z-stacks (Supplementary Video 2), and a still image displaying GFP-WIPI1 puncta within a TNT is presented (left panel). Likewise, a video was generated from the 3D reconstruction of confocal z-stacks (Supplementary Video 3), and a still image revealing the presence of RFP-GFP-LC3 puncta within a TNT is shown (right panel). **d** U2OS GFP-WIPI1 cells were fed for 24 h with high (10%, fed) or low (2.5%, low serum) serum or starved as indicated. GFP-WIPI1 puncta-positive cells were counted (left panel), as well as the numbers of TNTs per 100 cells (TNT index, middle panel) and the numbers (%) of TNTs containing GFP-WIPI1 puncta (right panel). One-way ANOVA with Holm-Sidak post-hoc test, up to 952 cells from $n = 4$ for each condition. **e** U2OS cells were transfected with plasmids encoding GFP or GFP-WIPI1 in the concentrations of 0.1 µg or 0.25 µg for 48 h, then re-seeded onto coverslips and cultured for 24 h in fed conditions. After fixation, cells were stained with DAPI, and F-actin stained with phalloidin-AF546 and tubulin with anti-αTubulin/AF647. The TNT index was calculated from up to 1057 cells per condition ($n = 4$). Two-way ANOVA, Tukey's post-hoc test. Scale bar: 20 µm. **f** U2OS Cas9 control and U2OS WIPI1 KO were seeded onto coverslips and cultured overnight (16 h) and then fed for 24 h with high (10%, fed) or low (2.5%, low serum) serum or starved as indicated. Cells were stained with DAPI, WGA-AF488, phalloidin-AF546, anti-αTubulin/AF647 and the TNT index determined from up to 1440 cells per condition ($n = 4$, two-way ANOVA, Tukey's post-hoc test). Representative image panels are shown in Supplementary Fig. 8c, d. **g** Airyscan superresolution live time-series microscopy (~30 min., Supplementary Video 4) of U2OS cells stably expressing GFP-WIPI1 was conducted, and merged GFP and brightfield channels are displayed (left image). Using the plug-in MTrackJ in Fiji, GFP-WIPI1 puncta were tracked within a TNT connecting two cells, and GFP-WIPI1 tracks of different puncta are indicated in distinct colours whereby the movement direction is indicated with colour-corresponding arrows (Supplementary Video 5). Scale bar: 20 µm. **h** U2OS GFP-WIPI1, **i** U2OS GFP-WIPI2 or **j** U2OS GFP-LC3 donor cells were cocultured (ratio 1:1) in fed conditions for 24 h with recipient U2OS cells either expressing wild-type ATG16L1 (WT) or not (U2OS ATG16L1 KO), along with ATG16L1 KO cells reconstituted for WT ATG16L1 (ATG16L1 KO + ATG16L1 WT). GFP puncta fluorescence from GFP-WIPI1, GFP-WIPI2 or GFP-LC3 within recipient MLS-EGFP-mCherry ATG16L1 U2OS cell lines bearing labelled mitochondria was clearly distinguishable from mitochondria, which appeared as orange fluorescence in recipient cells and which lacked GFP only puncta. Based on this, the numbers of recipient cells harbouring GFP-WIPI1 (**h**), GFP-WIPI2B (**i**) or GFP-LC3 (**j**) puncta were counted (one-way ANOVA with Holm-Sidak post-hoc test, up to 650 cells from $n = 3$ for each condition). **k** Representative merged images are displayed from (**h**) to (**j**), and green fluorescent puncta (arrows) in recipient cells (white asterisks), marked by mitochondrial staining (orange), are indicated (arrows). White boxes display zoomed-in sections. All cells, donor and recipient cells were stained with phalloidin-AF647 (violet) and DAPI (blue). All recipient cell lines were able to take up autophagic membranes decorated with GFP-WIPI1, GFP-WIPI2B or GFP-LC3, derived from respective donor cell lines in coculture settings. Extended image presentation in Supplementary Fig. 8e. **l**, **m** Donor U2OS cells stably expressing GFP-LC3 were transfected with different concentrations (0.2, 0.4 or 0.6 µg) of either control (9E10) or WIPI1 (9E10-WIPI1) expression plasmid for 24 h and then co-cultured with recipient U2OS cells stably expressing NLS-Scarlet for an additional 24 h. Subsequently, cells were stained with phalloidin-AF647 and DAPI. Representative images are shown (left panels). The percentage of recipient cells containing GFP-LC3 puncta derived from donor cells was calculated by manual counting (right panels, up to 700 cells per condition, two-way ANOVA with Tukey's post-hoc test, mean ± SD, $n = 3$). Scale bar: 20 µm. Supplementary material is available (Supplementary Fig. 8; Supplementary Videos 2–5; Supplementary Data 1). *P* values: $*p < 0.05$; $**p < 0.01$; $***p < 0.001$; ns not significant.

abl-1(ok171) nematodes carrying a GFP::LGG1 reporter transgene (Fig. 7d).

Further, to determine whether we could observe a difference in ATG-18 gene expression in ABL-1-deficient nematodes, as we did for WIPI1 in human cells, we examined ATG-18 mRNA levels at three different time points in the lifespan of *C. elegans*, day 1, day 6 and day 11 of adulthood. Indeed, we observed a significant increase in ATG-18 mRNA levels from day 1 to day 6 as well as to day 11 in adult nematodes lacking ABL-1 function (Fig. 7e, middle panel), such increase was not observed in wild-type nematodes (Fig. 7e, left and right panels).

We further performed adult lifespan assessment for all four *C. elegans* strains (Fig. 8a**;** Supplementary Table 1), which strikingly showed that ABL-1 deficiency in *abl-1(ok171)* nematodes significantly extended both the mean lifespan and the overall lifespan (Fig. 8a; Supplementary Table 1) compared to wild-type nematodes. ABL-1 deficiency-mediated lifespan extension was dependent on autophagy, since *abl-1;atg-18* double mutant nematodes showed survival rates similar to those of *atg-18(gk378)* nematodes, whose lifespans were expected to be shortened[77] (Fig. 8a; Supplementary Table 1). We have also confirmed that lifespan extension due to ABL-1 deficiency is dependent on autophagy, since depleting UNC-51, the ULK homologue in *C. elegans*, in the ABL-1 deficient strain by RNA interference (*abl-1(ok171); unc-51 (RNAi)*) counteracted lifespan extension (Fig. 8b; Supplementary Table 2). Furthermore, we show by RNA interference in wild-type nematodes that the lack of MML-1, which shares some functional similarities with mammalian MYC[78–80], also contributes to an extended lifespan, but to a much lesser extent than ABL-1-deficient *C. elegans* (Fig. 8b; Supplementary Table 2).

Taken together, these results strongly suggest that ABL-1 signalling inhibits autophagy, and when this negative impact is removed, *C. elegans* lifespan is prolonged through increased ATG-18 gene expression and autophagy enhancement.

Discussion

According to the current paradigm, lifespan-extending signalling pathways culminate in the process of autophagy, which essentially defines the lifespan of eukaryotes[2,71,72]. In this context, model organisms' orthologues of human WIPI1, such as ATG-18 in *C. elegans*, have been identified as one of the most critical autophagic factors for lifespan extension[72,77]. However, since ATG-18 is the orthologue for both human WIPI1 and WIPI2[7,76] and the lack of WIPI2 but not WIPI1 severely impairs autophagosome formation[9], the specific role of human WIPI1 in autophagy and lifespan control remains unclear. Nevertheless, it has been found that in human cells and in response to PI3P production at the onset of autophagy, WIPI1 assists WIPI2[9] in efficiently recruiting the ATG16L1 complex to the nascent autophagosome for subsequent LC3/GABARAP lipidation and autophagosome maturation[9,27,28]. Interestingly, in the context of human lifespan, it has been reported that centenarians are characterized by an increased expression of WIPI1[81], indicating that WIPI1 gene expression may be relevant to autophagy-related lifespan determination. Here, we provide a mechanistic explanation for why WIPI1 should indeed play this important role.

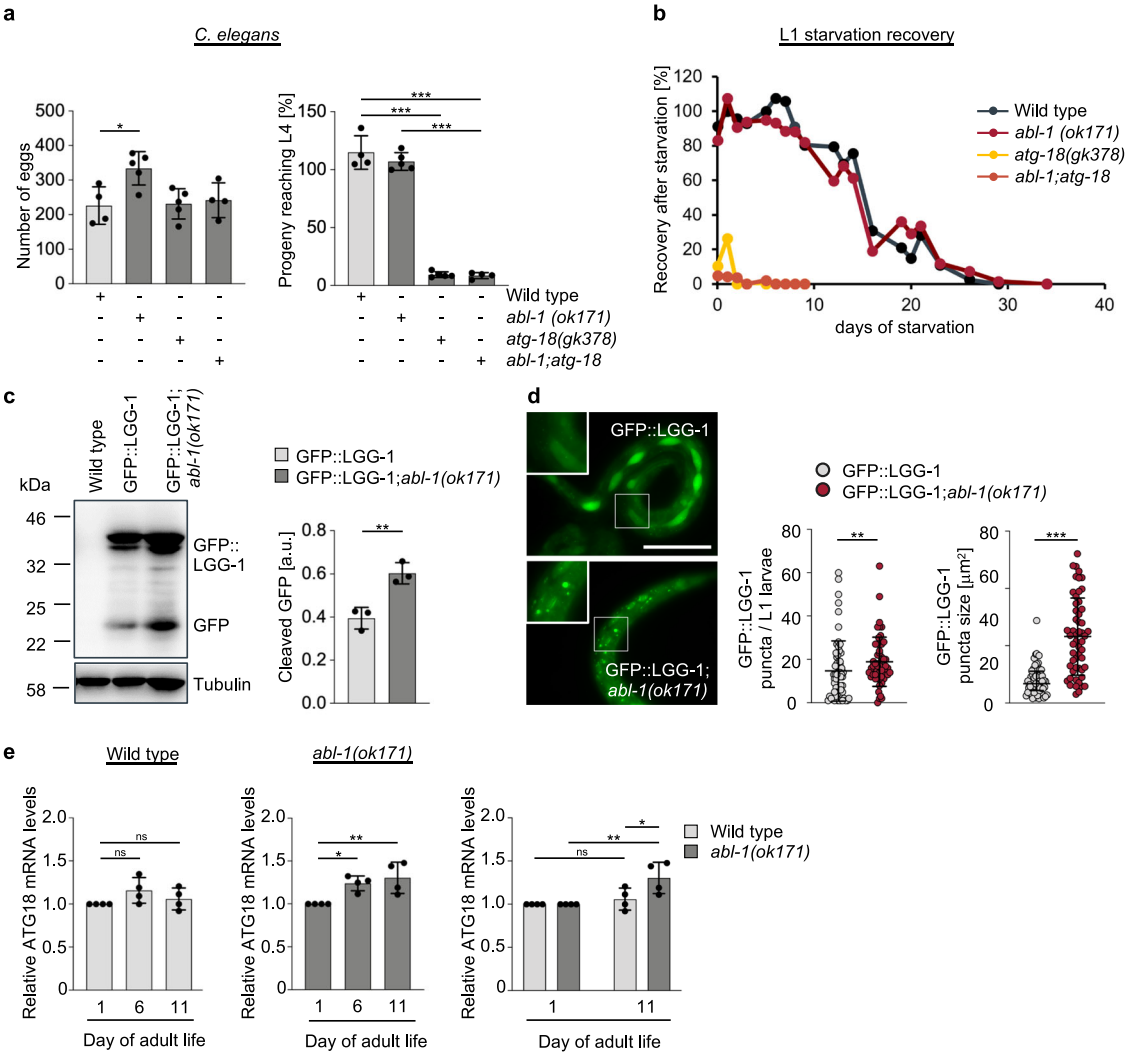

Fig. 7 ABL1 deficiency in *C. elegans* increases ATG-18 gene expression and autophagic flux. a Hermaphrodites of the N2 wild type, *abl-1(ok171)* mutant, *atg-18 (gk378)* mutant or *abl-1(ok171);atg-18 (gk378)* double mutant strains were singly transferred to NGM plates, and eggs per hermaphrodite were counted over the whole reproductive period, $n \geq 4$ (left panels). The number of L4 nematodes was calculated as a percentage of the total number of eggs laid (right panels). One-way ANOVA with Holm-Sidak post-hoc test, mean ± SD, $n \geq 4$. **b** For the L1 starvation assay, eggs were isolated, and L1 larvae hatched in nutrient-free medium, in which they were kept for up to 34 days. Every 2-3 days, larvae were removed from starvation and spotted onto NGM/OP50 plates. After 2 days of unrestricted feeding, nematodes that reached the L2 larval stage or later were scored, and the percentage of developing larvae was calculated. The corresponding results for WT, *abl-1(ok171)* mutant, *atg-18 (gk378)* mutant or the *abl-1(ok171);atg-18 (gk378)* double mutant strain are shown. **c** N2 wild-type, and wild-type (GFP::LGG1) or *abl-1(ok171)* mutant (GFP::LGG1; *abl-1(ok171)* L1 larvae expressing the adIS2122 transgene GFP::LGG1 were starved for 16 h. Protein extracts from whole larvae were analysed by immunoblotting against GFP or tubulin (left panels). Relative protein levels of cleaved GFP over tubulin were quantified (right panel, Welch's *t* test, mean ± SD, $n = 3$). **d** Likewise, wild-type (GFP::LGG1) or *abl-1(ok171)* mutant (GFP::LGG1; *abl-1(ok171)*) L1 larvae expressing the adIS2122 transgene GFP::LGG1 were imaged (left panels) and GFP-LGG1 puncta number (middle panels) as well as the mean puncta size (right panels) per nematode determined using CellProfiler. For statistical analysis, an unpaired *t*-test with Welch's correction was performed (GFP::LGG1, 61 nematodes; GFP::LGG1; *abl-1(ok171*, 55 nematodes; mean ± SD). Scale bar = 50 µm. **e** Total RNA from synchronised and sterilised wild-type or *abl-1(ok171)* nematodes was extracted on day 1, day 6 and day 11 of adulthood. Relative ATG-18 mRNA levels were analysed (Welch's *t* test, mean ± SD, $n = 4$). Left panel: ATG-18 expression in wild type nematodes. Middle panels: ATG-18 expression in *abl-1(ok171)* nematodes. Right panel: Additional comparative display of results (left panels, middle panels) of day 1 and day 11 only. Supplementary material is available (Supplementary Data 1). *P* values: $*p < 0.05$; $**p < 0.01$; $***p < 0.001$; ns not significant.

We have identified here the ABL-MYC signalling axis to repress WIPI1 gene expression and have shown that eliminating this negative impact increases WIPI1 mRNA levels, promotes autophagy and extends *C. elegans* lifespan (Fig. 8c). This finding is consistent with the notion that MYC counteracts lifespan extension in mice[82] and provides insight into a novel pathway that controls lifespan through autophagy. In this context, WIPI1 can be viewed as an autophagy enhancer since elevated WIPI1 protein levels can promote abundant formation of autophagic membranes. Although this increase in autophagic membranes is not essential for the process of autophagy, because WIPI1 deficiency does not abolish autophagy[9], it should become relevant under circumstances of reduced autophagic activity, for example, during the ageing process[83]. WIPI1 seems to be predestined for this function, since WIPI1 is generally weakly expressed and the protein interactome of WIPI1, in contrast to the other WIPI proteins, is limited and with regard to interacting ATG proteins, is restricted to self-interaction and heterodimerization with

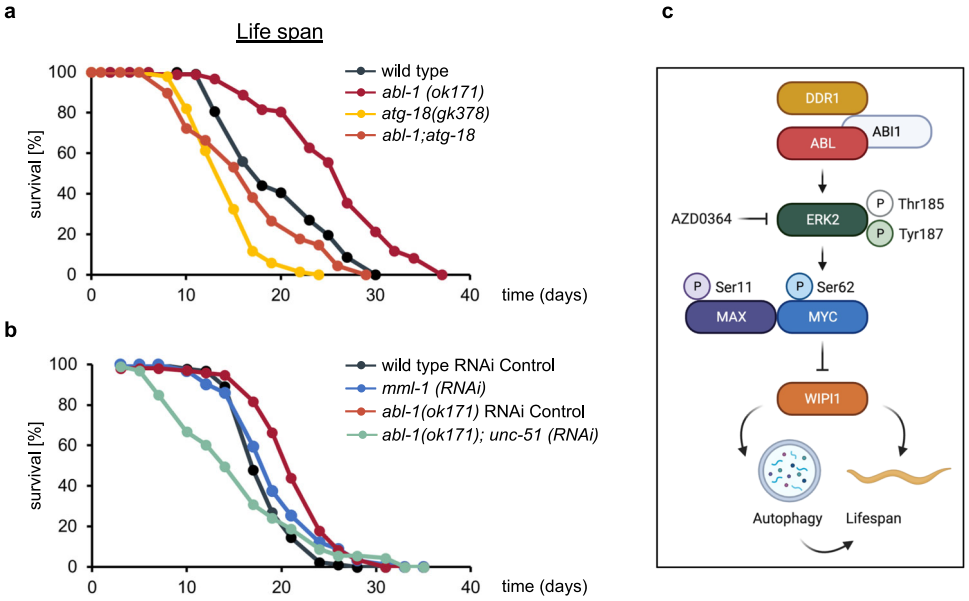

Fig. 8 ABL1 deficiency in *C. elegans* increases lifespan in an ATG18-dependent manner. a For lifespan assessments, eggs were isolated by hypochlorite treatment and grown on NGM/OP50 plates until they reached the L4 larval stage. L4 nematodes were then transferred to NGM/OP50/FUdR plates to sterilise the nematodes, and surviving nematodes were counted every 2–3 days. The resulting lifespan curves are shown (statistical OASIS analysis, Supplementary Table 1). **b** Likewise, lifespan assessments were conducted while depleting the c-MYC homologue MML-1 in N2 wild type (*mml-1 (RNAi)*) or the ULK homologue UNC-51 in the *abl-1(ok171) strain (abl-1(ok171); unc-51 (RNAi))* by RNA interference. Lifespan curves are shown and statistical OASIS analysis is displayed in Supplementary Table 2). **c** A predicted model for the regulation of WIPI1 gene expression by the ABL/MYC axis and its impact on autophagy and lifespan in *C. elegans*. Created with BioRender.com.

WIPI2. This is ideal for strengthening the WIPI2 function by having more WIPI1 without disturbing the balance of or sequestering other ATG functions. That elevated WIPI1 levels are associated with improved survival is also indicated by the finding that elevated WIPI1 levels have prognostic survival value in human melanoma patients[84].

Surprisingly, while analysing the abundance of WIPI1-decorated autophagic membranes, we observed their presence in tunnelling nanotubes (TNTs), which are direct connections between cells that mediate intercellular communication[66,68] and have a role in organelle transfer[67,69]. Since we considered WIPI1 as an enhancer of autophagic membrane formation, we hypothesized that this role might be extended to neighbouring cells and reasoned that this fact might be relevant to special circumstances such as extremely unequal levels of autophagy in neighbouring cells. Ultimately, using coculture conditions with human cells lacking ATG16L1 that were therefore autophagy incompetent[39], and with cells expressing GFP-tagged WIPI1, WIPI2 or LC3, we provide evidence that autophagic membranes are indeed found in autophagy-deficient cells if they can form TNTs with autophagy-competent cells. Furthermore, our study showed that WIPI1 deficiency reduces both the formation of TNTs and the transport of LC3-positive autophagic membranes through TNTs. Although this finding now warrants the collection of molecular details in future studies, important for a mechanistic understanding of TNT formation and selectivity in autophagic cargo transport by TNTs, it underscores that autophagic membrane transport through TNTs should be a vital mechanism by which cells with high autophagic activity may rescue cells with low autophagic activity.

In the context of our functional assignment of WIPI1 as an autophagy enhancer relevant to lifespan extension, we propose that this autophagy enhancement may not be confined to single cells but that such a surplus can be spread through TNTs to neighbouring cells if needed. During the ageing process, this scenario may explain why a WIPI1-mediated increase in autophagy can have far-reaching beneficial effects. Hence, it can be speculated that an increase in WIPI1 gene expression with age, as seen in centenarians[81], could have beneficial effects on human health span. In line with our results and deduced paradigm, it has recently been shown that mild elevation of autophagy through forced overexpression of Atg1 (ULK1 in humans) extended lifespan[85].

However, it should be noted that our presented lifespan data in the context of the ABL-MYC-WIPI1 axis, was carried out in the model organism *C. elegans*. Hence the question arises as to whether the outcome can be transferred to the organismic complexity of the aging process in humans. However, our study integrates with the current focus on deciphering the regulation of human aging, with the goal of being able to extend human healthspan in the future. To what extent an increased WIPI1 expression could have a positive effect in this context can currently only be speculated. Nevertheless, the finding that centenarians have elevated WIPI1 levels warrants further study.

Methods

Primary antibodies. The following primary antibodies were used: c-Abl (Cell Signaling Technologies, 2862; WB: 1:1000), CrkL (Santa Cruz Biotechnologies, sc-319; WB: 1:1000), DDR1 (Cell Signaling Technologies, 5583; WB: 1:1000), ERK2 (Cell Signaling Technologies, 9108; WB: 1:1000), GAPDH (Santa Cruz Biotechnologies, sc-47724; WB: 1:1000), GABARAPL1 (Cell Signaling Technologies, 26632; WB: 1:1000), GFP (Roche, 11814460001; WB: 1:1000), LC3 (nanoTools, 0231-100/LC3-5F10; WB: 1:1000), c-myc (9E10) (Santa Cruz Biotechnologies, sc-40; WB: 1:1000), c-myc (Cell Signaling Technologies, 9402S; WB: 1:500), p62 (Santa Cruz Biotechnologies, sc-28359; WB: 1:1000, IF: 1:50), p62 (Medical and Biological Laboratories, PM045; WB: 1:500-1:1000), S6K (Cell Signaling Technologies, 2708, WB: 1:500-1:1000), TFEB (Cell Signaling Technologies, 37785, WB: 1:500), α-Tubulin (Sigma–Aldrich, T5168; WB: 1:50000, IF 1:2000) and ULK1 (Cell Signaling Technologies, 8054; WB: 1:500–1:1000).

The following phospho-specific primary antibodies were used: phospho-CrkL (Tyr207) (Cell Signaling Technologies, 3181S; WB: 1:1000), phospho-p44/42 ERK1/ERK2 (Y204/Y187) (Cell Signaling Technologies, 5726; WB: 1:1000), phospho-MAX (S11) (Thermo Fisher, PA5-97346; WB: 1:500), phospho-c-Myc (Ser62) (Cell Signaling Technologies, 13748; WB: 1:500), phospho-S6K (Cell Signaling Technologies, 9234, WB: 1:500-1:1000), phospho-TFEB (Ser211) (Cell Signaling Technologies, 37681, WB: 1:500) and phospho-ULK1 (Ser757) (Cell Signaling Technologies, 6888, WB: 1:500-1:1000).

Secondary antibodies. The following secondary antibodies were used: Alexa Fluor 488 goat anti-rabbit IgG (Life Technologies, A-11008, IF 1:200), anti-mouse IgG HRP-linked (Cell Signaling, 7076; WB 1:5000–1:10,000), and anti-rabbit IgG HRP-linked (Cell Signaling, 7074; WB 1:5000–10,000).

Dyes. The following dyes were used: 4,6-diamidino-2-phenylindole (DAPI) (AppliChem, A1001), Alexa FluorTM 546 Phalloidin, hereafter Phalloidin-AF546 (Thermo Fisher, A22283, 1:1000), Alexa FluorTM 647 Phalloidin, hereafter Phalloidin-AF647 (Thermo Fisher, A22287, 1:1000), and Wheat Germ Agglutinin, Alexa FluorTM 647 Conjugate, hereafter WGA-AF647 (Thermo Fisher, W32466, 1:200).

Plasmids. The following plasmids were used to express tagged WIPI1 and WIPI2 fusion proteins: GFP-WIPI1[7,9], GFP-WIPI2B[7,9], 9E10-WIPI1[14] and mCherry-WIPI1[86]. pCMV6-MAPK1 (MR222304-OR) and pCMV6-Entry (PS100001) were purchased from Origene. pCMV-myc-ERK2-MEK1_fusion was provided by Melanie Cobb (Addgene, #39197). pCMV3-untagged negative control plasmid (CV011) and pCMV3-untagged c-MYC cDNA ORF (HG11346-UT) were purchased from SinoBiological through BIOZOL Germany. For conducting dual-luciferase assays, the plasmids pGL4.73[hRluc/SV40] (E6911) and pGL4.23[luc2/minP] (E8411) were purchased from Promega. Using pGL4.23[luc2/minP], the plasmids pGL4.23-5xE-box and pGL4.23-WIPI1promotor employed for luciferase assays in this study, were prepared by AZENTA Life Sciences, GENEWIZ Germany custom cloning service. The pGL4.23-5xE-box plasmid was generated by custom order synthesis of a 312 bp DNA fragment that contained 5 canonical E-boxes (GCCACGTGCA) spaced by 50 nucleotides (referred to as 5xE-box), while the 5'-site was designed to match the XhoI and 3'-site to match the HindIII restriction site of the pGL4.23[luc2/minP] multiple cloning region. Subsequently, the 5xE-box fragment was cloned into pGL4.23[luc2/minP] (XhoI/HindIII) to generate pGL4.23-5xE-box. The pGL4.23-WIPI1promotor plasmid was generated by custom order synthesis of the WIPI1 promotor sequence (1555 bp) spanning the region from minus 1226 bp upstream to plus 329 bp downstream of the transcription start site, harbouring all three MYC-binding sites identified in this study (M + 1, M11, M19). In addition, 5'-NheI and 3'-HindIII recognition sites were added for cloning into pGL4.23[luc2/minP] (NheI/HindIII) to generate pGL4.23-WIPI1promotor. Plasmid integrities were verified by DNA sequencing (AZENTA Life Sciences, GENEWIZ Germany). The plasmids pLentiGuide (Addgene, # 117986), pLenti_mx2-PGK-BSD (a gift from Koraljka Husnjak Frankfurt CRISPR/Cas Screening Center (FCSC), Goethe University Frankfurt am Main, Germany), pPAX2 (Addgene, #12260), pMD2.G (Addgene, #12259) were used for lentiviral particle production in the course of generating U2OS WIPI KO cells.

Cell culture. Human U2OS osteosarcoma cells (ATCC, HTB-96) or human G361 malignant melanoma cells (ATCC; CRL-1424) were cultured in Dulbecco's modified Eagle medium (DMEM) GlutaMAX (Life Technologies, 31966)/10% fetal bovine serum (Life Technologies, 10270-106) supplemented with 100 U/ml penicillin/100 mg/ml streptomycin (Life Technologies, 15140-122) at 37 °C and 5% CO2. Monoclonal U2OS cells stably expressing GFP-WIPI1, GFP-WIPI2B, GFP-LC3[9], or RFP-GFP-LC3 were obtained by G418 selection and cultured in the presence of 0.6 mg/ml G418 sulfate (Life Technologies, 11811-031). Monoclonal U2OS cell lines deficient in ATG16L1 (ATG16L1 KO) or reconstituted for ATG16L1 expression (here referred to as ATG16L1 KO + ATG16L1 WT) stably expressing MLS-EGFP-mCherry were cultured in DMEM GlutaMAX (Life Technologies, 31966) supplemented with 10% fetal bovine serum (Life Technologies, 10270-106) and 100 U/ml penicillin/100 mg/ml streptomycin
(Life Technologies, 15140-122) at 37 °C and 5% CO_2. Monoclonal U2OS cell line stably expressing NLS-mScarlet was likewise cultured in DMEM GlutaMAX (Life Technologies, 31966) supplemented with 10% fetal bovine serum (Life Technologies, 10270-106) and 100 U/ml penicillin/100 mg/ml streptomycin (Life Technologies, 15140-122) at 37 °C and 5% CO_2.

Generation of WIPI1 knockout U2OS cells. For generating U2OS cells deficient in WIPI1 (here referred to as WIPI1 KO), CRISPR-Cas gRNA sequences targeting human WIPI1 were designed using a gradient-boosted regression trees model with an augmented feature set (Rule Set 2)[87]. The top three scoring gRNAs
WIPI1-1 GAGCAGCTGGATCAAGTCCA,
WIPI1-2 TAGTCAGTCACACAAAACCA,
WIPI1-3 GACCAGAAGAGCCTTCGACC
were selected and 3Cs-based cloned as mini-pool into pLentiGuide[88,89]. Generation of lentiviral particles were performed by using HEK293T cells and lentiviral supernatant was harvested 48 hours after transfection and stored at −80 °C. Subsequently, hTERT-U2OS Cas9 cells (a gift from Andrew Holland, John Hopkins School of Medicine, Baltimore, MD, USA) were used to generate WIPI1 KO cells that were cultured in DMEM/F-12 (Life Technologies, 11320-074) supplemented with 10% fetal bovine serum (Life Technologies, 10270-106), 100 U/ml penicillin/100 mg/ml streptomycin (Life Technologies, 15140-122) and 0.1% Blasticidin (Gibco, A11139-03) at 37 °C and 5% CO_2.

Autophagy assays. Cells were washed three times with Dulbecco's phosphate buffered saline (DPBS, Life Technologies, 14190144) before incubation in full (fed, DMEM/10% FCS), serum starvation (DMEM) or starvation (starved, Earle's balanced salt solution (EBSS), Life Technologies, 24010-043) medium in the presence or absence of 200 nM (AppliChem; A7823) or 100 nM (EMD Millipore, 196000) bafilomycin A1. Autophagy assays were generally performed for three hours unless stated otherwise. Moreover, AZD0364 (final concentration: 10 µM, Selleckchem, S8708), MG132 (final concentration: 10 µM, Selleck Chemicals, S2619), DPH (final concentration: 10 µM, Sigma–Aldrich, SML0202), cycloheximide (final concentration: 10 µg/ml Applichem, A0879), LY294002 (SelleckChem, S1105; final concentration: 100 µM), 10058-F4 (SelleckChem S7153; final concentration: 1 µM), 10074-G5 (SelleckChem S8426; final concentration: 1 µM), and dasatinib (SelleckChem, S5254; final concentration: 1 µM) were added for the indicated times.

DNA transfection. Transient DNA transfections were conducted using Lipofectamine 2000 (Invitrogen, 11668019). When using 24-well plates, 0.1-0.8 µg DNA and 0.2–2.0 µl Lipofectamine 2000 were diluted in 25-30 µl OPTI.MEM (Life Technologies, 51985026) each and incubated for 5–20 min at room temperature.

Both mixtures were combined and incubated for another 20–30 min at room temperature before the addition of 50 µl of the mix into one well of a 24-well plate containing 50,000 cells in 200–500 µl DMEM/10% fetal bovine serum (FBS) or OPTI.MEM and transfection was carried out up to 48 h. When using 96-well plates, 100 ng of DNA and 0.25 µl Lipofectamine 2000 were diluted in 5 µl OPTI.MEM each and incubated for 5 min at room temperature prior combining the mixtures and subsequent incubation (20 min at room temperature). This mix (10 µl) was added to one well of a 96-well plate containing 10,000 cells in 100 µl DMEM/10% fetal calf serum (FCS).

RNA interference. Knockdown experiments using siRNAs were performed using Lipofectamine RNAiMAX (Invitrogen, 13778150) as follows. siRNAs (Santa Cruz: 25 nM or Origene: 3 × 20 nM) and 1 µl Lipofectamine RNAiMAX were diluted in 100 µl OPTI.MEM (Life Technologies, 51985-026) and incubated at room temperature for 20 min. The mixture was then added to one well of a 24-well plate, and 500 µl of cell suspension containing 50,000 U2OS cells in DMEM/10% FCS was seeded on top of the transfection solution for 48 h. Knockdown was confirmed by qPCR and Western blotting. The following siRNAs were purchased from Santa Cruz Biotechnology: c-Abl (Abl1) siRNA (h) (sc-29843), Arg siRNA (Abl2) siRNA (h) (sc-38945), DDR1 siRNA (h) (sc-35187), and control siRNA-A (sc-37007). The following siRNAs were purchased from OriGene Technologies: c-Abl (ABL1) Human siRNA Oligo Duplex (SR3000017/SR319232), ABL2 Human siRNA Oligo Duplex (SR3000019/SR319233), MCK10 (DDR1) Human siRNA Oligo Duplex (SR300547/SR319533), c-Myc (MYC) Human siRNA Oligo Duplex (SR321047), MAX Human siRNA Oligo Duplex (SR302818), and Trilencer-27 Universal scrambled negative control siRNA duplex (SR30003/SR30004).

RNA extraction and quantitative PCR (qPCR). Total RNA extraction was performed using the RNeasy Mini Kit (QIAGEN, 74104) in combination with QIAshredder (QIAGEN, 79654) and the RNase-free DNase Set (QIAGEN 79254). After washing, the cells were resuspended in RLT buffer. The cell suspension was then added onto the QIAshredder column and lysed at 14,200 rpm for 2 min. The flowthrough was mixed with an equal volume of 70% ethanol, immediately transferred to a RNeasy extraction column, and centrifuged at 10,000 rpm for 15 s. After one wash with RW1 buffer, DNA was digested on-column for 15 min using DNase I, after which the column was washed again once with RW1 and twice with RPE buffer. RNA was then eluted in RNase free water. Concentrations were determined using a Nanodrop 1000, and the RNA was transcribed using TaqMan Reverse Transcription Reagents (Thermo Fisher, N8080234). qPCR was performed using 2x Taqman Fast Advanced Master Mix (Applied Biosystems, 4444963) and the following 20x Taqman Gene Expression Assays (Applied Biosystems, 4331182) with the following assay identification (ID) numbers: Hs01104728_m1 (Abl1), Hs00943652_m1 (Abl2), Hs01058430_m1 (DDR1), Hs04194186_s1 (FOS), Hs00420895_gH (RPLPO), Hs00215872_m1 (WIPI1), Hs00255379_m1 (WIPI2), Hs00750495_s1 (WIPI3/WDR45B), and Hs01079049_g1 (WIPI4/WDR45). In 384-well plates, 6.25 ng of cDNA was used per 10 µl reaction containing 1x Taqman Fast Advanced Master Mix and the appropriate 1x Taqman Gene Expression Assay and qPCR was run using a QuantStudio7Flex Real-Time PCR System.

Autophagy pathway-focused gene expression analysis using qPCR arrays. RNA was extracted for qPCR analysis of single genes (see above). The RNA concentration was determined using a Nanodrop 1000 and Qubit. cDNA was synthesized using the RT2 First Strand Kit (QIAGEN, 330404). Genomic DNA was eliminated by adding 4 µl GE buffer to 800 ng RNA in 16 µl RNase-free water and incubating the mixture at 42°C for 5 min and subsequently cooling it on ice. The reverse transcription mix was prepared by combining 8 µl 5x Buffer BC3, 2 µl Control P2, 4 µl RE3 Reverse Transcriptase Mix, 6 µl RNase-free water and 20 µl of the genomic DNA elimination mix. Synthesis of cDNA was conducted with the following PCR cycler program: 15 min 42 °C and 5 min 95 °C. After that, 40 µl of cold RNase-free water were added to each reaction and the samples were placed on ice. Downregulation of the kinases was confirmed by TaqMan qPCR (see above). The cDNA was then used in the RT2 Profiler PCR Array (QIAGEN, PAHS-084Z) in combination with RT2 SYBR Green qPCR Mastermix (QIAGEN, 330529) using a QuantStudio7Flex Real-Time PCR System. Per 10 µl reaction, 5 µl RT2 SYBR Green qPCR Mastermix, 0.78 µl cDNA synthesis reaction and 4.22 µl RNase-free water were used. qPCR reaction was conducted with the following program: 1 cycle with 10 min 95 °C, 40 cycles with 15 s 95 °C and 1 cycle with 1 min 60 °C. Data analysis was performed in the data analysis webportal at Qiagen.com/geneglobe using the following parameters: CT Cut-off: 35, Normalisation method: Automatic Selection from Full Panel; Settings for visualization: fold regulation: 2, *P* value: 0.05.

Fluorescence microscopy. Cells were grown on sterile coverslips and fixed using 3.7% formaldehyde. If appropriate, cells were stained with primary antibodies and secondary antibodies. Cell nuclei were stained with 4,6-diamidino-2-phenylindole (DAPI) (AppliChem, A1001) for 20 min at room temperature. Cells were mounted on glass slides using ProLong Gold Antifade Mountant (Life Technologies, P36930) and imaged using a laser scanning microscope (LSM) 800 (Zeiss) and a C Plan-Apochromat 63x/1.4 oil differential interference contrast (DIC) objective or a Leica SP8/HCX PL APO 100x/1.44 oil objective. Z-stacks were acquired with a slice distance of 0.5 µm. For 3D reconstruction, Z-stack images were obtained with a 40x/1.3 DIC Plan-Apochromat Oil-Immersion Objective (Zeiss).

Automated quantitative confocal microscopy analysis. Image acquisition and analysis was performed in 96-well plates with glass bottom (Cellvis, P96-0-N) using a laser scanning microscope (LSM) 800 (Zeiss) and a C Plan-Apochromat 63x/1.4 oil differential interference contrast (DIC) objective. The automated image acquisition was carried out with the 'tiles' module of the ZEISS ZEN system 3.0 blue edition software (Carl Zeiss Microscopy Deutschland GmbH). Automated image analysis for the quantitative assessments of fluorescent puncta was then performed using CellProfiler (Version 4.2.1) with a pipeline designed for cell and puncta recognition[90]. In this CellProfiler pipeline, cell nuclei were identified as primary objects on DAPI images using the Otsu thresholding method to calculate a global thresholding value for each image. Cells were identified as secondary objects with the watershed method, using the nuclei as seed objects. Prior to puncta identification, the background of the images was subtracted using a median filter. Subsequently, the puncta were identified using the Otsu method to calculate a global threshold for each image. Then the puncta were assigned to cells based on spatial overlap and single cell values exported as a CSV spreadsheet for statistical analysis.

Automated high throughput fluorescence-based imaging. Image acquisition and analysis were performed in 96-well plates. Cells were fixed using 3,7% formaldehyde, and cell nuclei were stained with 4,6-diamidino-2-phenylindole (DAPI) (AppliChem,

A1001). Cells were kept in PBS, and images were acquired using the IN Cell Analyzer 1000 (GE Healthcare) using the Nikon Plan Fluor ELWD 40 × 0,6 objective. In each well of a 96-well plate, 20 images were taken, each with an average of 10 cells per image. Subsequent automated image analysis was performed using IN Cell Analyzer Workstation 3.4 software[9,30].

Lentiviral shRNA screen. The MISSION® LentiExpress™ Human Kinases (Sigma–Aldrich, SHX001) shRNA library was screened as follows. 96-well plates precontaining shRNAs were thawed at room temperature for 10 min before centrifugation for 1 min at 1000 rpm. U2OS-GFP-WIPI1 cells were resuspended in DMEM/10% FCS supplemented with 11.4 µg/ml hexadimethrinbromide (Sigma Aldrich, H9268). A total of 2000 cells in 70 µl DMEM/10% FCS were seeded into each well of 96-well plates and incubated at 37 °C/5% CO_2. After 24 h, the medium was replaced with 100 µl DMEM/10% FCS supplemented with 0.6 mg/ml G418 and 1 µg/ml puromycin for selection. The medium change was repeated after an additional 48 h. Twenty-four hours after the last medium change, the cells were washed twice with EBSS and starved for 3 h. The cells were then fixed with warm 3.7% paraformaldehyde (PFA) and stained with DAPI for 20 min. Automated image acquisition and analysis were performed using the IN Cell Analyzer 1000 and the In Cell Analyzer 1000 Workstation 3.4 software (GE Healthcare). Candidate kinases were chosen if they had two or more individual shRNAs showing >0,4 difference in fold increase or decrease compared to the mean of the control shRNAs. To identify overrepresented pathways, we performed statistical enrichment analysis of selected genes using the R (version 3.6.0) package gprofiler2 (version 0.1.8) with a hypergeometric test and the default gSCS method for multiple testing correction[91]. Pathways with p value less than 0.05 were treated as significantly overrepresented. Gene network plots of selected enriched pathways were generated using the clusterProfiler (version 3.12.0) R package[92].

Immunoblotting. Proteins were extracted by washing cells once with PBS and subsequently lysing in boiling 2x Laemmli buffer. The chromatin was sheared using a 23 G needle, and samples were boiled for 5 min. Alternatively, cells were washed and scraped into ice-cold ACA lysis buffer (750 mM aminocaproic acid, 50 mM Bis-Tris, 0.5 mM ethylenediaminetetraacetic acid (EDTA), pH 7.0, 0.1% Tween 20) supplemented with cOmplete EDTA-free protease inhibitor cocktail (Roche, 04693132001) and PhosStop phosphatase inhibitor cocktail (Roche, 04906837001). Cells were lysed by vortexing three times with a 5 min incubation on ice in between. After this, the protein extracts were spun down at 20,000 × g for 20 min, the supernatant was transferred to a fresh tube, and 4x Laemmli buffer was added. Before gel separation, the samples were boiled for 5 min. Proteins were separated by sodium dodecyl sulfate–polyacrylamide gel electrophoresis (SDS-PAGE) and transferred to a 0,45 µm polyvinylidene difluoride (PVDF) transfer membrane (Thermo Scientific, 88518). Nonspecific binding was blocked by 5% BSA/TBS/T or 5% milk in TBS/T for one hour before antibody incubation overnight at 4 °C. The secondary antibody was incubated for one hour at 4 °C, and ECL analysis was performed using Signal West Femto Maximum Sensitivity Substrate (Thermo Scientific, 34095). Signal detection and analysis was conducted using the Amersham Imager 600 (GE healthcare) or the Fusion Sl instrument (Vilber Lourmat) and the Fusion Capt advance software (Vilber Lourmat). Alternatively, the iBright CL750 instrument (Thermo Scientific, A44116) was used along with the iBright Analysis Software (Thermo Scientific, Version 4.01).

Phospho-SILAC analysis. In order to conduct phospho-SILAC based proteomics[93–99], U2OS cells were labelled using light (SILAC-DMEM (PAN-Biotech, P04-02505S1) containing lysine-0/arginine-0/1% PenStrep (PAN-Biotech, P06-07100)/10% dialyzed FBS (PAN-Biotech, P30-2102)) or heavy (SILAC-DMEM containing lysine-8/arginine-10/1% PenStrep/10% dialyzed FBS) culture medium. ABL1/2 or DDR1 were transiently downregulated as described above, replacing OPTI.MEM with the appropriate heavy or light DMEM. siABL1/2 or siDDR1 KD was performed in heavy DMEM, while siControl KD was done in light DMEM. After 48 h, cells were lysed in lysis buffer (6 M urea, 2 M thiourea, 10 mM Tris pH 8.0, 1% N-octylglucoside (NOG)) for 10 min on ice. DNA and RNA were digested using Benzonase (Merck, 101695) for 10 min at room temperature followed by centrifugation at 2800 × g for 20 min. Proteins were precipitated by acetone/methanol (acetone:MeOH:sample 8:1:1) overnight at −20 °C, centrifuged (2000 × g, 20 min, 4 °C), and the protein pellet washed with 80% acetone and resuspended in lysis buffer without NOG. Bradford assay was performed to determine the protein concentration, and corresponding heavy and light samples were mixed 1:1. Proteins were digested with trypsin (Promega, V5113) overnight[93]. Twenty µg of peptides were directly desalted with C18 StageTips[94]. The rest of the peptide mixture was purified on Sep-Pak 18 cartridges (Waters), and phosphopeptides were enriched using TiO_2 beads (Titansphere, 10 µm, GL Sciences) that were equilibrated in 80% acetonitrile (ACN), 1% trifluoroacetic acid (TFA), 3% 2,5-dihydroxybenzoic acid (DHB).Purified peptides were added in a bead to protein ratio of 1:2, and washed first with 30% ACN, 1% TFA, followed by 50% ACN, 1% TFA, and 80% ACN, 1% TFA. Elution of peptides was facilitated in two steps, first with 5% NH_4OH in 20% TFA, and then with 80% ACN in 1% FA[99]. In total 10 enrichment cycles were run. All peptides were analysed on an Easy-nLC 1200 system coupled to a Q Exactive HF mass spectrometer (both Thermo Fisher Scientific)[95] that was operated in positive ion mode in the m/z range of 300 to 1,650 with the following settings: peptides were separated with a 227 (proteome) or 57 min (phosphoproteome) segmented gradient from 10-33-50-90% of HPLC solvent B (80% ACN in 0.1% formic acid (FA)) in HPLC solvent A (0.1% FA) at a flow rate of 200 nl/min. The resolution of the MS full scan was 60,000 with target values of 3×10^6 charges and a fill time of 25 ms. The twelve (proteome) or seven (phosphoproteome) most intense precursor ions were sequentially fragmented in each scan cycle using higher energy collisional dissociation (HCD) fragmentation, and sequenced precursor masses were excluded from further selection for 30 s. The target values for MS/MS fragmentation were 10^5 charges with fill times of 45 (proteome) and 220 ms (phosphoproteome) and a resolution of 30,000 and 60,000, respectively. The data was processed with MaxQuant software (version 1.5.2.8) with integrated Andromeda search engine. The data was processed with MaxQuant software (version 1.5.2.8) with integrated Andromeda search engine. Database search was performed against a *Homo sapiens* database obtained from Uniprot, (93,827 entries, downloaded 20th of December 2017), and 286 commonly observed contaminants. Trypsin was defined as digestion enzyme with full specificity and a maximum of two missed cleavages. Carbamidomethylation on cysteine was defined as fixed modification, whereas phosphorylation of serine, threonine, and tyrosine, as well as oxidation of methionine and protein N-terminal acetylation were set as variable modifications. The precursor mass tolerance was set to 4.5 parts per million (ppm), whereas on fragment ion level 20 ppm was tolerated. The false discovery rate (FDR) was calculated by the target/decoy approach[97] and set to 0.01 on peptide, protein and modification site level. Protein group quantitation was based on a minimum of two quantified peptides. Further downstream

analyses were done with R (v 3.5.1). The requirement for a localized phosphorylation site was a reported localization probability of at least 0.75. The detected phosphorylation sites were normalised for changes in protein abundance. Taking into account the intensity distribution as well as ratios of all quantified peptides, a *P* value was calculated for each of the heavy to light ratio specifying significantly regulated phosphosites. A P value < 0.01 was defined as significantly regulated[98].

In silico prediction of MAX/MYC binding sites in the WIPI1 promoter. The online tool ConTra v3 was used to look for putative MAX/MYC binding sites in the WIPI1 promoter using the following parameters: Type of analysis: visualization; reference organism: Human (*Homo sapiens*); Transcript: WIPI1 chr17:66453653, number of introns:12, NM_017983; Sequence parts: promoter 5000 bp; Transcription factor: c-Myc:Max TRANSFAC20113,V$MYCMAX_B,M00322; stringency: core = 0.95, similarity matrix 0.85.

Chromatin immunoprecipitation (ChIP). Chromatin immunoprecipitation was carried out using the SimpleChIP® Enzymatic Chromatin IP Kit (Cell Signaling Technologies, 9002). U2OS cells were crosslinked using 1% formaldehyde for 10 min, washed once with ice-cold PBS/protease inhibitor cocktail (PIC) and pelleted at 2000 × *g*. After resuspension in Buffer A/DTT/PIC and 10 min incubation on ice with frequent inversion, nuclei were pelleted at 2000 × *g* for 5 min, washed once with Buffer B/DTT and resuspended in Buffer B/DTT for 20 min micrococcal nuclease treatment at RT. Nuclei were pelleted again and resuspended in ChIP buffer/PIC. After 10 min incubation on ice, the nuclear membrane was fragmented by sonication (BioRuptor Plus, 12 cycles, 20 s pulse/30 s rest at 4 °C). Samples were clarified by centrifugation, and the DNA quality was determined using a Nanodrop 1000 and agarose gel. Per immunoprecipitation 8 µg chromatin were used with the following antibodies: c-myc (Cell Signaling Technologies, 9402 S; ChIP: 2,4 µg), Di-Methyl-Histone H3 (Lys9) (H3KMe2) (Cell Signaling, 9753S; ChIP: 7,7 µg), G9a (Cell Signaling, 3306; ChIP: 0,8 µg), Max (Abcam, ab53570; ChIP: 3 µg), and Normal Rabbit IgG (Cell Signaling, 2729; ChIP: 6 µg). Immunoprecipitation was performed overnight at 4°C and Protein G agarose beads were used to capture antibodies. After three washing steps with ChIP buffer and one washing step with high salt buffer, elution was done in ChIP elution buffer for 30 min at 65 °C and 1200 rpm shaking. Proteinase K treatment was performed overnight and the DNA was cleaned up using DNA purification columns. qPCR analysis was performed using 2 µl of the DNA, SYBR Green PCR Master Mix (Applied Biosystems, 4309155) and 0.5 µM of the following primers:

M + 1_1F 5′-TTTCAACCAGGACTGCACGTAAGC-3′,
M + 1_1R 5′-ACAAGATCCCAATGCGTCCGAA-3′,
M11F 5′-TTGGAGTCTAACGCTCTCTGCTA-3′,
M11R 5′-AGGGTGACAGGAGGACGCGCTA-3′,
M19F 5′-ACAATCCAAAGCTGGCAGAGCTC-3′,
M19R 5′-CTCACGTAATTCGAGATAAACCTT-3′.

Dual-Luciferase Reporter Assay. For luminescence measurement, U2OS cells were seeded into a 96-well plate (Greiner, 655083) co-transfected with pGL4.73[hRluc/SV40] and pGL4.23[luc2/minP], pGL4.23-WIPI1promotor or pGL4.23-5xE-box using Lipofectamine 2000 and incubated for 24 h. For cell lysis and luminescence detection, the Dual-Luciferase Reporter Assay System (Promega, E1969) was used. Cells were lysed by adding 20 µl of the 1× passive lysis buffer per well and shaking the culture plate for 15 min at room temperature. Addition of the firefly and Renilla luciferase substrates as well as luminescence measurement was performed using the Synergy Neo2 Multimode Microplate reader with the software BioTek Gen5 (Version 3.11) for automated liquid handling and luminescence intensity measurement. Firefly and Renilla luciferase activities were measured, and firefly activities normalized to Renilla luciferase activities.

Correlative light electron microscopy (CLEM). U2OS-GFP-WIPI1 cells were seeded to 50% confluency and starved for 6 h (see autophagy assay protocol above). Cells were fixed in 4% PFA/0.2 M 4-(2-hydroxyethyl)-1-piperazineethanesulfonic acid (HEPES) buffer pH 7.4 for 10 min at room temperature. PFA was replaced with 0.2 M HEPES buffer, and wide field images of GFP fluorescence and bright field images were acquired at 20x, 40x and 63x. Cells were further fixed using 2% glutaraldehyde for 2 h at room temperature and kept in 0.2 M HEPES buffer until processing for EM. For electron microscopy, the cells were washed twice with 0.1 M sodium cacodylate (NaCac) buffer, pH 7.4, and osmicated using 1% OsO4, 0.1 M NaCac buffer and 15 mg/ml $K_4[Fe(CN)_6]$ for 1 h at room temperature. After two washes with 0.1 M cacodylate buffer and three washes with water, samples were incubated with 1% uranyl acetate for 1 h at 4 °C and washed three times with water. The samples were then dehydrated stepwise in 50%, 70%, 96%, and 100% ethanol for 3 min each. Finally, the samples were embedded in Epon resin (TAAB 812, TAAB Laboratories Equipment, 030) for 2 h at room temperature and baked at 60 °C for >14 h. Samples were then thin sectioned into 100 nm sections, which were stained with 0.5% uranyl acetate for 30 min and 3% lead citrate for 1 min before acquiring electron microscopy images on a Jeol JEM-1400 (Jeol) microscope at 80 kV.

Live-cell microscopy. Live-cell imaging was performed using a Zeiss Cell Observer, consisting of an Axiovert 200 inverted microscope, EXFO X-Cite 120 illuminaCon system, Apotome module, and Pecon Incubator XL-3 equipped with a CO_2/temperature control unit and heating unit. The incubation chamber of the microscope was brought to 37 °C, 5% CO_2 prior to the start of the imaging. For live-cell microscopy, cells were cultivated to a confluency of 80–90% in custom-made 6-well plates with glass bottom. A 63x/1.4 DIC Plan Apochromat, EC Plan-Neofluor 100x/1.3 or an EC Plan Neofluor 40x/1.3 oil immersion objective were used to acquire a series of images in 5–15 s intervals. With the ApoTome module, a transmission grid (Grid H) was inserted into the beam path, and 3 images with different grid positions were acquired. The final images were calculated from the three raw images. The videos were generated with ImageJ by displaying 5 images per second[100].

Live-time tracking. Live time series microscopy was performed using a laser scanning microscope (LSM 800; Carl Zeiss GmbH) with a 40×/1,3 DIC Plan-Apochromat Oil-Immersion Objective (Zeiss). Cells were imaged in live cell imaging solution (Invitrogen, A14291DJ) supplemented with 5 mM or 20 mM glucose after starvation or full medium treatment for 24 h. During time series imaging, the cells were kept at 37 °C and 5% CO_2. Airyscan superresolution images were obtained in combination with an electronically switchable illumination and detection module (ESID), with time intervals ranging between 30 and 60 s per position. Projects were processed with ZEN software (ZEISS), whereas the time series stacks were extracted and processed into videos in Fiji. Manual tracking of GFP-WIPI1 puncta within TNTs was performed with the free Fiji Plug-in MTrackJ, where GFP-WIPI1 puncta's positions were manually selected through

each time-lapse frame. Overlay videos were exported displaying tracks of each selected object.

Giant unilamellar vesicles (GUVs). For binding studies of GFP-WIPI with GUVs containing either PI3P or PI(3,5)P_2, freshly prepared native cell extracts[9,14] from U2OS cells stably expressing GFP-WIPI1 were used, along with control native extracts made from U2OS cells stably expressing GFP or from the parental U2OS cell line. GUVs were generated using a modified polyvinyl alcohol (PVA)-assisted swelling method. Coverslips were coated with a PVA solution (Sigma, 363065; 1% in double-distilled water (ddH_2O)) and dried at 60 °C for 20 min. One hundred microlitres of each lipid mix was prepared in chloroform in a 4 ml glass bottle. All lipids were purchased from Avanti Polar Lipids. Lipid mixes containing 1,2-dioleoyl-sn-glycero-3-phosphocholine (DOPC, 850375 C), 18:1 PI(3)P (850150) or 18:1 PI(3,5)P_2 (850154) and rhodamine-PE (810150) were prepared in chloroform at a molar ratio of 97:2:1. DOPC and rhodamine-PE in a 99:1 ratio were also employed as controls. Two microlitres of each lipid mix was spread onto the PVA-coated slide and then dried for 30 min at RT. Slide chambers with silicone isolators (Invitrogen, P18174) were assembled, and the lipid films were hydrated for 20 min at RT by adding 100 µl of 0.75 M sucrose solution. Protein extracts were diluted 1:5 in 0.8 M glucose solution and incubated for 50 min with GUVs (ratio 1:1) in slide chambers before imaging. Confocal LSM images were acquired with a Zeiss LSM 800 using a 40× air objective, and microscopy images were quantified using CellProfiler (Version 4.2.4), while GUVs were detected and filtered based on their rhodamine fluorescence, followed by correlation analysis and fluorescence-based size measurements.

Tunnelling nanotubes (TNTs). Using fluorescence microscopy (Zeiss, Axiovert 200 M) and a 100x oil objective, structures were counted as TNTs if they (i) connected two or more cells, (ii) contained F-actin and iii) did not touch the substrate. Phalloidin-AF546 or phalloidin-AF647 was used to stain F-actin filaments, whereas WGA-AF488 was applied to stain the plasma membrane. For the assessment of autophagic membranes moving between two cells through TNT connections, cocultures of donor and recipient cells were performed at a ratio of 1:1. For TNT inhibition, nocodazole (Sigma, M1404) or latrunculin A (Merck, 428021) was applied to inhibit microtubules and G-actin polymerization, respectively. The TNT index was defined as the number of TNTs per 100 cells.

***C. elegans* strain maintenance**. *Caenorhabditis elegans* strains were grown on NGM (nematode growth medium, 3 g/L NaCl, 17 g/L agar, 2.5 g/L peptone, 5 mg/L cholesterol, 1 mM $MgSO_4$, 1 mM $CaCl_2$, 2.5% v/v KPO_4-buffer pH 6) (KPO_4 buffer: 0.87 M KH_2PO_4, 0.13 M K_2HPO_4) plates seeded with *E. coli* OP50 at 15(°C using standard techniques. During the experiments, the nematodes were kept at 20 °C. The following strains were used in this study and provided by the CGC: N2 (wild-type/WT), VC893: *atg-18(gk378)*, XR1: *abl-1(ok171)*, DA2123: *lgg-1::GFP+rol-6(su1006)* and *E. coli* OP50. The *abl-1(ok171);atg-18(gk378)* and *abl-1(ok171);gfp::lgg-1* strains were generated in this study. OP50 bacterial cultures were prepared by inoculating the bacteria from the glycerol stock in liquid Luria-Bertani broth (LB) medium (10 g/L tryptone, 5 g/L yeast extract, 5 g/L NaCl) overnight at 37 °C and 180 rpm before seeding onto the NGM plates the next day.

***C. elegans* egg isolation**. Gravid adult nematodes were washed off nematode growth media (NGM) plates using water, spun down at 2000 rpm for 2 min and resuspended in bleach solution (2–4% NaOCl, 1.5 M NaOH). The tube was shaken until all worms were lysed and then filled with M9 buffer (3 g/L KH_2PO_4, 6 g/L Na_2HPO_4, 5 g/L NaCl, 1 mM MgSO4). The eggs were pelleted at 2000 rpm for 2 min and washed three times with M9 buffer.

***C. elegans* brood-size assay**. L4 hermaphrodites were singly transferred to NGM/OP50 plates and kept at 20 °C. The hermaphrodites were transferred to a fresh plate every day, and eggs on the previous plate were counted immediately after transfer. Two to three days later, the number of L4/adults hatched and developed from the eggs was determined.

***C. elegans* L1 survival assay**. Eggs were isolated from gravid adult nematodes by hypochlorite treatment and suspended in M9 buffer at a density of 1000 eggs/ml. The liquid culture was incubated at 20 °C and shaken at 180 rpm without the addition of food. Every day for the first week, and afterwards, every 2–3 days, a 50 µl aliquot of the liquid culture was placed on an NGM/OP50 plate. The number of L1 larvae was immediately counted, and after 2–4 days at 20 °C, the number of larvae that developed past the L1 stage was analysed.

***C. elegans* adult lifespan assay**. Nematodes were synchronized by hypochlorite treatment and allowed to grow on NGM/OP50 plates until the L4 larval stage. L4 stage larvae were then transferred to NGM/OP50 plates supplemented with 5 mg/l 5-Fluoro-20-deoxyuridin (FUdR, Sigma–Aldrich, F0503). One hundred nematodes (5 plates with 20 nematodes each) were counted for every strain and set.

Knockdown experiments in *C. elegans* were conducted using RNAi ORF constructs cloned into the pL4440-DEST vector (Horizon Discovery) and transformed into *E. coli* HT115(DE3) feeder bacteria, expressing double stranded (ds)RNA against the following target mRNAs: unc-51 (RCE1182-202301424, CloneId: Y60A3A.1), mml-1 (RCE1182-202299302, CloneId: T20B12.6). Bacterial cultures were prepared by streaking bacteria from the glycerol stock onto LB plates containing ampicillin (100 µg/ml) and tetracycline (12.5 µg/ml). After single colony picking, cultures were maintained in liquid LB medium with antibiotics. Bacterial cultures were seeded onto NGM plates supplemented with 5 mg/l 5-Fluoro-20-deoxyuridin (FUdR, Sigma-Aldrich, F0503), 25 µg/ml Carbenicillin (AppliChem, A1491) and 1 mM Isopropyl-β-D-1-thiogalactopyranosid (IPTG, Sigma-Aldrich, I6758). Nematodes were synchronized by hypochlorite treatment and allowed to grow on NGM/OP50 plates until the L4 larval stage. L4 stage larvae were then transferred to NGM/HT115 plates. Here, 100 nematodes (4 plates with 25 nematodes each) were counted for every strain.

The day of transfer to FUdR-containing plates was considered day 0 of the lifespan. The nematodes were kept at 20°C and counted every 2–3 days. Nematodes were scored dead when they did not respond to gentle prodding with a platinum wire and were then removed from the plate. Missing/dried worms on the plastic of the plate were excluded. Basic survival analysis was performed using OASIS 2[101].

***C. elegans* imaging**. Eggs from nematodes were extracted via hypochlorite treatment and seeded onto NGM/OP50 plates. After 6 and 30 hours, nematodes were washed off the plates with M9 and anaesthetized with 0.1 M NaN_3. L1 Larvae were subsequently mounted onto glass slides with pads of 2.5% agar solution. Images of L1 larvae were acquired using a Zeiss Axiovert 200 M microscope with a 63×1.4 DIC Plan-Apochromat oil-immersion objective. Puncta number and size were quantified using CellProfiler (Version 4.2.1).

RNA extraction and qPCR from *C. elegans*. RNA extraction was performed using a TRIzol/RNeasy hybrid protocol[102]. Eggs were isolated by hypochlorite treatment from gravid adults on 4 10 cm NGM/OP50 plates, and the eggs were dispersed on 15 cm NGM/OP50 dishes. Two days later, L4 larvae were distributed onto NGM/FUdR/OP50 plates (day 0 of lifespan), 1000 nematodes for day 1 and 2000 nematodes for day 11 RNA extraction. On the day of extraction, nematodes were harvested in M9 and washed twice. The nematodes were frozen in liquid nitrogen and quickly thawed to room temperature. RNA was extracted using TRIzol Reagent (Life Technologies, 15596026) as follows. TRIzol Reagent was added to the animals, followed by 15 min of incubation while vortexing repeatedly. Thereafter, chloroform was added, followed by 3 min of incubation, again while vortexing repeatedly. After centrifugation for 15 min at 12,000 × *g*, the aqueous phase was transferred to a new vessel and isopropanol was added and the mixture incubated for 10 min. Then, the mixture was centrifuged at 12,000 × *g* for 10 min, the supernatant discarded, and the pellet resuspended in 75% ethanol. Finally, the RNA was pelleted by centrifugation at 7500 × *g* for 5 min and the supernatant removed. Afterwards, the RNA was resuspended in 100 µl nuclease-free water and further purified using the RNeasy Mini Kit and RNase-free DNase Set (QIAGEN). The RNA concentration was determined using a Nanodrop 1000, and cDNA was prepared from 350 ng/sample in a 30 µl reaction using TaqMan Reverse Transcription Reagents as follows. qPCR (10 µl reaction volume) was performed using SYBR Green PCR Master Mix (Applied Biosystems, 4309155), 2 µl of the cDNA reaction and 0.5 µM of the following primers:

PMP-3_fw 5′-GTTCCCGTGTTCATCACTCAT-3′,
PMP-3_rev 5′-ACACCGTCGAGAAGCTGTAGA-3′,
ATG-18_fw 5′-AGTGCACGTCTTCAAACTTGAG-3′,
ATG-18_rev 5′-TGACTTGGCATATACGCAGAGA-3′.

Protein extraction from *C. elegans*. To obtain synchronous nematodes, eggs were isolated through bleaching and seeded onto NGM plates, which were kept at 20 °C until the L4 larval stage was reached. Then, the nematodes were harvested, washed twice with M9 buffer and kept in M9 buffer in liquid culture at 20 °C with shaking at 150 rpm for 18 h. Subsequently, the nematodes were washed with M9 buffer and lysed by adding hot Laemmli buffer and boiling for 10 min. Chromatin was sheared with a 26 G needle, extracts were centrifuged, and supernatants were used for Western blotting.

Statistics and reproducibility. The statistical analysis methods used in this study are indicated in the legend for each subfigure. Statistical tests and graphs were performed with GraphPad Prism 9.2.0. Data are presented as mean ± standard deviation (SD) in bar graphs or scatter plots. Normal distribution of the data sets was assessed using normality tests and QQ plots. The following parametric tests were applied to data with normal distribution. Two-tailed heteroscedastic *t*-test (Welch's *t* test) was used for pairwise comparisons. One-way ANOVA was used for multiple comparisons with one factor, followed by the Dunnett's or Holm-Sidak post-hoc testing. Two-way ANOVA with Dunnett's or Tukey's post hoc test was used for multiple comparisons with more than one factor. When datasets were not normally distributed, they were logarithmically transformed (X log (Y) or x log (Y + 1)) and when they fit a Gaussian distribution, parametric tests were run using the transformed data. In this case, the graphs presented in this study display original data with statistical analysis resulting from transformed data[103]. If Gaussian distribution was not achieved through logarithmic transformation, Kruskal–Wallis testing was conducted for multiple comparisons. ***C. elegans* lifespan assays were quantified by employing OASIS 2**. The following *P* values were considered significant: $^{*}p < 0.05$; $^{**}p < 0.01$; $^{***}p < 0.001$.

Reporting summary. Further information on research design is available in the Nature Portfolio Reporting Summary linked to this article.

Data availability

Source data for Figures and Supplementary Figures are provided as Supplementary Data File (Supplementary Data 1) and uncropped Western blots are provided in Supplementary Fig. 9 along with this article. Newly generated plasmids have been deposited to Addgene: pGL4.23-WIPI1promotor (Addgene ID 206840), pGL4.23-5xE-box (Addgene ID 206841) and mass spectrometry proteomics data to the ProteomeXchange Consortium via the PRIDE partner repository with the dataset identifier PXD023146.

Received: 22 December 2022; Accepted: 10 August 2023;
Published online: 24 August 2023

References

1. Ohsumi, Y. Historical landmarks of autophagy research. *Cell Res.* **24**, 9–23 (2014).
2. Hansen, M., Rubinsztein, D. C. & Walker, D. W. Autophagy as a promoter of longevity: insights from model organisms. *Nat. Rev. Mol. Cell Biol.* **19**, 579–593 (2018).
3. Aman, Y. et al. Autophagy in healthy aging and disease. *Nat. Aging* **1**, 634–650 (2021).
4. Dikic, I. & Elazar, Z. Mechanism and medical implications of mammalian autophagy. *Nat. Rev. Mol. Cell Biol.* **19**, 349–364 (2018).
5. Klionsky, D. J. et al. Autophagy in major human diseases. *EMBO J.* **40**, e108863 (2021).
6. Mizushima, N. & Levine, B. Autophagy in human diseases. *N. Engl. J. Med.* **383**, 1564–1576 (2020).
7. Proikas-Cezanne, T. et al. WIPI-1alpha (WIPI49), a member of the novel 7-bladed WIPI protein family, is aberrantly expressed in human cancer and is linked to starvation-induced autophagy. *Oncogene* **23**, 9314–9325 (2004).
8. Proikas-Cezanne, T., Takacs, Z., Donnes, P. & Kohlbacher, O. WIPI proteins: essential PtdIns3P effectors at the nascent autophagosome. *J. Cell Sci.* **128**, 207–217 (2015).
9. Bakula, D. et al. WIPI3 and WIPI4 beta-propellers are scaffolds for LKB1-AMPK-TSC signalling circuits in the control of autophagy. *Nat. Commun.* **8**, 15637 (2017).
10. Krick, R. et al. Structural and functional characterization of the two phosphoinositide binding sites of PROPPINs, a beta-propeller protein family. *Proc. Natl. Acad. Sci. USA* **109**, E2042–E2049 (2012).
11. Baskaran, S., Ragusa, M. J., Boura, E. & Hurley, J. H. Two-site recognition of phosphatidylinositol 3-phosphate by PROPPINs in autophagy. *Mol. Cell* **47**, 339–348 (2012).
12. Watanabe, Y. et al. Structure-based analyses reveal distinct binding sites for Atg2 and phosphoinositides in Atg18. *J. Biol. Chem.* **287**, 31681–31690 (2012).
13. Jeffries, T. R., Dove, S. K., Michell, R. H. & Parker, P. J. PtdIns-specific MPR pathway association of a novel WD40 repeat protein, WIPI49. *Mol. Biol. Cell* **15**, 2652–2663 (2004).
14. Proikas-Cezanne, T., Ruckerbauer, S., Stierhof, Y. D., Berg, C. & Nordheim, A. Human WIPI-1 puncta-formation: a novel assay to assess mammalian autophagy. *FEBS Lett.* **581**, 3396–3404 (2007).
15. Gomez-Sanchez, R., Tooze, S. A. & Reggiori, F. Membrane supply and remodeling during autophagosome biogenesis. *Curr. Opin. Cell Biol.* **71**, 112–119 (2021).
16. Samari, H. R. & Seglen, P. O. Inhibition of hepatocytic autophagy by adenosine, aminoimidazole-4-carboxamide riboside, and N6-mercaptopurine riboside. Evidence for involvement of amp-activated protein kinase. *J. Biol. Chem.* **273**, 23758–23763 (1998).
17. Blommaart, E. F., Luiken, J. J., Blommaart, P. J., van Woerkom, G. M. & Meijer, A. J. Phosphorylation of ribosomal protein S6 is inhibitory for autophagy in isolated rat hepatocytes. *J. Biol. Chem.* **270**, 2320–2326 (1995).
18. Lardeux, B. R. & Mortimore, G. E. Amino acid and hormonal control of macromolecular turnover in perfused rat liver. Evidence for selective autophagy. *J. Biol. Chem.* **262**, 14514–14519 (1987).
19. Hosokawa, N. et al. Nutrient-dependent mTORC1 association with the ULK1-Atg13-FIP200 complex required for autophagy. *Mol. Biol. Cell* **20**, 1981–1991 (2009).

20. Jung, C. H. et al. ULK-Atg13-FIP200 complexes mediate mTOR signaling to the autophagy machinery. *Mol. Biol. Cell* **20**, 1992–2003 (2009).
21. Ganley, I. G. et al. ULK1.ATG13.FIP200 complex mediates mTOR signaling and is essential for autophagy. *J. Biol. Chem.* **284**, 12297–12305 (2009).
22. Petiot, A., Ogier-Denis, E., Blommaart, E. F., Meijer, A. J. & Codogno, P. Distinct classes of phosphatidylinositol 3'-kinases are involved in signaling pathways that control macroautophagy in HT-29 cells. *J. Biol. Chem.* **275**, 992–998 (2000).
23. Ktistakis, N. T. ER platforms mediating autophagosome generation. *Biochim. Biophys. Acta Mol. Cell Biol. Lipids* **1865**, 158433 (2020).
24. Axe, E. L. et al. Autophagosome formation from membrane compartments enriched in phosphatidylinositol 3-phosphate and dynamically connected to the endoplasmic reticulum. *J. Cell Biol.* **182**, 685–701 (2008).
25. Hayashi-Nishino, M. et al. A subdomain of the endoplasmic reticulum forms a cradle for autophagosome formation. *Nat. Cell Biol.* **11**, 1433–1437 (2009).
26. Bakula, D., Mueller, A. J. & Proikas-Cezanne, T. WIPI beta-propellers function as scaffolds for STK11/LKB1-AMPK and AMPK-related kinase signaling in autophagy. *Autophagy* **14**, 1082–1083 (2018).
27. Polson, H. E. et al. Mammalian Atg18 (WIPI2) localizes to omegasome-anchored phagophores and positively regulates LC3 lipidation. *Autophagy* **6**, 506–522 (2010).
28. Dooley, H. C. et al. WIPI2 links LC3 conjugation with PI3P, autophagosome formation, and pathogen clearance by recruiting Atg12-5-16L1. *Mol. Cell* **55**, 238–252 (2014).
29. Fracchiolla, D., Chang, C., Hurley, J. H. & Martens, S. A PI3K-WIPI2 positive feedback loop allosterically activates LC3 lipidation in autophagy. *J. Cell Biol.* **219**, e201912098 (2020).
30. Thost, A. K., Donnes, P., Kohlbacher, O. & Proikas-Cezanne, T. Fluorescence-based imaging of autophagy progression by human WIPI protein detection. *Methods* **75**, 69–78 (2015).
31. Yogalingam, G. & Pendergast, A. M. Abl kinases regulate autophagy by promoting the trafficking and function of lysosomal components. *J. Biol. Chem.* **283**, 35941–35953 (2008).
32. Kabeya, Y. et al. LC3, a mammalian homologue of yeast Apg8p, is localized in autophagosome membranes after processing. *EMBO J.* **19**, 5720–5728 (2000).
33. Tanida, I., Tanida-Miyake, E., Ueno, T. & Kominami, E. The human homolog of Saccharomyces cerevisiae Apg7p is a Protein-activating enzyme for multiple substrates including human Apg12p, GATE-16, GABARAP, and MAP-LC3. *J. Biol. Chem.* **276**, 1701–1706 (2001).
34. Bjorkoy, G. et al. p62/SQSTM1 forms protein aggregates degraded by autophagy and has a protective effect on huntingtin-induced cell death. *J. Cell Biol.* **171**, 603–614 (2005).
35. Lamark, T., Svenning, S. & Johansen, T. Regulation of selective autophagy: the p62/SQSTM1 paradigm. *Essays Biochem.* **61**, 609–624 (2017).
36. Sanchez-Arevalo Lobo, V. J. et al. Dual regulation of Myc by Abl. *Oncogene* **32**, 5261–5271 (2013).
37. Sears, R. et al. Multiple Ras-dependent phosphorylation pathways regulate Myc protein stability. *Genes Dev.* **14**, 2501–2514 (2000).
38. Zurzolo, C. Tunneling nanotubes: reshaping connectivity. *Curr. Opin. Cell Biol.* **71**, 139–147 (2021).
39. Lystad, A. H. et al. Distinct functions of ATG16L1 isoforms in membrane binding and LC3B lipidation in autophagy-related processes. *Nat. Cell Biol.* **21**, 372–383 (2019).
40. Itakura, E. & Mizushima, N. Characterization of autophagosome formation site by a hierarchical analysis of mammalian Atg proteins. *Autophagy* **6**, 764–776 (2010).
41. Mercer, T. J., Gubas, A. & Tooze, S. A. A molecular perspective of mammalian autophagosome biogenesis. *J. Biol. Chem.* **293**, 5386–5395 (2018).
42. Han, W. et al. EGFR tyrosine kinase inhibitors activate autophagy as a cytoprotective response in human lung cancer cells. *PLoS ONE* **6**, e18691 (2011).
43. El Azreq, M. A. et al. Discoidin domain receptor 1 promotes Th17 cell migration by activating the RhoA/ROCK/MAPK/ERK signaling pathway. *Oncotarget* **7**, 44975–44990 (2016).
44. Kharbanda, S. et al. Activation of MEK kinase 1 by the c-Abl protein tyrosine kinase in response to DNA damage. *Mol. Cell Biol.* **20**, 4979–4989 (2000).
45. Khatri, A., Wang, J. & Pendergast, A. M. Multifunctional Abl kinases in health and disease. *J. Cell Sci.* **129**, 9–16 (2016).
46. Wang, J. Y. The capable ABL: what is its biological function? *Mol. Cell Biol.* **34**, 1188–1197 (2014).
47. Kimura, S., Noda, T. & Yoshimori, T. Dissection of the autophagosome maturation process by a novel reporter protein, tandem fluorescent-tagged LC3. *Autophagy* **3**, 452–460 (2007).
48. Braun, T. P., Eide, C. A. & Druker, B. J. Response and resistance to BCR-ABL1-targeted therapies. *Cancer Cell* **37**, 530–542 (2020).
49. Yang, J. et al. Discovery and characterization of a cell-permeable, small-molecule c-Abl kinase activator that binds to the myristoyl binding site. *Chem. Biol.* **18**, 177–186 (2011).
50. Kumar, V. et al. Regulation of the rapamycin and FKBP-target 1/mammalian target of rapamycin and cap-dependent initiation of translation by the c-Abl protein-tyrosine kinase. *J. Biol. Chem.* **275**, 10779–10787 (2000).
51. Vehlow, A. et al. Interaction of discoidin domain receptor 1 with a 14-3-3-beclin-1-Akt1 complex modulates glioblastoma therapy sensitivity. *Cell Rep.* **26**, 3672–3683.e3677 (2019).
52. Settembre, C. et al. TFEB controls cellular lipid metabolism through a starvation-induced autoregulatory loop. *Nat. Cell Biol.* **15**, 647–658 (2013).
53. Bordi, M. et al. A gene toolbox for monitoring autophagy transcription. *Cell Death Dis.* **12**, 1044 (2021).
54. Tsuyuki, S. et al. Detection of WIPI1 mRNA as an indicator of autophagosome formation. *Autophagy* **10**, 497–513 (2014).
55. Anderson, N. G., Maller, J. L., Tonks, N. K. & Sturgill, T. W. Requirement for integration of signals from two distinct phosphorylation pathways for activation of MAP kinase. *Nature* **343**, 651–653 (1990).
56. Shi, Y., Alin, K. & Goff, S. P. Abl-interactor-1, a novel SH3 protein binding to the carboxy-terminal portion of the Abl protein, suppresses v-abl transforming activity. *Genes Dev.* **9**, 2583–2597 (1995).
57. Grandori, C., Cowley, S. M., James, L. P. & Eisenman, R. N. The Myc/Max/Mad network and the transcriptional control of cell behavior. *Annu. Rev. Cell Dev. Biol.* **16**, 653–699 (2000).
58. Bousset, K., Henriksson, M., Luscher-Firzlaff, J. M., Litchfield, D. W. & Luscher, B. Identification of casein kinase II phosphorylation sites in Max: effects on DNA-binding kinetics of Max homo- and Myc/Max heterodimers. *Oncogene* **8**, 3211–3220 (1993).
59. Gupta, S., Seth, A. & Davis, R. J. Transactivation of gene expression by Myc is inhibited by mutation at the phosphorylation sites Thr-58 and Ser-62. *Proc. Natl. Acad. Sci. USA* **90**, 3216–3220 (1993).
60. Robinson, M. J., Stippec, S. A., Goldsmith, E., White, M. A. & Cobb, M. H. A constitutively active and nuclear form of the MAP kinase ERK2 is sufficient for neurite outgrowth and cell transformation. *Curr. Biol.* **8**, 1141–1150 (1998).
61. Kreft, L. et al. ConTra v3: a tool to identify transcription factor binding sites across species, update 2017. *Nucleic Acids Res.* **45**, W490–W494 (2017).
62. Blackwood, E. M. & Eisenman, R. N. Max: a helix-loop-helix zipper protein that forms a sequence-specific DNA-binding complex with Myc. *Science* **251**, 1211–1217 (1991).
63. Artal-Martinez de Narvajas, A. et al. Epigenetic regulation of autophagy by the methyltransferase G9a. *Mol. Cell Biol.* **33**, 3983–3993 (2013).
64. Tu, W. B. et al. MYC interacts with the G9a histone methyltransferase to drive transcriptional repression and tumorigenesis. *Cancer Cell* **34**, 579–595.e578 (2018).
65. Perna, D. et al. Genome-wide mapping of Myc binding and gene regulation in serum-stimulated fibroblasts. *Oncogene* **31**, 1695–1709 (2012).
66. Cordero Cervantes, D. & Zurzolo, C. Peering into tunneling nanotubes-The path forward. *EMBO J.* **40**, e105789 (2021).
67. Dilsizoglu Senol, A. et al. alpha-Synuclein fibrils subvert lysosome structure and function for the propagation of protein misfolding between cells through tunneling nanotubes. *PLoS Biol.* **19**, e3001287 (2021).
68. Rustom, A., Saffrich, R., Markovic, I., Walther, P. & Gerdes, H. H. Nanotubular highways for intercellular organelle transport. *Science* **303**, 1007–1010 (2004).
69. Vignais, M. L., Caicedo, A., Brondello, J. M. & Jorgensen, C. Cell connections by tunneling nanotubes: effects of mitochondrial trafficking on target cell metabolism, homeostasis, and response to therapy. *Stem Cells. Int.* **2017**, 6917941 (2017).
70. Abounit, S. et al. Tunneling nanotubes spread fibrillar alpha-synuclein by intercellular trafficking of lysosomes. *EMBO J.* **35**, 2120–2138 (2016).
71. Lapierre, L. R. & Hansen, M. Lessons from *C. elegans*: signaling pathways for longevity. *Trends Endocrinol. Metab.* **23**, 637–644 (2012).
72. Toth, M. L. et al. Longevity pathways converge on autophagy genes to regulate life span in *Caenorhabditis elegans*. *Autophagy* **4**, 330–338 (2008).
73. Deng, X. et al. *Caenorhabditis elegans* ABL-1 antagonizes p53-mediated germline apoptosis after ionizing irradiation. *Nat. Genet.* **36**, 906–912 (2004).
74. Takacs, Z. et al. ATG-18 and EPG-6 are both required for autophagy but differentially contribute to lifespan control in *Caenorhabditis elegans*. *Cells.* https://doi.org/10.3390/cells8030236 (2019).
75. Lu, Q. et al. The WD40 repeat PtdIns(3)P-binding protein EPG-6 regulates progression of omegasomes to autophagosomes. *Dev. Cell* **21**, 343–357 (2011).
76. Behrends, C., Sowa, M. E., Gygi, S. P. & Harper, J. W. Network organization of the human autophagy system. *Nature* **466**, 68–76 (2010).
77. Melendez, A. et al. Autophagy genes are essential for dauer development and life-span extension in *C. elegans*. *Science* **301**, 1387–1391 (2003).
78. Pickett, C. L., Breen, K. T. & Ayer, D. E. A *C. elegans* Myc-like network cooperates with semaphorin and Wnt signaling pathways to control cell migration. *Dev. Biol.* **310**, 226–239 (2007).
79. McFerrin, L. G. & Atchley, W. R. Evolution of the Max and Mlx networks in animals. *Genome Biol. Evol.* **3**, 915–937 (2011).

80. Johnson, D. W. et al. The *Caenorhabditis elegans* Myc-Mondo/Mad complexes integrate diverse longevity signals. *PLoS Genet.* **10**, e1004278 (2014).
81. Xiao, F. H. et al. Transcriptome evidence reveals enhanced autophagy-lysosomal function in centenarians. *Genome Res.* **28**, 1601–1610 (2018).
82. Hofmann, J. W. et al. Reduced expression of MYC increases longevity and enhances healthspan. *Cell* **160**, 477–488 (2015).
83. Nieto-Torres, J. L. & Hansen, M. Macroautophagy and aging: The impact of cellular recycling on health and longevity. *Mol. Aspects Med.* **82**, 101020 (2021).
84. D'Arcangelo, D. et al. WIPI1, BAG1, and PEX3 autophagy-related genes are relevant melanoma markers. *Oxid. Med. Cell Longev.* **2018**, 1471682 (2018).
85. Bjedov, I. et al. Fine-tuning autophagy maximises lifespan and is associated with changes in mitochondrial gene expression in Drosophila. *PLoS Genet.* **16**, e1009083 (2020).
86. Nemazanyy, I. et al. Defects of Vps15 in skeletal muscles lead to autophagic vacuolar myopathy and lysosomal disease. *EMBO Mol. Med.* **5**, 870–890 (2013).
87. Doench, J. G. et al. Optimized sgRNA design to maximize activity and minimize off-target effects of CRISPR-Cas9. *Nat. Biotechnol.* **34**, 184–191 (2016).
88. Wegner, M. et al. Circular synthesized CRISPR/Cas gRNAs for functional interrogations in the coding and noncoding genome. *Elife* https://doi.org/10.7554/eLife.42549 (2019).
89. Diehl, V. et al. Minimized combinatorial CRISPR screens identify genetic interactions in autophagy. *Nucleic Acids Res.* **49**, 5684–5704 (2021).
90. Schussele, D. S. et al. Autophagy profiling in single cells with open source CellProfiler-based image analysis. *Autophagy* **19**, 338–351 (2023).
91. Raudvere, U. et al. g:Profiler: a web server for functional enrichment analysis and conversions of gene lists (2019 update). *Nucleic Acids Res.* **47**, W191–W198 (2019).
92. Yu, G., Wang, L. G., Han, Y. & He, Q. Y. clusterProfiler: an R package for comparing biological themes among gene clusters. *OMICS* **16**, 284–287 (2012).
93. Borchert, N. et al. Proteogenomics of Pristionchus pacificus reveals distinct proteome structure of nematode models. *Genome Res.* **20**, 837–846 (2010).
94. Rappsilber, J., Mann, M. & Ishihama, Y. Protocol for micro-purification, enrichment, pre-fractionation and storage of peptides for proteomics using StageTips. *Nat. Protoc.* **2**, 1896–1906 (2007).
95. Kliza, K. et al. Internally tagged ubiquitin: a tool to identify linear polyubiquitin-modified proteins by mass spectrometry. *Nat. Methods* **14**, 504–512 (2017).
96. Taumer, C. et al. Parallel reaction monitoring on a Q Exactive mass spectrometer increases reproducibility of phosphopeptide detection in bacterial phosphoproteomics measurements. *J. Proteomics* **189**, 60–66 (2018).
97. Elias, J. E. & Gygi, S. P. Target-decoy search strategy for increased confidence in large-scale protein identifications by mass spectrometry. *Nat. Methods* **4**, 207–214 (2007).
98. Franz-Wachtel, M. et al. Global detection of protein kinase D-dependent phosphorylation events in nocodazole-treated human cells. *Mol. Cell Proteomics* **11**, 160–170 (2012).
99. Schmitt, M. et al. Proteogenomics reveals perturbed signaling networks in malignant melanoma cells resistant to BRAF inhibition. *Mol. Cell Proteomics* **20**, 100163 (2021).
100. Proikas-Cezanne, T. & Pfisterer, S. G. Assessing mammalian autophagy by WIPI-1/Atg18 puncta formation. *Methods Enzymol.* **452**, 247–260 (2009).
101. Han, S. K. et al. OASIS 2: online application for survival analysis 2 with features for the analysis of maximal lifespan and healthspan in aging research. *Oncotarget* **7**, 56147–56152 (2016).
102. Van Gilst, M. R., Hadjivassiliou, H., Jolly, A. & Yamamoto, K. R. Nuclear hormone receptor NHR-49 controls fat consumption and fatty acid composition in *C. elegans*. *PLoS Biol.* **3**, e53 (2005).
103. Olivier, J., Johnson, W. D. & Marshall, G. D. The logarithmic transformation and the geometric mean in reporting experimental IgE results: what are they and when and why to use them? *Ann. Allergy Asthma Immunol.* **100**, 333–337 (2008).

Acknowledgements

This work was funded by the following grants to T.P.-C.: the Deutsche Forschungsgemeinschaft (DFG, German Research Foundation) Germany's Excellence Strategy Project-ID 390900677 – EXC 2180 (iFIT project 10076-1), the DFG Project-ID 31490540 – TRR 209 (project B02), the DFG Project-ID 323732846 – FOR 2625 (project 1), the DFG Project-ID 259130777 – SFB 1177 (project E03), the DFG Project-ID 327043846 – GRK 2364 (project 12), the DFG Project-ID 464254052 – GRK 2816 (project 6). R.L.K. was funded by the DFG Project-ID 460056461. E.-L.E. was funded by the Academy of Finland (grant 286787). A.S. received funding from the Research Council of Norway through its Centres of Excellence funding scheme (Project: 262652) and FRIPRO (Project: 249753). T.P.-C., E.-L.E. and A.S. received further funding from a Marie Skłodowska-Curie ETN grant under the European Union's Horizon 2020 Research and Innovation Programme (Grant Agreement No 765912). We thank Andrew Holland (John Hopkins School of Medicine, Baltimore, MD, USA) for providing puromycin-sensitive hTERT-U2OS Cas9 cells, and Koraljka Husnjak (Frankfurt CRISPR/Cas Screening Center (FCSC), Goethe University Frankfurt am Main, Germany) for providing pLenti_mx2-PGK-BSD plasmid used for generation of WIPI1 knock-out cells. We appreciate the initial data collection by Mona Grimmel, Amelie Müller, Ann-Katrin Thost, Marcel Wacker, Theresia Zuleger (T.P.-C. laboratory), and pathway enrichment analysis by Praveen Baskaran and Sven Nahnsen (Quantitative Biology Center, Eberhard Karls University Tuebingen, Germany). We acknowledge Ana Tapia Abellan and Alexander Weber (Interfaculty Institute of Cell Biology, Eberhard Karls University of Tübingen) for technical help and availability of the Synergy Neo2 Multi-mode Microplate reader. We thank the Electron Microscopy Unit (Institute of Biotechnology, University of Helsinki, Finland) for technical help and availability of instruments.

Author contributions

K.S., M.L.H., C.J.P.-M., D.S.S., C.H., Z.T., A.L.D.O., S.G.P., and P.K.H. conducted the experiments and analysed the data. C.C. and A.S. provided ATG16L1-deficient and NLS-mScarlet U2OS cell models, and A.G., M.K. generated WIPI1-deficient U2OS cells. M.F.-W. and B.M. conducted mass spectrometry. E.-L.E. conducted CLEM analysis. R.K. and T.P.-C. conceived GUV experiments and analysed data. A.S. and T.P.-C. conceived TNT experiments with ATG16L1-deficient cells and analysed data. T.P.-C. acquired the main funding, conceived, and designed the study, analysed the data and wrote the manuscript. All authors contributed to the drafting of the manuscript, approved the final version of the manuscript, and agreed on the content and conclusions.

Funding

Open Access funding enabled and organized by Projekt DEAL.

Competing interests

The authors declare no competing interests.

Additional information

Supplementary information The online version contains supplementary material available at https://doi.org/10.1038/s42003-023-05236-9.

Correspondence and requests for materials should be addressed to Tassula Proikas-Cezanne.

Peer review information *Communications Biology* thanks Shuhei Nakamura and the other, anonymous, reviewer(s) for their contribution to the peer review of this work. Primary Handling Editor: Manuel Breuer. A peer review file is available.